

Eigenmode Analysis in Plasmonics: Application to Second Harmonic Generation and Electron Energy Loss Spectroscopy

Thèse N° 9265

Présentée le 15 février 2019

à la Faculté des sciences et techniques de l'ingénieur
Laboratoire de nanophotonique et métrologie
Programme doctoral en photonique

pour l'obtention du grade de Docteur ès Sciences

par

GABRIEL DAVID BERNASCONI

Acceptée sur proposition du jury

Prof. J.-E. Moser, président du jury
Prof. O. Martin, Dr J. Butet, directeurs de thèse
Prof. M. Kauranen, rapporteur
Prof. U. Hohenester, rapporteur
Prof. C. Hébert, rapporteuse

2019

I am no poet, but if you think for yourselves,
as I proceed, the facts will form a poem in your minds.

—Michael Faraday

We may find illustrations of the highest doctrines of science
in games and gymnastics,
in travelling by land and by water,
in storms of the air and of the sea,
and wherever there is matter in motion.

—James C. Maxwell

Abstract

Eigenmodes are central to the study of resonant phenomena in all areas of physics. However, their use in nano-optics seems to have been hindered and delayed for various reasons. First, due to their small size, the response of nanostructures to a far-field optical excitation is mainly dipolar. Thus, preliminary studies of nanosystems through optical methods meant that only very few eigenmodes of the system were probed, and a complete eigenmode theory was not required. Second, rigorously defining eigenmodes of an open and lossy cavity is far from trivial. Finally, only few geometries allow for an analytical solution of Maxwell's equations that can be expressed in terms of modes, rendering the use of numerical methods mandatory to study non-trivial shapes. On the other hand, modern spectroscopy techniques based on fast electron excitation, instead of optical excitation, allow going beyond the above-mentioned dipolar regime and enable the observation of high order modes. In addition, the generation of second harmonic light (SHG) by nanoparticles permits revealing higher order modes that weakly couple to planewave far-field probing. Thus, to be able to analyze the data collected with such experimental methods and comprehend them in order to make appropriate nanostructure designs, one needs to develop suitable numerical tools for the computation of eigenmodes. This is the focus of this thesis, where eigenmodes are used throughout to analyze and understand experimental and numerical results.

First, different approaches used to define and compute eigenmodes are presented in details together with the surface integral equation method used in this manuscript.

The second chapter presents the use of eigenmodes to study the SHG in plasmonic nanostructures. A single mode is used as an SHG source to disentangle the modal contributions from different SHG channels. For three different nanostructures, the dipolar mode gives a pure quadrupolar second harmonic (SH) response. Then, the interplay of dipolar and quadrupolar SH radiations in nanorods of different sizes is revealed through a multipolar analysis, explaining the experimental observation of the flip between forward and backward maximum SH emissions. Finally, the dynamics of the SHG from a silver nanorod generated by short pulses is investigated. By tuning the spectral position and width of the pulses, the dynamics of a single mode is observed, both in the linear and SH responses, and fits extremely well with a harmonic oscillator model.

The last chapter presents the utilization of the eigenmodes to interpret electron energy loss spectroscopy (EELS) measurements. An alternative approach to compute EELS

signal is presented, revealing the different paths through which the energy of the electron is dissipated. Instead of computing the work done by the electron against the scattered electric field, the Ohmic and the radiation losses are evaluated. Then, heterodimers with several shapes and compositions are studied. A rich variety of modes is found, due to the additional degree of freedom associated with the different metals. Dolmen shaped nanostructures are also investigated in great details. A rigorous analysis of the eigenmode evolution when the central horizontal nanorod is moved is performed. Finally, we study the EELS for three iterations of a Koch snowflake nanoantenna. The evolution of the modes with the iteration of the fractal is analysed and the modes are linked to the experimental EELS map.

Keywords: plasmonics, second harmonic generation, nonlinear optics, eigenmode, eigenfrequency, simulations, surface integral equation, electron energy loss spectroscopy.

Résumé

Dans tous les domaines de la physique, les modes propres constituent un outil important. Cependant, leur utilisation en nano-optique a été entravée pour diverses raisons. Premièrement, de par leurs petites tailles, la réponse des nanostructures à une excitation optique en onde plane est avant tout dipolaire. De ce fait, les premières études optiques de nanosystèmes ne sondaient qu'une petite partie des modes du système et une théorie complète des modes n'était pas requise. Ensuite, définir rigoureusement les modes d'une cavité ouverte et avec pertes s'est révélé très complexe. Enfin, peu de géométries permettent des solutions analytiques pour les modes, rendant l'utilisation de méthodes numériques obligatoire pour l'étude de formes non-triviales. En revanche, les techniques de spectroscopies à l'aide d'excitation par électron rapide, au lieu d'une excitation optique, permettent de surpasser la limite dipolaire et autorise l'observation de modes de haut ordre. De plus, la génération de seconde harmonique (GSH) par les nanoparticules permet d'observer des modes faiblement couplés aux excitations en champ lointain. Pour ces raisons, et afin d'être capable d'analyser les données venant de telles expériences ainsi que de les comprendre pour concevoir des nanostructures adaptées, il faut développer des méthodes numériques adéquates de calculs de mode. C'est le point central de cette thèse, où les modes sont utilisés pour l'analyse et la compréhension de données expérimentale et numérique.

Les approches utilisées pour définir et calculer les modes est d'abord présentée, ainsi que la méthode numérique d'équations intégrales de surfaces utilisée tout dans ce manuscrit. Le deuxième chapitre présente l'utilisation des modes pour l'étude de la GSH de nanostructure plasmonique. Un unique mode est utilisé comme source de GSH afin de désentrelacer la contribution modale de différents canaux de GSH. Différentes nanostructures sont étudiées, et dans chaque cas un mode dipolaire mène à une réponse quadrupolaire de seconde harmonique (SH). Ensuite, l'interaction des radiations dipolaire et quadrupolaire en SH de nano-bâtonnets de différentes tailles est révélée par une analyse multipolaire, expliquant ainsi le changement de direction d'émission maximale de SH. Finalement, la dynamique de la GSH d'un nano-bâtonnets d'argent générée par des pulses courts est étudiée. En réglant les paramètres du pulse, la dynamique d'un seul mode est observée, dans les réponses linéaire et SH, et est en accord avec un modèle d'oscillateur harmonique. Le dernier chapitre présente l'utilisation des modes pour l'analyse de mesures par spectroscopie de perte d'énergie des électrons (EELS). Un procédé alternatif pour le calcul du EELS est proposé, révélant les différents chemins par lesquels l'électron perd

de l'énergie. Au lieu du travail fait par l'électron contre le champ diffusé, les pertes Ohmique et radiative sont additionnées. Ensuite, des hétéro-dimères de diverse formes et compositions sont étudiés. Une grande variété de modes apparaît, due au degré de liberté additionnel venant des différents métaux. Des nanostructures en forme de dolmens sont aussi étudiées en détails. Une analyse de l'évolution des modes lorsque la partie centrale de la structure est déplacée est effectuée. Finalement, le EELS des trois premières itérations d'une nano-antenne flocon de Koch est étudiée. Les modes des différentes itérations sont analysés, et mis en correspondance avec les cartes EELS expérimentale.

Mots clés : plasmonique, generation de second harmonique, optique non-linéaire, mode propre, fréquence propre, simulations, equation integrale de surface, spectroscopie de perte d'énergie des électrons.

Contents

Abstract (English/Français)	v
Introduction and Thesis Objectives	1
Thesis Objectives and Organization	1
Plasmonics	2
Second Harmonic Generation	5
Electron Energy Loss Spectroscopy	8
Eigenmodes	10
Surface Integral Equation	12
Bibliography	20
1 Eigenmode Analysis	21
1.1 Theory	21
1.2 Numerical Methods	27
1.3 Conclusion	40
Bibliography	44
2 Eigenmode Analysis and Second-Harmonic Generation	45
2.1 Mode Analysis of Second-Harmonic Generation in Plasmonic Nanostructures	46
2.2 Revealing a Mode Interplay That Controls Second-Harmonic Radiation in Gold Nanoantennas	72
2.3 Dynamics of Second Harmonic Generation in a Plasmonic Silver Nanorod	92
3 Eigenmode Analysis and Electron Energy Loss Spectroscopy	115
3.1 Where does the Energy go in Electron Energy Loss Spectroscopy of Nanostructures?	116
3.2 Mode Coupling in Plasmonic Heterodimers Probed with Electron Energy Loss Spectroscopy	142
3.3 Mode Evolution in Strongly Coupled Plasmonic Dolmens Fabricated by Templated Assembly	170
3.4 Self-Similarity of Plasmon Edge Modes on Koch Fractal Antennas	193

Contents

4 Conclusion and Outlook	225
Conclusion	225
Future Developments	227
Bibliography	230
Publications and Conferences	231
Acknowledgements	234
Curriculum Vitae	237

Introduction and Thesis Objectives

Thesis objectives and organization

Plasmonics is one of the major topics in the current nano-optics research and holds many promises regarding applications in sensing and spectroscopy [1, 2], nonlinear and ultrafast optics [3, 4], enhancement of emission processes [5], light control at the nanoscale [6, 7] and metasurfaces [8, 9]. This diversity of applications stems principally from two tightly related properties of surface plasmons, namely the electromagnetic field confinement at the nanometer scale and the resulting strong field enhancement. The former effect enables the control of light well below the conventional half-wavelength diffraction limit [10], allowing for example the creation of metasurfaces, where elements need to be appreciably smaller than the wavelength of the light that is to be controlled [11]. The latter effect enables all sorts of enhanced optical molecular interactions [12, 13]. Furthermore, nonlinear effects that depend on higher powers of the light intensity take direct advantage of the field enhancement [3, 14]. Additionally, the resonance frequencies of plasmonic systems are particularly sensitive to the electrical properties of the local environment, making them well suited for localized and extremely sensitive probes [2]. Finally, the small mode volume associated with the plasmonic resonances offers a perfect tool for decay-rate enhancement of single emitters [5].

In all these applications, the resonances supported by plasmonic systems (localized entities or extended surfaces) play a fundamental role. Although the study of such resonances was initially often limited to dipolar contributions, resonances due to higher order modes are now routinely used and engineered to increase the efficiency and versatility of plasmonic nanostructures. Consequently, there is a need for powerful numerical methods that guide scientists in the design of plasmonic systems and in the subsequent analysis of diverse spectroscopy measurements.

This thesis objective is to develop numerical methods for the computation of eigenmodes in plasmonic systems and to use them for the analysis and interpretation of experimental

results. The first chapter presents elements of the theory pertaining to the eigenmodes, followed by the description of the numerical methods I have implemented for their search. The next two chapters are composed by seven articles I have published in peer-reviewed journals. Throughout those two chapters, numerical computations based on a surface integral equation (SIE) method are used to analyse experimental results.

The second chapter deals with the use of eigenmodes in the scope of second harmonic generation (SHG) in plasmonic nanostructure. The first article, Sec. 2.1, presents the method initially implemented to compute the eigenmodes (see Sec. 1.2 for more details) and its application to the study of SHG when the fundamental sources are given by a mode as opposed to the linear response to an excitation. In Sec. 2.2 the SHG of nanorods with different sizes is analysed through a multipolar decomposition with a link to the eigenmodes. Finally, in Sec. 2.3, the dynamical SHG response of a silver nanorod excited by femtosecond Gaussian pulses is numerically studied and the role of the eigenmodes is investigated in details.

The third chapter is concerned with the analysis of electron energy loss spectroscopy (EELS) data. First, in Sec. 3.1, I describe the implementation of EELS simulations in the SIE framework as well as a novel way to compute EELS that reveals the different loss channels contributing to the signal. Then, in the following three articles, experimental EELS spectra and maps are systematically compared to numerical simulations and to the eigenmodes of the different systems. Section 3.2 presents the study of dimers of compositionally asymmetric particles with different shapes and materials, Sec. 3.3 deals with dolmen shaped nanostructures and investigates the eigenmodes for different geometries and, finally, Sec. 3.4 presents the plasmonic eigenmodes of the first three iterations of a Koch snowflake fractal nano-antenna.

The remainder of this introduction briefly presents the five principal topics of this thesis, namely plasmonics, SHG, EELS, eigenmodes, and the SIE method.

Plasmonics

Plasmonics is the study of the interaction of light with metals [15]. In everyday life, this interaction is normally limited to an almost total reflection of light by metallic objects, mirrors being often made of aluminium or silver smooth surfaces. However, in certain cases, some peculiar phenomena can be observed. A first example is the colour of colloidal metals, i.e. metallic micro/ nano-particles in solution. They were already, although without much control, used to stain glass in the 4th century with the famous example of the Lycurgus cup [16], but it was not until the 19th century that colloidal metals were scientifically investigated. Faraday, in 1847, was the first to suggest that the vivid colour of gold colloids, strikingly different from bulk gold, is due to the small (nano) sizes of the particles, and that different sizes result in different colours [17]. Later on,

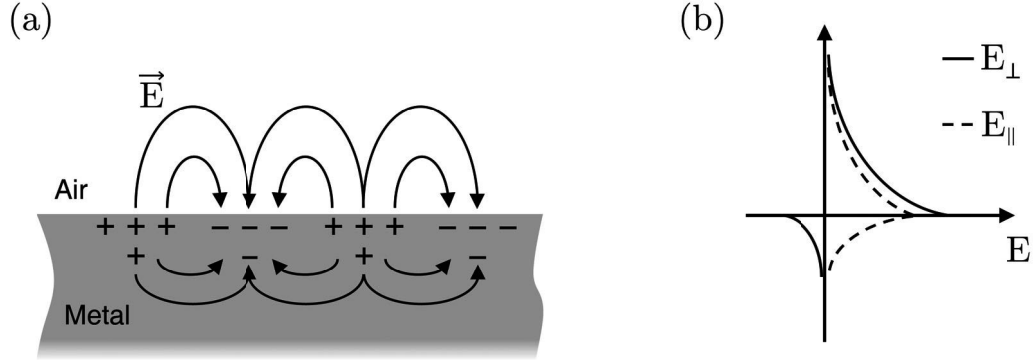


Figure 1 – Sketch of a SPP. (a) Negative charges are oscillating near the surface in the direction parallel to the interface. Note that due to the momentum mismatch with free-space light, this configuration of charges does not radiate. (b) Amplitude of the normal (\perp) and parallel (\parallel) components of the electric field. Notice the change of sign of the normal component at the interface due to the negative permittivity of the metal.

the full theory of electromagnetic wave scattering by a sphere proposed by Mie in 1908 gave the mathematical tools to explain and confirm the observations and suppositions of Faraday [18]. Another example is the anomalous reflection of light on structured metal films, first observed by Wood in 1902 [19]. This observation can be explained by the excitation of a surface wave by the impinging light as was proposed by Fano in 1941 [20], using the theory of surface waves previously developed by Sommerfeld [21] and Zenneck [22], respectively in 1899 and 1907. These two experimental observations and the corresponding theoretical analysis can be considered as the first scientific investigations in plasmonics and nano-optics.

A surface plasmon polaritons (SPP), the surface wave proposed by Sommerfeld, is now understood to be a coupled state (polariton) between light and electrons oscillations (surface plasmon) at the surface of a metal. From Maxwell's equations, it naturally arises as propagating solutions at the interface between a dielectric (with a positive permittivity, $\epsilon > 0$) and a metal ($\epsilon < 0$). It is strongly confined to the surface owing to the exponential (evanescent) decay of its field in the two directions normal to the surface, as well as to be excitable only by TM waves, i.e. waves having an electric field along the propagation direction. Figure 1 pictures a sketch of a SPP, showing a snapshot of the free charges oscillations and associated fields. One can see that, to be able to move the charges back and forth, there must indeed be an electric field in that direction. Furthermore, it appears that the SPP dispersion relation, the relation between momentum and frequency, makes them impossible to excite by simply shining light onto the surface. Indeed, for a given frequency, SPPs have a momentum larger than that of a planewave propagating in vacuum, and one thus needs to give an additional momentum to light in order for it to

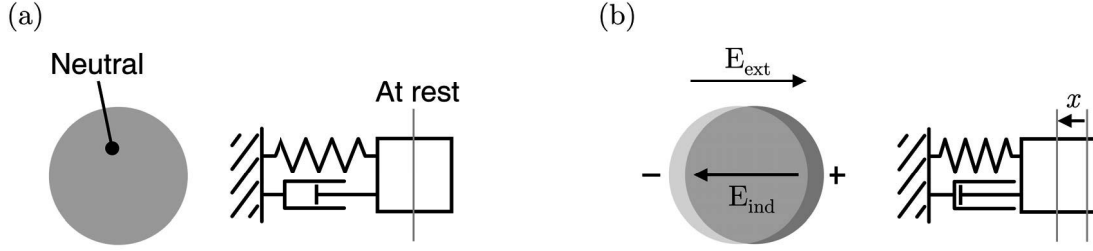


Figure 2 – Sketch of a LSPR on a spherical nanoparticle and an analogous damped spring mass system. (a) Metallic nano-particle at rest. (b) An external electric field E_{ext} displaces the free electrons cloud, creating a negative charge surplus on one side and leaving a net positive charge on the other side.

couple to SPPs. This can be achieved with a grating, as in Wood’s experiment, or by using the evanescent wave created by total internal reflection inside a dielectric as first done by Kretschmann and Raether in 1968 [23].

As is the case for many wave phenomena, when boundary conditions are imposed, standing waves corresponding to discrete states appear in the system. Thus, one can see a metal nanoparticle as a planar surface wrapped up on itself resulting in a closed cavity, and the localized surface plasmon resonance (LSPR) that it supports as the standing SPP wave due to the boundaries of the particle. Another way to understand LSPRs, is to think about the free electrons of the metallic nanoparticle as a cloud of free charges. If one displaces homogeneously all the free electrons from their equilibrium position, they will feel a restoring force from the positively charged nuclei. When the cloud is let free, it oscillates back and forth, like a classical mechanical oscillator, see Fig. 2. Due to the finite conductivity of metals, the moving electrons loose energy trough collisions and the oscillation is damped. Additionally, accelerating charges radiate electromagnetic waves so that the electron cloud also loses energy by radiating light. Now, if this oscillating cloud emits an electromagnetic wave, it also means that an electromagnetic wave can make this cloud oscillate. This is indeed the case, and that is precisely what Faraday observed in his experiments: light excites LSPRs in metallic nanoparticles and is thus absorbed and scattered at particular frequencies, giving rise to specific colours [24]. Without invoking a rigorous theory, it is perfectly reasonable to assume that the oscillating cloud of electrons acts like a damped harmonic oscillator and that its resonance frequency and damping rate depends on the size and shape of the nanoparticle, as well as the permittivity of the metal. Interestingly, the range of sizes for which nanoparticles possess plasmonic resonances (i.e. resonances of the free electron cloud) in the near infrared and visible part of the spectrum is from ten to hundreds of nanometers [25]. This means that in many cases, the nanoparticles into consideration are much smaller that the wavelength of the light at which they resonate. Consequently, in this approximation, the *size* of the nanoparticle does not influence the resonance frequency and width, whereas its *shape* does [26]. Indeed, since the nanoparticle is considered much smaller than the wavelength,

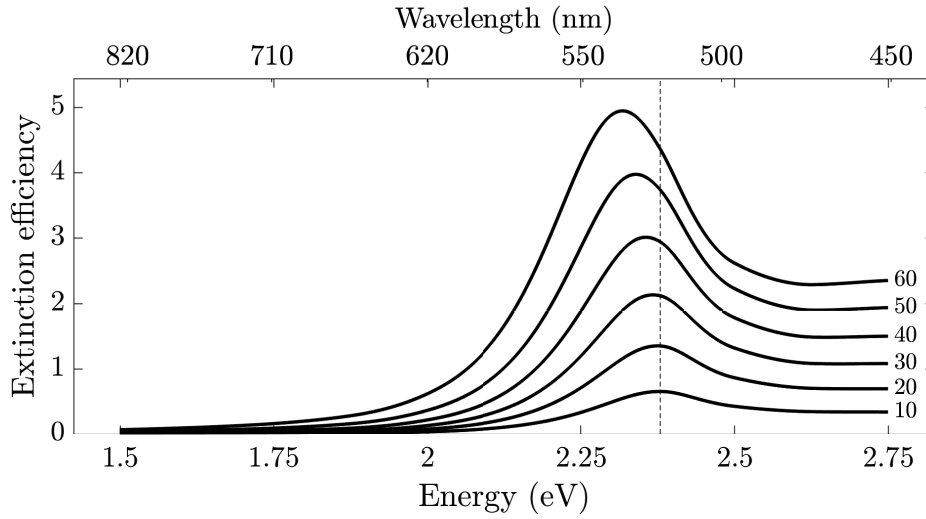


Figure 3 – Extinction efficiency of small spheres: the absolute size of the sphere, indicated on the right end of each curve, does not affect significantly the resonance frequency for a large range of diameters. The energy shift of the peak from 10 to 60 nm diameters is only 2.5%. The sphere is made of gold and the background medium is water. The permittivity of gold is taken from the experimental data of Johnson and Christy [28].

any changes in the size (but not in the shape) that keeps the approximation valid cannot influence the resonant properties of the nanoparticle. Mathematically, it allows solving Maxwell's equations in the static regime, and then multiply the solution with a harmonic time dependence. This procedure is referred to as the quasistatic approximation and is largely used in the study of plasmonic nano-systems [15, 24, 27]. To illustrate this phenomenon, Fig. 3 shows the extinction spectra of gold nanospheres with different sizes computed with Mie's theory. One can observe that for a wide range of diameters the resonant frequency hardly changes at all. On the other hand, if the size does not matter, the shape is the key parameter to change the resonances properties of nanoparticles. As a simple example, Fig. 4, shows how the resonance frequencies of gold nano-spheroids evolve with their aspect ratio; those results are computed according to the analytical formula given in Ref. [24]. A rich variety of resonances and spectral features can thus be obtained by a careful design of the nanoparticle shapes, and this point constitutes one of the main topics of today's research in plasmonics. Together with the resonant excitation of the free electrons cloud, there is a large field enhancement around the metallic nanoparticle. The electric field near the surface can typically be hundreds of times larger than the one of the impinging planewave. Such large fields and intensities offer a platform of choice to study phenomena such as Raman spectroscopy [29], dipole emitter decay rate enhancement [5] and nonlinear effects [3].

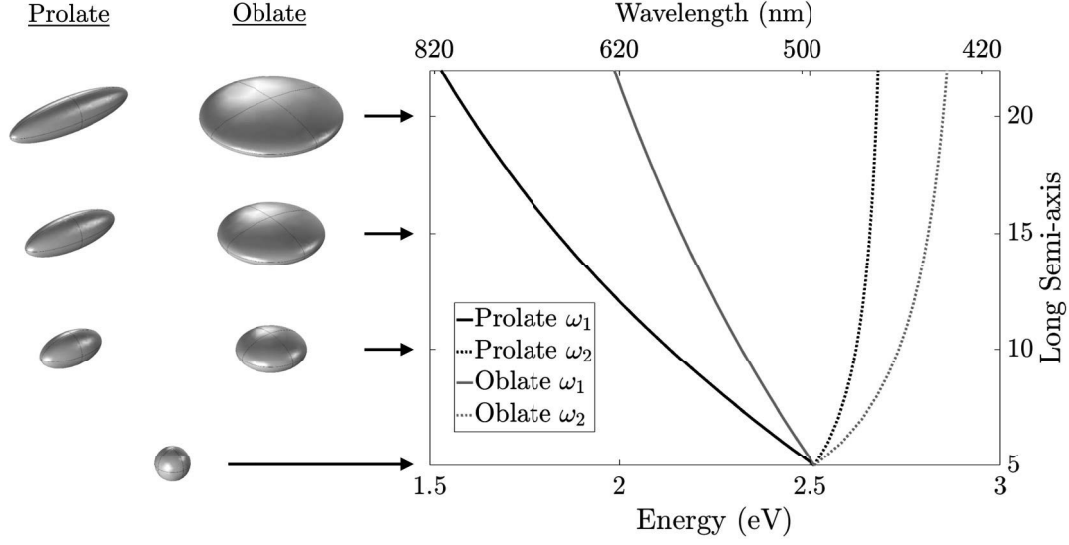


Figure 4 – Resonance frequency of gold nano-spheroids in water, with sizes small compared to the wavelength. As the aspect ratio of the two kind of spheroids evolves, the shift in resonance frequencies covers almost all the visible spectrum. The frequency for the dipolar resonances along the long(s) and short(s) axis are denoted ω_1 and ω_2 respectively.

Second Harmonic Generation

Linearity is a fundamental concept in physics; it allows the use of the superposition principle, upon which are based much of the mathematical methods used by scientists. One of the most important example is the ubiquitous use of Fourier analysis in the study of wave related phenomena (see Chap. 2). However, in most (if not all) real physical systems where oscillations are observed, a large enough departure from the equilibrium state leads to a nonlinear response. Indeed, a linear restoring force implies a harmonic (quadratic) potential, which is the first non-vanishing term in a Taylor expansion around a local minimum of potential energy (ignoring the constant term that can be set to zero without changing the physics). Thus, the linear response is often the first approximation for "small" displacement. D'Alembert's wave equation derivation in mechanics assumes small displacements or deformations (Hooke's law [30]), while in electromagnetism the Lorentz model for the refractive index assumes small displacements of the electron's position around the nucleus [24]; virtually, all derivations of d'Alembert's equation in a given domain of physics assume a linear response. One of the most striking features of nonlinear behaviours is the generation of harmonics. Everyday examples are scarce, but let us mention green laser pointers where the electromagnetic wave of an IR laser at 1064 nm is (partially) transformed into a 532 nm green beam by a crystal with a strong second order susceptibility.

Depending on the strength of the nonlinearity, one can distinguish between the weak

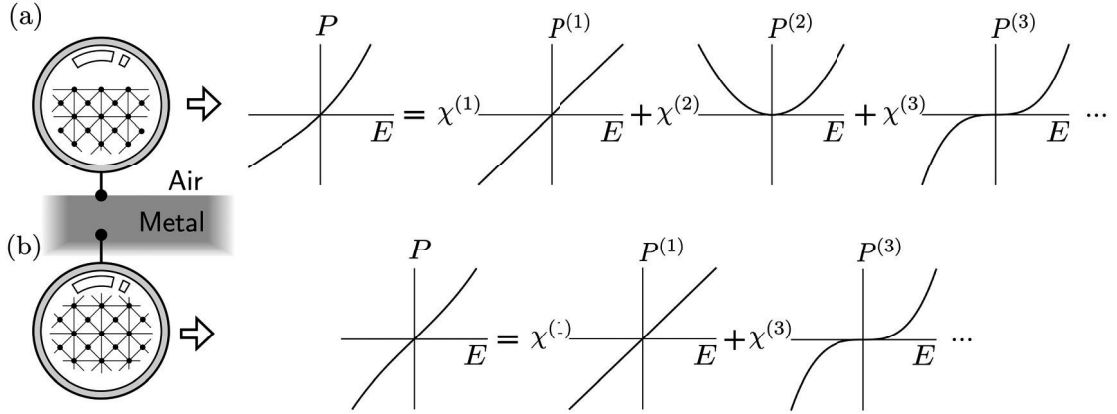


Figure 5 – Nonlinearity of the polarization P versus the driving electric field E and its decomposition in a Taylor series. (a) Near the surface, the centrosymmetry of the crystal is broken, allowing for even and odd order terms. (b) Inside the bulk, the crystal is centrosymmetric, thus allowing only odd order terms. Notice that for small electric fields the contribution of the second and third order is negligible compared to the linear response.

and strong regimes. The nonlinearity is considered to be weak when the energy transfer from the fundamental pump signal to the nonlinear one is small enough so that one can consider no decrease in the amplitude of the pump wave. This so-called undepleted pump approximation allows great simplifications of the coupled nonlinear differential equations and is accurate enough for many situations [14]. Additionally, due to the relative weakness of the nonlinear signal, one can also neglect any back transfer of energy to the pump signal. Thus, the nonlinear response can be decoupled into two separate problems: one can first compute the linear response of the system and then the nonlinearities, ignoring the complex interplay between the two. When the nonlinearity is too strong, the full interaction and energy exchange between the fundamental and nonlinear part cannot be ignored, leading to a more complex behaviour.

The departure from linearity for a strong enough driving field can be mathematically expressed as a Taylor expansion around the equilibrium position. In the case of interest in this thesis, namely electromagnetism, we consider the response of a material, the polarisation $P(t)$, to an external electric field $E(t)$ [14]:

$$\begin{aligned} P(t) &= \epsilon_0 \left(\chi^{(1)}E(t) + \chi^{(2)}E^2(t) + \chi^{(3)}E^3(t) + \dots \right) \\ &= P^{(1)}(t) + P^{(2)}(t) + P^{(3)}(t) + \dots, \end{aligned} \quad (1)$$

where $\chi^{(n)}$ is the (non)linear susceptibility tensor of order n and ϵ_0 the vacuum permittivity. This expansion is depicted graphically in Fig. 5(a). In the particular case of harmonic excitation at a frequency ω , Eq. (1) directly shows that each order of nonlinearity leads to the generation of a harmonic of the same order. This is one of the main applications of

nonlinear optics as it allows the generation of coherent light at wavelengths non attainable otherwise. Of particular interest in this thesis is the SHG from metallic nanoparticles.

If one looks at the second order response $P^{(2)}(t) = \epsilon_0 \chi^{(2)} E^2(t)$, it actually dictates that for positive and negative values of the fundamental electric field $E(t)$, the induced polarisation is positive. This is indeed impossible if the unit cell of the crystal under consideration is centro-symmetric, Fig. 5(b), which is often the case in plasmonics, since gold, silver, and aluminium (the most used metals in plasmonics) are centro-symmetric. Nonetheless, this consideration takes the symmetry of the crystal into account, but not the symmetry of the exciting field. This is the so-called dipolar approximation, where the wavelength of the light is considered far larger than the atoms and the crystal's unit cell [31, 32]. Thus, one way to locally break the symmetry is through retardation effects, i.e. the field's phase variation across the unit cell. Indeed, if the field of the fundamental wave varies spatially fast enough, it can induce a local asymmetry and enable even order nonlinearities in centro-symmetric media. However, in the case of nanoparticles, since they are often small compared to the wavelength, the above mentioned retardation effects can hardly account for the SHG observed from small plasmonic nanoparticles [33]. There is yet another way to break the symmetry of the crystal: at the boundary between the metal and the environment, the symmetry of the lattice is broken [32]. In a more visual way, an electron oscillating at the surface does not feel a symmetric potential as does an electron in the middle of the particle, see Fig. 5(b), so that its response to a driving electric field is asymmetric and contains even order terms. In the numerical method used to compute SHG in this thesis, only the contribution of the surface to the SHG is considered as it was shown that it is appreciably larger than the bulk one [34]. Furthermore, among all the possible tensor elements of $\chi_{\text{surf}}^{(2)}$, we consider the component $\chi_{\text{surf}, \perp \perp \perp}^{(2)}$ to be the dominant one [35]. Although this last statement is often used to justify the use of $\chi_{\text{surf}, \perp \perp \perp}^{(2)}$ only, one should be careful about one detail: the tensor components can be defined in two ways, with the internal or external fields, thus potentially changing the relative values of the different components of $\chi_{\text{surf}}^{(2)}$. Consequently, the pertinent figure of merit should be the component that leads to the largest contribution to SHG, as opposed to the largest component itself [35].

Electron Energy Loss Spectroscopy

During the last decade, EELS has become a popular tool in the nano-optics community [36]. Indeed, progress in the quality of electron beam sources as well as in detectors efficiency now allows probing resonances in nanostructures with LSPR below 1 eV with nanometer spatial resolution and <0.1 eV energy resolution [36]. Conducted in a scanning transmission electron microscope, EELS consists in analysing the energy lost

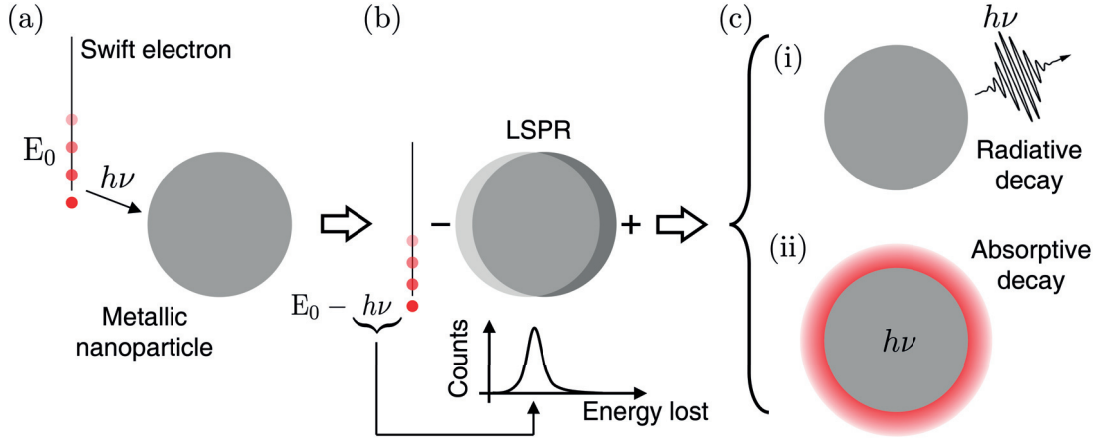


Figure 6 – Schematic representation of the EELS. (a) A swift electron passes near a metallic nanoparticle. Its electric field interacts with the free electrons of the nanoparticle and gives an energy $h\nu$ to the LSPR. (b) The electron has lost an energy $h\nu$ and the LSPR is excited. The energy of the electron is recorded to build the spectrum. (c) The LSPR can decay radiatively by emitting a photon of energy $h\nu$ (i), or be absorbed internally (ii).

by swift electrons¹ that interacted with the nanostructure of interest. By building a histogram of the number of electrons having lost a given amount of energy, one obtains a spectrum that shows peaks at positions corresponding to the LSPRs of the investigated nanostructure [36, 37]. A schematic of the principle of EELS is shown in Fig. 6. A fast electron interacting with a localized scatterer can be viewed as an extremely short impulse-like excitation that thus acts as a spectrally broad source. Additionally, the inherent cylindrical symmetry of the excitation beam allows exciting modes that couple weakly to far-field planewave excitations. The different ways the fast electron and a planewave couple to the two first two modes of a nanosphere dimer is depicted in Fig. 7. EELS is then able to probe LSPRs inaccessible to optical spectroscopy, with an unprecedented spatial resolution. Consequently, there is a need for adequate numerical methods that allow obtaining the eigenmodes in order to identify them to the spectral and spatial features of EELS measurement.

The implementation of EELS computation in the SIE framework is detailed in Sec. 3.1. Briefly, one can derive the frequency-dependent electric and magnetic fields generated by an electron moving along a straight path. Those fields are then used as a source in the same way that a planewave or a dipole excitation is used to compute scattering spectra. Once the scattered field is computed, the work done by the electron through the Lorentz force against the scattered electric field is evaluated to give the EEL signal at one frequency. An alternative method relying on energy conservation consideration is

¹The energy of the electron is typically between 50 keV and 300 keV, corresponding to speeds between 41% and 78% of the speed of light in vacuum.

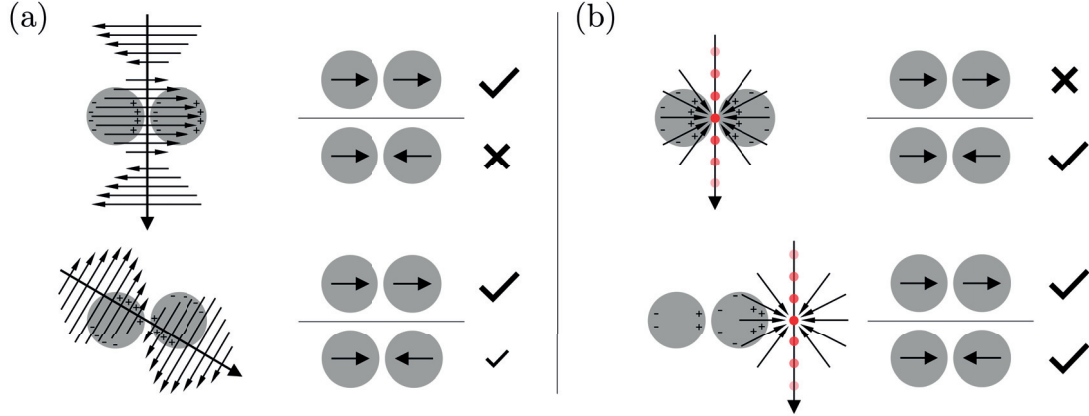


Figure 7 – Comparison between planewave (a) and swift electron (b) excitation of a nanosphere dimer. The arrows inside the spheres represent their dipolar moment. Although it is possible to probe the anti-bonding dark ($\rightarrow\leftarrow$) mode with a planewave at oblique incidence, its response is usually weak. On the other hand, by placing the electron beam in the middle of the dimer, symmetry forbids the excitation of the bright bonding ($\rightarrow\rightarrow$) mode whereas placing it on the side of the dimer allows the excitation of both modes with appreciable amplitude.

also presented in Sec. 3.1.

Eigenmodes

Resonant and wave phenomena pervade all domains of physics. From the standing wave on a string studied by Pythagoras [38], passing through the discovery of electromagnetic waves by Maxwell and Hertz [39, 40], to the standing wave pattern of the electron wavefunction around the nucleus [41] and the very recent discovery of gravitational waves [42], this subject has always occupied the forefront of research in physics. Owing to their intrinsic characteristics and the basis they offer to study the system response to arbitrary excitation, eigenmodes often offer a deep physical insight into the system properties.

Even though the study of resonant phenomena is arguably as old as physics itself, the case of resonances in open and lossy cavities, often referred to as non-Hermitian systems, is still an active field of research in modern physics, especially in nano/quantum optics and in general relativity [43]. The reasons for this relatively late development is that resonant cavities are often designed to minimize energy dissipation, making a full theory of resonances in lossy cavity unnecessary in many areas of physics. Additionally, perturbation theory is often sufficient to account for small dissipations in cavities with large quality factors. However, plasmonic and dielectric nano-optical resonators exhibit resonances with high damping rate due to radiation losses for the latter, and additional Ohmic losses for the former: the perturbation approach is not adequate anymore and one needs to fully consider losses in the derivation of the eigenmodes [44].

Unfortunately, the afore-mentioned non-Hermiticity leads to several problems concerning normalization and completeness of the mode basis that have only been (partially) solved in the last two decades [44]. One of the most striking effect is due to the complex value of the eigenfrequency: a decaying amplitude of the eigen-fields with time inherently leads to a diverging amplitude of the fields far from the nanoparticle(s) [44, 45]. In such systems, the modes are no longer orthogonal (as e.g. the vibration modes on a string) and can thus couple to each-other; for this reason, they are often called quasinormal modes (QNM).²

In this thesis, we do not burden ourself with such complex considerations and treat the eigenmodes/ QNMs normally, for various reasons. First, the diverging amplitude of the field associated with a QNM is not directly problematic in the SIE method used throughout this manuscript as it is for finite-difference time-domain (FDTD) solvers: indeed, with the SIE the whole problem is formulated on the surface of the scatterer so that there is no special care to be taken regarding the field far from the structure. Second, the eigenmodes are not rigorously used as a basis, and are only used to qualitatively understand scattering spectra, EELS measurements and SHG. In many cases, symmetry considerations as well as their resonance frequencies allow to unambiguously attribute spectral features to given eigenmodes without the use of a rigorous projection on the eigenmode basis.

Finally, let us mention that alternative approaches exist to define modes in nano-optics. To begin with, one can define eigenmodes at *real* frequencies, thus avoiding the problematic field divergence at infinity. The cost of this well-behaved spatial decay is that a new and different set of eigenmodes must be generated at each real frequency (each eigenmode can nevertheless be qualitatively similar to one QNM) [47]. Another method using modes at real frequencies is presented by Chen et al. [48] where the permittivity, instead of the frequency, is considered as the eigenvalue; this results in a linear eigenvalue problem, instead of a nonlinear one like in the case of the QNMs [44]. Another approach, which is tightly linked to the previous one, is the so called material independent modes presented by Forestiere and Miano [49], also considering the permittivity as the quantity of interest. The resonances/modes are defined at specific complex values of the permittivity, without specification about the frequency, and offer direct information about the multipolar character of those modes. Those last two approaches, although apparently lacking the direct physical interpretation of the QNMs³, allow gaining insights into the separate influences of the material and the geometry onto the eigenmodes. Detailed discussion about the QNMs can be found in [44], and interesting discussions and comparisons between the QNMs and the real frequency modes of Chen et al. are found in [48]. Lastly, as stated in the previous section on plasmonics, since the quasistatic approximation is often valid in nano-optics, one can also study eigenmodes in this special case. In this

²They are also sometimes called leaky modes, resonant states or decaying states [46].

³In the sense that the QNMs are the most natural way to extend the normal modes of closed cavities, with which most people are familiar.

approximation, it is possible to extract the real part of the eigenfrequency associated with an eigenmode described by a real surface charge distribution [50, 51]. The problematic field divergence of the QNMs is also absent in this special case, since there is no radiation.

One can also approach the problem from an antenna perspective by looking at the impedance of the system and use the so-called characteristic modes, first introduced by Garbacz and Turpin [52, 53] and then further developed by Harrington and co-workers [54, 55]; a more recent account on the subject can be found in Ref. [56]. Although first introduced for perfect electric conductor materials (PEC), this formalism has recently been extended to non-PEC materials, i.e. plasmonic scatterers [57]. A comprehensive analysis of the link between all those definitions is yet to be done, but discussions between characteristic modes and complex natural/external resonances (the equivalent of the QNM in antenna theory) can be found in Refs. [58] and [59] respectively for a dielectric and a PEC infinite cylinder, and for other PEC structures in [60]. A general and comprehensive discussion about the characteristic modes and external resonances is found in [56].

Since the QNMs bear a strong physical meaning as a natural extension of the modes of closed cavities, one can wonder what is the use of the previously mentioned alternative definitions. However, in addition to the (potential) insights that modes give to the response of a system, their use as a basis for fast computations is of great practical importance, unfortunately this is precisely where the QNMs are problematic [44]. In any case, those alternative definitions remain a way to reach a mathematically better suited, but often more complex definition, at the cost of a direct physical insight.⁴

Surface Integral Equation

There are few problems that allow for a full analytical solution of Maxwell's equations, such problems being limited to geometries exhibiting high degrees of symmetry [61, 62]. Consequently, a variety of numerical approaches have flourished in order to study more complicated and realistic systems [63]. Initially developed for simulations in the microwave/radio frequency regimes, the SIE method relies on a Green's function approach to solve the electromagnetic wave equation [64–67]. It thus differs from the more common FDTD and finite element methods (FEM) that rely on a differential equation formulation approach. Here we shortly describe the main steps in the derivation of the surface integral equation, a rigorous mathematical development can be found in Ref. [68]. Using the vectorial wave equation and its Green's function, one can derive a volume integral relation between the field imposed by a source and the resulting field inside a bounded domain [69]. The central point is the use of Gauss's theorem to transform the volume integral to

⁴It does not mean however that those alternative modes are completely devoid of physical meaning, and each approaches leads to a different point of view that can enlighten some particular aspect of the structure's response.

a surface one, taking advantage of the homogeneous properties (the permittivity and permeability) of the structure. The background medium does not need to be discretized (as it is the case in FDTD and FEM) as its influence is included in the the integral formulation through the Green's function and the boundary conditions are automatically fulfilled at the edge of the computation window. Although first developed for perfectly conducting media where the fields do not penetrate the scatterer and where it thus makes sense to consider only surfaces, the SIE method was successfully extended to optical regimes where the finite conductivity of metals is finite [68]. The principal limitation of the SIE method is the restriction to piecewise isotropic and homogeneous media; this is however not a severe drawback as most nanostructures studied in nanophotonics are composed of such media. On the other hand, the surface discretization by triangular elements allows for the creation of realistic and smooth geometries [68], and for the possibility of localized mesh refinement, something not directly possible in FDTD. The SIE method at optical frequency was successfully extended to periodic media [70], stratified media [71] and to the computation of SHG [72]. Mathematical details about the SIE method as well as the SHG computation can be found in Sec. 2.1.

Bibliography

- [1] M. I. Stockman, “Nanoplasmonic sensing and detection,” *Science* **348**, 287–288, (2015).
- [2] A. B. Taylor and P. Zijlstra, “Single-Molecule Plasmon Sensing: Current Status and Future Prospects,” *ACS Sens.* **2**, 1103–1122, (2017).
- [3] M. Kauranen and A. V. Zayats, “Nonlinear plasmonics,” *Nat. Photonics* **6**, 737–748, (2012).
- [4] B. Metzger, M. Hentschel, and H. Giessen, “Ultrafast Nonlinear Plasmonic Spectroscopy: From Dipole Nanoantennas to Complex Hybrid Plasmonic Structures,” *ACS Photonics* **3**, 1336–1350, (2016).
- [5] O. L. Muskens, V. Giannini, J. A. Sánchez-Gil, and J. Gómez Rivas, “Strong Enhancement of the Radiative Decay Rate of Emitters by Single Plasmonic Nanoantennas,” *Nano Lett.* **7**, 2871–2875, (2007).
- [6] V. Giannini, A. I. Fernández-Domínguez, S. C. Heck, and S. A. Maier, “Plasmonic Nanoantennas: Fundamentals and Their Use in Controlling the Radiative Properties of Nanoemitters,” *Chem. Rev.* **111**, 3888–3912, (2011).
- [7] L. Piatkowski, N. Accanto, and N. F. van Hulst, “Ultrafast Meets Ultrasmall: Controlling Nanoantennas and Molecules,” *ACS Photonics* **3**, 1401–1414, (2016).
- [8] V.-C. Su, C. H. Chu, G. Sun, and D. P. Tsai, “Advances in optical metasurfaces: Fabrication and applications [Invited],” *Opt. Express* **26**, 13148–13182, (2018).
- [9] F. Ding, Y. Yang, R. A. Deshpande, and S. I. Bozhevolnyi, “A review of gap-surface plasmon metasurfaces: Fundamentals and applications,” *Nanophotonics* **7**, no. 6, 1129–1156, (2018).
- [10] B. E. A. Saleh and M. C. Teich, *Fundamentals of Photonics*. Wiley-Interscience, 2nd ed., (2007).
- [11] S. B. Glybovski, S. A. Tretyakov, P. A. Belov, Y. S. Kivshar, and C. R. Simovski, “Metasurfaces: From microwaves to visible,” *Physics Reports* **634**, 1–72, (2016).

Bibliography

- [12] C. D. Geddes, ed., *Metal-Enhanced Fluorescence*. Wiley, (2010).
- [13] B. Sharma, R. R. Frontiera, A.-I. Henry, E. Ringe, and R. P. Van Duyne, “SERS: Materials, applications, and the future,” *Materials Today* **15**, 16–25, (2012).
- [14] R. W. Boyd, *Nonlinear Optics, Third Edition*. Orlando, FL, USA: Academic Press, Inc., 3rd ed., (2008).
- [15] S. A. Maier, *Plasmonics: Fundamentals and Applications*. Springer US, (2007).
- [16] D. J. Barber and I. C. Freestone, “An investigation of the origin of the colour of the Lycurgus cup by analytical transmission electron microscopy,” *Archaeometry* **32**, 33–45, (1990).
- [17] M. Faraday, “The Bakerian Lecture: Experimental Relations of Gold (and Other Metals) to Light,” *Philos. Trans. Royal Soc.* **147**, 145–181, (1857).
- [18] G. Mie, “Beiträge zur Optik trüber Medien, speziell kolloidaler Metallösungen,” *Ann. Phys.* **330**, 377–445, (1908).
- [19] R. W. Wood, “On a Remarkable Case of Uneven Distribution of Light in a Diffraction Grating Spectrum,” *Proc. Phys. Soc* **18**, no. 1, 269, (1902).
- [20] U. Fano, “The Theory of Anomalous Diffraction Gratings and of Quasi-Stationary Waves on Metallic Surfaces (Sommerfeld’s Waves),” *J. Opt. Soc. Am.* **31**, 213, (1941).
- [21] A. Sommerfeld, “Ueber die Fortpflanzung elektrodynamischer Wellen längs eines Drahtes,” *Ann. Phys.* **303**, 233–290, (1899).
- [22] J. Zenneck, “über die Fortpflanzung ebener elektromagnetischer Wellen längs einer ebenen Leiterfläche und ihre Beziehung zur drahtlosen Telegraphie,” *Ann. Phys.* **328**, 846–866, (1907).
- [23] E. Kretschmann and H. Raether, “Radiative Decay of Non Radiative Surface Plasmons Excited by Light,” *Z. Naturforsch. A* **23**, no. 12, 2135–&, (1968).
- [24] C. F. Bohren and D. R. Huffman, *Absorption and Scattering of Light by Small Particles*. Wiley-VCH, (2004).
- [25] J. P. Kottmann, O. J. F. Martin, D. R. Smith, and S. Schultz, “Plasmon resonances of silver nanowires with a nonregular cross section,” *Phy. Rev. B* **64**, 235402, (2001).
- [26] J. P. Kottmann and O. J. F. Martin, “Plasmon resonant coupling in metallic nanowires,” *Opt. Express* **8**, 655–663, (2001).
- [27] S. Enoch and N. Bonod, eds., *Plasmonics: From Basics to Advanced Topics*. Springer Series in Optical Sciences, Berlin Heidelberg: Springer-Verlag, (2012).

-
- [28] P. B. Johnson and R. W. Christy, “Optical Constants of the Noble Metals,” *Phy. Rev. B* **6**, 4370–4379, (1972).
- [29] P. L. Stiles, J. A. Dieringer, N. C. Shah, and R. P. Van Duyne, “Surface-Enhanced Raman Spectroscopy,” *Annual Rev. Anal. Chem.* **1**, 601–626, (2008).
- [30] L. D. Landau and E. M. Lifshitz, *Theory of Elasticity*. Pergamon Press, (1989).
- [31] R. Loudon, *The Quantum Theory of Light*. Oxford, New York: Oxford University Press, 3rd ed., (2000).
- [32] Y. Shen, “Optical Second Harmonic Generation At Interfaces,” *Annu. Rev. Phys. Chem.* **40**, 327–350, (1989).
- [33] J. Butet, P.-F. Brevet, and O. J. F. Martin, “Optical Second Harmonic Generation in Plasmonic Nanostructures: From Fundamental Principles to Advanced Applications,” *ACS Nano* **9**, 10545–10562, (2015).
- [34] D. Krause, C. W. Teplin, and C. T. Rogers, “Optical surface second harmonic measurements of isotropic thin-film metals: Gold, silver, copper, aluminum, and tantalum,” *J. Appl. Phys.* **96**, 3626–3634, (2004).
- [35] F. X. Wang, F. J. Rodríguez, W. M. Albers, R. Ahorinta, J. E. Sipe, and M. Kauranen, “Surface and bulk contributions to the second-order nonlinear optical response of a gold film,” *Phy. Rev. B* **80**, 233402, (2009).
- [36] F. J. García de Abajo, “Optical excitations in electron microscopy,” *Rev. Mod. Phys.* **82**, 209–275, (2010).
- [37] R. F. Egerton, “Electron energy-loss spectroscopy in the TEM,” *Rep. Prog. Phys.* **72**, 016502, (2009).
- [38] H. E. White and D. H. White, *Physics and Music: The Science of Musical Sound*. Dover Publications, (2014).
- [39] J. C. Maxwell, “VIII. A dynamical theory of the electromagnetic field,” *Philos. Trans. Royal Soc.* **155**, 459–512, (1865).
- [40] J. F. Mulligan, “Heinrich Hertz and the Development of Physics,” *Physics Today* **42**, 50, (2008).
- [41] R. P. Feynman, R. B. Leighton, and M. Sands, *The Feynman Lectures on Physics*. Addison–Wesley, (1963).
- [42] LIGO Scientific Collaboration and Virgo Collaboration, “Observation of Gravitational Waves from a Binary Black Hole Merger,” *Phy. Rev. Lett.* **116**, 061102, (2016).

Bibliography

- [43] K. D. Kokkotas and B. G. Schmidt, “Quasi-Normal Modes of Stars and Black Holes,” *Living Rev. Relativ.* **2**, 2, (1999).
- [44] P. Lalanne, W. Yan, K. Vynck, C. Sauvan, and J.-P. Hugonin, “Light Interaction with Photonic and Plasmonic Resonances,” *Laser Photonics Rev.* **12**, 1700113, (2018).
- [45] H. Lamb, “On a Peculiarity of the Wave-System due to the Free Vibrations of a Nucleus in an Extended Medium,” *Proc. Lond. Math. Soc.* **s1-32**, 208–213, (1900).
- [46] B. Stout and R. McPhedran, “Egocentric physics: Just about Mie,” *EPL* **119**, 44002, (2017).
- [47] J. Mäkitalo, M. Kauranen, and S. Suuriniemi, “Modes and resonances of plasmonic scatterers,” *Physical Review B* **89**, 165429, (2014).
- [48] P. Y. Chen, D. J. Bergman, and Y. Sivan, “Generalizing normal mode expansion of electromagnetic Green’s tensor to lossy resonators in open systems,” *arXiv:1711.00335 [physics]* (2017).
- [49] C. Forestiere and G. Miano, “Material-independent modes for electromagnetic scattering,” *Physical Review B* **94**, 201406, (2016).
- [50] U. Hohenester and J. Krenn, “Surface plasmon resonances of single and coupled metallic nanoparticles: A boundary integral method approach,” *Physical Review B* **72**, (2005).
- [51] I. D. Mayergoyz, D. R. Fredkin, and Z. Zhang, “Electrostatic (plasmon) resonances in nanoparticles,” *Physical Review B* **72**, (2005).
- [52] R. J. Garbacz, “Modal expansions for resonance scattering phenomena,” *Proceedings of the IEEE* **53**, 856–864, (1965).
- [53] R. Garbacz and R. Turpin, “A generalized expansion for radiated and scattered fields,” *IEEE Transactions on Antennas and Propagation* **19**, 348–358, (1971).
- [54] R. Harrington and J. Mautz, “Theory of characteristic modes for conducting bodies,” *IEEE Transactions on Antennas and Propagation* **19**, 622–628, (1971).
- [55] R. Harrington, J. Mautz, and Y. Chang, “Characteristic modes for dielectric and magnetic bodies,” *IEEE Transactions on Antennas and Propagation* **20**, 194–198, (1972).
- [56] T. K. Sarkar, E. L. Mokole, and M. Salazar-Palma, “An expose on internal resonance, external resonance, and characteristic modes,” *IEEE Trans. Antennas Propag.* **64**, 4695–4702, (2016).

-
- [57] P. Yla-Oijala, D. C. Tzarouchis, E. Raninen, and A. Sihvola, “Characteristic Mode Analysis of Plasmonic Nanoantennas,” *IEEE Trans. Antennas Propag.* **65**, 2165–2172, (2017).
- [58] T. Bernabeu-Jiménez, A. Valero-Nogueira, F. Vico-Bondia, and A. A. Kishk, “Relation between Characteristic Modes and Complex Natural Resonances,” in *Antennas and Propagation & USNC/URSI National Radio Science Meeting, 2015 IEEE International Symposium On*, 452–453, IEEE, (2015).
- [59] T. Bernabeu-Jimenez, A. Valero-Nogueira, F. Vico-Bondia, and A. A. Kishk, “A Comparison Between Natural Resonances and Characteristic Mode Resonances of an Infinite Circular Cylinder,” *IEEE Trans. Antennas Propag.* **65**, 2759–2763, (2017).
- [60] S. Huang, J. Pan, and Y. Luo, “Study on the Relationships between Eigenmodes, Natural Modes, and Characteristic Modes of Perfectly Electric Conducting Bodies,” (2018).
- [61] J. D. Jackson, *Classical Electrodynamics*. Wiley, (1999).
- [62] J. A. Stratton, *Electromagnetic Theory*. John Wiley & Sons, (2007).
- [63] B. Gallinet, J. Butet, and O. J. F. Martin, “Numerical methods for nanophotonics: Standard problems and future challenges,” *Laser Photonics Rev.* **9**, 577–603, (2015).
- [64] A. Poggio and E. Miller, “Integral Equation Solutions of Three-dimensional Scattering Problems,” in *Computer Techniques for Electromagnetics*, 159–264, Elsevier, (1973).
- [65] Y. Chang and R. Harrington, “A surface formulation for characteristic modes of material bodies,” *IEEE Trans. Antennas Propag.* **25**, 789–795, (1977).
- [66] T. Wu and L. L. Tsai, “Scattering from arbitrarily-shaped lossy dielectric bodies of revolution,” *Radio Sci.* **12**, 709–718, (1977).
- [67] R. F. Harrington, “Boundary Integral Formulations for Homogeneous Material Bodies,” *J Electromagnetic Waves Appl.* **3**, 1–15, (1989).
- [68] A. M. Kern and O. J. F. Martin, “Surface integral formulation for 3D simulations of plasmonic and high permittivity nanostructures,” *J. Opt. Soc. Am. A* **26**, 732, (2009).
- [69] O. J. F. Martin and N. B. Piller, “Electromagnetic scattering in polarizable backgrounds,” *Phy. Rev. E* **58**, 3909–3915, (1998).
- [70] B. Gallinet, A. M. Kern, and O. J. F. Martin, “Accurate and versatile modeling of electromagnetic scattering on periodic nanostructures with a surface integral approach,” *J. Opt. Soc. Am. A* **27**, 2261, (2010).

Bibliography

- [71] Y. P. Chen, W. E. I. Sha, W. C. H. Choy, L. Jiang, and W. C. Chew, “Study on spontaneous emission in complex multilayered plasmonic system via surface integral equation approach with layered medium Green’s function,” *Opt. Express* **20**, 20210–20221, (2012).
- [72] J. Butet, B. Gallinet, K. Thyagarajan, and O. J. F. Martin, “Second-harmonic generation from periodic arrays of arbitrary shape plasmonic nanostructures: A surface integral approach,” *J. Opt. Soc. Am. B* **30**, 2970, (2013).

1 Eigenmode Analysis

In this chapter, I first introduce the theory pertaining to the search of the eigenmodes in general systems described by wave equations. Then, I present different numerical approaches to solve for the eigenmodes of a discretized system. Although mainly aimed towards the study of plasmonic nanostructures in the framework of the SIE method, the content of this chapter is introduced in a very general manner and most of the considerations are valid for any resonant system. The words "mode" and "eigenmode" are used interchangeably to design the eigen-solutions of the wave equation, and usually refer to the eigenfunction/eigenvector and the eigenfrequency.

1.1 Theory

From a physical point of view, eigenmodes are states of a system that can exist without external influences [1]. Equivalently, if the system is in a state corresponding to an eigenmode, it will remain as such. Another property of eigenmodes, and certainly one of the most useful, is that any state of the system can be expressed as a either finite, or generally infinite, sum of the eigenmodes [2]. Such systems are defined by boundary conditions and characterized by a certain set of differential equations that describe the physical quantities of interest and the laws of physics that they obey. The boundary conditions can be seen as defining a cavity and the eigenmodes as the "preferred" state of that cavity. Examples are numerous: a mass on a spring [3], a microwave oven [4], a taut string [2], and virtually any (partially) closed geometry.

On a more mathematical ground, eigenmodes are solutions of the differential equation(s) describing the cavity without sources (i.e. the homogeneous equation). Many, if not all, resonant systems are described by a wave-like equation that accounts for their resonant nature. The most common of the wave equations is d'Alembert's (aka *the* wave equation)

Chapter 1. Eigenmode Analysis

and takes the following form:

$$\nabla^2 A(\mathbf{r}, t) - \frac{1}{c^2} \partial_t^2 A(\mathbf{r}, t) = F(\mathbf{r}, t), \quad (1.1)$$

with $A(\mathbf{r}, t)$ the quantity of interest (electromagnetic field, pressure, mechanical deformation, displacement etc...), $F(\mathbf{r}, t)$ the source term, c the speed of the wave, ∇^2 the Laplacian operator acting on the spatial coordinates \mathbf{r} (which exact expression depends on the coordinate system), and ∂_t^2 second order partial derivative with respect to the time t . The specific problem at hand sets boundary conditions on the variable $A(\mathbf{r}, t)$, which in turn dictates the form of the modes. A single set of given boundary conditions on the spatial dependence of $A(\mathbf{r}, t)$ can describe many different physical systems. For example, the solution describing a taut string where $A(\mathbf{r}, t)$ is the height of the string [2], is the same as the solution for a cavity consisting of two perfectly conducting planes, with $A(\mathbf{r}, t)$ the electric field parallel to the sides of the cavity [5].

Often, boundary conditions on the time variable, called initial and final conditions, are not given and the time dependence of $A(\mathbf{r}, t)$ is straightforwardly obtained. To show this, the separation of variable technique is often employed. It consists in writing $A(\mathbf{r}, t)$ as a product of a space dependent function and time depended one, $A(\mathbf{r}, t) = X(\mathbf{r})T(t)$. By doing so, the wave equation (1.1) with $F(\mathbf{r}, t) = 0$ becomes

$$\begin{aligned} T(t) \nabla^2 X(\mathbf{r}) - X(\mathbf{r}) \frac{1}{c^2} \partial_t^2 T(t) &= 0, \\ \frac{1}{X(\mathbf{r})} \nabla^2 X(\mathbf{r}) &= \frac{1}{c^2} \frac{1}{T(t)} \partial_t^2 T(t). \end{aligned} \quad \downarrow \times \frac{1}{X(\mathbf{r})T(t)} \quad (1.2)$$

Equation (1.2) says that two functions of different variables, \mathbf{r} and t , are always equal. This is possible only if they are each constant. Indeed, if one differentiates (1.2) with respect to t , the left side gives zero because it does not depend on t . Consequentially, the right side is also vanishing, meaning that it does not depend on t too. This also works for a space derivative and one can thus see that both sides are indeed constant. We note this constant $-k^2$ and obtain two equations,¹

$$\nabla^2 X(\mathbf{r}) = -k^2 X(\mathbf{r}), \quad (1.3)$$

$$\partial_t^2 T(t) = -k^2 c^2 T(t). \quad (1.4)$$

Both are Helmholtz-type equations that can be viewed as an eigenvalue problem. For example, the solutions X of Eq. (1.3) are the eigenvectors of ∇^2 with eigenvalue $-k^2$. Given the lack of initial and final conditions, Eq. (1.4) is readily solved. By setting

¹In more general contexts, especially in mathematics, this constant is often noted λ as it appears as an eigenvalue. However, λ is already used as the wavelength in wave physics, and, as it will appear, the quantity of physical importance is here $\sqrt{\lambda}$, hence the choice of $-k^2$

$\omega = ck$ and imposing $k, T \in \mathbb{R}$, an adequate solution is

$$T(t) = A_0 \cos(\omega t + \varphi), \quad (1.5)$$

with A_0 and φ arbitrary amplitude and phase, respectively. Thus, whatever the spatial boundary conditions, the geometry of the problem and the form of the Laplacian, the time dependence of an eigenmode of the wave equation (1.1) is the one given by Eq. (1.5). Mathematically this is because the sine and cosine functions (and more generally a sum of two complex exponentials) are the eigenfunctions of the operator ∂_t^2 , with eigenvalue $-\omega^2$ [6]. In mechanics, this operator appears through Newton's second law, explaining why wave equations appear throughout this domain of physics. In electromagnetism the ∂_t^2 appears through the combination of Maxwell-Ampère's and Faraday's laws and leads to a wave equation for the electromagnetic field; this point being one of the greatest scientific discovery of the modern era. This property of the sinusoidal functions thus justifies the almost omnipresent use of frequency domain methods to solve wave problems in physics. Indeed, Fourier's analysis tells us that any temporal signal can be constructed as the sum of sine and cosine functions. One can then directly assume a time dependence of the form (1.5) in the wave equation, effectively taking its Fourier transform, and work only with the Helmholtz equation (1.3); this is what frequency domain numerical solvers do [7]. Let us show this point explicitly by assuming now that $A(\mathbf{r}, t) = \text{Re}\{\tilde{A}(\mathbf{r})e^{-i\omega t}\}$, with $\tilde{A}(\mathbf{r}) \in \mathbb{C}$. It follows that $\partial_t^2 A(\mathbf{r}, t) = -\omega^2 \text{Re}\{\tilde{A}(\mathbf{r})e^{-i\omega t}\}$. The wave equation being linear in A , one can take the real part of the whole equation and solve for the complex functions inside, taking the real part of the solution at the end. By further simplifying the $e^{-i\omega t}$ factor, we obtain

$$\nabla^2 \tilde{A}(\mathbf{r}) + \frac{\omega^2}{c^2} \tilde{A}(\mathbf{r}) = 0, \quad (1.6)$$

which is equivalent to Eq. (1.3) with $\omega = ck$.

The geometry of the problem dictates the boundary conditions on $X(\mathbf{r})$ or $\tilde{A}(\mathbf{r})$ and thus its exact form. More importantly, the boundary conditions impose certain discrete values of k and thus of ω through the dispersion relation $\omega = ck$. The simplest example being the taut string: only sine functions having a wavelength such that their amplitudes vanish at both end points are valid solutions, leading to the well-known standing wave pattern and associated harmonics. On the other hand, waves in free-space can exist at any frequency since they are not spatially bounded.

In all generality, there is no analytical solutions to Eq. (1.6), the exception being simple symmetric structures where the Laplacian operator ∇^2 can be written in a simple manner in the appropriate coordinate system [8]; other geometries need a numerical approach to be solved. In Cartesian coordinates the Laplacian separates nicely the three orthogonal components so that three separate Helmholtz's equations are obtained, for which linear combination of sine and cosine functions are solutions. In spherical coordinates (r, ϕ, θ)

the trigonometric functions are solutions for the azimuthal angle ϕ , Bessel functions are solutions for the radial component r and associated Legendre polynomials of $\cos(\theta)$ are solutions for the polar angle θ . The separate solutions on the (ϕ, θ) components form the so called spherical harmonics that constitute the basis for the study of eigenmodes in 2D spherical geometries [8].

Unfortunately, real systems are usually described by the wave equation (1.1) only at first approximation. This first approximation is the linearity of the system, which is valid only for "small" values of the quantity of interest (see the Second Harmonic Generation part in the introduction, p. 6). However, this is very often a good approximation and nonlinearities are rarely considered in eigenmode analysis. The other approximation is the omission of losses: every physical systems show some loss mechanisms, either internal (e.g. Ohmic losses, friction etc...) or external (e.g. radiation losses). The wave equation thus has to be modified to take into account the energy dissipation. Even if in most applications of resonant systems, the goal is to reduce as much as possible any losses, lossy systems are still of interest in many fields, and especially in plasmonics. Indeed, metals are inherently lossy at optical frequencies, leading to a strong damping of the LSPRs. In plasmonics, systems are often characterized by quality factors (Q-factor) below 100, whereas Fabry-Pérot cavity can reach Q-factor of tens of thousands at the same optical frequencies [5, 9]. It is thus worth studying how the wave equation is modified when losses are taken into account.

Concerning LSPRs, the losses occur through two distinct channels. The first one is the Ohmic losses, due to electrons collisions with the lattice and other internal loss mechanisms. The other channel is the radiation losses, due to the charge oscillatory movement. This last mechanism depends on the geometry of the nanoparticle whereas the Ohmic losses depend only on the material.² Thus, as an example of how losses modify the wave equation, we simply consider a wave propagating inside a conductor, and analyse how the finite conductivity leads to losses. To do that, let us derive the wave equation for a conducting and neutral medium. Let us first recall the microscopic Maxwell's equations:

$$\nabla \cdot \mathbf{E} = \frac{\rho}{\epsilon_0}, \quad (1.7)$$

$$\nabla \cdot \mathbf{H} = 0, \quad (1.8)$$

$$\nabla \times \mathbf{E} + \mu_0 \partial_t \mathbf{H} = 0, \quad (1.9)$$

$$\nabla \times \mathbf{H} - \epsilon_0 \partial_t \mathbf{E} = \mathbf{J}, \quad (1.10)$$

with \mathbf{E} and \mathbf{H} the electric and magnetic fields, ρ and \mathbf{J} the charge and current densities, and μ_0 and ϵ_0 respectively the vacuum permeability and permittivity. The conductor is neutral so $\rho = 0$, and obeys Ohm's law $\mathbf{J} = \sigma \mathbf{E}$, with σ the conductivity. Taking the curl

²However, the actual amount of losses is dependent on the geometry, since it is proportional to the field inside the nanoparticles that is indeed geometry dependent.

of Eq. (1.9) and substituting Eq. (1.10) inside (the curl and the partial time derivative commute) we obtain

$$\begin{aligned} \nabla \times \nabla \times \mathbf{E} + \mu_0 \partial_t (\mathbf{J} + \epsilon_0 \partial_t \mathbf{E}) &= 0, \\ \nabla \times \nabla \times \mathbf{E} + \mu_0 \sigma \partial_t \mathbf{E} + \mu_0 \epsilon_0 \partial_t^2 \mathbf{E} &= 0. \end{aligned} \quad \left. \begin{array}{l} \\ \end{array} \right\} \mathbf{J} = \sigma \mathbf{E} \quad (1.11)$$

We further use the vectorial identity $\nabla \times \nabla \times \mathbf{A} = \nabla \nabla \cdot \mathbf{A} - \nabla^2 \mathbf{A}$ with $\mathbf{A} = \mathbf{E}$, and use $\rho = 0 \xrightarrow{\text{Eq. (1.7)}} \nabla \cdot \mathbf{E} = 0$ leading to

$$\nabla^2 \mathbf{E} - \mu_0 \sigma \partial_t \mathbf{E} - \mu_0 \epsilon_0 \partial_t^2 \mathbf{E} = 0. \quad (1.12)$$

This is the usual wave equation, with $c = 1/\sqrt{\mu_0 \epsilon_0}$, provided with an additional first order term $\mu_0 \sigma \partial_t \mathbf{E}$. To find solutions of this new equation, we assume time-harmonic solutions, i.e. we take the Fourier transform of Eq. (1.12) for the time variable. This is done by the following substitution, $\partial_t \leftrightarrow -i\omega$, and we obtain

$$\nabla^2 \mathbf{E} + i\omega \mu_0 \sigma \mathbf{E} + \omega^2 \mu_0 \epsilon_0 \mathbf{E} = 0. \quad (1.13)$$

We can now factor out the \mathbf{E} ,

$$\nabla^2 \mathbf{E} + \omega^2 \mu_0 \epsilon_0 \left(1 + i \frac{\sigma}{\epsilon_0 \omega} \right) \mathbf{E} = 0. \quad (1.14)$$

We thus observe that the additional term in ∂_t (that comes from the conductivity) in the wave equation leads to a new imaginary term in the associated Helmholtz equation. This new term can be interpreted as a modification of the permittivity, giving an effective relative permittivity $\epsilon_r = (1 + i\sigma/(\epsilon_0 \omega))$ that is now a function of the frequency. Additionally, if one uses the frequency dependent conductivity $\sigma = \sigma_0/(1 + i\omega\tau)$ [10] with τ the relaxation time of the free electrons and σ_0 the DC conductivity, the above mentioned relative permittivity corresponds to the so-called Drude model that is often used in plasmonics [11,12]. Let us remark here that if we wanted to consider the frequency dependence of the conductivity in the temporal domain, i.e. in Eq. (1.12), we would have to write a cumbersome temporal convolution of the electric field with the current density; a relation that is easily handled in frequency domain thanks to Fourier's transform properties [8].

If one identifies Eq. (1.14) with the Helmholtz equation (1.3), it appears that instead of the simple relation $k^2 = \omega^2/c^2$ we now have $k^2 = \omega^2/c(\omega)^2 \in \mathbb{C}$. Thus, since for now $\omega \in \mathbb{R}$, it appears that the propagation vector is complex,³ the imaginary part giving the spatial decay rate of the wave. Additionally, the speed is now frequency dependent, leading to dispersion: each harmonic component has a different phase speed given by the

³Keeping a real wavevector together with a real frequency would mean having a complex phase speed, which, at least here, bears little sense. However, as shown later, choosing a complex frequency can have a physical meaning.

dispersion relation. The modified wave equation Eq. (1.11) is a prototypical example of how the inclusion of losses in the governing equations of the system leads to dispersion, and is particularly adequate since this thesis deals with the optics of metals.

The main point to retain from the above derivation is that when working in frequency domain with losses, the equivalent Helmholtz equation contains complex coefficients of different powers of ω and that, consequently, the eigen-solutions of such an equation have complex eigenfrequencies or eigen-wavevectors. In the above development, we assumed harmonic time dependence, i.e. real frequencies. However, things can be less trivial in certain cases and it appears that the choice between a complex frequency or a complex wavevector is dictated by the definition of the problem. To show that, let us first consider a harmonic planewave impinging on a metallic surface. A part of the wave is reflected, but a part penetrates the metal and obeys the lossy wave equation (1.14). One has to choose which of a complex frequency or wave-vector makes sense. If one takes a complex frequency, the amplitude of the wave inside the metal will decay over time. This does not make sense since the impinging planewave has constant amplitude, as imposed by the source. On the other hand, a complex wavevector leads to a decay over the distance, meaning that the wave is attenuated as it penetrates inside the metal and this indeed corresponds to what one could observe in such a case. As another example, let us consider a cavity composed of two parallel perfect conductors, separated by a lossy medium. Searching for the eigenmodes of this cavity, one can deduce that discrete values of the wave vector are defined by the distance between the two planes and translate the standing wave pattern inside the cavity. Consequently, a complex valued wavevector would bear little sense. However, a complex frequency leads to a decay in time, indicating that the modes are damped, a conclusion in agreement with what one could expect from a lossy cavity.

In the case of a leaky cavity, radiation losses occur even when the material building up the cavity is lossless. Thus, the eigenfrequencies of the cavity modes have to be complex in order to account for their damping. Even without additional terms in the wave equation like in Eq. (1.12), the losses appear through the boundary conditions defining the problem. For example, if one studies a Fabry-Pérot resonator and looks for the eigenmodes inside the cavity, a complex eigenfrequency naturally arises to compensate the transmission of the wave to the external medium [1].

Having seen how losses can be accounted for into the wave equation, and more specifically into the associated Helmholtz equation, let us now go back to the problem of finding the eigenmodes of a cavity. The Helmholtz equation of the lossless problem can generally be written in the form $\mathbf{K}\phi = \omega^2\mathbf{M}\phi$, with \mathbf{K} , \mathbf{M} operators (or matrices in the discretized case)⁴ describing the system, and ϕ a function or vector representing the quantity of interest. This case is a conventional linear eigenvalue problem and can generally be solved numerically without difficulties. On the other hand, the inclusion of losses as presented

⁴Often, the matrix \mathbf{M} is proportional to the unit matrix \mathbf{I} , so that it is not explicitly written.

before leads to a problem of the form $\mathbf{K}\phi = \omega^2\mathbf{M}\phi + i\omega\Gamma\phi$, which is a nonlinear, in this case quadratic, eigenvalue problem [13]. Indeed, there is now two different powers of ω , making the search for a solution less trivial than in the linear case. More complex systems can lead to even more complex forms of the problem and it is not always possible to have distinct matrices for each ω power. Fortunately, whatever the exact form of the operator \mathcal{O} describing the system, one can always write it $\mathcal{O}(\omega)\phi = 0$, corresponding to finding solutions ϕ that can exist without sources, i.e. with a vanishing right-hand term. Indeed, the problem with a source \mathcal{F} would be written $\mathcal{O}(\omega)\phi = \mathcal{F}$, and that is the general form of the problem that frequency-based numerical approaches try to solve by inverting $\mathcal{O}(\omega)$.

Below we show a few examples of wave-related problems and the corresponding operators, in frequency domain. The harmonic oscillator is abbreviated H.O., x is a scalar variable, \vec{x} is a vector of scalars, $\phi(\mathbf{r})$ is a position dependent scalar function and \mathbf{O} is a square matrix:

$$\mathcal{O} = \omega_0^2 - \omega^2 \quad \phi = x \in \mathbb{R} \quad \text{H.O.} \quad (1.15)$$

$$\mathcal{O} = \omega_0^2 - i\omega\gamma - \omega^2 \quad \phi = x \in \mathbb{C} \quad \text{Damped H.O.} \quad (1.16)$$

$$\mathcal{O} = \mathbf{M} - \omega^2 \quad \phi = \vec{x} \in \mathbb{R}^n \quad n \text{ Coupled H.O.} \quad (1.17)$$

$$\mathcal{O} = \mathbf{M} - i\omega\Gamma - \omega^2 \quad \phi = \vec{x} \in \mathbb{C}^n \quad n \text{ Coupled Damped H.O.} \quad (1.18)$$

$$\mathcal{O} = \nabla^2 - \omega^2/c^2 \quad \phi = \phi(\mathbf{r}) \in \mathbb{R} \quad \text{Helmholtz} \quad (1.19)$$

$$\mathcal{O} = \nabla^2 - i\omega\gamma - \omega^2/c^2 \quad \phi = \phi(\mathbf{r}) \in \mathbb{C} \quad \text{Damped Helmholtz} \quad (1.20)$$

$$\mathcal{O} = \mathbf{O}(\omega) \quad \phi = \vec{x} \in \mathbb{C}^n \quad n \text{ Elements Discretized Problem} \quad (1.21)$$

Those operators can be classified in two categories, those with operators corresponding to continuous problems, and those with matrices associated to discrete problems. When discretizing a continuous problem, the operator will transform into a matrix. For example, if one discretizes the Helmholtz equation (1.19) to solve the 1D wave equation numerically, one obtains an equation similar to Eq. (1.17). In other words, if one considers infinitely many harmonic oscillators coupled in a line, i.e. each one is coupled to its two neighbours, it can be shown that Eq. (1.17) tends to Eq. (1.19) [14]. This is because the matrix \mathbf{M} in Eq. (1.17) contains off-diagonal elements describing differences between the positions of adjacent oscillators, which is equivalent to the discretization of the second order derivative operator. This relation also shows the importance of the coupled oscillator model when studying wave phenomena and resonant systems.

1.2 Numerical Methods

Having presented the nonlinear eigenvalue problem that arises from the wave equation when losses are present, we can now look at how one can find the complex eigenfrequencies and the associated eigenmodes. Before exposing the different approaches that can be

used to compute eigenmodes, there is an important point that needs to be addressed. As exemplified by the case of a wave in a conducting medium in the previous section, the local response of the medium constituting the system and its surrounding is characterized by a complex function; in the present case of electromagnetism for non-magnetic materials, this response is the permittivity. The frequency dependence of the permittivity translates the fact that the polarization (i.e. the response of the matter to an electric field) takes time to establish, and this is intimately linked to the losses as dictated by the Kramers-Krönig relations [5]. In practice, ellipsometry measurements allow retrieving the full complex permittivity in a given frequency range. In an experiment however, for obvious experimental reasons, this frequency range is bounded to the real axis. Thus, in order to obtain the material response at a complex frequency to find eigenmodes, one needs to use an analytical model fitted to experimental data. Such a model can be prolonged in the complex plane allowing finding eigenmodes for structures described by a realistic permittivity function. In plasmonics, the Drude model is widely used due to its simplicity and its good match with experimental data, generally in the lower range of the frequency spectrum [11]. Indeed, the conduction electrons response is often more complicated than the simple model exposed before, consisting of freely moving point charges occasionally colliding with the lattice. The main departure from this model is due to the interband transitions that create an additional loss channel not described by a Drude model. In gold, the imaginary part of the permittivity starts to depart from the Drude model due to the interband transitions at around 2.0 eV/ 620 nm, whereas for silver this occurs at around 3.8 eV/ 326 nm [15]. Up to those energies, both gold and silver are relatively well described by an adequate Drude model. A way to take the interband transitions into account, i.e. an increase in the imaginary part of the permittivity at high energy, is to add into the Drude model new resonant terms. These so-called Lorentz terms contain poles in the complex plane, and it is not yet clear how those poles affect the search for eigenfrequencies in the complex plane. Since the interband transitions strongly damp the plasmonic resonances, one often designs metallic nanostructures so that the modes of interest are at energies below the interband transition threshold. Thus, the Drude model is often adequate for the eigenmode analysis, but one still has to keep in mind the possible differences between the real/experimental permittivities and that given by the model. In this thesis, all eigenmode computations are made using a Drude model fitted to experimental data, whereas the spectra are often computed directly with those experimental values.

We now concern ourselves with discretized numerical problems, i.e. when the operator describing the problem is a matrix. We consider a general square, complex valued matrix $\mathbf{O}(\omega)$ with $\omega \in \mathbb{C}$ which entries \mathbf{O}_{nm} are complex functions of ω . The general way to find non-trivial ($\phi \neq 0$) solutions to the equation $\mathbf{O}(\omega)\phi = 0$ is to solve $\det(\mathbf{O}(\omega)) = 0$. To use the adequate mathematical terminology, we say that we look for the kernel of $\mathbf{O}(\omega)$ [16]. In the case of square matrices, the determinant is equal to the product of the eigenvalues λ_i so that a vanishing determinant also means that at least one eigenvalue

vanishes. This offers two possible ways to numerically look for the eigenfrequencies. Depending on the size and the condition number of the matrix, one possibility can be more advantageous than the other since different algorithms exist for those two tasks. Additionally, there exist algorithms that directly look for the smallest eigenvalue of a matrix, without having to compute all of them and then sort them out [17]. Let us recall that the vanishing eigenvalue λ that is sought here is not the eigenfrequency of the mode, as it can be the case in other problems, but an abstract number that expresses the fact that a solution, the eigenvector, exists without any sources. On the other hand, the eigenfrequency ω_{eig} is the eigenvalue of the nonlinear eigen-problem $\mathbf{O}(\omega_{\text{eig}})\phi_{\text{eig}} = 0$. We can summarize this as follow:

$$\underbrace{\det(\mathbf{O}(\omega_{\text{eig}}))}_{\text{eigenfrequency}} = 0 \quad \Leftrightarrow \quad \underbrace{\mathbf{O}(\omega_{\text{eig}})}_{\text{eigenvector}} \underbrace{\phi_{\text{eig}}}_{\text{eigenvalue}} = \lambda_{\text{eig}} \phi_{\text{eig}} = 0, \quad \lambda_{\text{eig}} \rightarrow 0 \Leftrightarrow \text{no sources} . \quad (1.22)$$

Once an eigenfrequency ω_{eig} is found, one can easily obtain the associated eigenvector ϕ_{eig} that solves the eigenvalue equation $\mathbf{O}(\omega_{\text{eig}})\phi_{\text{eig}} = 0$. Let us mention that the eigenvalues λ of $\mathbf{O}(\omega)$ are indeed complex numbers, but since only their magnitude is important here, we implicitly refer to $|\lambda|$ when talking about a vanishing eigenvalue. Concerning the notation, λ designates any eigenvalue of $\mathbf{O}(\omega)$, λ_{\min} is the smallest one of them and λ_{eig} is the eigenvalue that vanishes, i.e. if $\lambda_{\min} \rightarrow 0$, $\lambda_{\min} = \lambda_{\text{eig}}$.

The goal is now to find a particular point in the complex plane where the determinant/eigenvalue of the matrix vanishes. Brut-force scanning of the complex plane is not a practical solution for matrices larger than a few tens of elements, and one has to proceed differently. We first outline several ways one can get a first estimate of the position of the eigenfrequencies in the complex plane. To begin with, the different spectra obtainable with different excitation conditions already give a first hint as to where the eigenfrequencies are located in the complex plane. Indeed, for a single eigenmode, the resonant frequency (the frequency of the maximum response) is related to the real part of the eigenfrequency, whereas the width of the resonance is linked to the imaginary part. One can then first acquire a spectrum, measure the resonances lineshape, and use these two parameters as starting point in the complex plane. Unfortunately, except for very simple systems and/or for a few sets of eigenvalues, it is rarely as simple as that. Realistic systems have more than one eigenmode, and thus resonances often overlap and interfere, making the use of the above-mention relation hard or even impossible. This is especially the case in plasmonic systems where resonances are broad, i.e. easily overlapping, but also in dielectric nano-systems where different multipoles easily interfere, creating a strong asymmetric lineshape [18]. Different excitation geometries may allow the discrimination of specific eigenmodes thanks to their symmetry, but this trick is indeed limited to relatively simple systems possessing certain symmetries. Additionally, looking at the fields at particular points and/or in particular directions can also allow discriminating eigenmodes with specific symmetries. Finally, in most cases, two or more

eigenmodes couple to the same excitation and one of the eigenmode may have a response much smaller than the other one, making it impossible to extract its resonance lineshape. One way to increase the amount of information deducible from a spectrum is to artificially set the imaginary part of the permittivity to zero. This will cancel the absorption losses, thus narrowing the peaks and allowing an easier estimation of the lineshapes parameters. The eigenfrequency found without losses gives then a relatively good starting point in the complex plane, with the additional information that the corresponding lossy eigenfrequency exists at a larger negative imaginary frequency and at a real part generally only slightly different. This loss-cancelling approach is especially efficient for high order modes that often occur in the interband transitions region of metals and are strongly damped.⁵ Another approach is to conduct a decomposition of the scattering spectrum into vector spherical harmonics (VSH). It allows a first disentanglement of the spectrum that can help isolate the contribution of a single eigenmode, even though a single mode cannot always be related to a single multipole coefficient (see for example Fig. S5 in Sec. 3.2 and Fig. 2 in Sec. 3.3). Another approach is to fit the resonant lineshape with a coupled oscillator model in order to extract the eigenfrequencies of each modes. Finally, one is not restricted to monitor far-field scattering: monitoring the near-field is also a possibility, as the relative weight between radiative and non-radiative components associated with different modes can change appreciably.

Once an estimate of the eigenfrequency position is obtained, one needs a criterion to be able to converge to the vanishing determinant. Ideally, the 2D map created by $\det(\mathbf{O}(\omega))$ or $\lambda_{\min}(\omega) = \min(\text{eig}(\mathbf{O}(\omega)))$ ⁶ is smooth and has local minima at the positions of the eigenfrequencies. One may thus use various algorithms, such as Householder's methods, to converge to the minima by functions fitting and extrapolation [19]. Unfortunately, it can be that the 2D map is not smooth at all and that neither method is ideal, see Sec. 2.1. For example, for large and ill-conditioned matrix, the computation of the determinant is hard or even impossible so one has to look at the smallest eigenvalue [17]. On the other hand, there is a priori no reason for the 2D map created by $\lambda_{\min}(\omega)$ to be smooth. Indeed, as stated before, in the case of the SIE matrix the eigenvalue $\lambda_{\min}(\omega)$ has no particular physical meaning and is only indicating the frequency at which there is a non-trivial solution to the problem $\mathbf{O}(\omega)\phi = 0$. Thus, far from an eigenfrequency, $\lambda_{\min}(\omega)$ can take any value and is not related in any way to the physics of the problem, but rather to the mathematical structure of the matrix. The consequence is that, except if the initial guess ω_1 of the eigenfrequency ω_{eig} is really accurate, the evaluation of $\lambda_{\min}(\omega)$ around ω_1 will not yield any hint to where ω_{eig} is located, see Fig. 1.1(a). Let us note here that for different problems the minimal eigenvalue map can be smooth and allow a fast

⁵Since eigenmodes are here found with Drude models, the interband transitions are in fact not a problem. Practically, even if the spectra used as final results are computed with experimental values of the permittivity, a spectrum with the corresponding Drude model is often computed in addition as to remove the interbands contribution, with or without setting the losses to zero, to get a better insight into the modes.

⁶ $\text{eig}(\cdot)$ meaning the set of eigenvalues of (\cdot) .

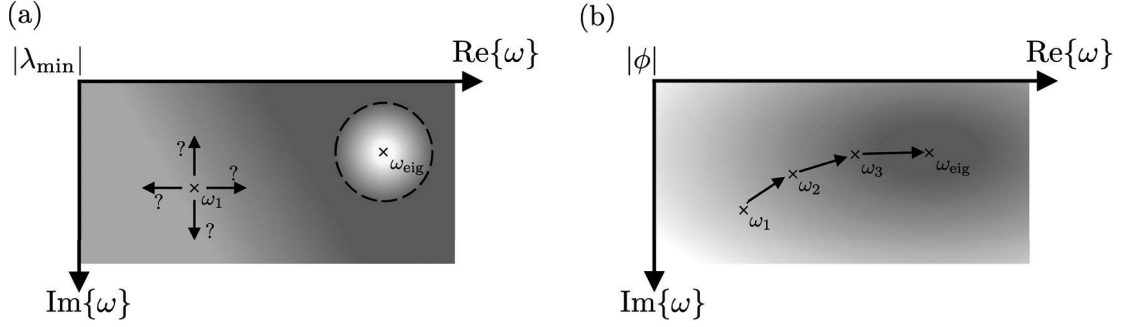


Figure 1.1 – Looking for an eigenfrequency in the complex plane. Bright/dark shades indicate minimal/maximal values. (a) Monitoring the minimal eigenvalue. Outside a narrow region around the eigenfrequency (dashed circle), $|\lambda_{\min}|$ does not give information about the location of ω_{eig} . It is thus impossible to know where to compute the next eigenvalue. (b) Monitoring the response $|\phi|$ to a complex frequency excitation. The evolution of $|\phi|$ is smooth, enabling an algorithm to converge easily to ω_{eig} through a few intermediate steps ω_{1-3} .

convergence to the eigenfrequency, see Ref. [19] for an example with scattering matrices.

Although the general problem of finding eigenmodes was presented as a search for solutions without sources, approaching the problem from the point of view of a system response's yields another way to study eigenmodes. Let us first consider a simple undamped harmonic oscillator for which the frequency dependent amplitude x has the form

$$x \propto \frac{1}{\omega_0^2 - \omega^2}. \quad (1.23)$$

When driven at its resonant frequency ω_0 , energy keeps being built up in its motion and its amplitude diverges to infinity. One can remedy to this non-physical divergence problem by adding a damping term γ proportional to the speed of the oscillator, leading to a finite maximal amplitude. Mathematically, Eq. (1.23) is modified as follows:

$$x \propto \frac{1}{\omega_0^2 - \omega^2 - i\omega\gamma}. \quad (1.24)$$

Thus, due to the imaginary part of the denominator, the amplitude of x cannot diverge. However, this is true only for a real frequency excitation, i.e. $\omega \in \mathbb{R}$. Indeed, by setting $\omega = \pm\sqrt{\omega_0^2 - (\frac{\gamma}{2})^2} - i\frac{\gamma}{2}$, which is precisely the eigenfrequency of the system, in Eq. (1.24) the denominator vanishes, leading again to a diverging amplitude. Here, and in the rest of this thesis we use the $e^{-i\omega t}$ convention for the time varying harmonic quantities; the consequence is that the imaginary part of the eigenfrequencies needs to be negative to correspond to time decaying amplitudes. If one now considers the problem of finding the eigenmodes of the matrix $\mathbf{O}(\omega)$, instead of solving for the vanishing determinant, one can look for solutions leading to diverging responses ϕ [20]. The problem is different than before as we now have to solve $\mathbf{O}(\omega)\phi = s(\omega)$ for ϕ , with s the excitation vector, and we

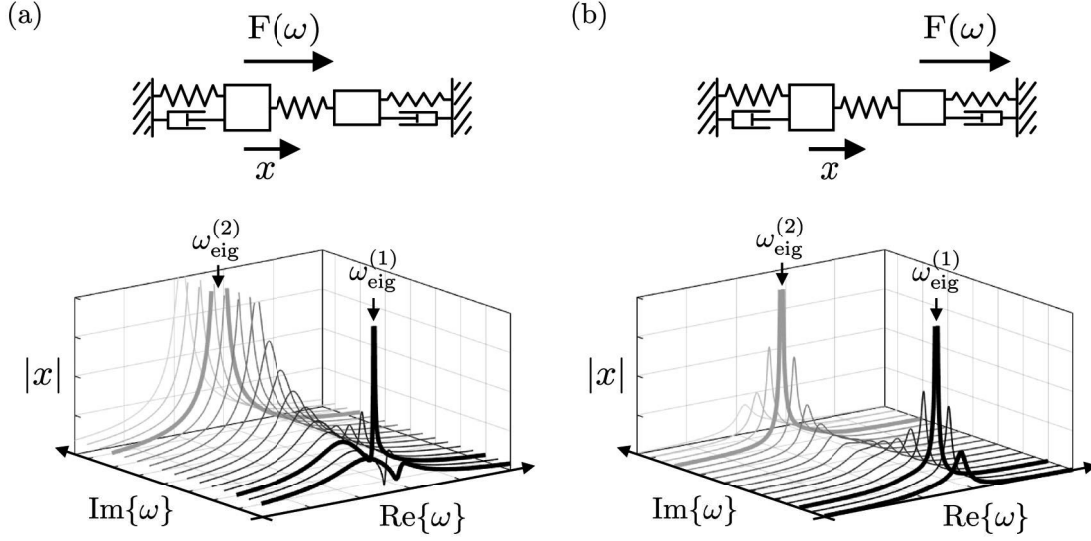


Figure 1.2 – Complex excitation method applied to a coupled system of two different damped oscillators. On the plots, each line represents a spectrum at a constant imaginary frequency. (a) The mass on the left is excited and its amplitude is monitored. It appears that its amplitude diverges at two distinct complex frequencies, corresponding to the eigenfrequencies of the coupled system $\omega_{\text{eig}}^{(1,2)}$. (b) If the second mass is excited, and the amplitude of the first one is monitored, we also observe the divergence of the response at the two eigenfrequencies. The same effect happens if one monitors the second mass. The lines computed at the imaginary frequencies corresponding to the two eigenfrequencies as well as the spectra computed at real frequencies are shown thicker. In (a), at $\text{Im}\{\omega\}=0$ one can see a typical Fano lineshape.

can formally write $\phi_{\text{eig}} = \mathbf{O}^{-1}(\omega_{\text{eig}})s(\omega_{\text{eig}}) \rightarrow \infty$. In all generality, not all elements of ϕ_{eig} necessarily diverge, and one has to specify what is exactly meant by $\phi_{\text{eig}} \rightarrow \infty$. In practice, monitoring e.g. the electric field at one adequate point is sufficient, but the exact quantity will depend on the nature of the numerical method used to approximate Maxwell's equations. In the case of SIE, it makes more sense to monitor the effective surface currents as they are the quantities constituting ϕ . Contrary to the minimal eigenvalue method described above, the response that is now monitored is evolving smoothly with the frequency since it describes a physical quantity, enabling to quickly converge to the actual eigenfrequency, see Fig. 1.1(b). This is exemplified in Fig. 1.2 where a system of two non-identical coupled lossy oscillators is driven in two different configurations. It is clearly apparent that the two modes give a divergent response at the two respective eigenfrequencies in both cases, and that the evolution of the amplitude is smooth. Additionally, we notice that the two spectra on the real axis ($\text{Im}\{\omega\}=0$) do not show a clean resonant lineshape from which the real and imaginary part of the eigenfrequencies can be easily guessed. In this example, the operator \mathcal{O} is of the form (1.18), with $n = 2$.

Finally, let us remark that the complex frequencies at which the amplitudes of the responses diverge are precisely those where the determinant of the matrix vanishes, and the vector $\phi_{\text{eig}} = \mathbf{O}^{-1}(\omega_{\text{eig}})s(\omega_{\text{eig}})$ tends (with appropriate scaling) to the eigenvector of the equation $\mathbf{O}(\omega_{\text{eig}})\phi_{\text{eig}} = 0$ [20]. Indeed, recalling that $\det(\mathbf{O}^{-1}) = (\det(\mathbf{O}))^{-1}$, it follows that if $\det(\mathbf{O}(\omega_{\text{eig}})) = 0$ then $\det(\mathbf{O}^{-1}(\omega_{\text{eig}})) \rightarrow \infty$. In practice, once an eigenfrequency is found with the complex excitation method, the smallest eigenvalue of the SIE matrix at this eigenfrequency is computed and verified to be sufficiently small. The fact that this approach relies on an excitation inherently implies that one can only find eigenmodes that couple to this excitation. Although it is relatively easy to design an excitation that couples to all modes by suitable symmetry breaking, it is to be expected that some eigenmodes will respond far better than others, thus possibly dwarfing the response of the latter in comparison. All the modes will still present a divergent response at their eigenfrequencies, but if one mode is located near another better-coupled one it can appear to be relatively narrow and it can be harder to converge to it without being attracted by the maximum of the neighbouring stronger resonance (see for example the 2D map presented afterwards in Fig. 1.4 where some maxima are extremely broader compared to others). Thus, one can still expect to have to adapt the excitation to the sought eigenmode symmetries in order for this method to be efficient, implying a prior knowledge of the modal structure of the system. On the other hand, the previous approach based on the determinant is indeed excitation free so that all eigenmodes can be expected to have comparable behaviour in the complex plane, this being however of no importance in our case since this method is not efficiently applicable to SIE.

The two methods mentioned above have direct physical interpretations, respectively a solution without excitation and a diverging response to a complex frequency excitation. Both approaches arise naturally as ways to find the eigenmodes when the problem is studied mathematically. Unfortunately their efficiency as a whole depends on how accurate the first estimate of the eigenfrequency is, if one is obtainable at all. However, an ingenious trick allows one to find all the eigenfrequencies included in a given contour inside the complex plane. This method is based on Cauchy's integral formula and the residue theorem [8]. Since both theorems deal with poles of functions, we need to use the inverse of the matrix of which we are seeking the kernel (i.e. the eigenvectors ϕ_{eig}). We will thus use the matrix $\mathbf{S}(\omega) = \mathbf{O}^{-1}(\omega)$ and, as just shown above for the frequency excitation method, the positions of the poles of the inverse operator coincide with the position of the zero of the operator. We first show below how this method works on a scalar function and then extend it to matrices; additional details can be found in [19, 21–24].

Let us consider a closed contour γ in the complex plane, a complex number z_0 inside this contour, as well as a function $f(z) \in \mathbb{C}$ that is holomorphic inside the contour.⁷ Cauchy's

⁷A function is holomorphic if it is complex-differentiable in the domain under consideration. The terms analytic and regular are also often employed.

Chapter 1. Eigenmode Analysis

integral formula states that

$$\oint_{\gamma} \frac{f(z)}{z - z_0} dz = 2\pi i f(z_0). \quad (1.25)$$

One can compute the same integral with $zf(z)$ as the denominator and obtain

$$\oint_{\gamma} \frac{zf(z)}{z - z_0} dz = 2\pi i z_0 f(z_0). \quad (1.26)$$

If we now divide Eq. (1.26) by Eq. (1.25) we have,

$$\frac{\oint_{\gamma} \frac{zf(z)}{z - z_0} dz}{\oint_{\gamma} \frac{f(z)}{z - z_0} dz} = z_0. \quad (1.27)$$

Thus, the computation of two integrals allows extracting the value of the pole z_0 . In the above example, this may seem trivial since we have constructed the pole ourselves, but in practical problems, the poles are not necessarily known and this method is very powerful. To apply this method to the problem of finding a complex frequency at which a given function vanishes, it suffices to use the inverse of the function, since the positions of its zero will correspond to the position of the poles of the inverse function.

We now extend this method to a matrix $\mathbf{S}(\omega)$, the elements of which are frequency dependent complex functions, i.e. $\mathbf{S}_{nm}(\omega) = f_{nm}(\omega)$. The poles will be the values of ω for which $\det(\mathbf{S}(\omega)) \rightarrow \infty$. Since the determinant is the product of the eigenvalues, this will also correspond to at least one diverging eigenvalue. Additionally, if $\mathbf{S}(\omega) = \mathbf{O}^{-1}(\omega)$ and $\mathbf{O}(\omega)$ has eigenvalues λ_i , then $\mathbf{S}(\omega)$ has eigenvalues $\eta_i = \lambda_i^{-1}$. This is straightforwardly shown:

$$\begin{array}{ccc} \text{Eigenvalue problem} \\ \text{with } \mathbf{O}, u \text{ and } \lambda \\ \underbrace{\mathbf{O}u = \lambda u} & \xrightarrow{\mathbf{O}^{-1} \times} & \mathbf{O}^{-1}\mathbf{O}u = \mathbf{O}^{-1}\lambda u \\ & & u = \mathbf{O}^{-1}\lambda u \xrightarrow{\lambda^{-1} \times} \underbrace{\lambda^{-1}u = \mathbf{O}^{-1}u}_{\substack{\text{Eigenvalue problem} \\ \text{with } \mathbf{O}^{-1}, u \text{ and } \lambda^{-1}}} \end{array}, \quad (1.28)$$

the first and last equations correspond to eigenvalue problems for \mathbf{O} and \mathbf{O}^{-1} with λ and u , respectively λ^{-1} and u , as eigenvalues and eigenvectors.

We first begin by showing the validity of the method for a diagonal matrix, the extension to any matrix following afterwards. Let us consider a 2×2 diagonal matrix $\mathbf{S}(\omega)$

containing two meromorphic⁸ functions with two poles ω_1 and ω_2 inside the contour γ ,

$$\mathbf{S}(\omega) = \begin{bmatrix} \frac{f(\omega)}{\omega-\omega_1} & 0 \\ 0 & \frac{g(\omega)}{\omega-\omega_2} \end{bmatrix}, \quad (1.29)$$

with $f(\omega)$ and $g(\omega)$ two holomorphic functions. According to Eq. (1.25) and Eq. (1.26), the computation of the closed integrals of \mathbf{S} and $\omega\mathbf{S}$ around γ gives

$$\frac{1}{2\pi i} \oint_{\gamma} \mathbf{S}(\omega) d\omega = \begin{bmatrix} f(\omega_1) & 0 \\ 0 & g(\omega_2) \end{bmatrix} = \mathbf{I}_1, \quad (1.30)$$

$$\frac{1}{2\pi i} \oint_{\gamma} \omega \mathbf{S}(\omega) d\omega = \begin{bmatrix} \omega_1 f(\omega_1) & 0 \\ 0 & \omega_2 g(\omega_2) \end{bmatrix} = \mathbf{I}_2. \quad (1.31)$$

We then compute $\mathbf{I}_2 \mathbf{I}_1^{-1}$:

$$\begin{aligned} \mathbf{I}_2 \mathbf{I}_1^{-1} &= \begin{bmatrix} \omega_1 f(\omega_1) & 0 \\ 0 & \omega_2 g(\omega_2) \end{bmatrix} \frac{1}{f(\omega_1)g(\omega_2)} \begin{bmatrix} g(\omega_2) & 0 \\ 0 & f(\omega_1) \end{bmatrix} \\ &= \begin{bmatrix} \omega_1 & 0 \\ 0 & \omega_2 \end{bmatrix}. \end{aligned} \quad (1.32)$$

We thus see that the two poles appear in the diagonal of the resulting matrix. This result is easily extended to a square diagonal matrix of arbitrary size.

The extension to non-diagonal square matrices is not straightforward and is addressed in ref. [22, p. 313] and [23]; here we briefly summarize the main result. If $\mathbf{S}(\omega)$ is not diagonal, the two matrices \mathbf{I}_1 and \mathbf{I}_2 resulting from the integral will not be either. To show how we can make this method work for non-diagonal matrices, let us first write the quotient of the two integrals of a given diagonal matrix \mathbf{D} ,

$$\frac{\oint \omega \mathbf{D} d\omega}{\oint \mathbf{D} d\omega} = \frac{\mathbf{D}_2}{\mathbf{D}_1} = \mathbf{D}_p, \quad (1.33)$$

where \mathbf{D}_p is a diagonal matrix with the poles of \mathbf{D} . We note that since \mathbf{D}_p is diagonal, the poles of \mathbf{D} are also the eigenvalues of \mathbf{D}_p .⁹ We now introduce a non-diagonal matrix \mathbf{P} and multiply the previous equation by \mathbf{P} on the left and \mathbf{P}^{-1} on the right:

$$\begin{aligned} \mathbf{P} \mathbf{D}_p \mathbf{P}^{-1} &= \mathbf{P} \frac{\mathbf{D}_2}{\mathbf{D}_1} \mathbf{P}^{-1} = \mathbf{P} \mathbf{D}_2 \mathbf{D}_1^{-1} \mathbf{P}^{-1} \\ &= \mathbf{P} \mathbf{D}_2 \underbrace{\mathbf{P}^{-1} \mathbf{P}}_{\mathbf{I}} \mathbf{D}_1^{-1} \mathbf{P}^{-1} = \mathbf{P} \mathbf{D}_2 \mathbf{P}^{-1} (\mathbf{P} \mathbf{D}_1 \mathbf{P}^{-1})^{-1} = \frac{\mathbf{P} \mathbf{D}_2 \mathbf{P}^{-1}}{\mathbf{P} \mathbf{D}_1 \mathbf{P}^{-1}}. \end{aligned} \quad (1.34)$$

⁸A meromorphic function is a function that is holomorphic everywhere except in a discrete set of points which are the poles of the function.

⁹The eigenvalues of a diagonal matrix are its diagonal elements.

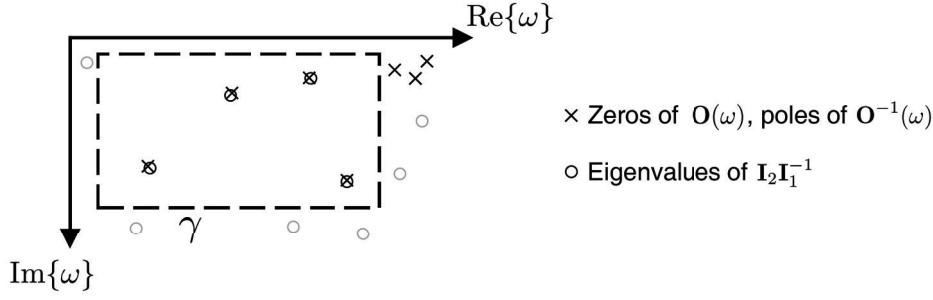


Figure 1.3 – Schematic representation of the contour integral method to locate the poles of $\mathbf{O}^{-1}(\omega)$. The eigenvalues of the matrix $\mathbf{I}_2 \mathbf{I}_1^{-1}$ give a very good approximation of the poles positions inside the contour γ . The eigenvalues located outside the contour (gray circle) are simply ignored. If needed, they can be refined by using either of the methods shown in Fig. 1.1.

The term $\mathbf{P} \mathbf{D}_p \mathbf{P}^{-1}$ is by definition the diagonalization of an unknown matrix,¹⁰ which eigenvalues are in the diagonal of \mathbf{D}_p .

We now assume that \mathbf{I}_1 and \mathbf{I}_2 , resulting from the integrals of a non-diagonal square matrix, can be both diagonalized by the same matrix \mathbf{P} , and that \mathbf{P} contains the eigenvectors of both \mathbf{I}_1 and \mathbf{I}_2 . This point is crucial but is non-trivial to prove, see Refs. [22, 23] for the mathematical details. We can thus write $\mathbf{I}_1 = \mathbf{P} \mathbf{D}_1 \mathbf{P}^{-1}$ and $\mathbf{I}_2 = \mathbf{P} \mathbf{D}_2 \mathbf{P}^{-1}$, with \mathbf{D}_1 and \mathbf{D}_2 diagonal matrices containing respectively the eigenvalues of \mathbf{I}_1 and \mathbf{I}_2 . If we now compute $\mathbf{I}_2 \mathbf{I}_1^{-1}$ using their diagonalization explicitly, we just have to read Eq. (1.34) backward and see that consequently, $\mathbf{P} \mathbf{D}_p \mathbf{P}^{-1}$ represents a diagonalization of the matrix $\mathbf{I}_2 \mathbf{I}_1^{-1}$. The eigenvalues of $\mathbf{I}_2 \mathbf{I}_1^{-1}$ are thus the elements of \mathbf{D}_p , which are the poles of the matrix \mathbf{S} . Figure 1.3 shows the method schematically.

In the previous examples, we considered implicitly that the matrix \mathbf{O} had as many zeros as its number of rows and columns. However, in practical problems it can very well be that only a few eigenfrequencies are inside the contour and that the matrix has a larger number of elements. This means that some elements of the matrix will be holomorphic, and that analytically they will give a vanishing contribution to the contour integrals. To see how this situation may cause a problem in numerical applications, let us take the following example of a matrix containing one meromorphic and one holomorphic entry:

$$\mathbf{S}(\omega) = \begin{bmatrix} \frac{f(\omega)}{\omega - \omega_1} & 0 \\ 0 & g(\omega) \end{bmatrix}. \quad (1.35)$$

¹⁰Since here \mathbf{P} is for now a general matrix, i.e. not the eigenvectors of \mathbf{D}_p , the diagonalization is not necessarily an eigenvalue decomposition.

The two integrals \mathbf{I}_1 and \mathbf{I}_2 directly give

$$\mathbf{I}_1 = \frac{1}{2\pi i} \oint_{\gamma} \mathbf{S}(\omega) d\omega = \begin{bmatrix} f(\omega_1) & 0 \\ 0 & \epsilon \end{bmatrix}, \quad (1.36)$$

$$\mathbf{I}_2 = \frac{1}{2\pi i} \oint_{\gamma} \omega \mathbf{S}(\omega) d\omega = \begin{bmatrix} \omega_1 f(\omega_1) & 0 \\ 0 & \epsilon' \end{bmatrix}, \quad (1.37)$$

where ϵ and ϵ' are small quantities indicating that the integrals of $g(\omega)$ and $\omega g(\omega)$ do not identically vanish due to numerical errors. Thus, computing $\mathbf{I}_2 \mathbf{I}_1^{-1}$ we obtain

$$\mathbf{I}_2 \mathbf{I}_1^{-1} = \begin{bmatrix} \omega_1 & 0 \\ 0 & \epsilon/\epsilon' \end{bmatrix}. \quad (1.38)$$

Unfortunately, ϵ/ϵ' can be pretty much anywhere in the complex plane, and indeed inside the contour γ ; spurious poles may thus arise due to numerical inaccuracies. It is especially critical in the case of SIE because the original matrix \mathbf{O} is inverted to obtain the matrix \mathbf{S} at points where \mathbf{O} is almost singular. To remedy this problem, one needs to distinguish between the holomorphic and the meromorphic elements of the matrix. If ϵ vanishes, the two column of \mathbf{I}_1 are not linearly independent and the matrix is singular. Stated otherwise, \mathbf{I}_1 is rank deficient.¹¹ For non-diagonal matrices, this rank deficiency is not apparent like in the previous example. Fortunately, the singular value decomposition (SVD) of a matrix allows extracting a diagonal matrix containing elements called singular values [17]. Roughly said, a vanishing singular value corresponds to a column of the matrix that is linearly dependent on the others. By conducting a SVD on the matrix \mathbf{I}_1 , one can then discard the vanishing parts due to the holomorphic components of \mathbf{S} and extract a full rank sub-matrix that contains only information about the poles. Due to numerical errors, the singular values that can be discarded are not identically vanishing and one has to set a threshold to distinguish between meaningful/large and useless/small singular values [19, 23].

In the case of SIE, I found that for metallic structures no spurious poles appear and that this method is astoundingly effective. Indeed, computing the integral with typically hundred constant steps with the rectangle rule already yields eigenfrequencies estimates that are accurate enough for the complex frequency excitation method to converge in a few steps.

Due to the behaviour of the real part of the permittivity of metals, the resonant frequencies of the plasmonic modes are bounded to a frequency where the real part of the permittivity is the opposite of the background permittivity [12]. This is indeed also the limiting frequency of a SPP and one can interpret the link as follows: due to its extremely short surface wavelength, a mode of high order will locally see the surface of the nanoparticle as

¹¹The rank of a matrix is the number of its columns that are linearly independent. A matrix is said to be full rank if its rank is equal to its size, and rank deficient otherwise. If a matrix is rank deficient, its determinant is zero.

planar and thus act as a SPP. Therefore the real part of the eigenfrequency of plasmonic resonances is bounded to a value dictated by the model used for the permittivity, giving a practical upper bound for the real part of the integration contour. Practically, the discretization of the nanostructure with a finite number of elements reduces this limit. Indeed, the surface charges associated with high order modes possess spatially fast variations that need to be resolved accurately by the mesh. The upper bound¹² on the imaginary part of the contour is 0 whereas the lower bound can be estimated by looking at the width of the different spectral features and by taking a comfortable margin that does not excessively increase the length of the contour.

Concerning the implementation of the numerical methods described in this chapter together with the SIE approach, the method of the vanishing eigenvalue was the first one to be implemented as it is the most straightforward. Its limitation, namely the impossibility to converge to the eigenfrequency if the first guess is not accurate enough, has led to the subsequent implementation of the complex frequency excitation method. This method works extremely well for simple structures and when the different spectra allow for a good guess of the eigenfrequencies. However, it became relatively tedious to find eigenmodes for complex structures like the fractals presented in Sec. 3.4 or the heterodimers of Sec. 3.2. This method reached its limit when applied to dielectric structures, where the modes can easily interfere together and thus strongly hinder the analysis of the spectrum. Consequently, the contour integral method was finally implemented.

As an example of the application of the contour integral method, I use it here for the study of the eigenmodes of a silver nanorod; the eigenmodes of this nanorod are used in Sec. 2.3 for the study of the dynamics of SHG under femtosecond pulse illumination. The results are shown in Fig. 1.4 for three different numbers of discretization points for the contour integral. The poles found with the contour integral method are compared to the eigenfrequencies obtained with the complex excitation method, the latter having been obtained before the contour integral method was implemented. Additionally, a complete 2D map of the complex frequency excitation response is shown to evidence the global behaviour of the response in the complex plane. For this 2D map, the source is a dipole situated near the tip of the nanorod and the amplitude electric field is probed at one point ~ 120 nm away from the nanorod; the map in Fig. 1.4(b) is composed of $90 \times 112 = 10080$ points whereas the map detailing larger frequencies in Fig. 1.4(c) contains $80 \times 60 = 4800$ points. The eigencharge surface distributions for the first few eigenmodes are also shown. The contour integral is computed with a rudimentary rectangle rule, i.e. a constant interpolation of the function value between the two successive points. First, one can notice that even with 50 steps and with this crude integral evaluation method, the results are remarkably accurate;¹³ the improvement in accuracy obtained with 100 and 200 steps

¹²In our case, with the convention of harmonic signals evolving according to $e^{-i\omega t}$, the imaginary part of the eigenfrequency is negative.

¹³We consider here that the eigenfrequencies obtained with the complex excitation method and indicated

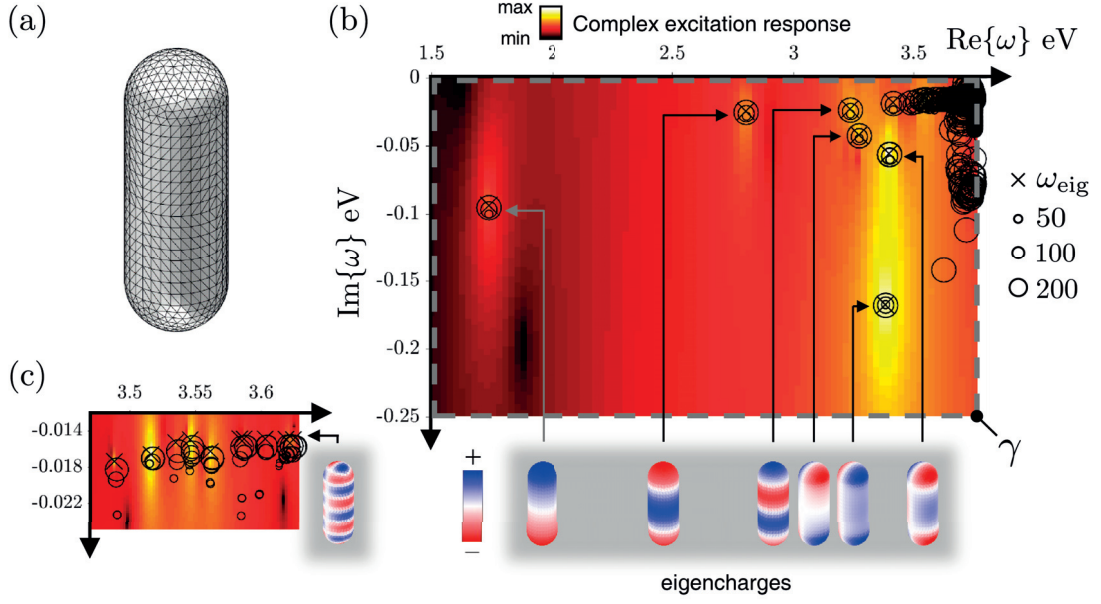


Figure 1.4 – Contour integral method applied to a silver nanorod in water. (a) Surface mesh used for the simulations. (b) Complex frequency plane. The contour γ is discretized with 50, 100, and 200 steps, the resulting poles being shown respectively as black circles of increasing sizes. The crosses indicate eigenfrequencies found with the complex excitation before the contour integral method was implemented. The colormap shows the amplitude of the electric field, in logarithmic scale, at a single point ~ 120 nm away from the nanorod due to a dipolar source situated near the tip of the nanorod and oriented in such a way that all the modes are excited. Red-blue plots show the eigencharges for a few eigenfrequencies. (c) Zoom at high energy.

is useful only for the high order modes at high energy, see Fig. 1.4(c). Second, one can observe the bunching of poles near the upper limit of the real axis. This is expected to be due to the permittivity reaching the critical value $\epsilon(\omega) = -\epsilon_{bg}$, occurring here at $\omega = 3.78$ eV. On the other hand, the eigencharges of the modes at energies larger than ~ 3.6 eV show variations that start to be poorly resolvable by the mesh, see Fig. 1.4(c). Thus, those eigenfrequencies cannot be expected to accurately describe the nanorod true eigenfrequencies because of the limitation of the discretization. However, those poles and the associated eigenvectors can still describe mathematically correctly the meshed, approximated structure. Finally, it can also be that some of the poles located at high real frequencies are spurious poles as explained previously. In this case however, knowing that the mesh limits the order of the modes accurately resolved, the poles above ~ 3.6 eV can be discarded without further concerns. Although not visible at the scale of the 2D maps shown here, the degeneracy of the modes is apparent, namely that poles corresponding to degenerated modes come by pairs, as is also the case for the vanishing minimal eigenvalues (not shown here).¹⁴

Concerning dielectric systems, the results of the integral method (the eigenvalues of the matrix $\mathbf{I}_2\mathbf{I}_1^{-1}$) are plagued with spurious poles inside all the contour. To remedy to this issue, the method using the SVD was implemented as described in [23]. This method consists of sampling an increasing subset of the matrix \mathbf{I}_1 and monitoring the singular values of the resulting matrix. Since the SVD automatically sorts the singular values in decreasing order, ideally, when all the meromorphic components (that are associated with a large singular value) are included in the subset, the next iteration should be accompanied by a small singular value indicating the inclusion of a holomorphic component into the sampled matrix. One can then stop the algorithm and extract only the meaningful poles of the original matrix. Unfortunately, when applied to dielectric nanostructures, no clear drop of the singular value was ever observed. It was noted in Ref. [18] that the RWG basis functions could lead to the presence of spurious poles, thus offering a possible explanation for the difficulty encountered with dielectric structures.

1.3 Conclusion

In this chapter, the theory of eigenmodes was briefly presented and a few examples were given. It was shown how the wave equation is affected by the presence of losses in the system it describes, and how one can solve for the eigenmodes. It was then explained how one can numerically search for the eigenfrequencies/eigenvectors of a matrix with three different methods. The first two methods need a first estimate of the eigenfrequency position in the complex plane that can be obtained by monitoring spectra acquired at

with the cross are the "true" eigenfrequencies.

¹⁴In the case of this nanorod, the modes that show a degeneracy are the ones having eigencharges having at least one node in the transverse direction of the nanorod (along the short axis), like the last three modes shown in Fig. 1.4(b).

various positions and with different excitations. Once an estimate is obtained, the first method consists in looking for the vanishing of the determinant/smallest eigenvalue of the matrix. For large matrices, the computation of the determinant is not practical, so it is preferable to compute the minimal eigenvalue. Unfortunately, in the case of SIE, the 2D map created by the minimal eigenvalue is not smooth and if the first estimate of the eigenfrequency is not accurate enough, it is not possible to know where it is located. The second method also relies on a first estimate of the eigenfrequency's position, but uses an excitation with a complex frequency. When the complex frequency of excitation matches the eigenfrequency of the mode, the amplitude of the system's response diverges. In this case, the 2D map created by the amplitude of the response is smooth and one can use an algorithm to quickly converge to the eigenfrequency. The last method uses a contour integral approach to isolate all the eigenfrequencies included in a given closed path. Thus, no first guess of the possible positions of the eigenfrequencies is needed, making this method extremely practical and powerful. Unfortunately, its applicability to dielectric structures seems to be more complicated due to numerical problems that still need to be addressed. From a global point of view, it is now possible with the SIE method to easily and quickly obtain eigenmodes for complex plasmonic nanostructures allowing a better understanding of their responses to various kinds of excitations.

Bibliography

- [1] P. Lalanne, W. Yan, K. Vynck, C. Sauvan, and J.-P. Hugonin, “Light Interaction with Photonic and Plasmonic Resonances,” *Laser Photonics Rev.* **12**, 1700113, (2018).
- [2] R. P. Feynman, R. B. Leighton, and M. Sands, *The Feynman Lectures on Physics*. Addison–Wesley, (1963).
- [3] B. H. Tongue, *Principles of Vibration*. Oxford University Press, (2002).
- [4] S. Kamol, P. Limsuwan, and W. Onreabroy, “Three-dimensional standing waves in a microwave oven,” *Am. J. Phys.* **78**, 492–495, (2010).
- [5] B. E. A. Saleh and M. C. Teich, *Fundamentals of Photonics*. Wiley-Interscience, 2nd ed., (2007).
- [6] B. R. Kusse and E. A. Westwig, *Mathematical Physics: Applied Mathematics for Scientists and Engineers*. Weinheim: Wiley-VCH, 2nd ed., (2006).
- [7] B. Gallinet, J. Butet, and O. J. F. Martin, “Numerical methods for nanophotonics: Standard problems and future challenges,” *Laser Photonics Rev.* **9**, 577–603, (2015).
- [8] G. B. Arfken, H.-J. Weber, and F. E. Harris, *Mathematical Methods for Physicists: A Comprehensive Guide*. Academic Press, (2013).
- [9] M. A. Tadayon, M.-E. Baylor, and S. Ashkenazi, “High quality factor polymeric Fabry-Perot resonators utilizing a polymer waveguide,” *Opt. Express* **22**, 5904–5912, (2014).
- [10] J. D. Jackson, *Classical Electrodynamics*. Wiley, (1999).
- [11] C. F. Bohren and D. R. Huffman, *Absorption and Scattering of Light by Small Particles*. Wiley-VCH, (2004).
- [12] S. A. Maier, *Plasmonics: Fundamentals and Applications*. Springer US, (2007).
- [13] F. Tisseur and K. Meerbergen, “The quadratic eigenvalue problem,” *SIAM review* **43**, 235–286, (2001).

Bibliography

- [14] M. I. Rabinovich and D. I. Trubetskov, *Oscillations and Waves: In Linear and Nonlinear Systems*. Taylor & Francis, (1989).
- [15] P. B. Johnson and R. W. Christy, “Optical Constants of the Noble Metals,” *Phy. Rev. B* **6**, 4370–4379, (1972).
- [16] D. C. Lay, S. R. Lay, and J. J. McDonald, *Linear Algebra and Its Applications*. Pearson, 5th ed., (2015).
- [17] J. W. Demmel, *Applied Numerical Linear Algebra*. SIAM, (1997).
- [18] D. A. Powell, “Interference between the Modes of an All-Dielectric Meta-atom,” *Phys. Rev. Appl.* **7**, (2017).
- [19] D. A. Bykov and L. L. Doskolovich, “Numerical Methods for Calculating Poles of the Scattering Matrix With Applications in Grating Theory,” *J. Light. Technol.* **31**, 793–801, (2013).
- [20] Q. Bai, M. Perrin, C. Sauvan, J.-P. Hugonin, and P. Lalanne, “Efficient and intuitive method for the analysis of light scattering by a resonant nanostructure,” *Opt. Express* **21**, 27371, (2013).
- [21] D. Felbacq, “Finding resonance poles by means of Cauchy integrals,” in *2011 13th International Conference on Transparent Optical Networks*, 1–4, (2011).
- [22] F. Zolla, G. Renversez, B. Kuhlmeier, S. Guenneau, and D. Felbacq, *Foundations of Photonic Crystal Fibres*. Imperial College Press, (2005).
- [23] W.-J. Beyn, “An integral method for solving nonlinear eigenvalue problems,” *Linear Algebra Appl.* **436**, 3839–3863, (2012).
- [24] W.-J. Beyn, Y. Latushkin, and J. Rottmann-Matthes, “Finding Eigenvalues of Holomorphic Fredholm Operator Pencils Using Boundary Value Problems and Contour Integrals,” *Integr. Equat. Oper. Th.* **78**, 155–211, (2014).

2 Eigenmode Analysis and Second-Harmonic Generation

This chapter contains three publications studying SHG with emphasis on the role played by the eigenmodes in the response of different plasmonic nanostructures. Each article appears as a section followed by its bibliography and supplementary informations. The first article presents the initial method implemented (cf. Chap. 1.2) and used to compute the eigenmodes, as well as an analysis of the SHG coming from dipolar eigenmodes of different nanostructures. It is shown that the SHG resulting from the dipolar eigenmodes has a quadrupolar nature for a nanosphere, a nanorod and a nanospheres dimer. Furthermore, the value of the permittivity at the SH frequency is shown to be a key parameter to obtain a strong SHG enhancement, Sec. 2.1.

The second article presents the mode interplay between the transverse dipolar and quadrupolar SHG emission in nanorods that leads to a shift between the emission maximum from forward to backward directions for increasing nanorod length. As the size of the nanorod increases, the resonant frequencies of the two modes decrease and their relative phase changes. This change is apparent in their far field interference and leads to a change in the direction of the maximum SHG emission as the nanorod sizes are varied, Sec. 2.2.

The third article studies numerically the dynamics of the SHG for a silver nanorod under different femtosecond pulse illuminations. The contribution of the few dominant eigenmodes participating in the dynamical SH response is studied in detail. Here, the interference effect described in the second article is observed dynamically: due to the short lifetime of the transverse dipolar mode, the interference only appears while the pulse drives the nanorod. It is further shown how the dynamical SH response is affected by the tuning of the pulse central frequency and width.

2.1 Mode Analysis of Second-Harmonic Generation in Plasmonic Nanostructures

Manuscript state: Published

Reference: Gabriel D. Bernasconi, Jérémy Butet, and Olivier J. F. Martin, "Mode analysis of second-harmonic generation in plasmonic nanostructures", *J. Opt. Soc. Am. B* **33**, 768-779, (2016).

Publication date: March 30, 2016

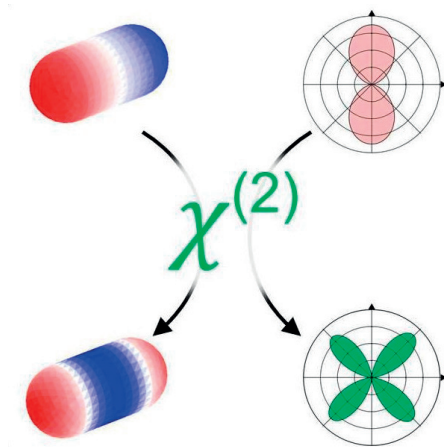
DOI: 10.1364/JOSAB.33.000768

URL: <https://www.osapublishing.org/josab/abstract.cfm?uri=josab-33-4-768>

Adapted with permission from the above-mentioned reference.
Journal Of the Optical Society of America B.

Author contributions

G. D. Bernasconi wrote the eigenmode analysis code, made the simulations and wrote the manuscript.



Mode Analysis of Second-Harmonic Generation in Plasmonic Nanostructures

Gabriel D. Bernasconi, J  r  my Butet, and Olivier J. F. Martin

Nanophotonics and Metrology Laboratory (NAM), Swiss Federal Institute of Technology Lausanne (EPFL), 1015, Lausanne, Switzerland.

Corresponding author: gabriel.bernasconi@epfl.ch

ABSTRACT: Using a surface integral equation approach based on the tangential Poggio–Miller–Chang–Harrington–Wu–Tsai formulation, we present a full wave analysis of the resonant modes of 3D plasmonic nanostructures. This method, combined with the evaluation of second-harmonic generation, is then used to obtain a better understanding of their nonlinear response. The second-harmonic generation associated with the fundamental dipolar modes of three distinct nanostructures (gold nanosphere, nanorod, and coupled nanoparticles) is computed in the same formalism and compared with the other computed modes, revealing the physical nature of the second-harmonic modes. The proposed approach provides a direct relationship between the fundamental and second-harmonic modes in complex plasmonic systems and paves the way for an optimal design of double resonant nanostructures with efficient nonlinear conversion. In particular, we show that the efficiency of second-harmonic generation can be dramatically increased when the modes with the appropriate symmetry are matched with the second-harmonic frequency.

Introduction

Optical resonances in photonic nanostructures represent a vivid field of research, with emphasis on plasmonic nanostructures, where the extreme field enhancement and confinement, behind the classical diffraction limit [1–3], are promising for many applications such as biological sensing and optical signal processing down to the nanoscale [4–7]. Furthermore, the control of the resonant response of individual plasmonic and dielectric nanoparticles (including the resonance wavelength, the radiation pattern, and the resonance width, in both the linear and nonlinear regimes) is important for the design of metasurfaces that incorporate several subwavelength structures to produce an exotic behavior, such as a wavefront with controlled phase, for example [8,9]. Using the coupling and hybridization between different modes is a convenient method for tailoring and controlling all these properties [10–12].

In this context, it is crucial to understand the underlying mode properties of dielectric

and plasmonic nanostructures. Indeed, the response of a resonant system to an external excitation can be understood as the projection of the excitation field onto its eigenmodes. The coupling strength between one given eigenmode and the excitation field depends on several parameters, including the symmetry, the polarization, and the frequency mismatch between the eigenfrequency and the frequency of the driving field. In the case of plasmonics, the knowledge of the modes can be used to obtain substantial near-field enhancement, absorption, and/or scattering at a specific wavelength. Several methods have been developed in order to obtain the electromagnetic resonances of a nanostructure. These methods can be separated into two main categories: those developed in the quasi-static [13–21] and dipolar [22] approximations and those using a full wave analysis method [23–26]. Each category includes several formulations, such as volume [27] and surface integral equations methods [23], direct application of the Green’s tensor method [22,28], and direct expression of the electrostatic interaction between surface charges [14,16–19]. All these methods correspond to the derivation of an eigenvalue problem. However, it is important to note that, due to the presence of losses (both ohmic and radiative), the eigenfrequencies are complex and the eigenmodes are referred to as quasi-normal modes, in opposition to the normal modes observed in lossless cavities [24,26,29–36]. The completeness and orthogonality of the basis formed by the quasi-normal modes have been discussed in detail [29–31] and were proved for simple dielectric nanoparticles [37,38]. In a more general case, the quasi-normal modes orthogonality has been proven neglecting the spectral dispersion of the permittivity [34]. One of the main concerns about the quasi-normal modes is that the associated fields diverge with the distance from the system due to the imaginary part of the eigenfrequency, making their normalization challenging [33]. It was recently proposed to use perfectly matched layer (PML) to bound the quasi-normal modes and to normalize them [34]. Such an issue is not problematic in the surface integral equation (SIE) method used here because only the scatterer’s surface needs to be discretized and no external boundary conditions for the outgoing waves need to be imposed, with the radiation condition being directly fulfilled in this approach.

Since plasmonic systems are, in general, small in comparison with the incident wavelength, and because many applications rely mainly on the lowest order dipolar modes, methods developed in the quasi-static approximation are often adequate for understanding the underlying physical mechanisms in those systems. On the other hand, it is mandatory to go beyond this approximation when the nanostructures grow in size, with their dimensions becoming close to the wavelength of light. This is particularly true in nonlinear plasmonics, when the generated nonlinear signal has a wavelength shorter than the incident light [39]. In this case, retardation effects become nonnegligible and the calculations must account for the field variations over the considered structure. This point is particularly important for one of the nonlinear optical processes, secondharmonic generation (SHG), which represents the focus of this paper and is forbidden in centrosymmetric media in the electric dipole approximation [40]. As a direct consequence, SHG from centrosymmetric nanoparticles, such as nanospheres, requires retardation effects and the excitation of

2.1. Mode Analysis of Second-Harmonic Generation in Plasmonic Nanostructures

high-order multipoles, like quadrupoles and octupoles [41–45].

Recently, mode matching between fundamental and second-harmonic modes in both the spatial and frequency domains has been demonstrated to yield a high nonlinear conversion [46–48]. Knowledge of the mode structure offers a useful tool for engineering the nonlinear properties. The simplest, but limited, method to characterize the modes of a given nanostructure is to study its response to plane wave illumination over a large wavelength range and to extract the mode information from the scattering or absorption peaks. Such a method is very easy to implement, because any numerical method suitable for scattering calculations can be used [49]; unfortunately, this method cannot provide complete information on the modes for the following two reasons. First, a plane wave interacts weakly with any mode having a small net dipolar moment (the so-called dark modes [50]). Second, even though those dark modes can be excited, they often overlap spectrally with broad dipolar modes; the resulting response is, in general, a superposition of several resonances and a clear identification of the modes is not straightforward. As a consequence, the evaluation of the scattering spectrum is not the best tool for the investigation of the eigenmodes, in particular when weakly radiative modes are involved.

In this article, we combine a full wave analysis of the eigenmodes for 3D plasmonic nanostructures based on the SIE method with the computation of surface SHG based on the same formalism [51]. In Section 3, the SHG associated with the fundamental dipolar modes is computed and compared with the high-order modes, revealing the quadrupolar nature of the second-harmonic mode for three distinct nanostructures, namely, a gold nanosphere, a nanorod, and coupled nanoparticles. In the final section, we discuss how the proposed approach provides the direct relationship between fundamental and second-harmonic modes in complex plasmonic systems and demonstrate that this method is very well suited for designing multiresonant nanostructures with efficient secondharmonic generation. It is worth noting that the method proposed in this article is very general and not limited to noncentrosymmetric nanostructures, as reported in the case of the effective nonlinear susceptibility method, for example [52,53].

Numerical Methods

Surface Integral Equation

The SIE allows the computation of the spatial distribution of the electric and the magnetic fields from fictitious currents defined solely on the surface of the scatterers. Starting from Maxwell’s equations and using vector analysis theorems and the properties of the Green’s function, two equations can be derived for each homogeneous domain (e.g., the scatterer and the background), one for each field: the electric field integral equation (EFIE) and the magnetic field integral equation (MFIE). They relate the excitation and the scattered electromagnetic fields to the electric surface currents \mathbf{J} and the magnetic surface currents

M. The method of moment (MoM) [54] together with Rao–Wilton–Glisson (RWG) [55] basis functions and a triangular surface mesh are used to numerically solve those two equations. The electric and magnetic surface current densities of the domain n are expanded on the RWG basis functions building a triangular mesh approximating the boundary surface [56],

$$\mathbf{J}_n = \sum_u \alpha_u \mathbf{f}_u^n, \quad (1)$$

$$\mathbf{M}_n = \sum_u \beta_u \mathbf{f}_u^n, \quad (2)$$

where the summations occur on all the mesh edges; \mathbf{f}_u^n is the RWG function of the edge u associated with the domain n . α_u and β_u are the unknown coefficients that need to be determined. Each integral equation becomes a linear matrix equation relating a vector (the equivalent surface currents) to the excitation field. The corresponding matrix depends on the nanostructure geometry and the properties of the domains (dielectric constant). The elements of the vectors \mathbf{J} and \mathbf{M} are associated with an edge of the mesh and a RWG function.

Although only the EFIE or the MFIE is sufficient to compute the fields in all the domains, a combination of the two equations into one matrix (implying the same solution for the EFIE and MFIE) is found to lead to more accurate numerical results [57–59]. In other words, in order to further increase the numerical accuracy, one forms a linear combination of the EFIE and MFIE. Furthermore, the integral equations for each domain are added together. This can be written as

$$\begin{bmatrix} \sum_n i\omega\mu_n \mathbf{D}^n & \sum_n \mathbf{K}^n \\ \sum_n \mathbf{K}^n & -\sum_n i\omega\epsilon_n \mathbf{D}^n \end{bmatrix} \cdot \begin{bmatrix} \{\alpha\} \\ \{\beta\} \end{bmatrix} = \sum_n \begin{bmatrix} \mathbf{q}^{(E),n} \\ \mathbf{q}^{(H),n} \end{bmatrix}, \quad (3)$$

where the following submatrices and vectors have been introduced:

$$D_{u,v}^n = \int_{\partial V_n^\Omega} dS \mathbf{f}_u^n(\mathbf{r}) \cdot \int_{\partial V_n^\Omega} dS' \overline{\mathbf{G}}_n(\mathbf{r}, \mathbf{r}') \mathbf{f}_v^n(\mathbf{r}'), \quad (4)$$

$$K_{u,v}^n = \int_{\partial V_n^\Omega} dS \mathbf{f}_u^n(\mathbf{r}) \cdot \int_{\partial V_n^\Omega} dS' [\nabla' \times \overline{\mathbf{G}}_n(\mathbf{r}, \mathbf{r}')] \cdot \mathbf{f}_v^n(\mathbf{r}'), \quad (5)$$

$$q_u^{(E),n} = \int_{\partial V_n^\Omega} dS \mathbf{f}_u^n(\mathbf{r}) \cdot \mathbf{E}_n^{inc}(\mathbf{r}), \quad (6)$$

$$q_u^{(H),n} = \int_{\partial V_n^\Omega} dS \mathbf{f}_u^n(\mathbf{r}) \cdot \mathbf{H}_n^{inc}(\mathbf{r}), \quad (7)$$

where $\overline{\mathbf{G}}_n(\mathbf{r}, \mathbf{r}')$ is the dyadic Green's function, and $\mathbf{E}_n^{inc}(\mathbf{r})$ and $\mathbf{H}_n^{inc}(\mathbf{r})$ are the electric and magnetic incoming fields, respectively. Equation (3) shows the final linear system: the first and second subrows correspond to the EFIE (relating $\{\alpha\}$ and $\{\beta\}$ to $q^{(E),n}$) and MFIE (relating $\{\alpha\}$ and $\{\beta\}$ to $q^{(H),n}$), respectively.

2.1. Mode Analysis of Second-Harmonic Generation in Plasmonic Nanostructures

At this step, it is worth saying a few words about the different SIE formulations. When constructing the EFIE and MFIE, one can consider either the tangential or the normal components of the fields at the domain surface. This leads to two distinct formulations denoted as T- for the formulations considering the tangential components of the fields and N- for those considering the normal components [60]. In the present work and on the basis of our previous studies on linear scattering and SHG, we use the T-PMCHWT [61–63] formulation, since it provides accurate results for plasmonic nanostructures [56,57]. Note that the mN-Müller formulation was used in a previous study of the modal decomposition for plasmonic systems [23].

Eigenmodes

In this section, we show how the scattering formulation presented in the previous section can be transformed into an eigenvalue problem. Equation (3) can be re-expressed in the simple form¹

$$\mathbf{S}(\omega)\psi = \mathbf{q}, \quad (8)$$

where the frequency-dependent SIE matrix is denoted $\mathbf{S}(\omega)$. At a resonance frequency, oscillations can exist in the system without external driving forces. Let us seek a solution ψ for the system of Eqs. (8) without any external excitation ($\mathbf{q} = 0$). Rewriting Eq. (8) as the eigenvalue problem

$$\mathbf{S}(\omega)\psi_i = \xi_i\psi_i = \mathbf{0}, \quad (9)$$

where ψ_i and ξ_i are the eigenvectors and eigenvalues, respectively, it is possible to search for the angular frequencies ω where one of the eigenvalues ξ_i tends to zero. In this case, the eigenvector associated with the vanishing eigenvalue corresponds to a resonant mode of the structure. The same approach has already been used, for example in Refs. [22,23], to evaluate the eigenmodes of different plasmonic multimers. Since radiative and ohmic losses are present in plasmonic systems, both the resonant frequencies and the eigenvalues associated with the modes are complex. The complex angular frequency is defined as $\omega = \omega_r + i\omega_i$ with $\omega_i < 0$, where this choice of sign is dictated by the chosen temporal dependence $\exp(-i\omega t)$ used throughout. For convenience, the resonant wavelength is considered instead of the frequency in the following. The complex wavelength is defined as $\lambda = \lambda_r + i\lambda_i$ with $\lambda_i > 0$ since $\lambda = 2\pi c/\omega$, c being the speed of light. The eigenvalue ξ_i itself does not have a particular physical meaning, but the frequency associated with a vanishing eigenvalue corresponds to the resonance frequency of one mode of the considered nanostructure. In the following, the word “eigenvalue” refers to the norm of the complex

¹Note that in this article, the notation is different than the one presented in Sec. 1.2 of this thesis. In the following, the matrix that was previously noted \mathbf{O} is now noted \mathbf{S} , whereas the matrix that was previously noted $\mathbf{S} = \mathbf{O}^{-1}$ does not appear in this article. The eigenvalue that was previously noted λ , is now written ξ and λ now stands for the wavelength.

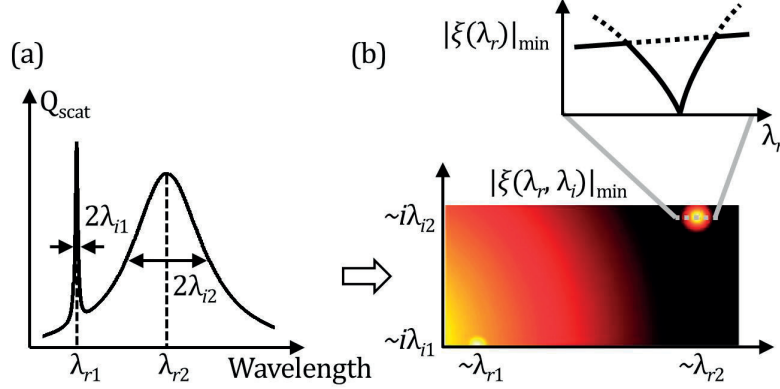


Figure 1 – (a) A typical example of the scattering spectrum used to find the approximate position and width of the maxima. In this case, the broad resonance would correspond to the dipolar mode and the narrow one to the quadrupolar dark mode. (b) Norm of the smallest eigenvalues in the complex plane as a function of the real and imaginary parts of the wavelength for a single sphere. Bright color corresponds to small values. The cut illustrates the emergence of the eigenvalue corresponding to the mode; see text.

quantity ξ_i . The complex character of ξ_i does not have a physical meaning here and we seek solutions of Eq. (9) for $\xi_i = 0$, implicitly meaning that $|\xi_i| \rightarrow 0$. In order to find all the eigenfrequencies associated with a given geometry, one can scan the entire complex frequency plane, but this represents a brute force inefficient approach. To avoid the computation of too many “useless” points in the complex plane, which is very time consuming and computationally inefficient, one can use the scattering spectrum of the studied structure to obtain prior knowledge of the spectral position of the eigenmodes, as illustrated in Fig. 1. This scattering spectrum can be obtained either by a plane wave excitation or by a suitable dipolar excitation in order to couple to both bright and dark modes. Indeed, at the wavelength for which the norm of the smallest eigenvalue tends to zero, the real part of the wavelength is closely related to the resonant wavelength and its imaginary part relates to the half width at half-maximum of the scattering peak, i.e., to the losses [Fig. 1(a)]. When only one resonance is present, the spectrum is a Lorentzian and the real part of the wavelength corresponds exactly to the resonant wavelength. From a practical point of view, we first extract the central wavelengths and widths of the different peaks from the scattering spectrum, and then use them as starting points for the scan of the complex frequency plane [Fig. 1(b)]. The eigenvalues of the SIE matrix are then computed around those points until a dip leading to a minimum close to zero is found (typical residual value $\sim 10^{-9}$, depending on the number of edges). The advantage of obtaining the eigenmodes, in comparison with a mere analysis of the scattering, is that several modes can spectrally overlap at one frequency since plasmonic resonances are broad (typical quality factor $Q \sim 30$). For this reason, the near-field distribution associated with one scattering peak will not necessarily correspond exactly

2.1. Mode Analysis of Second-Harmonic Generation in Plasmonic Nanostructures

to that of a resonant eigenmode. This is particularly true for modes with low associated dipolar moments (dark modes) which are weakly coupled to far-field radiation. Figure 1 summarizes this approach.

Practically, only the smallest eigenvalue of the matrix was considered at each frequency. Indeed, since one looks for vanishing eigenvalues, considering only the smallest one does not lead to any loss of useful information. However, the subsequent smallest eigenvalues can also have a physical meaning in the case of degenerate modes, as discussed in Section 3. ARPACK routines ZNAUPD and ZNEUPD that apply the shift invert method were used to find the smallest eigenvalue of the matrix [64]. The 2D map of the smallest eigenvalue of the SIE matrix seems to follow a similar general behavior as does the absolute value of the permittivity, i.e., increasing both along the real and imaginary wavelengths. The fact of mapping only the smallest eigenvalue results in a sharp hole around the resonant frequency where the mapped smallest eigenvalue suddenly vanishes when it corresponds to the mode. This is visible in the cut in Fig. 1(b), where one observes the localized decrease of the smallest eigenvalue amplitude at the proximity of the resonant frequency.

Analytically, when an eigenvalue of a matrix is equal to zero, the matrix determinant is also zero. Another approach for finding the eigenfrequencies would be to compute the determinant of the SIE matrix for different complex frequencies instead of examining the smallest eigenvalue. Unfortunately, although the T-PMCHWT formulation is one of the most accurate SIE formulation for plasmonic nanostructures [56], the SIE matrix was found to lead to a very broad range of eigenvalues. This is expected, since the matrix is very ill-conditioned in this formulation [65]. The magnitude of the eigenvalues roughly ranges from 10^{-3} to 10^3 , with a higher density at higher values. Furthermore, because the number of eigenvalues is equal to the number of edges in the mesh, commonly larger than a few hundred, computing the determinant for the SIE matrix appeared to be numerically challenging since it would quickly reach the highest or the lowest number storable by a computer, namely, 2^{1023} in double precision [e.g., for 200 edges and an average eigenvalue magnitude of 10^3 : $(10^3)^{200} = 10^{600} > 2^{1023} \cong 10^{308}$]. In addition, the large number of eigenvalues with large magnitude does not allow for a smooth variation of the determinant, thus hiding the influence of a single vanishing eigenvalue. For those reasons, the approach described here, which limits the search to the smallest eigenvalue, seems the most suitable. Let us finally emphasize that the method described here and based on the SIE approach represents a full wave analysis and thus goes beyond the dipolar/quasi-static approximation. Furthermore, it is worth saying a few words about the mode amplitudes. The relative weights of the different modes have a physical meaning only when a specific excitation or state is projected on the eigenmodes basis: a mode does not have any intrinsic amplitude. However, as emphasized in the introduction, the projection of a plasmonic response on the eigenvector basis is a nontrivial problem since the fundamental question of the completeness and orthogonality of the quasi-normal modes basis is still under discussion.

Second-Harmonic Generation

The SIE method has been extended by Mäkitalo et al. to SHG from nanostructures driven by an incoming plane wave [66]. A similar approach is used here for the computation of SHG from the eigenmodes. It is well known that SHG is forbidden in the bulk of centrosymmetric media in the dipolar approximation and the main source of SHG is the surface nonlinear polarization oscillating at the second-harmonic frequency:

$$P_{\perp}(2\omega, \mathbf{r}^+) = \chi_{\perp\perp\perp}^{(2)} : E_{\perp}(\omega, \mathbf{r}^-) E_{\perp}(\omega, \mathbf{r}^-). \quad (10)$$

The $+$ and $-$ superscripts denote that the nonlinear polarization sheet is located just above the metal and the fundamental electric field is estimated just below the interface [67,68], respectively. The symbol \perp denotes the component normal to the interface, and \parallel denotes the tangential component. All components of the nonlinear susceptibility tensor, including the bulk contributions, can be implemented in this formalism. However, the $\chi_{\perp\perp\perp}^{(2)}$ component is known to be the strongest component of the nonlinear surface susceptibility for plasmonic nanostructures [69–71]. As a consequence, only this component will be considered in the following. The fundamental electric field close to the interface in domain n is related to the electric and magnetic surface current densities by [66]

$$\mathbf{M}_n = -\mathbf{E}_n \times \hat{\mathbf{n}}_n, \quad \nabla_{\parallel} \cdot \mathbf{J}_n = -i\omega\epsilon_n \hat{\mathbf{n}}_n \cdot \mathbf{E}_n \quad (11)$$

where $\hat{\mathbf{n}}_n$ is the outward normal vector on the boundary surface ∂V_n . In order to determine the second-harmonic electromagnetic field, the required set of boundary conditions, including the nonlinear polarization sheet standing at the interfaces, are used [66,72],

$$(\mathbf{E}^{SH}(\mathbf{r}^+) - \mathbf{E}^{SH}(\mathbf{r}^-))_{\parallel} = -\frac{1}{\epsilon'} \nabla_{\parallel} P_{\perp}, \quad (12)$$

$$(\mathbf{H}^{SH}(\mathbf{r}^+) - \mathbf{H}^{SH}(\mathbf{r}^-))_{\parallel} = 0, \quad (13)$$

where ϵ' is the so-called selvedge region permittivity [54]. As for the fundamental wave, the second-harmonic problem is solved using the MoM and expanding the equivalent second-harmonic surface densities on the RWG functions [55]. Using Galerkin's testing, a linear system of equations is derived from the boundary conditions in Eqs. (12) and (13). This linear system permits us to determine the electric surface current \mathbf{J}_{SHG} and the magnetic surface current \mathbf{M}_{SHG} oscillating at the second-harmonic frequency and then to compute the second-harmonic electromagnetic field associated with a given eigenmode.

Results and Discussion

In the following, we illustrate the utilization of this approach by studying three distinct structures: a gold nanosphere, a dimer of gold nanospheres, and a gold nanorod. First,

2.1. Mode Analysis of Second-Harmonic Generation in Plasmonic Nanostructures

their eigenmodes are evaluated using the method described here and the fundamental (dipolar) modes are then used as sources of SHG. Finally, the properties of the computed second-harmonic signals are compared with those of the higher order modes of the nanostructure. The aim of this comparison is to retrieve the multipolar nature of SHG in plasmonic nanostructures. All the nanostructures studied in this work are made of gold, the permittivity of which is obtained using the Drude model:

$$\epsilon(\omega) = \epsilon_{\infty} - \frac{\omega_p^2}{\omega^2 + i\gamma\omega}, \quad (14)$$

with $\epsilon_{\infty} = 9$, $\omega_p = 8.9$ eV, and $\gamma = 0.07$ eV. The first step is to obtain the resonance wavelengths for the structures and compute the corresponding charge distributions associated with the different eigenmodes. Indeed, losses result in a broadening and slight shift of the peak wavelength in the scattering spectrum, but our interest lies in the real part of the eigenfrequencies and in spatial distributions of the modes, quantities that are only slightly affected by losses. Furthermore, our analysis is only qualitative and we choose, without loss of generality, to ignore the losses in the Drude model. In addition, by neglecting the ohmic losses, the losses are limited to the radiative ones and will allow us to distinguish easily between bright and dark modes. In the case of dark modes, the research for the small eigenvalues is limited to the area close to the real line, i.e., for wavelengths with small imaginary parts [Fig. 1(b)]. All the nanostructures are considered in water (refractive index of the background $n = 1.33$), as it is the case in experiments performed on colloidal suspensions.

The method reported in this article is general, but we focus here on the design of double resonant nanostructures. As a consequence, we neglect the excitation channels involving cross coupling between different modes at the fundamental wavelength since their design for an efficient SHG is even more complicated. Indeed, in this case, the two fundamental modes must be resonant at the excitation wavelength. For example, using the dipolar mode as the source of the SHG, we neglect the channel $E_1 + E_2 \rightarrow E_1$, where the two terms on the left of the arrow refer to the nature of fundamental mode and the third term describes the second-harmonic emission mode and where subscript 1 stands for a dipolar mode and subscript 2 stands for a quadrupolar mode.

To validate our approach, modes were computed for a small sphere as well as for a small ellipsoid. The resulting resonance frequencies were then compared and found to be in agreement with the prediction of the Mie theory for the sphere and the electrostatic approximation for the ellipsoid [73]; see Tables 1 and 2. For convenience, the modes are presented in the following as surface charge distributions computed from the difference of the normal components of the electric field above and below the surface using Eq. (10) in [74].

Chapter 2. Eigenmode Analysis and Second-Harmonic Generation

Table 1 – Resonance Wavelength in nm for a $\varnothing 10$ nm Gold Sphere in Vacuum

	Dipolar Mode	Quadrupolar Mode
Mie	$463.16 + i0.013$	$452.32 + i0.000$
SIE	$463.12 + i0.013$	$452.26 + i0.000$

Table 2 – First Two Resonance Wavelengths in nm for a Gold Ellipsoid in Vacuum. The three semi axes are 5, 3.75, and 2.5 nm.

	Dipolar 1	Dipolar 2
Electrostatic	498.08	468.76
SIE	497.75	468.81

Gold Sphere

Analytically, the interaction between a sphere and an electromagnetic wave is described by the Mie theory. In this framework, the electric field \mathbf{E} is expanded onto the vector spherical harmonic basis as

$$\mathbf{E} = \sum_{l,m} A_{l,m} \mathbf{M}_{l,m} + B_{l,m} \mathbf{N}_{l,m}, \quad (15)$$

where $\mathbf{M}_{l,m}$ and $\mathbf{N}_{l,m}$ are the vector spherical harmonics associated with the transverse electric (TE) modes and transverse magnetic (TM) modes, respectively, and are derived from the spherical harmonics of degree l and order m

$$Y_l^m(\theta, \phi) = C e^{im\varphi} P_l^m(\cos(\theta)) \quad (16)$$

where P_l^m is the associated Legendre polynomial, and C is a normalization constant [75]. The collective oscillations of the conduction electrons, corresponding to localized surface plasmon resonances, induce strong surface polarization charges and are then associated with the TM modes. Indeed, the presence of surface polarization charges requires the discontinuity of the normal component of the electric field at the nanoparticle surface. Physically, the degree l is associated with the angular momentum of the mode and corresponds graphically to the number of nodes (appearing as a circle) present on the sphere. The order m ranges from $-l$ to l ($2l + 1$ possible values) and corresponds to half the number of azimuthal nodes. Each spherical harmonic Y_l^m exhibits a different set of nodes and antinodes. Note that the mode energy depends only on the degree l and not on the order m [75].

For a given degree l , there are $2l + 1$ different modes with distinct charge distributions. Therefore, the method described in Section 2.B will not be a priori able to distinguish between the modes with the same degree l and different orders m , since the only free parameter in this model is the energy/wavelength. It is, however, still possible to retrieve the different modes, as explained in the next paragraph.

2.1. Mode Analysis of Second-Harmonic Generation in Plasmonic Nanostructures

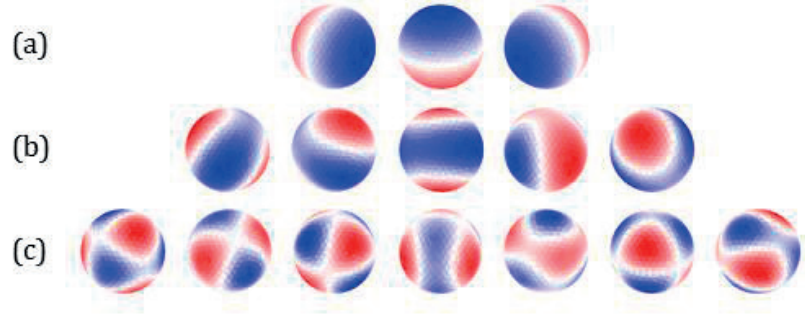


Figure 2 – First lower energy modes for a 40 nm gold sphere. The (a) first, (b) second, and (c) third rows correspond, respectively, to the dipolar mode ($l = 1$) at $\lambda = 504 + i2.77$ nm, quadrupolar mode ($l = 2$) at $\lambda = 478 + i0.02$ nm, and octupolar mode ($l = 3$) at $\lambda = 471 + i0.08$ nm. For $l > 1$ it appears that the spherical harmonics are not retrieved.

The modes obtained for a 40 nm spherical gold nanoparticle are shown in Fig. 2. The first, second, and third rows correspond to the dipolar ($l = 1$), quadrupolar ($l = 2$), and octupolar ($l = 3$) modes, respectively. At the first resonance wavelength ($\lambda = 504$ nm) corresponding to $l = 1$, three eigenvalues much smaller than the others are found and the three eigenvectors reveal three orthogonal dipoles (Fig. 2, first row). For $l = 2$ and $l = 3$, the number of distinguishably small eigenvalues is, respectively, 5 and 7, corresponding to $2l + 1$ as expected. However, the surface charge distributions associated with the eigenvectors are not associated with single spherical harmonic. From linear algebra it is known that any linear combination of eigenvectors sharing an eigenvalue is also an eigenvector, since a superposition of modes associated with one specific eigenfrequency also exhibits divergent amplitude and corresponds to a resonant mode of the system. Furthermore, due to the mesh symmetry an eigenvector a priori displays the resonant mode in an arbitrary orientation, and nothing guarantees that this orientation is the same from one eigenvector to another, even if they are associated with the same degenerate eigenvalue. For example, the surface charge distributions obtained for the modes with $l = 2$ do not correspond to a single spherical harmonic but to a linear combination of spherical harmonics $Y_{l=2}^m$ of the same degree with different orders m and specific orientations (see Appendix A). Similar effects have been observed in Fig. 3 of [21]. The fact that dipoles are directly found for the modes of degree $l = 1$ but that a superposition of spherical harmonics is found for the quadrupolar ($l = 2$) and octupolar ($l = 3$) modes is surprising at first sight. However, a superposition of three dipoles with different orientations results in a dipole with a different orientation. This is not the case for quadrupolar (and higher order) modes due to the more complex spatial distribution of the charges associated with different order m .

In this framework, the mesh describing the nanoparticle surface plays an important role. Indeed, a curved surface is difficult to approximate with planar triangles. In order to check the influence of the mesh on the found eigenmodes, the mesh reproducing the 40

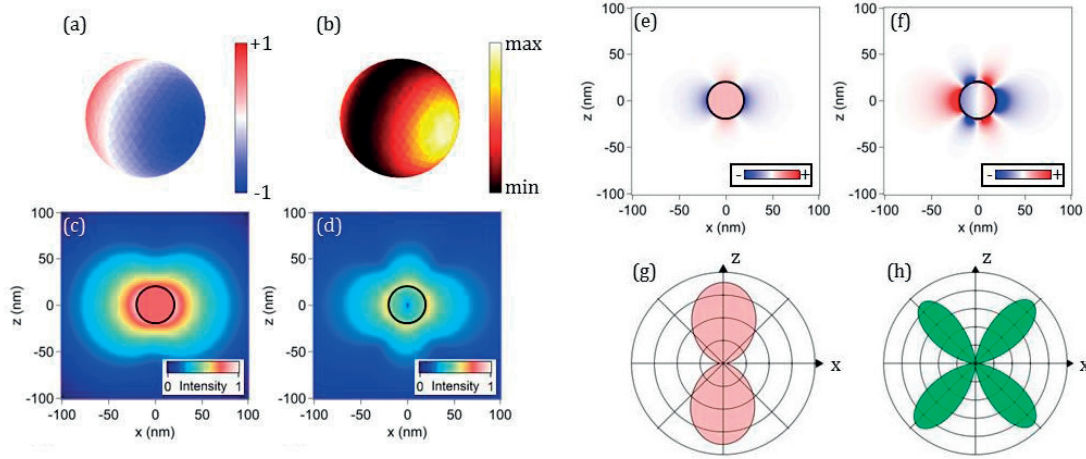


Figure 3 – Linear and second-harmonic response of a 40 nm gold nanosphere. (a) The charge distribution associated with the fundamental dipolar mode. (b) Nonlinear surface polarization associated with this mode computed using Eqs. (10) and (11). Near-field distributions of the (c) fundamental intensity and (e) real part of the x-component of the fundamental electric field. Near-field distribution of the (d) second-harmonic intensity and (f) real part of the x-component of the second-harmonic electric field. Far-field radiation patterns of the (g) fundamental mode and (h) second-harmonic signal.

nm nanosphere was tilted by a 45° angle. In this case, the two dipolar modes oriented perpendicularly to this rotation axis were also rotated with the same angle, following the asymmetry induced by the surface mesh (see Appendix B for a more detailed discussion). Let us emphasize that the previous considerations about degenerated eigenvalues and the influence of the mesh symmetry are less problematic when realistic structures (i.e., without specific symmetry) are considered.

Having confirmed with Mie theory the accuracy of the SIE method to compute the eigenmodes in the case of gold nanospheres, let us turn our attention to the main topic of this article, the SHG associated with these eigenmodes. Although the connection between fundamental and second-harmonic modes is now well-established for spherical nanoparticles [76–82], it is worth discussing it to benchmark the proposed approach for a better understanding of SHG in plasmonic nanostructures. In general, the incident fundamental wave is described by a linearly polarized plane wave propagating in the embedding medium. The expansion of plane wave polarized along the x-axis and propagating along the z-axis over the vector spherical harmonics basis involves only the terms with an order $m = \pm 1$, meaning that the set of excited fundamental modes is established by the symmetry of the driving field [73]. For this reason, we select the dipolar mode with its dipolar moment pointing along the x-axis as the fundamental mode [Fig. 3(a)]. The resonant wavelength of this mode is $\lambda = 504 + i2.77$ nm. As discussed in Section 2, SHG arises from the surface of the plasmonic nanostructures due to the local centrosymmetry breaking. The corresponding nonlinear source, the

2.1. Mode Analysis of Second-Harmonic Generation in Plasmonic Nanostructures

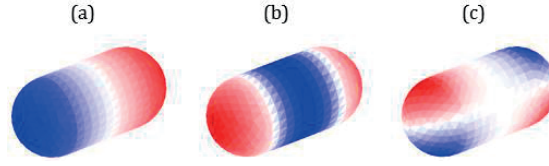


Figure 4 – Eigenmodes of a 40×85 nm gold nanorod: (a) the longitudinal dipolar mode at $\lambda = 647 + i13.9$ nm, (b) the longitudinal quadrupolar mode at $\lambda = 503 + i0.17$ nm, and (c) the transversal quadrupolar mode at $\lambda = 491 + i0.23$ nm.

surface nonlinear polarization, is computable using Eqs. (10) and (11), where the electric surface current \mathbf{J} is given by the coefficients α of the eigenvector associated with the fundamental mode [Fig. 3(b)]. In order to further emphasize the differences between the second-harmonic and fundamental modes, the corresponding near-field distributions of the intensity and of the real part of the x -component of the electric field associated with these two modes are shown in Fig. 3. The near-field distributions clearly reveal that the parity of the fundamental and second-harmonic modes is different. The fundamental mode corresponds to an odd (dipolar) mode, while the secondharmonic mode corresponds to an even (quadrupolar) mode. The multipolar nature of the SHG from spherical metallic structures has been extensively discussed in the past and is closely related to the centrosymmetry breaking induced by field retardation [43]. Here, the second-harmonic channel is $E_1 + E_1 \rightarrow E_2$. Indeed, the fundamental mode is an electric dipole, and the $E_1 + E_1 \rightarrow E_1$ mechanism, which would correspond to dipolar second-harmonic emission, is forbidden for centrosymmetric nano-objects. These results demonstrate that the proposed method is in agreement with previous experimental and theoretical investigations of the SHG from nanospheres [43]. It has been shown that deviations from a perfect sphere leads to a modification of the relative weight of the dipolar and quadrupolar contributions to the total second-harmonic emission [83]. Here, as observed in Fig. 3(h), the emission is perfectly quadrupolar, demonstrating that the mesh describing the sphere surface does not induce a dipolar second-harmonic emission resulting from any deviations from the perfectly symmetric case.

Gold Nanorod

Now, we turn our attention to nanostructures with lower symmetry, namely, gold nanorods. Plasmonic nanorods are important since they are the building blocks for optical antennas and several important metamolecules [84]. SHG from gold nanorods has been investigated, underlining the role played by the longitudinal plasmon resonance in the enhancement of the nonlinear response [85–87]. Here, we apply the same protocol as the one used previously for the study of the SHG from gold spheres.

The modes found for a 40×85 nm gold nanorod in water are shown in Fig. 4. The lower symmetry, in comparison with a spherical object, allows us to obtain well-defined

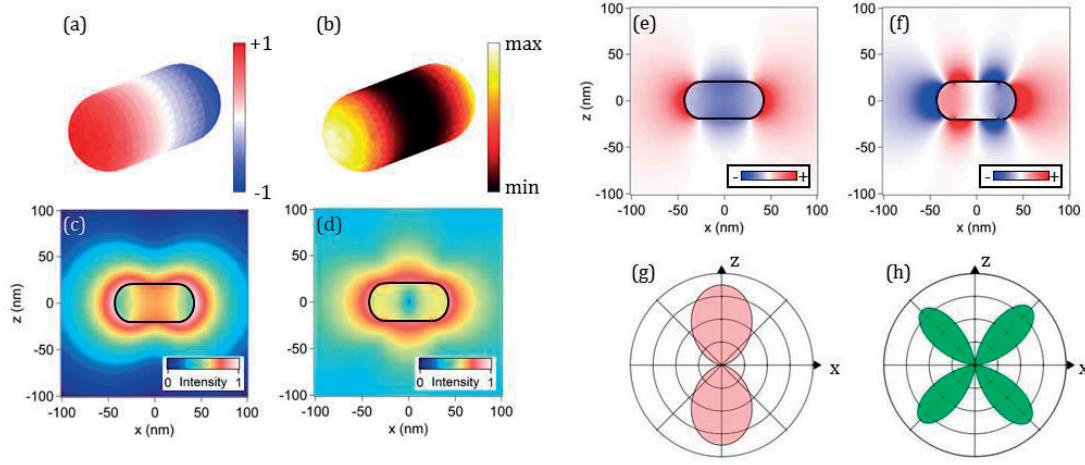


Figure 5 – Linear and second-harmonic response of a 40×85 nm gold nanorod. (a) Charge distributions associated with the fundamental dipolar mode. (b) Nonlinear surface polarization associated with this mode computed using Eqs. (10) and (11). Near-field distributions of the (c) fundamental intensity and (e) real part of the x-component of the fundamental electric field. Near-field distribution of the (d) second-harmonic intensity and (f) real part of the x-component of the second-harmonic electric field. Far-field radiation patterns of the (g) fundamental mode and (h) second-harmonic signals.

quadrupolar modes in the longitudinal, respectively, transverse directions, at $\lambda = 503 + i0.17nm$, respectively, $\lambda = 491 + i0.23nm$. Note that, due to the asymmetry, the two quadrupolar modes do not have the same resonant wavelength as observed for the sphere; here the longitudinal mode has a lower energy than the transverse one. The transverse quadrupolar mode has a degeneracy of 2 and, as expected, two modes are actually found at the same wavelength (with identical charge distributions but with a 90° rotation around the rod axis, data not shown).

The longitudinal dipolar mode supported by a gold nanorod is coupled to an incoming plane wave polarized along its long axis and is responsible for the strong SHG from gold nanorods [85–87]. The nonlinear surface polarization associated with this mode is shown in Fig. 5(b), revealing that the nonlinear sources are mainly localized at the nanorod apices. Despite a lower symmetry, nanorods are still centrosymmetric and SHG is still forbidden in the electric dipole approximation. As a consequence, the excitation channel involved here is also $E_1 + E_1 \rightarrow E_2$. The quadrupolar nature of the second-harmonic mode is confirmed by the computation of the electric field in both the near-field and far-field regions (Fig. 5). Even more interesting is that the second-harmonic mode corresponds to the eigenmode shown in Fig. 4(b). These results demonstrate that the proposed method permits us to clearly identify the link between the fundamental mode and the second-harmonic mode. This point is important for the design of efficient plasmonic sources of second-harmonic light and of sensitive nonlinear plasmonic sensors.

2.1. Mode Analysis of Second-Harmonic Generation in Plasmonic Nanostructures

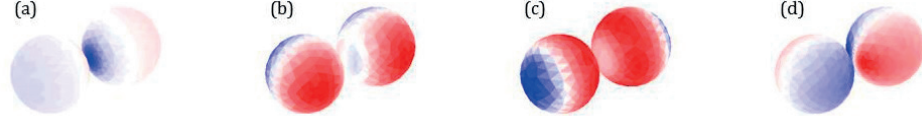


Figure 6 – Eigenmodes of a dimer of two 40 nm spheres with a gap of 5 nm. (a) Longitudinal dipolar mode at $\lambda = 551 + i13.9$ nm. (b) Transversal dipolar mode at $\lambda = 498 + i4.68$ nm. (c) Longitudinal dark mode at $\lambda = 489 + i0.167$ nm. (d) Transverse dark mode at $\lambda = 517 + i0.240$ nm.

Dimer of Gold Nanospheres

Finally, the case of coupled plasmonic nanostructures, the so-called nanoantennas, is considered. Previous studies on the SHG from plasmonic nanoantennas have revealed a singular behavior referred to as the silencing of SHG [88–90]. Indeed, despite strong fundamental near-field intensity in the gap, the SHG from plasmonic nanoantennas is not particularly enhanced. Although the nonlinear surface polarization is very large in this region, where the spheres are close to each other [see Fig. 7(b)], the second-harmonic sources standing at each side of the nanogap are out of phase, resulting in a far-field second-harmonic signal weaker than expected [88]. A dimer of two 40 nm gold spheres separated by a 5 nm gap is considered as an example of coupled nanostructures. Several modes are observed, as shown in Fig. 6. To be able to resolve the high concentration of the charges in the nanogap due to Coulombian interaction, the mesh is specially refined in this region (smallest element size: 1 nm). The longitudinal dark mode shown in Fig. 6(c), corresponding to two facing dipoles, exhibits clear charge repulsion in the gap, contrary to the charge concentration associated with the bright dipolar mode [Fig. 6(a)]. Transverse modes are also observed, see Figs. 6(b) and 6(d), with vanishing eigenvalues of multiplicity equal to two (in each case both modes are rotated by 90° around the dimer axis with respect to each other, data not shown). These observations are now used for understanding the SHG from coupled nanoparticles. The nonlinear surface polarization associated with the fundamental dipolar mode, Fig. 7(a), is shown in Fig. 7(b) as well as the corresponding near-field and far-field distributions in Figs. 7(d), 7(f), and 7(h). One can see that the nonlinear sources are extremely confined in the gap. As previously, the second-harmonic mode is an even mode (in the sense of parity) and the x -component of the second-harmonic field in the plane $x = 0$ vanishes. This observation is in agreement with our previous study on the SHG from coupled nanospheres [89]. However, even though it obeys to the right symmetry, the transverse mode shown in Fig. 6(b) does not correspond to the second-harmonic mode in the present case because its excitation requires retardation effects at the excitation stage [89] (i.e., at the fundamental wavelength).

This is not the case considering only a dipolar fundamental mode as done in the present eigenmode method. On the other hand, the design of efficient second-harmonic light

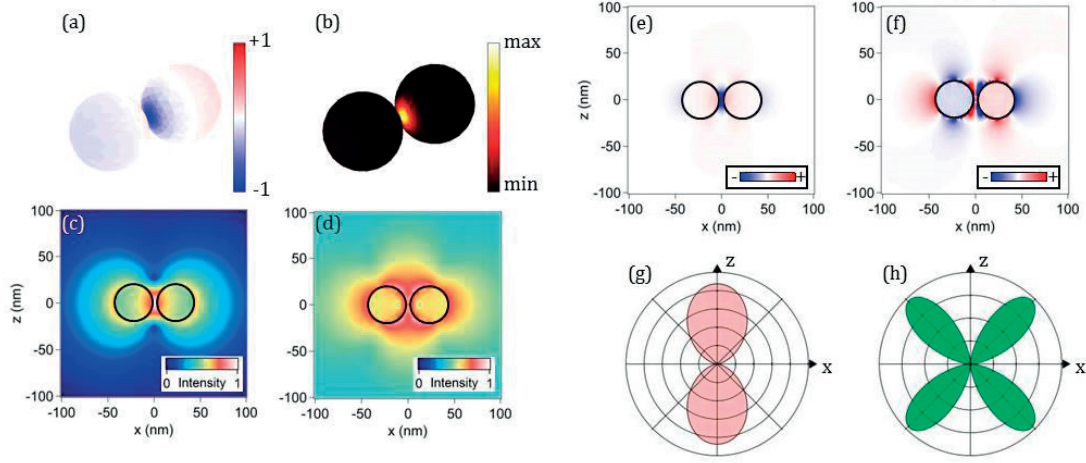


Figure 7 – Linear and second-harmonic responses of a dimer of two 40 nm gold nanospheres separated by a gap $g = 5$ nm. (a) The charge distribution associated with the fundamental dipolar mode. (b) Nonlinear surface polarization associated with this mode computed using Eqs. (10) and (11). Near-field distributions of the (c) fundamental intensity and (e) real part of the x-component of the fundamental electric field. Near-field distribution of the (d) second harmonic intensity and (f) real part of the x-component of the second-harmonic electric field. Far-field radiation patterns of the (g) fundamental mode and (h) second-harmonic signals.

generators must preferentially involve only one mode at the fundamental excitation since modes are, in general, resonant at distinct wavelengths. In other words and using the previous notation, second-harmonic channels with $E_1 + E_1$ as the fundamental step should be preferred for a strong SHG. In this case, our method based on the eigenmodes allows us to determine the excited second-harmonic mode and then optimize the nanostructure geometry in order to tune its resonant wavelength close to the second-harmonic wavelength. This method is expected to be more efficient and effective than the plane wave excitation approach used so far.

Toward Engineering of the Second-Harmonic Mode

In this last section, we make a study of double resonant nanostructures and show that the nonlinear conversion can be dramatically improved by tuning the modes supported by these structures. In the quasi-static approximation, the only parameter that influences the resonance wavelengths for a given geometry and surrounding medium is the permittivity $\epsilon(\omega)$ of the particle [91]. For example, in the case of small spheres (i.e., in the quasi-static approximation), the resonant permittivities are given by $\epsilon(\omega) = -\epsilon_{bg}(l + 1)/l$ with l a nonzero integer and ϵ_{bg} the background permittivity [73]. The dipolar and quadrupolar resonances are thus observed for $\epsilon_{dip} = -2\epsilon_{bg}$ and $\epsilon_{quad} = -1.5\epsilon_{bg}$, respectively. For larger nanostructures, retardation effects become non-negligible and the resonant frequencies

2.1. Mode Analysis of Second-Harmonic Generation in Plasmonic Nanostructures

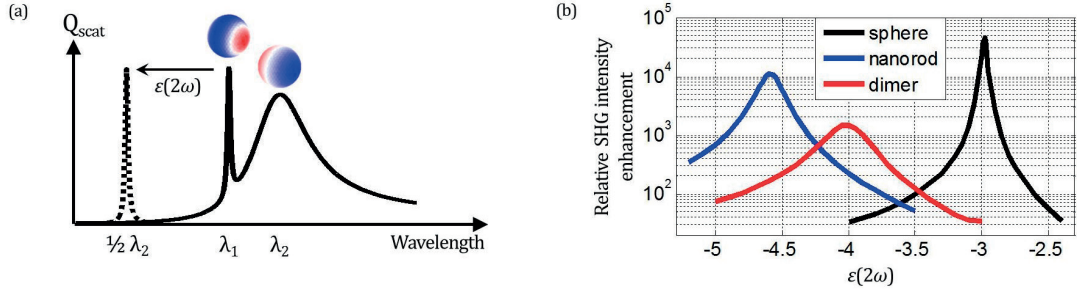


Figure 8 – (a) Scattering spectrum of a sphere. The quadrupolar mode can be shifted at half the wavelength of the dipolar mode by varying the nanostructure permittivity. (b) SHG intensity normalized to that obtained for the Drude model without losses at their respective second-harmonic frequencies (cf. Section 3) as a function of the second-harmonic permittivity $\epsilon(2\omega)$. Note that the Drude permittivity of gold at the second-harmonic frequencies is positive in the three cases and thus the second-harmonic plasmonic modes cannot be resonantly excited.

depend on the nanoparticle size. In this study, the second-harmonic wavelength is fixed and corresponds to half the resonant wavelength of the considered fundamental mode. From Section 3.C, we know that SHG from the centrosymmetric structures investigated here is associated with a quadrupolar emission. However, as illustrated in Fig. 8(a) for the case of a sphere, the quadrupolar mode is usually not resonant at the second-harmonic wavelength. For this reason, we consider a fictitious material with varying permittivity at the second-harmonic frequency $\epsilon(2\omega)$, such that the quadrupolar mode is shifted to the second-harmonic wavelength, in order to boost the SHG [Fig. 8(a)]. We apply this idea to the three geometries studied in Section 3 and observe the variation of the second-harmonic signal intensity. The results are shown in Fig. 8(b). The important point is the very substantial increase of SHG intensity around the optimal permittivity, indicating that SHG can be improved by optimizing the mode matching. In the Drude model, the permittivity of gold at the three second-harmonic frequencies is positive (thus far from the optimal negative values needed). The ratio of the SHG intensity for the optimal $\epsilon(2\omega)$ and for the Drude permittivity (without loss) is $4.6 \cdot 10^4$ for the sphere, $1.1 \cdot 10^4$ for the nanorod, and $1.5 \cdot 10^3$ for the dimer. Note that for the sphere we obtain as optimal permittivity $\epsilon_{\text{opt}} = -3$ instead of $\epsilon_{\text{quad}} = -1.5\epsilon_{\text{bg}} = -2.65$. This small discrepancy is a consequence of the retardation effects due to the finite nanoparticle size and to the refractive index of the surrounding medium [92]. It is important to note that the absolute value of the SHG intensity enhancement for the three different nanostructures cannot be compared since the fundamental mode amplitudes are not normalized. Nevertheless, for each structure, the enhancement still describes how SHG can be enhanced by a suitable design of the plasmonic system.

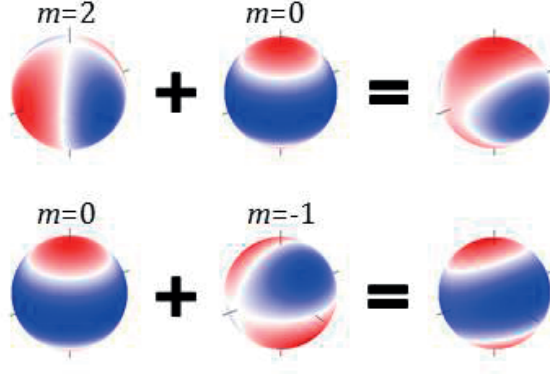


Figure 9 – Addition of a spherical harmonic of degree $l = 2$ with different order m . The similarity with the second row in Fig. 2 is obvious.

Conclusion

In summary, a new SIE method has been derived for the computation of the SHG directly from the fundamental eigenmodes. A gold nanosphere was considered as the first application, demonstrating that this method is able to accurately retrieve previously published results, especially the quadrupolar nature of the second-harmonic emission. SHG from a nanoparticle with a lower symmetry, a gold nanorod supporting longitudinal and transverse plasmon resonances, was then examined underlining that this approach can be extended to structures with low symmetry.

Finally, a coupled nanoparticle system, a gold nanodimer, has been investigated confirming the quadrupolar emission. These different examples illustrate the suitability of this approach for understanding the nonlinear response of complex plasmonic metamolecules. This approach will be instrumental for the design of efficient nonlinear sources of light at the nanoscale, as demonstrated in the last section, where a dramatic SHG is observed when modes with appropriate symmetry are matched with the second-harmonic frequency.

Appendix A: Spherical Harmonic Superposition

Figure 9 shows two examples of linear combinations of spherical harmonics with degree $l = 2$. The resemblance (not considering the orientations) with the five quadrupolar modes obtained for the sphere in Section 3.A is clearly observed.

Appendix B: Influence of the Mesh Symmetry

To investigate the role of the mesh geometry on the eigenmodes of the sphere, an asymmetry, stronger than the inherent one, has been purposely introduced. This higher

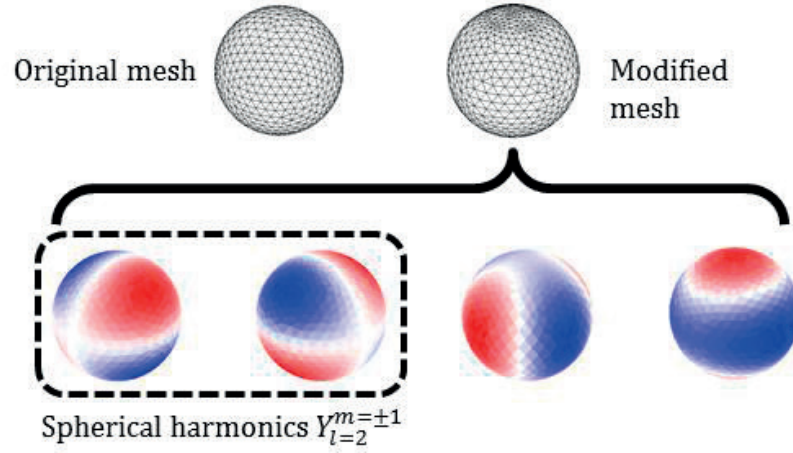


Figure 10 – Modified mesh with refined elements at two poles and associated eigenvectors. The degeneracy of the vanishing eigenvalue is reduced to 4 (instead of 5 with the original mesh). Two spherical harmonics are retrieved among the four eigenvectors. The eigenfrequency variation between the two meshes for this mode is less than 1 nm.

asymmetry results in a small splitting of the eigenfrequencies, previously degenerated, permitting us to partially retrieve the eigenmodes associated with single spherical harmonics. For example, when refining two opposite sides of the sphere (north and south poles) with triangles smaller than those used for the rest of the mesh, the quadrupolar modes ($l = 2$) appear with an eigenvalue degenerated only four times and the eigenmodes associated with the spherical harmonics $Y_{l=2}^{m=\pm 1}$ are observed. Figure 10 shows four modes found with the modified mesh. Only four eigenvectors are shown because the next eigenvectors (associated with eigenvalues with increasing magnitude) were not physical solutions. We then assess that the degeneracy of the vanishing eigenvalue is only four. In this case, there is not a strong separation in the eigenvalue magnitudes, as observed with the original mesh

Funding. Swiss National Science Foundation (SNSF) (200020_153662).

References

- [1] D. K. Gramotnev and S. I. Bozhevolnyi, “Plasmonics beyond the diffraction limit,” *Nat. Photonics* 4, 83–91 (2010).
- [2] J. A. Schuller, E. S. Barnard, W. S. Cai, Y. C. Jun, J. S. White, and M. L. Brongersma, “Plasmonics for extreme light concentration and manipulation,” *Nat. Mater.* 9, 193–204 (2010).
- [3] W. L. Barnes, A. Dereux, and T. W. Ebbesen, “Surface plasmon subwavelength optics,” *Nature* 424, 824–830 (2003).
- [4] K. A. Willets and R. P. Van Duyne, “Localized surface plasmon resonance spectroscopy

and sensing,” *Annu. Rev. Anal. Chem.* 58, 267–297 (2007).

[5] S. Lal, S. Link, and N. J. Halas, “Nano-optics from sensing to waveguiding,” *Nat. Photonics* 1, 641–648 (2007).

[6] J. N. Anker, W. P. Hall, O. Lyandres, N. C. Shah, J. Zhao, and R. P. Van Duyne, “Biosensing with plasmonic nanosensors,” *Nat. Mater.* 7, 442–453 (2008).

[7] K. F. MacDonald, Z. L. Samson, M. I. Stockman, and N. I. Zheludev, “Ultrafast active plasmonics,” *Nat. Photonics* 3, 55–58 (2009).

[8] N. Yu and F. Capasso, “Flat optics with designer metasurfaces,” *Nat. Mater.* 13, 139–150 (2014).

[9] P. Genevet and F. Capasso, “Holographic optical metasurfaces: a review of current progress,” *Rep. Prog. Phys.* 78, 024401 (2015).

[10] E. Prodan, C. Radloff, N. J. Halas, and P. Nordlander, “A hybridization model for the plasmon response of complex nanostructures,” *Science* 302, 419–422 (2003).

[11] N. J. Halas, S. Lal, W.-S. Chang, S. Link, and P. Nordlander, “Plasmons in strongly coupled metallic nanostructures,” *Chem. Rev.* 111, 3913–3961 (2011).

[12] A. Lovera, B. Gallinet, P. Nordlander, and O. J. F. Martin, “Mechanisms of Fano resonances in coupled plasmonic systems,” *ACS Nano* 7, 4527–4536 (2013).

[13] T. Sandu, “Eigenmode decomposition of the near-field enhancement in localized surface plasmon resonances of metallic nanoparticles,” *Plasmonics* 8, 391–402 (2013).

[14] I. D. Mayergoyz, D. D. Fredkin, and Z. Zhenyu, “Electrostatic (plasmon) resonances in nanoparticles,” *Phys. Rev. B* 72, 155412 (2005).

[15] G. Boudarham and M. Kociak, “Modal decompositions of the local electromagnetic density of states and spatially resolved electron energy loss probability in terms of geometric modes,” *Phys. Rev. B* 85, 245447 (2012).

[16] D. E. Gómez, K. C. Vernon, and T. J. Davis, “Symmetry effects on the optical coupling between plasmonic nanoparticles with applications to hierarchical structures,” *Phys. Rev. B* 81, 075414 (2010).

[17] C. Forestiere, L. Dal Negro, and G. Miano, “Theory of coupled plasmon modes and Fano-like resonances in subwavelength metal structures,” *Phys. Rev. B* 88, 155411 (2013).

[18] K. C. Vernon, A. M. Funston, C. Novo, D. E. Gómez, P. Mulvaney, and T. J. Davis, “Influence of particle-substrate interaction on localized plasmon resonances,” *Nano Lett.* 10, 2080–2086 (2010).

[19] T. J. Davis, K. C. Vernon, and D. E. Gómez, “Designing plasmonic systems using optical coupling between nanoparticles,” *Phys. Rev. B* 79, 155423 (2009).

[20] W. Zhang and O. J. F. Martin, “A universal law for plasmon resonance shift in biosensing,” *ACS Photon.* 2, 144–150 (2015).

[21] U. Hohenester and J. Krenn, “Surface plasmon resonance of single and coupled metallic nanoparticles: a boundary integral method approach,” *Phys. Rev. B* 72, 195429 (2005).

[22] S. Dutta-Gupta and O. J. F. Martin, “Insight into the eigenmodes of plasmonic nanoclusters based on the Green’s tensor method,” *J. Opt. Soc. Am. B* 32, 194–200

2.1. Mode Analysis of Second-Harmonic Generation in Plasmonic Nanostructures

(2015).

- [23] J. Mäkitalo, M. Kauranen, and S. Suuriniemi, “Modes and resonances of plasmonic scatterers,” *Phys. Rev. B* 89, 165429 (2014).
- [24] Q. Bai, M. Perrin, C. Sauvan, J.-P. Hugonin, and P. Lalanne, “Efficient and intuitive method for the analysis of light scattering by a resonant nanostructure,” *Opt. Express* 21, 27371–27382 (2013).
- [25] M. S. Khajeahsani, A. Shahmansouri, M. J. Armand, and B. Rashidian, “Plasmonic resonance mode extraction based on the T-matrix method,” *J. Opt. Soc. Am. B* 32, 2333–2342 (2015).
- [26] J. R. D. Lasson, J. Mørk, and P. T. Kristensen, “Three-dimensional integral equation approach to light scattering, extinction cross sections, local density of states, and quasi-normal modes,” *J. Opt. Soc. Am. B* 30, 1996–2007 (2013).
- [27] H. Guo, B. Oswald, and P. Arbenz, “3-dimensional eigenmodal analysis of plasmonic nanostructures,” *Opt. Express* 20, 5481–5500 (2012).
- [28] G. Colas des Francs, J. Grandier, S. Massenot, A. Bouhelier, J.-C. Weeber, and A. Dereux, “Integrated plasmonic waveguides: a mode solver based on density of states formulation,” *Phys. Rev. B* 80, 115419 (2009).
- [29] P. T. Leung, S. Y. Liu, and K. Young, “Completeness and orthogonality of quasi-normal modes in leaky optical cavities,” *Phys. Rev. A* 49, 3057–3067 (1994).
- [30] P. T. Leung, S. Y. Liu, S. S. Tong, and K. Young, “Time-independent perturbation theory for quasi-normal modes in leaky optical cavities,” *Phys. Rev. A* 49, 3068–3073 (1994).
- [31] P. T. Leung, S. Y. Liu, and K. Young, “Completeness and timeindependent perturbation of the quasi-normal modes of an absorptive and leaky cavity,” *Phys. Rev. A* 49, 3982–3989 (1994).
- [32] E. S. C. Ching, P. T. Leung, A. Maassen van den Brink, W. M. Suen, S. S. Tong, and K. Young, “Quasi-normal-mode expansion for waves in open systems,” *Rev. Mod. Phys.* 70, 1545–1554 (1998).
- [33] P. T. Kristensen and S. Hughes, “Modes and modes volumes of leaky optical cavities and plasmonic nanoresonators,” *ACS Photon.* 1, 2–10 (2013).
- [34] C. Sauvan, J. P. Hugonin, I. S. Maksymov, and P. Lalanne, “Theory of the spontaneous optical emission of nanosize photonic and plasmon resonators,” *Phys. Rev. Lett.* 110, 237401 (2013).
- [35] R.-C. Ge, P. T. Kristensen, J. F. Young, and S. Hughes, “Quasinormal mode approach to modelling light-emission and propagation in nanoplasmonics,” *New J. Phys.* 16, 113048 (2014).
- [36] P. T. Kristensen, C. V. Vlack, and S. Hughes, “Generalized effective mode volume for leaky optical cavities,” *Opt. Lett.* 37, 1649–1651 (2012).
- [37] P. T. Leung and K. M. Pang, “Completeness and time-independent perturbation of morphology-dependent resonances in dielectric spheres,” *J. Opt. Soc. Am. B* 13, 805–817 (1996).
- [38] K. M. Lee, P. T. Leung, and K. M. Pang, “Dyadic formulation of morphology-

- dependent resonances. I. Completeness relation,” *J. Opt. Soc. Am. B* 16, 1409–1417 (1999).
- [39] M. Kauranen and A. V. Zayats, “Nonlinear plasmonics,” *Nat. Photonics* 6, 737–748 (2012).
- [40] R. W. Boyd, *Nonlinear Optics* (Academic, 1992).
- [41] J. Butet, J. Duboisset, G. Bachelier, I. Russier-Antoine, E. Benichou, C. Jonin, and P.-F. Brevet, “Optical second harmonic generation of single metallic nanoparticles embedded in a homogeneous medium,” *Nano Lett.* 10, 1717–1721 (2010).
- [42] J. Butet, G. Bachelier, I. Russier-Antoine, C. Jonin, E. Benichou, and P. F. Brevet, “Interference between selected dipoles and octupoles in the optical second-harmonic generation from spherical gold nanoparticles,” *Phys. Rev. Lett.* 105, 077401 (2010).
- [43] J. I. Dadap, J. Shan, and T. F. Heinz, “Theory of optical secondharmonic generation from a sphere of centrosymmetric material: small-particle limit,” *J. Opt. Soc. Am. B* 21, 1328–1347 (2004).
- [44] I. Russier-Antoine, E. Benichou, G. Bachelier, C. Jonin, and P.-F. Brevet, “Multipolar contributions of the second harmonic generation from silver and gold,” *J. Phys. Chem. C* 111, 9044–9048 (2007).
- [45] E. C. Hao, G. C. Schatz, R. C. Johnson, and J. T. Hupp, “Hyper-Rayleigh scattering from silver nanoparticles,” *J. Chem. Phys.* 117, 5963–5966 (2002).
- [46] K. Thyagarajan, S. Rivier, A. Lovera, and O. J. F. Martin, “Enhanced second-harmonic generation from double resonant plasmonic antennae,” *Opt. Express* 20, 12860–12865 (2012).
- [47] M. Celebrano, X. Wu, M. Baselli, S. Großmann, P. Biagioni, A. Locatelli, C. De Angelis, G. Cerullo, R. Osellame, B. Hecht, L. Duò, F. Ciccacci, and M. Finazzi, “Mode matching in multiresonant plasmonic nanoantennas for enhanced second harmonic generation,” *Nat. Nanotech.* 10, 412–417 (2015).
- [48] K. Thyagarajan, J. Butet, and O. J. F. Martin, “Augmenting second harmonic generation using Fano resonances in plasmonic systems,” *Nano Lett.* 13, 1847–1851 (2013).
- [49] B. Gallinet, J. Butet, and O. J. F. Martin, “Numerical methods for nanophotonics: standard problems and future challenges,” *Laser Photon. Rev.* 9, 577–603 (2015).
- [50] B. Gallinet and O. J. F. Martin, “Influence of electromagnetic interactions on the line shape of plasmonic Fano resonances,” *ACS Nano* 5, 8999–9008 (2011).
- [51] J. Butet, B. Gallinet, K. Thyagarajan, and O. J. F. Martin, “Secondharmonic generation from periodic arrays of arbitrary shape plasmonic nanostructures: a surface integral approach,” *J. Opt. Soc. Am. B* 30, 2970–2979 (2013).
- [52] K. O’Brien, H. Suchowski, J. Rho, A. Salandrino, B. Kante, X. Yin, and X. Zhang, “Predicting nonlinear properties of metamaterials from the linear response,” *Nat. Mater.* 14, 379–383 (2015).
- [53] J. Butet and O. J. F. Martin, “Evaluation of the nonlinear response of plasmonic metasurfaces: Miller’s rule, nonlinear effective susceptibility method, and full-wave computation,” *J. Opt. Soc. Am. B* 33, A8–A15 (2016).

2.1. Mode Analysis of Second-Harmonic Generation in Plasmonic Nanostructures

- [54] R. F. Harrington, *Field Computation by Moment Methods*, Series on Electromagnetic Waves (IEEE, 1993).
- [55] S. Rao, D. Wilton, and A. Glisson, “Electromagnetic scattering by surfaces of arbitrary shape,” *IEEE Trans. Antennas. Propag.* 30, 409–418 (1982).
- [56] A. M. Kern and O. J. F. Martin, “Surface integral formulation for 3D simulations of plasmonic and high permittivity nanostructures,” *J. Opt. Soc. Am. A* 26, 732–740 (2009).
- [57] X. Q. Sheng, J. M. Jin, J. Song, W. C. Chew, and C. C. Lu, “Solution of combined-field integral equation using multilevel fast multipole algorithm for scattering by homogeneous bodies,” *IEEE Trans. Antennas Propag.* 46, 1718–1726 (1998).
- [58] P. Ylä-Oijala, “Application of a novel CFIE for electromagnetic scattering by dielectric objects,” *Microwave Opt. Technol. Lett.* 35, 3–5 (2002).
- [59] P. Ylä-Oijala and M. Taskinen, “Application of combined field Integral equation for electromagnetic scattering by dielectric and composite objects,” *IEEE Trans. Antennas Propag.* 53, 1168–1173 (2005).
- [60] C. Forestiere, G. Iadarola, G. Rubinacci, A. Tambourrino, L. D. Negro, and G. Miano, “Surface integral formulations for the design of plasmonic nanostructures,” *J. Opt. Soc. Am. A* 29, 2314–2326 (2012).
- [61] T.-K. Wu and L. L. Tsai, “Scattering from arbitrarily-shaped lossy dielectric bodies of revolution,” *Radio Sci.* 12, 709–718 (1977).
- [62] Y. Chang and R. F. Harrington, “A surface formulation for characteristic modes of material bodies,” *IEEE Trans. Antennas. Propag.* 25, 789–795 (1977).
- [63] A. J. Poggio and E. K. Miller, “Integral equations solutions of three dimensional scattering problems,” in *Computer Techniques for Electromagnetics* (Pergamon, 1973).
- [64] R. B. Lehoucq, D. C. Sorensen, and C. Yang, *ARPACK Users’ Guide: Solution of Large-Scale Eigenvalue Problems with Implicitly Restarted Arnoldi Methods* (Society for Industrial and Applied Mathematics, 1998).
- [65] A. Zhu and S. Gedney, “Comparison of the Müller and PMCHWT surface integral formulations for the locally corrected Nyström method,” in *IEEE Antennas and Propagation Society International Symposium (IEEE, 2004)*, Vol. 4, pp. 3871–3874.
- [66] J. Mäkitalo, S. Suuriniemi, and M. Kauranen, “Boundary element method for surface nonlinear optics of nanoparticles,” *Opt. Express* 19, 23386–23399 (2011).
- [67] J. E. Sipe, V. C. Y. So, M. Fukui, and G. I. Stegeman, “Analysis of second-harmonic generation at metal surfaces,” *Phys. Rev. B* 21, 4389–4402 (1980).
- [68] V. Mizrahi and J. E. Sipe, “Phenomenological treatment of surface second-harmonic generation,” *J. Opt. Soc. Am. B* 5, 660–667 (1988).
- [69] F. X. Wang, F. J. Rodríguez, W. M. Albers, R. Ahorinta, J. E. Sipe, and M. Kauranen, “Surface and bulk contributions to the second-order nonlinear optical response of a gold film,” *Phys. Rev. B* 80, 233402 (2009).
- [70] D. Krause, C. W. Teplin, and C. T. Rogers, “Optical surface second harmonic measurements of isotropic thin-film metals: gold, silver, copper, aluminum, and tantalum,” *J. Appl. Phys.* 96, 3626–3634 (2004).

- [71] G. Bachelier, J. Butet, I. Russier-Antoine, C. Jonin, E. Benichou, and P.-F. Brevet, “Origin of optical second-harmonic generation in spherical gold nanoparticles: local surface and nonlocal bulk contributions,” *Phys. Rev. B* 82, 235403 (2010).
- [72] I. Hanninen, M. Taskinen, and J. Sarvas, “Singularity subtraction integral formulae for surface integral equations with RWG, rooftop and hybrid basis functions,” *Progress Electromagn. Res.* 63, 243–278 (2006).
- [73] C. F. Bohren and D. R. Huffman, *Absorption and Scattering of Light by Small Particles* (Wiley Interscience, 1983).
- [74] A. Ji, T. V. Raziman, J. Butet, R. P. Sharma, and O. J. F. Martin, “Optical forces and torques on realistic plasmonic nanostructures: a surface integral approach,” *Opt. Lett.* 39, 4699–4702 (2014).
- [75] G. B. Arfken and H. J. Weber, *Mathematical Methods for Physicists*, 6th ed. (Elsevier Academic, 2005).
- [76] Y. Pavlyukh and W. Hubner, “Nonlinear Mie scattering from spherical particles,” *Phys. Rev. B* 70, 245434 (2004).
- [77] B. Schürer, S. Wunderlich, C. Sauerbeck, U. Peschel, and W. Peukert, “Probing colloidal interfaces by angle-resolved second harmonic light scattering,” *Phys. Rev. B* 82, 241404 (2010).
- [78] D. Östling, P. Stampfli, and K. H. Benneman, “Theory of nonlinear optical properties of small metallic spheres,” *Z. Phys. D* 28, 169–175 (1993).
- [79] G. Gonella and H.-L. Dai, “Determination of adsorption geometry on spherical particles from nonlinear Mie theory analysis of surface second harmonic generation,” *Phys. Rev. B* 84, 121402(R) (2011).
- [80] J. Butet, I. Russier-Antoine, C. Jonin, N. Lascoux, E. Benichou, and P.-F. Brevet, “Nonlinear Mie theory for the second harmonic generation in metallic nanoshells,” *J. Opt. Soc. Am. B* 29, 2213–2221 (2012).
- [81] J. Butet, I. Russier-Antoine, C. Jonin, N. Lascoux, E. Benichou, and P.-F. Brevet, “Sensing with multipolar second harmonic generation from spherical metallic nanoparticles,” *Nano Lett.* 12, 1697–1701 (2012).
- [82] A. G. F. de Beer and S. Roke, “Nonlinear Mie theory for second-harmonic and sum-frequency scattering,” *Phys. Rev. B* 79, 155420 (2009).
- [83] G. Bachelier, I. Russier-Antoine, E. Benichou, C. Jonin, and P.-F. Brevet, “Multipolar second-harmonic generation in noble metal nanoparticles,” *J. Opt. Soc. Am. B* 25, 955–960 (2008).
- [84] H. Fischer and O. J. F. Martin, “Engineering the optical response of plasmonic nanoantennas,” *Opt. Express* 16, 9144–9154 (2008).
- [85] C. Hubert, L. Billot, P. M. Adam, R. Bachelot, P. Royer, J. Grand, D. Gindre, K. D. Dorkenoo, and A. Fort, “Role of surface plasmon in second harmonic generation from gold nanorods,” *Appl. Phys. Lett.* 90, 181105 (2007).
- [86] A. Singh, A. Lehoux, H. Remita, J. Zyss, and I. Ledoux-Rak, “Second harmonic response of gold nanorods: a strong enhancement with the aspect ratio,” *J. Phys. Chem. A* 117, 3958–3961 (2013).
- [87] Y. El Harfouch, E. Benichou, F. Bertorelle, I. Russier-Antoine, C. Jonin, N. Lascoux,

2.1. Mode Analysis of Second-Harmonic Generation in Plasmonic Nanostructures

- and P.-F. Brevet, “Hyper-Rayleigh scattering from gold nanorods,” *J. Phys. Chem. C* 118, 609–616 (2014).
- [88] J. Berthelot, G. Bachelier, M. Song, P. Rai, G. Colas des Francs, A. Dereux, and A. Bouhelier, “Silencing and enhancement of secondharmonic generation in optical gap antennas,” *Opt. Express* 20, 10498–10508 (2012).
- [89] J. Butet, S. Dutta-Gupta, and O. J. F. Martin, “Surface second-harmonic generation from coupled spherical plasmonic nanoparticles: eigenmode analysis and symmetry properties,” *Phys. Rev. B* 89, 245449 (2014).
- [90] A. Slablab, L. Le Xuan, M. Zielinski, Y. de Wilde, V. Jacques, D. Chauvat, and J.-F. Roch, “Second-harmonic generation from coupled plasmon modes in a single dimer of gold nanospheres,” *Opt. Express* 20, 220–227 (2012).
- [91] S. A. Maier, *Plasmonics: Fundamentals and Applications* (Springer, 2007).
- [92] H. Kuwata, H. Tamaru, K. Esumi, and K. Miyano, “Resonant light scattering from metal nanoparticles: practical analysis beyond Rayleigh approximation,” *Appl. Phys. Lett.* 83, 4625–4627 (2003).

2.2 Revealing a Mode Interplay That Controls Second-Harmonic Radiation in Gold Nanoantennas

Manuscript state: Published

Reference: J  r  my Butet, **Gabriel D. Bernasconi**, Marl  ne Petit, Alexandre Bouhelier, Chen Yan, Olivier J. F. Martin, Beno  t Cluzel and Olivier Demichel, "Revealing a Mode Interplay That Controls Second-Harmonic Radiation in Gold Nanoantennas", *ACS Photonics* **4**, 2923-2929, (2017).

Publication date: September 26, 2017

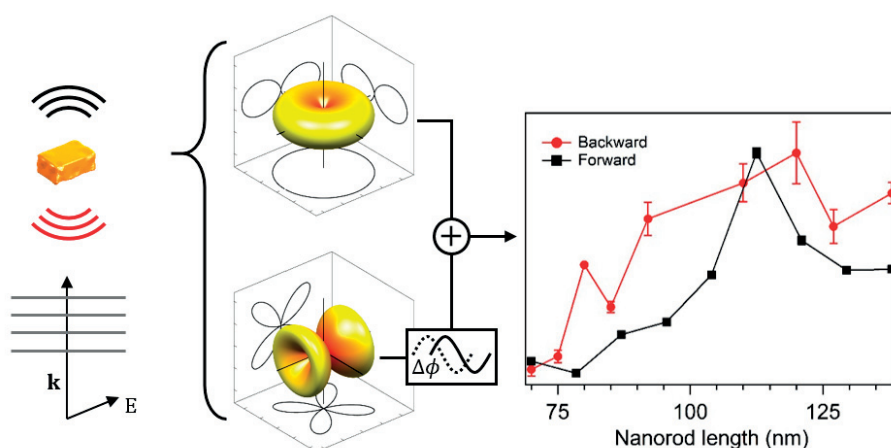
DOI: 10.1021/acsp Photonics.7b01027

URL: <http://dx.doi.org/10.1021/acsp Photonics.7b01027>

Adapted with permission from the above-mentioned reference.

Copyright (2017) American Chemical Society.

Author contributions: G. D. Bernasconi performed the multipolar analysis simulations, the theoretical analysis and contributed to the manuscript writing.



Revealing a Mode Interplay That Controls Second-Harmonic Radiation in Gold Nanoantennas

Jérémy Butet¹, Gabriel D. Bernasconi¹, Marlène Petit², Alexandre Bouhelier², Chen Yan¹, Olivier J. F. Martin¹, Benoît Cluzel² and Olivier Demichel²

¹Nanophotonics and Metrology Laboratory (NAM), Swiss Federal Institute of Technology Lausanne (EPFL), 1015, Lausanne, Switzerland.

²Laboratoire Interdisciplinaire Carnot de Bourgogne, UMR 6303 CNRS-Université Bourgogne Franche-Comté, 21078 Dijon, France.

Corresponding authors: jeremy.butet@epfl.ch, olivier.demichel@u-bourgogne.fr

ABSTRACT: In this work, we investigate the generation of second-harmonic light by gold nanorods and demonstrate that the collected nonlinear intensity depends upon a phase interplay between different modes available in the nanostructure. By recording the backward and forward emitted second-harmonic signals from nanorods with various lengths, we find that the maximum nonlinear signal emitted in the forward and backward directions is not obtained for the same nanorod length. We confirm the experimental results with the help of full-wave computations done with a surface integral equation method. These observations are explained by the multipolar nature of the second-harmonic emission, which emphasizes the role played by the relative phase between the second-harmonic modes. Our findings are of particular importance for the design of plasmonic nanostructures with controllable nonlinear emission and nonlinear plasmonic sensors as well as for the coherent control of harmonic generations in plasmonic nanostructures.

Introduction

Motivated by different specific features, the study of nonlinear optical processes in plasmonic nanostructures has become a vivid field of research [1,2]. First, the intrinsic nonlinear response of plasmonic materials enables the investigation of subtle nonlinear mechanisms associated with the surface [3,4], the shape [2], the roughness [5,6], and the symmetry [2] of plasmonic nanostructures. Second, local field enhancement associated with the plasmon resonances can boost nonlinear processes including second-harmonic generation (SHG) [7-9], third-harmonic generation [10-12], and nonlinear photoluminescence [13-16], such that these nonlinear signals provide indirect entry to the local field enhancement [17-19]. Third, the plasmonic modes associated with a nanostructure are the underlying framework upon which nonlinear processes can be built [20,21]. It is only

quite recently that the role played in nonlinear plasmonics by the interaction between the different modes available at the fundamental and harmonic frequencies has been recognized, leading to different multiresonant nanostructure designs that benefit from the interaction of several plasmonic modes at different frequencies [21-25]. This is especially the case for SHG where a dipolar excitation at the fundamental frequency produces a nonlinear signal that is essentially quadrupolar [26].

In this article, we shed new light on the interplay between the underlying modal structure supported by a plasmonic nanostructure and the corresponding SHG. Specifically, we show that the second-harmonic emission from gold nanorods can be controlled using interferences between two modes excited at the second-harmonic wavelength. By recording the backward and forward second-harmonic signals emitted by plasmonic nanorods with different lengths at a fixed pump wavelength, we observed that the nonlinear signal emitted in opposite directions is maximum for different nanorod lengths, revealing surprising enhancement mechanisms that do not fit with the well-established relation between the nonlinear response and the plasmonic enhancement. We explain these experimental findings with the help of full-wave computations performed with a surface integral equation method (SIE); the numerical results emphasize the multipolar nature of the second-harmonic emission and the associated interference effects [27]. These observations are interesting for the design of efficient second-harmonic nanosources as well as for the development of nonlinear plasmonic sensing, which aims at probing small refractive index changes with the help of nonlinear plasmonic nanostructures.

Results and Discussion

The gold nanorods used in this work are fabricated on a glass coverslip with a standard electron beam lithography fabrication method [28]. The nanorods were designed to reach a width of 80 nm and a length varying from $L = 90$ nm to $L = 160$ nm by 10 nm steps. For the sake of accuracy, we measured by SEM the real width and length of nanorods, (see SEM pictures of nanorods in Figure 1(b)). Widths have been found to be 75 ± 5 nm and lengths are 15 to 30 nm smaller than expected values from 75 to 138 nm with a precision of ± 5 nm. The thickness of the deposited gold layer is 50 nm. The linear optical response is obtained from dark-field spectroscopy. Figure 1(a) shows the evolution of the scattering spectrum for a series of gold nanorods whose lengths are reported close to the related spectrum. In order to perform the linear characterization in the same experimental conditions as those used for the nonlinear optical measurements, a drop of immersion oil is deposited on top of the nanostructures. The nanorods are thus immersed in a homogeneous medium with a refractive index of 1.5. The scattering spectra show that the localized surface plasmon resonance red-shifts as the nanorod length increases (from 650 nm for $L = 75$ to 890 nm for $L = 138$ nm), as reported in previous studies of the linear response of gold nanorods [29,30]. One can note that resonances between the 110 and 120 nm long antennas seem to slightly blue-shift. However, this shift—also

2.2. Revealing a Mode Interplay That Controls Second-Harmonic Radiation in Gold Nanoantennas

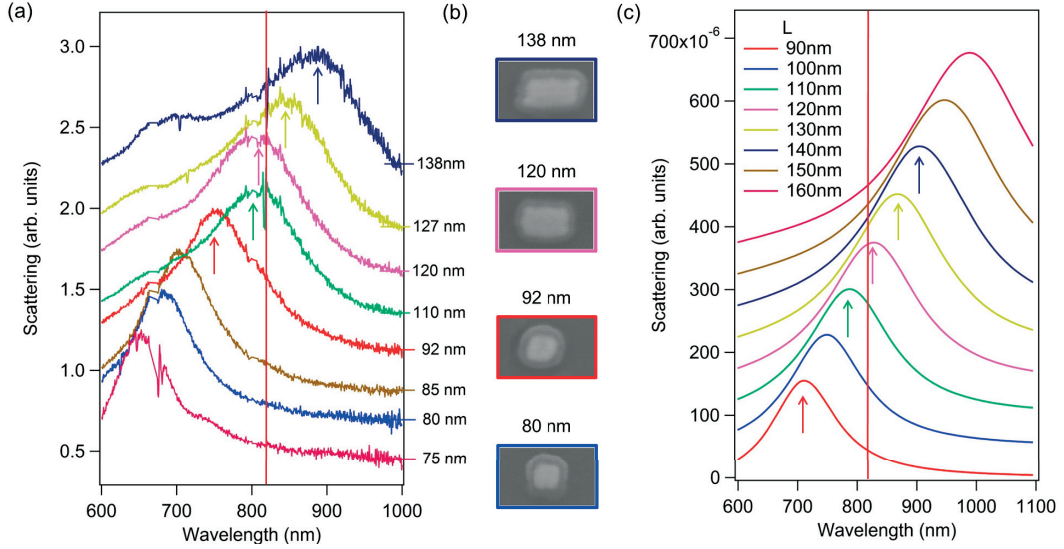


Figure 1 – (a) Dark-field spectra of the gold nanorods with length ranging from 75 to 138 nm. (b) SEM images of four nanorods. (c) The scattering spectra of the nanorods, whose length vary from 90 to 160 nm, evaluated with a surface integral equation method. The nanorod widths and thicknesses are 75 nm and 50 nm, respectively. The spectra are shifted vertically for clarity.

associated to a broadening of resonances —appears to be not relevant because the shift is smaller than the width at half-maximum of the resonance. To confirm numerically this behavior, we compute the scattering from nanorods with similar dimensions with an SIE method [31]. The edges and corners of the rectangular nanorods are rounded with a radius of 5 nm to provide a more realistic model [32]. The nanorods are excited by a planewave polarized along the long axis and placed in a homogeneous medium with a refractive index of 1.5, similar to the refractive indices of both the glass substrate and immersion oil. The calculated localized surface plasmon resonance redshifts from 710 nm for $L = 90$ to 990 nm for $L = 160$ nm. Both calculated and measured spectra are in quite good agreement.

Having characterized the linear responses of the gold nanorods, we now turn our attention to their second-harmonic responses. The second-harmonic generation from colloidal gold nanorods has already been investigated with hyper-Rayleigh scattering using a collection at a right angle [33,34] and for nanofabricated nanorods with a collection performed in the forward direction only [35,36]. Note that the second-harmonic intensity is also commonly collected in the backward direction using the same objective as that used for illumination [24,37,38]. All these works have emphasized the role played by localized surface plasmon resonances in the enhancement of the nonlinear emission. Inspired by a recent study of the second-harmonic light emitted from AlGaAs dielectric nanoantennas [39], we choose in the present work to collect simultaneously the second-harmonic intensity in

both the forward and backward directions, as depicted in Figure 2(a). A high numerical

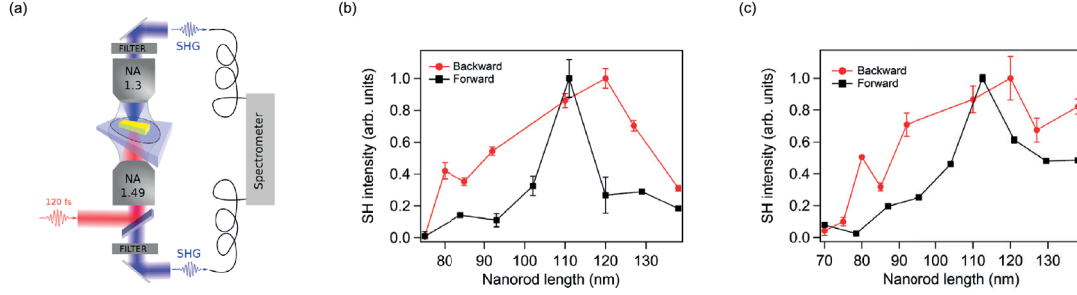


Figure 2 – (a) Sketch of the experimental setup used for the simultaneous detection of the forward and backward second-harmonic light. (b) Forward (shown in black) and backward (shown in red) second-harmonic intensities as functions of the nanorod length. The corresponding dark-field spectra are shown in Figure 1(a). (c) Forward (shown in black) and backward (shown in red) second-harmonic intensities for a second set of nanorods, showing the reproducibility of the experimental observations. The error bars represent the error in estimating the SHG intensity.

aperture oil-immersion objective (60 \times , NA 1.49) focuses on individual nanorods with a 120 fs pulsed laser beam emitted at a wavelength of 820 nm. The pulse energy is kept constant to a value as low as 4.75 pJ, well below the damage threshold of the nanorods (the mean laser power is 380 μ W). The intensity of the second-harmonic emitted in the backward direction is collected by the same objective (episcopic objective), while the second-harmonic intensity emitted in the forward direction is collected with a second oil-immersion objective (100 \times , NA 1.30, diasopic objective). Two microscope objectives with distinct working distances are used for convenience of the alignment procedure. Figure 2(b) shows the second-harmonic intensity collected in the forward and backward directions for nanorod lengths ranging from 90 to 160 nm (see the Supporting Information for the experimental details; the corresponding measured spectra are shown in Supporting Information Figure S1; both SHG and nonlinear photoluminescence are observed). The error bars correspond to the sum of the noise level and the error in estimating the SHG intensity (see Supporting Information for more details). The intensities of the nonlinear signals in the forward and backward directions reach a maximum for two different nanorod lengths. According to the literature, this length-dependent signal is understood from the resonant excitation of a localized surface plasmon mode at the fundamental wavelength [1,2]. This is confirmed by the experimental dark-field spectra, Figure 1(a), indicating a resonant excitation of the longitudinal dipolar plasmon mode at the pump wavelength ($\lambda = 820$ nm) for $L = 110$ nm and $L = 120$ nm. While the second-harmonic intensity peaks at $L = 110$ nm in the forward direction, the maximum is reached for $L = 120$ nm in the backward direction. A similar behavior has been observed for a dozen of nanorod arrays (see for example the second set of nanorods provided in Figure 2(c)), emphasizing the reproducibility of this observation. This observation cannot be inferred from the simple plasmonic enhancement of the nonlinear responses [36-38] and points toward a

2.2. Revealing a Mode Interplay That Controls Second-Harmonic Radiation in Gold Nanoantennas

more complex mechanism.

To understand this behavior, we perform full-wave computations of the second-harmonic response of the gold nanorod with a SIE method assuming a surface contribution to the nonlinearity [40] (see the Supporting Information for the implementation details). The second-harmonic spectra are evaluated for fundamental wavelengths spanning between 600 and 1100 nm and for nanorod lengths varying between 90 and 160 nm. The second-harmonic intensity is integrated over a sphere in the far-field region (sphere radius 50 μm). As expected and illustrated in Figure 3(a), the second-harmonic emission is generally enhanced when the fundamental wavelength matches the dipolar longitudinal plasmon resonance. However, compared to the calculated scattering cross sections displayed in Figure 1(b) that exhibit a stronger linear response for larger antennas, the simulations in Figure 3(a) indicate an enhanced SHG intensity for the small nanorods. Indeed, as the nanorod length decreases, the dipolar surface plasmon resonance blue-shifts at the fundamental wavelength, augmenting the retardation effects and then the SHG [26]. For a fixed pump wavelength centered at 820 nm, the strongest enhancement of the nonlinear response occurs for 120-130 nm nanorod lengths.

We then calculate the emission pattern of the second-harmonic wave for the different nanorod lengths considered in this work. Figure 3(b) shows the computed emission diagrams for four sizes ($L = 100, 110, 120$, and 130 nm). In the Supporting Information, Figure S3 gathers the computed patterns for all nanorod sizes. To compare these numerical results with experimental data, the computed second-harmonic pattern is divided into two parts, corresponding to the second-harmonic intensity integrated on the top hemisphere for the forward second-harmonic intensity and that integrated on the bottom hemisphere for the backward second-harmonic intensity. In the following, all the simulations are done with a fundamental wavelength of 820 nm. The results are shown in Figure 3(c). We find that the length of the nanorods drastically influences the emission pattern. For $L = 90$ nm, the second harmonic is essentially forward emitted, while for the longest nanorod, the diagram shows a stronger emission in the backward direction. We verified that this behavior is not modified by taking into account the different numerical apertures for the episcopic and diasopic objectives (see Supporting Information, Figure S3). The evolution of the forward and backward second-harmonic emissions in Figure 3(c) is similar to the one observed in the experimental results shown in Figure 2(b).

Before studying the underlying mechanisms of this effect, we recall that in the case of a normal planewave illumination of the nanorods the SHG signal comes essentially from (i) a dipolar mode oriented along the illumination propagation direction and (ii) a quadrupolar mode oriented along the nanorods axis [2]. The dipolar second-harmonic emission is thus due to the retardation effect induced by the fundamental wave: the phase variation of the fundamental wave across the rod thickness induces a second-harmonic dipolar moment along the wavevector of the pump wave; see the left inset in Figure 3(d). On the other hand, the quadrupolar second-harmonic emission arises from the

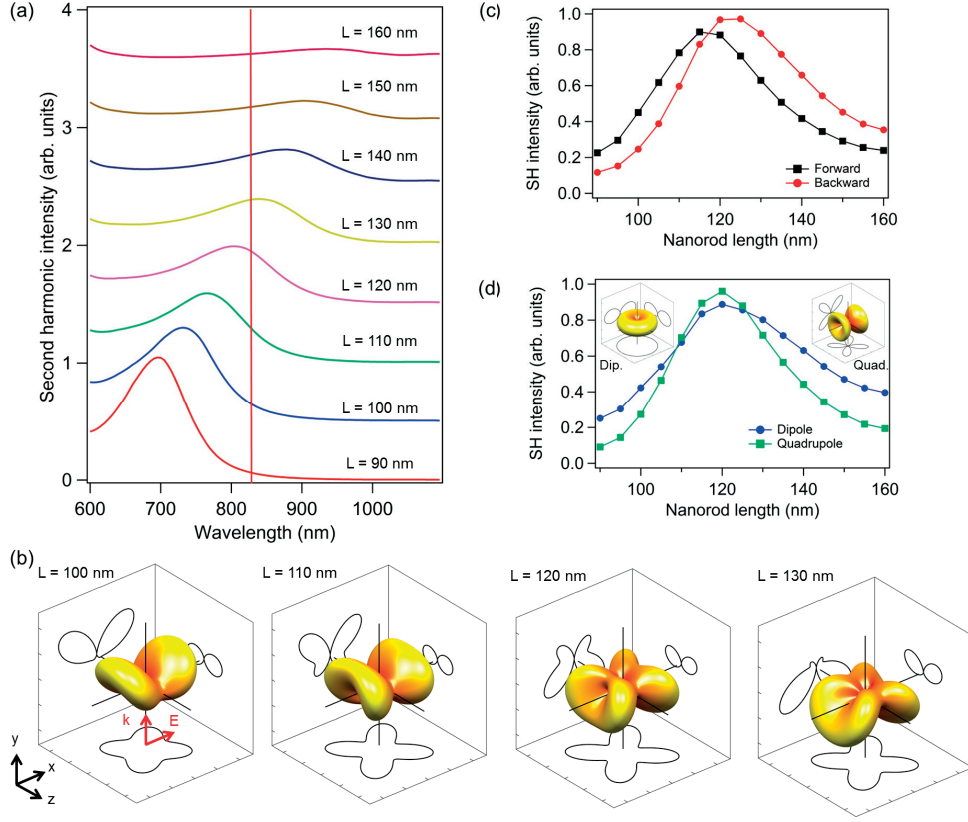


Figure 3 – (a) Second-harmonic intensity as a function of the illumination wavelength for nanorod lengths ranging from 90 to 160 nm. The spectra are shifted vertically for clarity. (b) Second-harmonic emission patterns for nanorod lengths of 100 to 130 nm. The black solid lines correspond respectively to the pattern profiles in the planes $x = 0$, $y = 0$, and $z = 0$. (c) Computed forward (shown in black) and backward (shown in red) second-harmonic intensities as functions of the nanorod length. (d) Decomposition of the second-harmonic intensity in dipolar (shown in blue) and quadrupolar (shown in green) emissions. The insets show the emission patterns of the dipolar and quadrupolar second-harmonic modes. The fundamental wavelength is 820 nm, except for panel (a).

2.2. Revealing a Mode Interplay That Controls Second-Harmonic Radiation in Gold Nanoantennas

fundamental dipole excited along the nanorods axis; see the right inset in Figure 3(d). In order to disentangle the contribution of these two modes, we perform a multipolar decomposition of the second-harmonic emission; that is, the second-harmonic field is expressed using the vector spherical harmonics (VSHs) [41] as

$$\mathbf{E}_{SHG} = \sum_{l=1}^{l_{max}} \sum_{m=-l}^l k_{SHG}^2 E_{l,m} [a_{l,m} \mathbf{N}_{l,m} + b_{l,m} \mathbf{M}_{l,m}] \quad (1)$$

where $a_{l,m}$ and $b_{l,m}$ are the complex expansion coefficients, $E_{l,m}$ is a normalization factor, $\mathbf{N}_{l,m}$ and $\mathbf{M}_{l,m}$ are the VSHs, and l_{max} is set to 8. The definition used for the VSHs and the normalization factor can be found in ref [41]. The expansion coefficients are found by projecting the computed electromagnetic fields onto the VSHs at a distance of 10 μm from the nanorods. The amplitudes of the three coefficients for the dipolar ($a_{1,m}$) or the five coefficients for the quadrupolar ($a_{2,m}$) second-harmonic emissions are then summed up to determine the relative weight of the dipolar or quadrupolar emissions; orders higher than the quadrupole as well as the magnetic modes, related to the $b_{l,m}$ coefficients in eq 1, are found to be negligible. In Figure 3(d), we observe that the second-harmonic dipolar mode is the highest contribution to the second-harmonic emission, except for nanorod lengths between 110 and 130 nm, for which the longitudinal dipolar mode is resonantly excited at the pump wavelength (820 nm); see Figure 1(b).

The evolution of the amplitudes of the dipolar and quadrupolar second-harmonic emissions cannot explain the flip of the nonlinear responses discussed previously since these two contributions are symmetric with respect to the forward and backward directions as pictured by the insets in Figure 3(d). The literature suggests that the interference between different second-harmonic modes, and thus their relative phase, plays an important role in the observed emission patterns [42,43]. Especially, it was shown that the phase induced by the fundamental dipolar mode allows controlling the forward and backward second-harmonic emission [27,42,44]. For this reason, the multipolar analysis is further refined in Figure 4. The projection of the second-harmonic field on the VSHs reveals that the dipole contribution comes from the two expansion coefficients $a_{1,-1}$ and $a_{1,1}$ and that the quadrupole contribution comes from the three coefficients $a_{2,-2}$, $a_{2,2}$, and $a_{2,0}$, with the remaining coefficients $a_{1,0}$, $a_{2,-1}$, and $a_{2,1}$ being negligible. Note that the coefficient values are dependent on the axis orientation; see Figure 3(b). A careful analysis of the dipole vector and the quadrupolar matrix (see the Supporting Information), combined with symmetry considerations, provides the relation between the coefficients $a_{1,m}$ and $a_{2,m}$. For the dipole, the relations $a_{1,1} = a_{1,-1}$ and $a_{1,0} = 0$ are obtained and, for the quadrupole, $|a_{2,-2}| = |a_{2,2}|$ and $\arg(a_{2,0}) = \arg(a_{2,-2}) + \pi = \arg(a_{2,2}) + \pi$, in agreement with the results shown in Figure 4(a,b). This observation confirms that second-harmonic emission corresponds to that of a transverse dipole and a longitudinal quadrupole. Since the phase between the quadrupole coefficients is roughly constant (close to π) over the whole nanorod size range (see the green curves in Figure 4(b)) and the two dipole coefficients are in phase, only the relative phase between the dipole coefficients and the

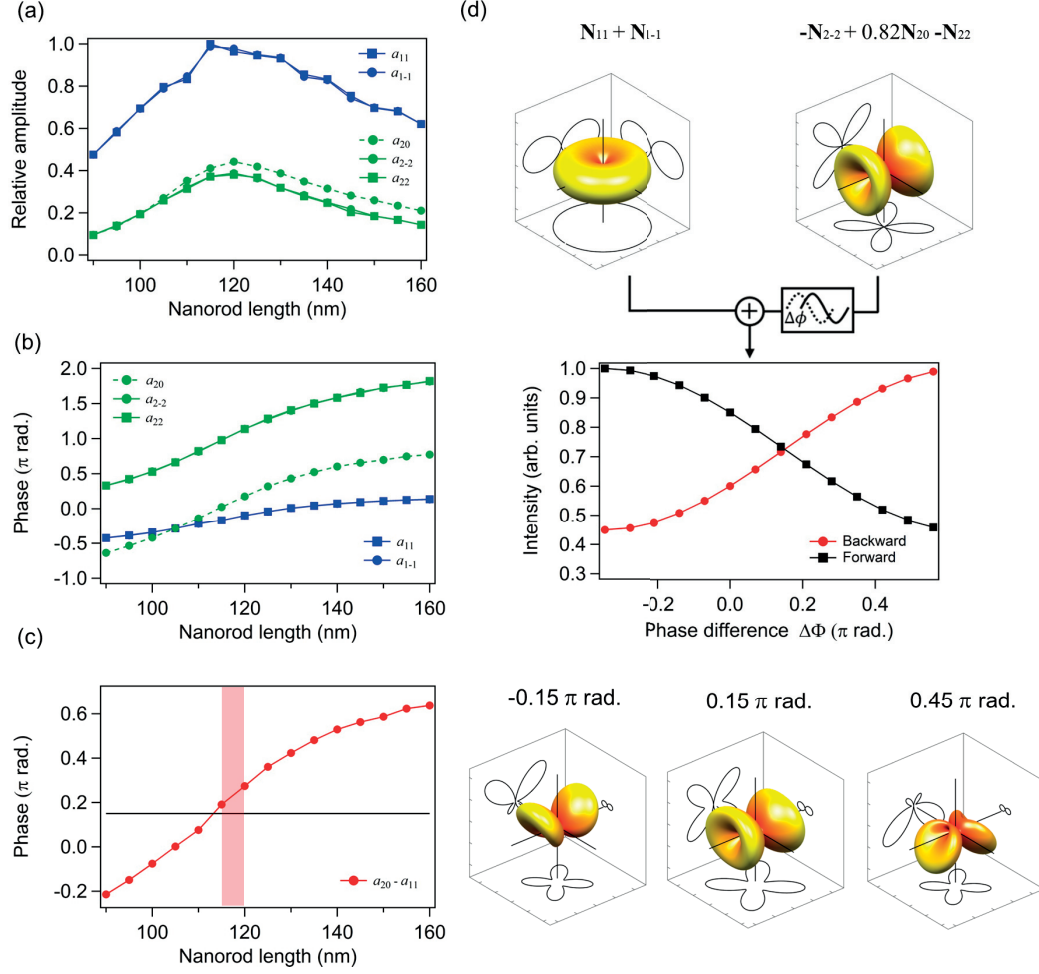


Figure 4 – (a) Normalized amplitude and (b) phase of the expansion coefficients a_{lm} for a nanorod length ranging from 90 to 160 nm. (c) Phase difference between the dipolar coefficient $a_{1,1}$ and the quadrupolar coefficient $a_{2,0}$. The horizontal line is at 0.15 rad and the vertical band shows where the flip occurs in the full-wave computations, Figure 3(c). (d) Evolution of the emission direction with the phase difference between $a_{1,1}$ and $a_{2,0}$. The black solid lines correspond respectively to the pattern profiles in the planes $x = 0$, $y = 0$ and $z = 0$. The second-harmonic emission is computed as $\mathbf{E}_{SHG} = [\mathbf{N}_{1,-1} + \mathbf{N}_{1,1}] + e^{i\Delta\Phi}[-\mathbf{N}_{2,-2} + 0.82\mathbf{N}_{2,0} - \mathbf{N}_{2,2}]$.

2.2. Revealing a Mode Interplay That Controls Second-Harmonic Radiation in Gold Nanoantennas

quadrupole coefficient $a_{2,0}$ is considered in the following. In Figure 4(b), we observe that the phases of the dipolar and quadrupolar components do not evolve at the same rate (compare the blue and green curves), hinting that the flip in the second-harmonic emission occurs when the phase difference between the two components reaches a specific value. Figure 4(c) shows the evolution of the phase difference between the dipole and quadrupole coefficients, revealing that the flip indeed occurs for a specific phase difference $\Delta\phi$ between 0.19π rad and 0.28π rad, corresponding to nanorod lengths between 115 and 120 nm. To confirm the role of this phase difference in the flip of the second-harmonic emission, the VSHs associated with the dipolar mode have been added to those of the quadrupole mode with expansion coefficients of constant amplitudes but different relative phase $\Delta\phi$ as

$$\mathbf{E}_{SHG} = [a_{1,-1}\mathbf{N}_{1,-1} + a_{1,1}\mathbf{N}_{1,1}] + e^{i\Delta\phi}[a_{2,-2}\mathbf{N}_{2,-2} + a_{2,0}\mathbf{N}_{2,0} + a_{2,2}\mathbf{N}_{2,2}] \quad (2)$$

with $a_{1,-1} = a_{1,1} = 1$, $a_{2,-2} = a_{2,2} = -1$, and $a_{2,0} = 0.82$ to reproduce the dipolar and quadrupolar emissions. The result is shown in Figure 4(d), where we observe that the direction flip occurs for a phase difference $\Delta\phi = 0.15\pi$ rad, a value very close to the one extracted from the scattering spectra in Figure 4(c). Concerning the relation between $|a_{2,-2}|$ and $|a_{2,0}|$, we observe that the flip between backward and forward emission does not depend upon the VSH $\mathbf{N}_{2,0}$ and thus of the amplitude of the $a_{2,0}$ coefficient (data not shown). This observation suggests that the flip in the nonlinear emission is due to a fundamental symmetry relation between the VSHs. Although not required to obtain the flip in the nonlinear emission, the specific relation $|a_{2,0}| = 0.82|a_{2,-2}| = 0.82|a_{2,2}|$ reproduces a radiation pattern with the expected cylindrical symmetry around the x-axis (see the Supporting Information). The electric field associated with a VSH does not have a constant phase over the sphere (i.e., is a function of both θ and ϕ), leading to a complex interference process.

Beyond their importance for the fundamental understanding of the mechanisms that lead to second-harmonic emission in plasmonic nanostructures, these observations are also very important for the development of nonlinear plasmonic sensing: the nonlinear analog of plasmonic sensing aiming at the detection of small refractive index changes using the nonlinear properties of plasmonic nanostructures [45-47]. Indeed, nonlinear signal collected in such an application, i.e., the second-harmonic intensity, is not necessarily maximized when the fundamental wavelength matches the scattering maximum. Furthermore, the modal interplay occurring between the dipolar and quadrupolar second-harmonic emissions could be directly used for sensing. Finally, when designing a practical device for nonlinear sensing, it is crucial to collect the signal where it is strongest. Figure 5(a) shows an example of such an application where the forward and backward second-harmonic intensities are plotted as a function of the refractive index of the surrounding medium. A nanorod length of 100 nm has been chosen as an example, and the fundamental wavelength is 820 nm. The dependence upon the refractive index is identical to the one discussed previously considering the nanorod length influence; that is, a flip of the

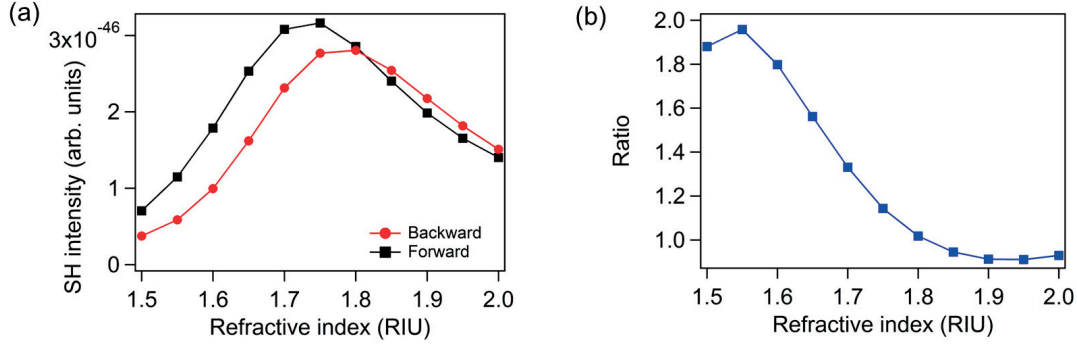


Figure 5 – (a) Computed forward (shown in black) and backward (shown in red) second-harmonic intensities as functions of the refractive index of the surrounding medium. (b) Ratio between the forward and backward second-harmonic intensities as a function of the refractive index of the surrounding medium. The nanorod length is 100 nm, and the fundamental wavelength is 820 nm.

nonlinear pattern is observed in Figure 5(a). To quantify this flip, the ratio between the forward and backward second-harmonic intensities is shown in Figure 5(b). This ratio evolves between 0.8 and 1.9 for a refractive index of the surrounding medium between 1.5 and 2. In the region of the largest slope, the estimated sensitivity is 4.7 RIU^{-1} (refractive index unit). Although the comparison with other methods, especially the ones developed in the linear regime, is not straightforward [48,49], the approach proposed here is a credible alternative to standard methods for in situ characterization during nonlinear and ultrafast optical measurements.

Conclusion

In conclusion, we have shown that the emission pattern of the SHG emitted from gold nanorods strongly depends on the length of the nanorods. We have experimentally demonstrated a different evolution of the second-harmonic intensities recorded in the forward and backward directions using an original experimental configuration. Specifically, we have observed that the nonlinear emission in these two directions is not maximal for the same nanorod length, a behavior departing from the well-known plasmonic enhancement of the nonlinear response. Using a full-wave numerical method, we have clearly identified the underlying mechanisms that lead to the experimental observation and revealed that it stems from the evolution of the phase between the different multipoles involved in the second-harmonic emission. This result indicates that, while the modal structure associated with a plasmonic nanostructure is key to understanding its spectral response, the dephasing between the different modes can govern fundamental properties, such as the emission direction and detected intensities. Since the recorded signal depends upon the experimental configuration of the detection, special care is required to determine

2.2. Revealing a Mode Interplay That Controls Second-Harmonic Radiation in Gold Nanoantennas

the nonlinear conversion rate and to design efficient nonlinear plasmonic nanostructures. Furthermore, we showed that the modal interplay occurring in the SHG from plasmonic nanostructures may be used to measure small refractive index changes [45-47]. These results can also open interesting directions for the dynamic control of harmonic generations in plasmonic nanostructures based on engineering the relative phase between the different modes [50,51].

Acknowledgement

This work has been performed in cooperation with the Labex ACTION Program (Contract No. ANR-11-LABX-0001-01). This research was performed while J.B. was at the Laboratoire Interdisciplinaire Carnot de Bourgogne as an invited scientist. J.B., G.D.B., C.Y., and O.J.F.M. acknowledge funding from the Swiss National Science Foundation (SNSF, Projects 200020_153662 and 200021_162453). O.J.F.M. and A.B. acknowledge funding from the European Research Council (ERC-2015-AdG-695206 Nanofactory) and FP7/2007-2013 Grant Agreement No. 30677, respectively.

References

- [1] Kauranen, M.; Zayats, A. V. Nonlinear Plasmonics. *Nat. Photonics* 2012, 6, 737-748.
- [2] Butet, J.; Brevet, P.-F.; Martin, O. J. F. Optical Second Harmonic Generation in Plasmonic Nanostructures: From Fundamental Principles to Advanced Applications. *ACS Nano* 2015, 9, 10545- 10562.
- [3] Bachelier, G.; Butet, J.; Russier-Antoine, I.; Jonin, C.; Benichou, E.; Brevet, P.-F. Origin of optical second-harmonic generation in spherical gold nanoparticles: Local surface and nonlocal bulk contributions. *Phys. Rev. B: Condens. Matter Mater. Phys.* 2010, 82, 235403.
- [4] Wang, F. X.; Rodriguez, F. J.; Albers, W. M.; Ahorinta, R.; Sipe, J. E.; Kauranen, M. Surface and bulk contributions to the second-order nonlinear optical response of a gold film. *Phys. Rev. B: Condens. Matter Mater. Phys.* 2009, 80, 233402.
- [5] Smolyaninov, I. I.; Zayats, A. V.; Davis, C. C. Near-Field Second Harmonic Generation from a Rough Metal Surface. *Phys. Rev. B: Condens. Matter Mater. Phys.* 1997, 56, 9290.
- [6] Stockman, M. I.; Bergman, D. J.; Anceau, C.; Brasselet, S.; Zyss, J. Enhanced Second-Harmonic Generation by Metal Surfaces with Nanoscale Roughness: Nanoscale Dephasing, Depolarization, and Correlations. *Phys. Rev. Lett.* 2004, 92, 057402.
- [7] Butet, J.; Duboisset, J.; Bachelier, G.; Russier-Antoine, I.; Benichou, E.; Jonin, C.; Brevet, P.-F. Optical Second Harmonic Generation of Single Metallic Nanoparticles Embedded in a Homogeneous Medium. *Nano Lett.* 2010, 10, 1717-1721.
- [8] Zhang, Y.; Grady, N. K.; Ayala-Orozco, C.; Halas, N. J. Three- Dimensional Nanos-structures as Highly Efficient Generators of Second Harmonic Light. *Nano Lett.* 2011, 11,

5519-5523.

- [9] Canfield, B. K.; Husu, H.; Laukkanen, J.; Bai, B. F.; Kuittinen, M.; Turunen, J.; Kauranen, M. Local Field Asymmetry Drives Second- Harmonic Generation in Noncentrosymmetric Nanodimers. *Nano Lett.* 2007, 7, 1251-1255.
- [10] Lippitz, M.; van Dijk, M. A.; Orrit, M. Third-Harmonic Generation from Single Gold Nanoparticles. *Nano Lett.* 2005, 5, 799- 802.
- [11] Schwartz, O.; Oron, D. Background-Free Third Harmonic Imaging of Gold Nanorods. *Nano Lett.* 2009, 9, 4093-4097.
- [12] Hentschel, M.; Utikal, T.; Giessen, H.; Lippitz, M. Quantitative Modeling of the Third Harmonic Emission Spectrum of Plasmonic Nanoantennas. *Nano Lett.* 2012, 12, 3778-3782.
- [13] Castro-Lopez, M.; Brinks, D.; Sapienza, R.; van Hulst, N. F. Aluminum for Nonlinear Plasmonics: Resonance-Driven Polarized Luminescence of Al, Ag, and Au Nanoantennas. *Nano Lett.* 2011, 11, 4674-4678.
- [14] Biagioni, P.; Brida, D.; Huang, J.-S.; Kern, J.; Duò, L.; Hecht, B.; Finazzi, M.; Cerullo, G. Dynamics of Four-Photon Photoluminescence in Gold Nanoantennas. *Nano Lett.* 2012, 12, 2941-2947.
- [15] Demichel, O.; Petit, M.; Viarbitskaya, S.; Méjard, R.; de Fornel, F.; Hertz, E.; Billard, F.; Bouhelier, A.; Cluzel, B. Dynamics, Efficiency, and Energy Distribution of Nonlinear Plasmon-Assisted Generation of Hot Carriers. *ACS Photonics* 2016, 3, 791-795.
- [16] Méjard, R.; Verdy, A.; Petit, M.; Bouhelier, A.; Cluzel, B.; Demichel, O. Energy-Resolved Hot-Carrier Relaxation Dynamics in Monocrystalline Plasmonic Nanoantennas. *ACS Photonics* 2016, 3, 1482-1488.
- [17] Kim, M.-K.; Sim, H.; Yoon, S. J.; Gong, S.-H.; Ahn, C. W.; Cho, Y.-H.; Lee, Y.-H. Squeezing Photons into a Point-Like Space. *Nano Lett.* 2015, 15, 4102-4107.
- [18] Hajisalem, G.; Nezami, M. S.; Gordon, R. Probing the Quantum Tunneling Limit of Plasmonic Enhancement by Third Harmonic Generation. *Nano Lett.* 2014, 14, 6651-6654.
- [19] Shen, S.; Meng, L.-Y.; Zhang, Y.; Han, J.; Ma, Z.; Hu, S.; He, Y.; Li, J.-F.; Ren, B.; Shih, T.-M. Plasmon-Enhanced Second-Harmonic Generation Nanorulers with Ultrahigh Sensitivities. *Nano Lett.* 2015, 15, 6716-6721.
- [20] Viarbitskaya, S.; Teulle, A.; Marty, R.; Sharma, J.; Girard, C.; Arbouet, A.; Dujardin, E. Tailoring and Imaging the Plasmonic Local Density of States in Crystalline Nanoprisms. *Nat. Mater.* 2013, 12, 426-432.
- [21] Bernasconi, G. D.; Butet, J.; Martin, O. J. F. Mode Analysis of Second-Harmonic Generation in Plasmonic Nanostructures. *J. Opt. Soc. Am. B* 2016, 33, 768-779.
- [22] Celebrano, M.; Wu, X.; Baselli, M.; Grossmann, S.; Biagioni, P.; Locatelli, A.; De Angelis, C.; Cerullo, G.; Osellame, R.; Hecht, B.; et al. Mode Matching in Multiresonant Plasmonic Nanoantennas for Enhanced Second Harmonic Generation. *Nat. Nanotechnol.* 2015, 10, 412-417.
- [23] Thyagarajan, K.; Butet, J.; Martin, O. J. F. Augmenting Second Harmonic Generation Using Fano Resonances in Plasmonic Systems. *Nano Lett.* 2013, 13, 1847-1851.
- [24] Ethis de Corny, M.; Chauvet, N.; Laurent, G.; Jeannin, M.; Olgeirsson, L.; Drezet, A.;

2.2. Revealing a Mode Interplay That Controls Second-Harmonic Radiation in Gold Nanoantennas

- Huant, S.; Dantelle, G.; Nogues, G.; Bachelier, G. Wave-Mixing Origin and Optimization in Single and Compact Aluminum Nanoantennas. *ACS Photonics* 2016, 3, 1840-1846.
- [25] Hasan, S.-B.; Etrich, C.; Filter, R.; Rockstuhl, C.; Lederer, F. Enhancing the Nonlinear Response of Plasmonic Nanowire Antennas by Engineering their Terminations. *Phys. Rev. B: Condens. Matter Mater. Phys.* 2013, 88, 205125.
- [26] Dadap, J. I.; Shan, J.; Eisenthal, K. B.; Heinz, T. F. Second-Harmonic Rayleigh Scattering from a Sphere of Centrosymmetric Material. *Phys. Rev. Lett.* 1999, 83, 4045-4048.
- [27] Rodrigo, S. G.; Harutyunyan, H.; Novotny, L. Coherent Control of Light Scattering from Nanostructured Materials by Second-Harmonic Generation. *Phys. Rev. Lett.* 2013, 110, 177405.
- [28] Thyagarajan, K.; Santschi, C.; Langlet, P.; Martin, O. J. F. Highly Improved Fabrication of Ag and Al Nanostructures for UV and Nonlinear Plasmonics. *Adv. Opt. Mater.* 2016, 4, 871-876.
- [29] Pérez-Juste, J.; Pastoriza-Santos, I.; Liz-Marzán, L. M.; Mulvaney, P. Gold Nanorods: Synthesis, Characterization and Applications. *Coord. Chem. Rev.* 2005, 249, 1870-1901.
- [30] Fischer, H.; Martin, O. J. F. Engineering the Optical Response of Plasmonic Nanoantennas. *Opt. Express* 2008, 16, 9144-9154.
- [31] Kern, A. M.; Martin, O. J. F. Surface Integral Formulation for 3D Simulations of Plasmonic and High Permittivity Nanostructures. *J. Opt. Soc. Am. A* 2009, 26, 732-740.
- [32] Raziman, T. V.; Martin, O. J. F. Polarisation Charges and Scattering Behaviour of Realistically Rounded Plasmonic Nanostructures. *Opt. Opt. Express* 2013, 21, 21500-21507.
- [33] Singh, A.; Lehoux, A.; Remita, H.; Zyss, J.; Ledoux-Rak, I. Second Harmonic Response of Gold Nanorods: A Strong Enhancement with the Aspect Ratio. *J. Phys. Chem. Lett.* 2013, 4, 3958-3961.
- [34] El Harfouch, Y.; Benichou, E.; Bertorelle, F.; Russier-Antoine, I.; Jonin, C.; Lascoux, N.; Brevet, P.-F. Hyper-Rayleigh Scattering from Gold Nanorods. *J. Phys. Chem. C* 2014, 118, 609-616.
- [35] Hubert, C.; Billot, L.; Adam, P.-M.; Bachelot, R.; Royer, P.; Grand, J.; Gindre, D.; Dorhenoo, K. D.; Fort, A. Role of Surface Plasmon in Second Harmonic Generation from Gold Nanorods. *Appl. Phys. Lett.* 2007, 90, 181105.
- [36] Metzger, B.; Gui, L.; Fuchs, J.; Floess, D.; Hentschel, M.; Giessen, H. Strong Enhancement of Second Harmonic Emission by Plasmonic Resonances at the Second Harmonic Wavelength. *Nano Lett.* 2015, 15, 3917-3922.
- [37] Berthelot, J.; Bachelier, G.; Song, M.; Rai, P.; Colas des Francs, G.; Dereux, A.; Bouhelier, A. Silencing and Enhancement of Second-Harmonic Generation in Optical Gap Antennas. *Opt. Express* 2012, 20, 10498-10508.
- [38] Slablab, A.; Le Xuan, L.; Zielinski, M.; de Wilde, Y.; Jacques, V.; Chauvat, D.; Roch, J.-F. Second-Harmonic Generation from Coupled Plasmon Modes in a Single Dimer of Gold Nanospheres. *Opt. Express* 2012, 20, 220-227.
- [39] Camacho-Morales, R.; Rahmani, M.; Kruk, S.; Wang, L.; Xu, L.; Smirnova, D. A.;

- Solntsev, A. S.; Miroschnichenko, A.; Tan, H. H.; Karouta, F.; Naureen, S.; Vora, K.; Carletti, L.; De Angelis, C.; Jagadish, C.; Kivshar, Y. S.; Neshev, D. N. Nonlinear Generation of Vector Beams From AlGaAs Nanoantennas. *Nano Lett.* 2016, 16, 7191-7197.
- [40] Mäkitalo, J.; Suuriniemi, S.; Kauranen, M. Boundary Element Method for Surface Nonlinear Optics of Nanoparticles. *Opt. Express* 2011, 19, 23386-23399.
- [41] Mühlig, S.; Menzel, C.; Rockstuhl, C.; Lederer, F. Multipole Analysis of Meta-Atoms. *Metamaterials* 2011, 5, 64-73.
- [42] Dadap, J. I.; Shan, J.; Heinz, T. F. Theory of Optical Second- Harmonic Generation from a Sphere of Centrosymmetric Material: Small-Particle Limit. *J. Opt. Soc. Am. B* 2004, 21, 1328.
- [43] Butet, J.; Raziman, T. V.; Yang, K.-Y.; Bernasconi, G. D.; Martin, O. J. F. Controlling the Nonlinear Optical Properties of Plasmonic Nanoparticles with the Phase of Their Linear Response. *Opt. Express* 2016, 24, 17138-17148.
- [44] Gennaro, S. D.; Rahmani, M.; Giannini, V.; Aouani, H.; Sidiropoulos, T. P. H.; Navarro-Cia, M.; Maier, S. A.; Oulton, R. F. The Interplay of Symmetry and Scattering Phase in Second Harmonic Generation from Gold Nanoantennas. *Nano Lett.* 2016, 16, 5278- 5285.
- [45] Ray, P. C. Size and Shape Dependent Second Order Nonlinear Optical Properties of Nanomaterials and their Application in Biological and Chemical Sensing. *Chem. Rev.* 2010, 110, 5332-5365.
- [46] Butet, J.; Russier-Antoine, I.; Jonin, C.; Lascoux, N.; Benichou, E.; Brevet, P.-F. Sensing with Multipolar Second Harmonic Generation from Spherical Metallic Nanoparticles. *Nano Lett.* 2012, 12, 1697-1701.
- [47] Mesch, M.; Metzger, B.; Hentschel, M.; Giessen, H. Nonlinear Plasmonic Sensing. *Nano Lett.* 2016, 16, 3155-3159.
- [48] Willets, K. A.; Van Duyne, R. P. Localized Surface Plasmon Resonance Spectroscopy and Sensing. *Annu. Rev. Phys. Chem.* 2007, 58, 267-297.
- [49] Lal, S.; Link, S.; Halas, N. J. Nano-Optics from Sensing to Waveguiding. *Nat. Photonics* 2007, 1, 641-648.
- [50] Zeuner, F.; Muldarisnur, M.; Hildebrandt, A.; Förstner, J.; Zentgraf, T. Coupling Mediated Coherent Control of Localized Surface Plasmon Polaritons. *Nano Lett.* 2015, 15, 4189-4193.
- [51] Sartorello, G.; Olivier, N.; Zhang, J.; Yue, Y.; Gosztola, D. J.; Wiederrecht, G. P.; Wurtz, G.; Zayats, A. V. Ultrafast Optical Modulation of Second- and Third-Harmonic Generation from Cut- Disk-Based Metasurfaces. *ACS Photonics* 2016, 3, 1517-1522.

Supplementary informations

Experimental Details

Nanofabrication

Plasmonic gold nanorods are fabricated by standard electron-beam lithography followed by gold deposition and lift-off. An array of gold nanorods with width around 80 nm and lengths varying from 90 nm to 160 nm is fabricated. The deposited gold thickness is 50 nm.

Linear characterization

Dark field spectra are obtained using an optical excitation through an oil-immersed objective with high numerical apertures comprised in the 1.1 to 1.3 range. The spectra scattered at numerical apertures shorter than 0.9 are collected with an oil-immersed objective in such a way that nanorods are oil-immersed in a 1.5 optical index medium similarly to the non-linear experiments.

SHG measurement

A Ti:Sapphire laser producing 120fs pulses at 820nm is focused into a diffraction-limited 300 nm spot by a high numerical aperture oil-immersion objective (x60, NA 1.49). The nanorod antennas are positioned in the focal plane of the objective. The dispersion induced along the optical path is carefully pre-compensated with a 4-f zero dispersion line to ensure Fourier transform limited chirp-free focused optical pulses [1]. The SHG signal is collected with the same objective for the backward emission while a high numerical aperture oil-immersion objective (x100, NA 1.30) is used for collecting the upward emission. Then nanorods are immersed into oil, the refractive index of which matches the one of the glass substrate, in such a way that nanorods are immersed into a uniform dielectric environment. A multimode optical fiber of 500 μm core diameter allows injecting the collected signals into a spectrometer in order to separate the SHG signal to the multi photon luminescence signal.

SHG estimation

The nonlinear spectra show that the SHG is obtained simultaneously with a broad multiphoton photoluminescence (MPPL) signal. To extract the SHG contribution and estimate the error made in evaluating the SHG signal, we model the MPPL spectra either with a linear function or a 5th order polynomial contribution. The linear fit maximizes the estimation of the SHG while the 5th order tends to minimize it (see Figure S2).

The SHG signal plotted in Figure 2 is then obtained as the average of these two values and the error bar length equals the differences between these two values.

Numerical Methods

SIE method

The linear optical responses have been calculated using a surface integral formulation [2]. All the nanostructures are considered in homogeneous medium ($n = 1.5$) and the dielectric constants for gold are taken from experimental data at both the fundamental and second harmonic wavelengths [3]. For the SHG computations, the linear surface currents, which are expanded on Rao-Wilton-Glisson (RWG) basis functions [2, 4], are used for the evaluation of the fundamental electric fields just below the gold surfaces and then used for the calculation of the surface SH polarization. For the sake of simplicity, only the component $\chi_{surf,nnn}$ of the surface tensor, where n denotes the component normal to the surface, is considered. Recent experimental results shows that this term dominate the surface response of metallic nanoparticles [5]. Note that other contributions to the SH signal, namely the component $\chi_{surf,ttn}$ of the surface tensor (where t denotes the component tangential to the surface) and bulk contribution, are theoretically allowed but these contributions weakly contribute to the total SH wave [5, 6]. Furthermore, the present work is focused on the nonlinear plasmon rulers and the obtained results are valid whatever the nonlinear sources. The SH surface currents are obtained solving the SIE formulation taking into account the nonlinear polarization and enforcing the boundary conditions at the nanostructure surfaces [7]. As the linear surface currents, the SH surface currents are expanded on RWG basis functions. The expanding coefficients are found applying the method of moments with Galerkin's testing [2, 7]. A Poggio-Miller-Chang-Harrington-Wu-Tsai formulation is used to ensure accurate solutions even at resonant conditions [2, 4]. The SH electric field is then deduced from the SH surface currents using a two-term subtraction method for the evaluation of the Green functions [2].

Multipoles

Here, the Cartesian multipole tensors for the dipole and quadrupole moments are expressed using the VSHs coefficients. The dipolar vector is given by [8]:

$$\begin{pmatrix} p_x \\ p_y \\ p_z \end{pmatrix} = \begin{pmatrix} a_{1,1} - a_{1,-1} \\ i(a_{1,1} + a_{1,-1}) \\ -\sqrt{2}a_{1,0} \end{pmatrix}. \quad (3)$$

For the chosen configuration, the second harmonic dipole (due to retardation effects) is oriented along the y-axis. This means that, in the previous equation, p_y should be the

2.2. Revealing a Mode Interplay That Controls Second-Harmonic Radiation in Gold Nanoantennas

only nonvanishing quantity. Thus $a_{1,1} = a_{1,-1}$ and $a_{1,0} = 0$. The Cartesian quadrupolar matrix is given by [8]:

$$\begin{pmatrix} Q_{xx} & Q_{xy} & Q_{xz} \\ Q_{yx} & Q_{yy} & Q_{yz} \\ Q_{zx} & Q_{zy} & Q_{zz} \end{pmatrix} = \begin{pmatrix} i(a_{2,-2} + a_{2,2}) - i\frac{\sqrt{6}}{2}a_{2,0} & a_{2,-2} - a_{2,2} & i(a_{2,-1} - a_{2,1}) \\ a_{2,-2} - a_{2,2} & -i(a_{2,-2} + a_{2,2}) - i\frac{\sqrt{6}}{2}a_{2,0} & (a_{2,-1} + a_{2,1}) \\ i(a_{2,-1} - a_{2,1}) & (a_{2,-1} + a_{2,1}) & i\sqrt{6}a_{2,0} \end{pmatrix}, \quad (4)$$

with the traceless condition : $Q_{xx} + Q_{yy} + Q_{zz} = 0$. The SH quadrupole should be oriented along the Ox axis, so its symmetry implies to $Q_{xy} = Q_{xz} = Q_{yz} = 0$, leading to $a_{2,-2} = a_{2,2}$ and $a_{2,-1} = a_{2,1} = 0$. Furthermore, the Q_{xx} component should be indeed the strongest one, then the phase relation between $a_{2,\pm 2}$ and $a_{2,0}$ is $\arg(a_{2,\pm 2}) + \pi = \arg(a_{2,0})$ in order to have $Q_{xx} > Q_{yy}$. Finally, it is observed that in order to obtain a radiation pattern cylindrically symmetric around the x-axis, the relation between the quadrupolar coefficients is $|a_{2,0}| = \frac{2}{\sqrt{6}}|a_{2,-2}| = \frac{2}{\sqrt{6}}|a_{2,2}|$ with $\frac{2}{\sqrt{6}} \cong 0.82$.

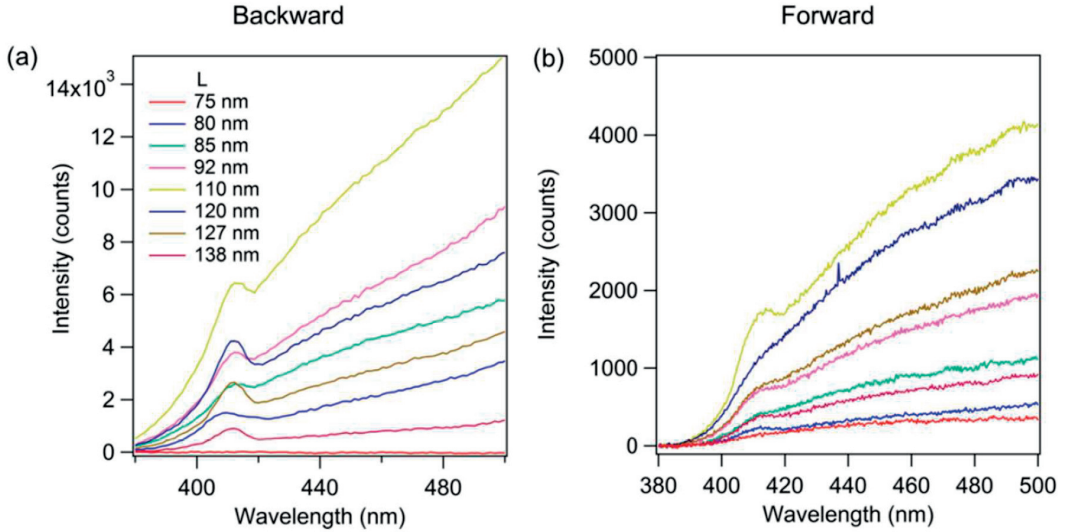


Figure S1 – Spectra collected in (a) the backward and (b) the forward directions for nanorod lengths ranging from 75 nm to 138 nm. The photoluminescence below the second harmonic peak is determined using a linear regression analysis. The second harmonic intensity is evaluated by integrating the remaining peak at 410 nm.

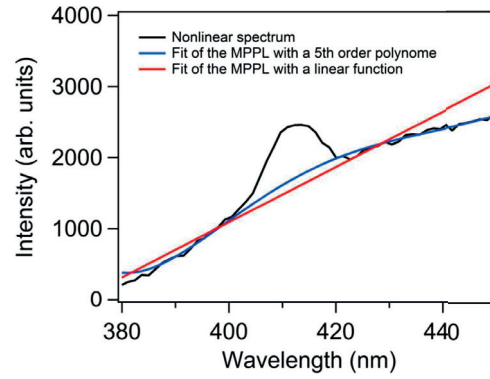


Figure S2 – Spectrum in the downward direction for the nanorod $L = 110$ nm. The two fits of the MPPL spectrum are shown. The SHG is then estimated by evaluating the area between the nonlinear spectrum and the related fit.

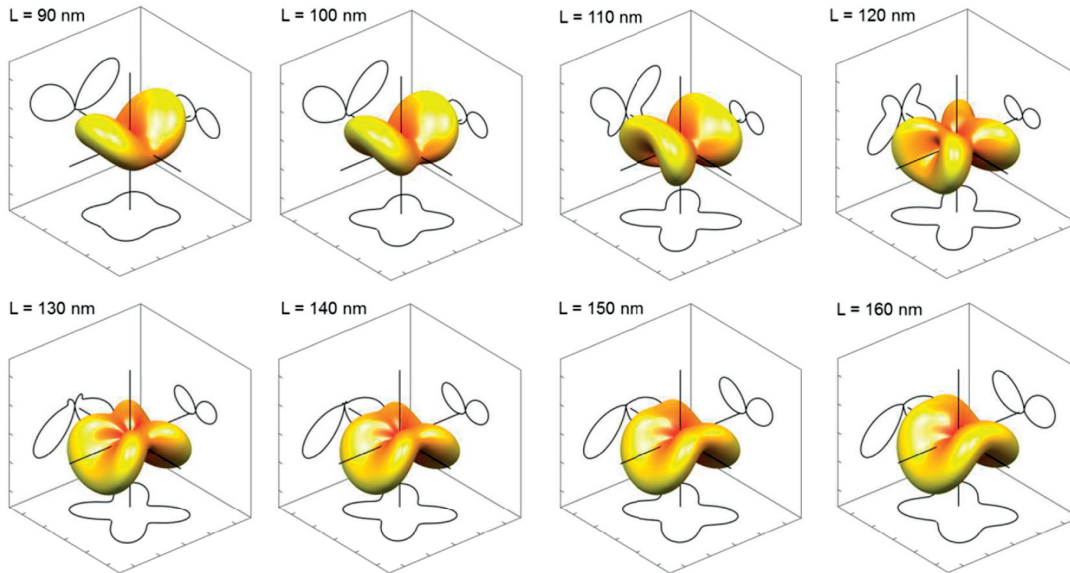


Figure S3 – Second harmonic emission patterns for nanorod lengths ranging from 90 nm to 160 nm. The fundamental wavelength is 800 nm.

2.2. Revealing a Mode Interplay That Controls Second-Harmonic Radiation in Gold Nanoantennas

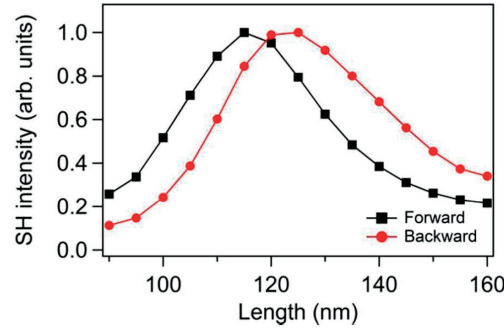


Figure S4 – Calculated forward (shown in black) and backward (shown in red) second harmonic intensities evaluated considering the numerical aperture of the objectives ($NA = 1.30$ for the collection in the forward direction and $NA = 1.49$ for the collection in the backward direction). The two curves are normalized to their respective maxima.

References

- [1]. Weiner, A. M. Ultrafast optical pulse shaping: A tutorial review. *Opt. Comm.* 2011, 284, 3669-3692.
- [2]. Kern, A. M.; Martin, O. J. F. Surface integral formulation for 3D simulation of plasmonic and high permittivity nanostructures. *J. Opt. Soc. Am. A* 2009, 26, 732-740.
- [3]. Johnson, P. B.; Christy, R. W. Optical Constants of the Noble Metals. *Phys. Rev. B* 1972, 6, 4370-4379.
- [4]. Mäkitalo, J.; Suuriniemi, S.; Kauranen, M. Boundary element method for surface nonlinear optics of nanoparticles. *Opt. Express* 2011, 19, 23386-23399.
- [5]. Bachelier, G.; Butet, J.; Russier-Antoine, I.; Jonin, C.; Benichou, E.; Brevet, P.-F. Origin of optical second-harmonic generation in spherical gold nanoparticles: Local surface and nonlocal bulk contributions. *Phys. Rev. B* 2010, 82, 235403.
- [6]. Wang, F. X.; Rodriguez, F. J.; Albers, W. M.; Ahorinta, R.; Sipe, J. E.; Kauranen, M. Surface and bulk contributions to the second-order nonlinear optical response of a gold film. *Phys. Rev. B* 2009, 80, 233402.
- [7]. Heinz, T. F. Second-order nonlinear optical effects at surfaces and interfaces, in *Nonlinear Surface Electromagnetic Phenomena*, H.-E. Ponath and G. I. Stegeman, Elsevier, Amsterdam, 1991.
- [8]. Mühlig, S.; Menzel, C.; Rockstuhl, C.; Lederer, F. Multipole Analysis of Meta-Atoms. *Metamaterials* 2011, 5, 64- 73

2.3 Dynamics of Second Harmonic Generation in a Plasmonic Silver Nanorod

Manuscript state: Published

Reference: Gabriel D. Bernasconi, Jérémy Butet, and Olivier J. F. Martin, "Dynamics of Second Harmonic Generation in a Plasmonic Silver Nanorod", *ACS Photonics* **5**, 3246-3254, (2018).

Publication date: May 18, 2018

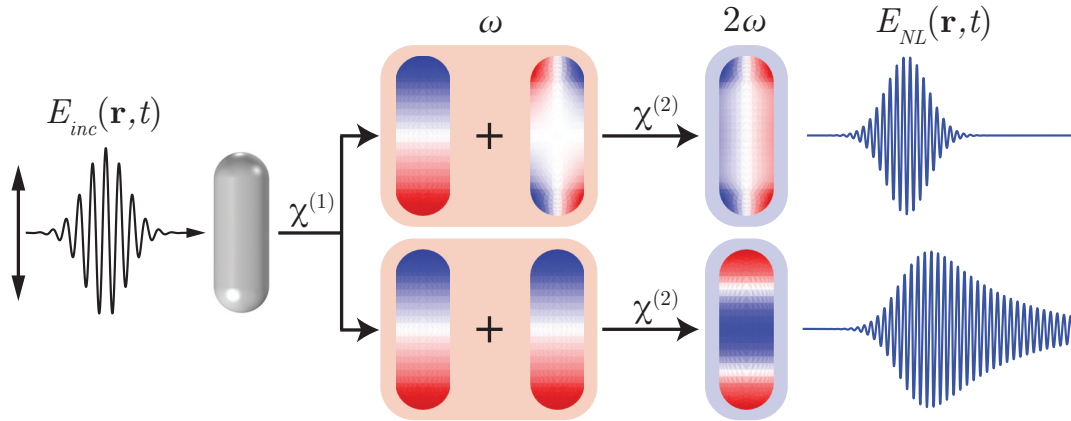
DOI: 10.1021/acsphotonics.8b00479

URL: <https://pubs.acs.org/doi/10.1021/acsphotonics.8b00479>

Adapted with permission from the above-mentioned reference.
Copyright (2018) American Chemical Society.

Author contributions

G. D. Bernasconi wrote the code, made the simulations and wrote the manuscript.



Dynamics of Second Harmonic Generation in a Plasmonic Silver Nanorod

Gabriel D. Bernasconi, J  r  my Butet, and Olivier J. F. Martin

Nanophotonics and Metrology Laboratory (NAM), Swiss Federal Institute of Technology Lausanne (EPFL), 1015, Lausanne, Switzerland.

Corresponding author: gabriel.bernasconi@epfl.ch

ABSTRACT: Second harmonic generation in plasmonic nanostructures is known to enable the observation of modes with vanishing dipolar moments, i.e. having small radiation losses and thus long lifetimes. With the aid of a full wave numerical method, we study the far field temporal dynamics of the linear and nonlinear responses of a silver nanorod driven by femtosecond pulses. The results show that the plasmons lifetime is observable in the decaying field oscillations surviving after the exciting pulse, for both processes, and fits with the damped harmonic oscillator model. In addition, using a detailed mode analysis, we find that the multipolar characteristic of the nonlinear radiation is strongly influenced by both the pulse central frequency and width. Implications for the accurate measurement of plasmon lifetime with the help of nonlinear optics are discussed, especially the need to carefully disentangle the linear and nonlinear plasmon dynamics.

Introduction

Plasmonic nanoparticles are well known for their ability to confine light below the diffraction limit [1,2]. As a consequence of this light concentration, the electromagnetic field intensity can be locally enhanced by several orders of magnitude [1-3]. These localized surface plasmon resonances are versatile and their properties depend upon several parameters, such as the nanostructure shape, material, surrounding medium as well as the coupling between nanoparticles [4,5]. Among the different parameters that describe a plasmon resonance, the lifetime is of prime importance, since it controls the field enhancement [6]. Furthermore, the coherent control of the field localization both in time and space is intrinsically linked to the plasmon lifetime [7-10]. However, the plasmon damping time is very short (10 fs and below) and is thus difficult to measure experimentally [11,12].

Recently, time-resolved photoemission electron microscopy has emerged as a useful approach for studying plasmon dynamics, allowing the detection of the electron oscillations at the nanoscale [13-15]. In this context, optical techniques used for the characterization

of ultrashort laser pulses have been extended for the investigation of the ultrafast response of plasmonic systems [16-18], including nonlinear effects [19]. These optical measurements are based on interferometry and rely on the evaluation of the autocorrelation function. This is generally performed by recording the nonlinear light conversion, either second harmonic generation (SHG) [16-18] or third harmonic generation (THG) [20,21], as a function of the time delay between the light traveling through the two branches of an interferometer. A broadening of the autocorrelation function, in comparison with a non-resonant reference (as a BBO crystal for example) is indeed caused by the field enhancement induced by the free electron collective oscillations.

During the last few years, a particular attention has been devoted to the SHG from plasmonic nanostructures [22,23] and SHG from plasmonic nanostructures with various shapes and properties have been reported [24,30]. A key recent advance in this field has been the design of double resonant nanostructures to boost the nonlinear optical conversion at the nanoscale [31,35]. These results emphasize the importance of the plasmonic modes at both the fundamental and second harmonic (SH) frequencies in the overall nonlinear optical conversion process. To investigate the relation between the modes at the excitation and emission wavelengths in detail, it was recently proposed to combine eigenmodes analysis with the evaluation of the SHG [36-38]. However, the distinct plasmon dynamics at the fundamental and SH frequencies have not been addressed so far, despite important implications for the coherent control of nonlinear radiation, as well as for the accurate measurement of the plasmon lifetime using nonlinear optical processes.

In this article, we study numerically the second order nonlinear response of a silver nanorod driven by femtosecond pulses under planewave illumination. We use a frequency domain surface integral equation (SIE) method to compute the linear and nonlinear fields as well as the eigenmodes of the silver nanorod. We show that single eigenmode dynamics behaves like a damped harmonic oscillator [12], in both the linear and nonlinear regimes. A multipolar analysis of the time-dependent far-field intensity for different pulse central frequencies and widths is also conducted, revealing the importance of the modal structure to interpret the radiated signals at the SH wavelength.

Theory

Numerical simulations are made using a frequency domain full wave method, namely the surface integral equation [39]. Only the surface of the nanorod is discretized with triangular elements and the scattering problem is solved by enforcing the boundary conditions on the fields at the nanostructure surface. Harmonic oscillations of the form $e^{-i\omega t}$ are assumed throughout the manuscript, with $i = \sqrt{-1}$. The angular frequency ω has $\text{rad}\cdot\text{s}^{-1}$ units, but we use electron-Volt (eV) to express it, i.e. $\omega = h\nu/q_0$ with ν the frequency in Hz, h Planck's constant and q_0 the elementary charge.

2.3. Dynamics of Second Harmonic Generation in a Plasmonic Silver Nanorod

A temporal signal with a finite duration is necessarily composed of more than one frequency and, the second order nonlinearity will lead to sum-frequency generation (SFG) in addition to SHG [40]. Neglecting optical rectification ($\omega_m - \omega_m$) and difference-frequency generation ($\omega_m - \omega_n$), the second order nonlinear polarization $P^{(2)}(t)$ due to the complex harmonic fields $E_1(t)$ and $E_2(t)$ of the form $E_m(t) = E_m(\omega_m)e^{-i\omega_m t}$ is [40]

$$P^{(2)}(t) = P_{2\omega_1}e^{-i2\omega_1 t} + P_{2\omega_2}e^{-i2\omega_2 t} + P_{\omega_1+\omega_2}e^{-i(\omega_1+\omega_2)t}, \quad (1)$$

with $P_{2\omega_1} = \epsilon_0\chi^{(2)}E_1^2$, $P_{2\omega_2} = \epsilon_0\chi^{(2)}E_2^2$ and $P_{\omega_1+\omega_2} = 2\epsilon_0\chi^{(2)}E_1E_2$. The first two terms in Eq. (1) correspond to SHG and the last one to SFG.

The second order nonlinearity is assumed to come uniquely from the surface of the nanoparticle where the centrosymmetry of the silver crystal is effectively broken. Furthermore, we consider only the $\chi_{\perp\perp\perp}^{(2)}$ component of the second order susceptibility tensor [41-43], the subscript \perp referring to the component normal to the surface. In the following, the method described in Refs. [44,45] to compute SHG is modified to also compute the nonlinear polarization due to SFG. We consider that the frequency range of interest is far from any electronic resonances in silver and that the second order process is parametric, thus leading to a $\chi_{\perp\perp\perp}^{(2)}$ that is real and frequency independent [40]. Furthermore, because no comparison is made between the relative amplitude of the linear and nonlinear fields, the value of the nonlinear susceptibility relatively to the linear susceptibility is not relevant and we set $\chi_{\perp\perp\perp}^{(2)} = 1$ without loss of generality. Additionally, we make the undepleted pump approximation and neglect the energy transfer of second-order waves back to fundamental waves.

The SFG computation can be schematized in 4 steps in the time domain, as shown in Fig. 1. First the incoming pulse E_{inc} excites the system and the resulting linear response E_L is computed. This linear response is then used to create the nonlinear sources P_{NL} at the surface, through the nonlinear susceptibility $\chi_{\perp\perp\perp}^{(2)}$. Those nonlinear sources in turn excite the system at the nonlinear frequencies to give the nonlinear fields E_{NL} . Throughout the manuscript P_{NL} is referred to as the nonlinear excitation; the color red is used for spectra at the excitation wavelength, while blue is used for the nonlinear response of the system.

In the small particle limit, the two main contributions to SHG are expected to be due to electric quadrupolar and dipolar modes, noted E_2 and E_1 , the latter being allowed by retardation effects [46]. Using the standard excitation-radiation schematic notation [47], these processes are written $E_1 + E_1 \rightarrow E_2$ and $E_1 + E_2 \rightarrow E_1$, where the symbols on the left and right refer to the nature of the modes respectively at the fundamental and nonlinear stages. The exact nature of the nanorod modes, transverse or longitudinal, has also to be detailed here. The nonlinear quadrupolar emission comes from the interaction of two dipoles, whereas the dipolar nonlinear emission comes from the interaction of a dipole and a quadrupole, both at the fundamental stage.

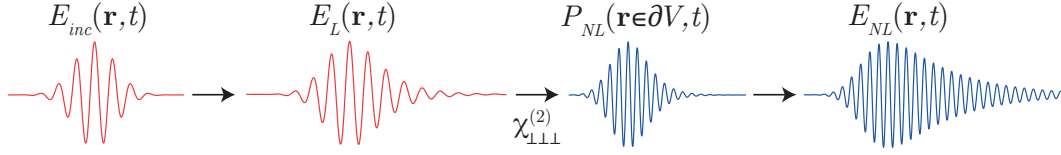


Figure 1 – Schematized computation of the SFG temporal signals. The incoming pulse $E_{inc}(\mathbf{r}, t)$ excites the structure and generates the linear response $E_L(\mathbf{r}, t)$. The linear response is used to obtain the nonlinear surface polarization $P_{NL}(\mathbf{r} \in \partial V, t)$ at the nanostructure boundary ∂V . Finally, these nonlinear sources are used to compute the scattered nonlinear field $E_{NL}(\mathbf{r}, t)$. This sketch illustrates the SFG process in time domain, although each computation step is performed in the frequency domain (see text).

Ohmic and radiative losses are both present in plasmonic systems, thus the plasmons oscillations are damped over time and each eigenmode is characterized by a complex eigenfrequency $\omega_c = \omega_r + i\omega_i$. If no excitation is present, any quantity A associated with one eigenmode (field, charge, current...) evolves according to the damped harmonic oscillator equation. Indeed, since the computations are done in the frequency domain, the temporal evolution is of the form $A(t) \propto \text{Re}\{e^{-i\omega t}\}$. Replacing ω by ω_c leads to

$$A(t) \propto \cos(\omega_r t) e^{\omega_i t}, \quad (2)$$

with $\omega_i < 0$, as required for having a decaying amplitude. An example of the response of a damped harmonic oscillator to a Gaussian pulse is shown in the supplementary information, Fig. (S1). Notably, there is a delay between the maximum of the driving pulse and the maximum of the response. Indeed, because of causality, the impulse response of a damped harmonic system vanishes for $t < 0$ and is thus asymmetric with respect to $t = 0$. The maximum of the response that is given by the convolution of the impulse response and the excitation, can then only occur at a time larger than the incoming pulse maxima. Additionally, as the exciting pulse becomes longer this delay increases, due to the fact that the system has more time to build up its response. As shown in Fig. (S2), this delay also increases as the central frequency of the pulse becomes close to the resonant frequency ω_r of the oscillator, and increases with the pulse temporal width Δt . This effect will be apparent in the subsequent analysis of the dynamical response of the silver nanorod.

The eigenmodes are obtained by using complex frequency excitation to find poles of the nanostructure response [48] and then verified to be eigenvectors of the SIE matrix [37]. An analytical continuation of the permittivity function in the complex plane is needed for the eigenmode computation, thus a Drude model is used to find the eigenmode. The model is fitted to the experimental values of Ref. [49] in the range $1.5 < \omega < 3$ eV. The parameters of the model are $\omega_p = 9.3$ eV, $\gamma = 0.03$ eV and $\epsilon_\infty = 4.3$, with ω_p the plasma frequency, γ the damping constant and ϵ_∞ the permittivity for $\omega \rightarrow \infty$. The background is assumed to be water, with refractive index $n_{bg} = 1.33$, i.e. $\epsilon_{bg} = 1.77$. This

2.3. Dynamics of Second Harmonic Generation in a Plasmonic Silver Nanorod

choice is made to render our result comparable to possible experimental findings, where nanoparticles are usually suspended in water or deposited on a substrate. The effective background permittivity of the latter medium depends on its composition but is indeed closer to that of water than vacuum.

For the femtosecond pulse, we consider a Gaussian pulse envelope $S(\omega)$ in the frequency domain, with width $\Delta\omega$ and centered at ω_0 ,

$$S(\omega) = e^{-\frac{(\omega-\omega_0)^2}{2\Delta\omega^2}}. \quad (3)$$

The corresponding temporal signal is also a Gaussian with width $\Delta t = 2\pi/\Delta\omega$ and the full width at half maximum is given by $\text{FWHM} = 2\sqrt{2\ln(2)}\Delta t \approx 2.35\Delta t$. The total energy of the pulse is given by $\int |S(\omega)|^2 \propto \Delta\omega$, so that it scales linearly with the width of the pulse, both in frequency and time domains. The construction of the temporal signal from the frequency domain computation is made using a Fourier transform as detailed in the Method section.

Results

In this section, we present the dynamic of the linear and second order nonlinear responses of a single silver nanorod of total length 120 nm and diameter 40 nm with hemispherical ends, Fig. 2(a).

We consider that the pulse excitation is built from planewaves with electric field polarization and propagation vectors respectively parallel and normal to the nanorod axis Oz and use the experimental values of Ref. [49] for the silver permittivity.

Harmonic response and eigenmodes

The scattering spectrum (electric field intensity integrated over the sphere) of the silver nanorod for monochromatic planewaves incident normally to the nanorod axis is shown in Fig. 2(b), as well as the corresponding SH spectrum. In the linear spectrum, a strong peak at ≈ 1.7 eV is observed due to the longitudinal dipolar mode (LD). Two other features between 3.0 and 3.5 eV also appear, due to higher order modes with a non-vanishing dipolar moment along Oz . The SH spectrum reveals a first small peak at 2.80 eV corresponding to the longitudinal quadrupole resonance (LQ), and one strong resonance at 3.5 eV. This SHG maximum is mainly due to the dipolar resonance linearly excited at 1.74 eV but is also expected to benefit from the transverse dipolar (TD) mode and higher order modes at the SH frequency. Indeed, since the real part of the permittivity becomes positive at $\omega \approx 3.8$ eV, all the plasmonic modes will have resonant frequencies below 3.8 eV. From Fig. 2(b), it is thus expected that some high order modes participate to the SHG scattering due to the fact that the nonlinear sources P_{NL} are

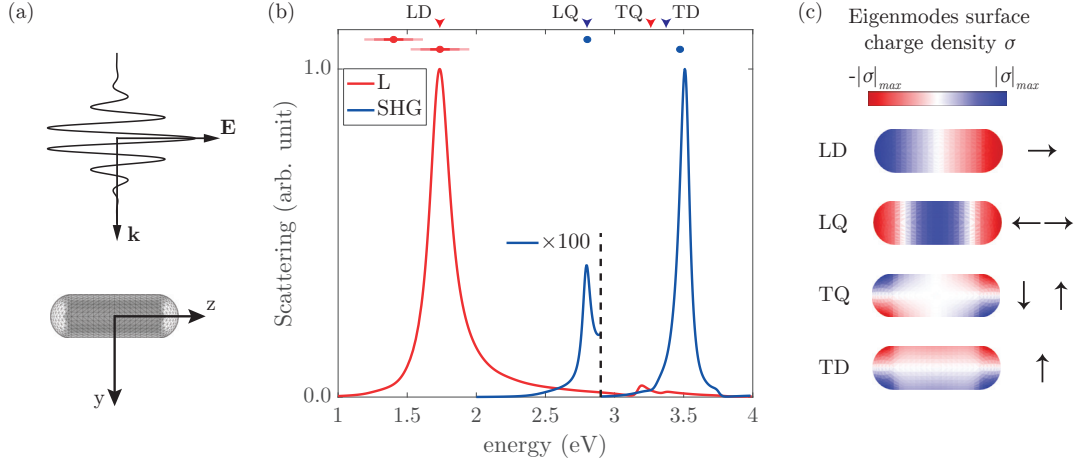


Figure 2 – (a) Sketch of the excitation configuration. (b) Planewave scattering spectrum, linear monochromatic response (red curve) and corresponding SHG (blue curve). The SHG on the left of the vertical dashed line is multiplied by a factor 100 to highlight the resonance of the LQ mode. The red dots and horizontal lines respectively indicate the central energies ω_0 and width $2\Delta\omega_0$ at the fundamental stage for the pulses used in the manuscript. The blue dots give the central frequency of the corresponding nonlinear excitation P_{NL} without taking into account the influence of the linear response, i.e. $\omega_0^{NL} = 2\omega_0$. The position of the eigenmodes presented in (c) are shown on the top abscissa. (c) Surface charge distributions σ of the four eigenmodes discussed in the manuscript. LD stands for longitudinal dipole, LQ for longitudinal quadrupole, TD for transverse dipole and TQ for transverse quadrupole, see Table I. Black arrows represent the local dipolar moment orientations.

spectrally near 3.5 eV. A multipolar decomposition of the far-field [50] is also conducted for the SHG signal, Fig. (S3), and reveals only dipolar and quadrupolar emissions. The small peak at 2.8 eV is composed of 85% of quadrupolar emission, whereas the emission peak at 3.5 eV is 98% dipolar. As stated in Section 2.3, the SHG emission arises mainly from two excitation channels, coming from the modes presented in (2)(c). The first one is the interaction of the LD mode with itself to excite the LQ mode at the SH frequency. Using the previously introduced notation and specifying the precise nature of the modes, this excitation channel is $E_1^{LD} + E_1^{LD} \rightarrow E_2^{LQ}$. Higher order modes with even charge distribution parity along the Oz axis, like the LQ mode, can be excited through identical processes involving higher order modes at the linear stage. The other excitation channel allows a dipolar emission at the SH frequency through the interaction of the LD and the transverse quadrupolar (TQ) mode, the latter being excited by retardation effects, i.e. phase difference of the driving field across the nanorod diameter in the Oy direction. This excitation channel is $E_1^{LD} + E_2^{TQ} \rightarrow E_1^{TD}$. As in the case of the quadrupolar nonlinear emission, other higher order modes having the transverse characteristic, i.e. odd charge distributions along Oy , can participate to the dipolar nonlinear radiation through similar processes, since their symmetry does not forbid it. Figure 2(c) shows the four

2.3. Dynamics of Second Harmonic Generation in a Plasmonic Silver Nanorod

eigenmodes discussed above, where the arrows indicate the dipolar moments orientations. Their complex eigenfrequencies, as well as their plasmon lifetimes and associated quality factors, are given in Table 1. The fit of the Drude model used to obtain the eigenmodes is optimized up to 3 eV, the parameters for the TQ and TD modes are thus expected to slightly deviate from those effectively existing with the experimental permittivity data. Since the real and imaginary parts of the permittivity are both underestimated around 3 eV in our case, the real part of the eigenfrequency would be smaller and the imaginary part larger i.e. the experimental mode is likely to be red-shifted and more lossy.

Table 1 – Eigenmodes eigenfrequencies, lifetimes given by $\tau = \hbar/(2\pi q_0|\omega_i|)$ and quality factors $Q = \omega_r/|\omega_i|$. LD stands for longitudinal dipole, LQ for longitudinal quadrupole, TQ for transverse quadrupole and TD for transverse dipole. Arrows indicate the local dipolar moments as in Fig. 2(c).

		ω_r (eV)	ω_i (eV)	τ (fs)	Q
LD	\rightarrow	1.74	-0.0936	7.03	18.5
LQ	$\leftarrow\rightarrow$	2.80	-0.0244	27.0	115
TQ	$\downarrow \uparrow$	3.27	-0.0418	15.7	78.3
TD	\uparrow	3.38	-0.168	3.93	20.1

Pulse excitation, linear regime

We now consider a pulse, centered at $t = 0$, with a Gaussian frequency envelope with $\omega_0 = \text{Re}\{\omega_{LD}\} = 1.74$ eV, i.e. centered at the longitudinal dipolar resonance, and width $\Delta\omega = 0.071$ eV leading to a Gaussian pulse with FWHM=22 fs. Figure 4 shows the spectrum and temporal dynamics of the E_z component of the electric field, oriented along the nanorod axis, at a distance $R = 10 \mu\text{m}$ in the forward direction ($x = 0, y = R, z = 0$). Even though the pulse spectral width is smaller than the width of the harmonic response $E_h(\omega)$, the response $E(\omega) = E_h(\omega)S(\omega)$ is indeed narrower than the pulse, Fig. 4(a), and must thus correspond to a longer time signature. This is indeed what is observed in the temporal plots shown in Fig. 4(b). At all times, the field corresponding to the blue curve shows a $\pi/2$ phase shift with respect to the driving pulse (black curve), see zoomed-in plot Fig. 4(c,d), a typical behavior for a forced oscillator driven at its resonant frequency. At larger times $t \gtrsim 75$ fs, Fig. 4(d), when the amplitude of the excitation pulse becomes negligible, an exponential decay of the oscillating field amplitude is observed, as expected for a free damped harmonic oscillator. In order to confirm that the behavior observed at $t \gtrsim 75$ fs is due to the LD resonance, the field evolution given by Eq. (2) with the parameters of the LD mode given in Table 1 is superposed to the full wave computations, blue circles in Fig. 4(d). The excellent agreement between the full wave computation and the dynamics associated with the LD mode demonstrates that the latter plays the dominant role in the system; furthermore, this demonstrates how the knowledge of the modes supported by a system can be used to reconstruct its dynamics

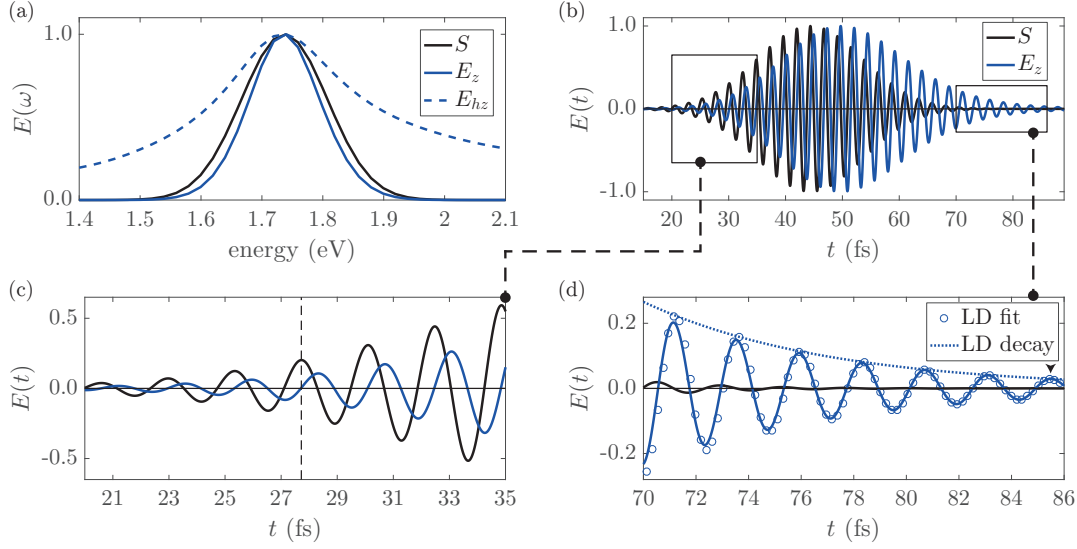


Figure 3 – Linear response of the E_z component at a distance of $10 \mu\text{m}$ in the forward (positive y) direction. (a) Spectra obtained with monochromatic planewave excitations (dashed blue curve), frequency envelope of the pulse centered at $\omega = 1.74 \text{ eV}$ with $\Delta\omega = 0.071 \text{ eV}$ (black curve) and the linear response driven by the pulse (blue curve). (b) Time domain electric field evolutions of the driving pulse (black line) and the linear response (blue curve). (c) Zoom on the forced regime. The vertical line to highlight the $\pi/2$ phase shift between the excitation and the response. (d) Zoom on the free harmonic motion and fit of the damped harmonic oscillator free response with the parameters of the longitudinal dipolar eigenmode. The black arrowhead indicates where the fit was made.

[12]. The exponential decay envelope is prolonged before $t \approx 78 \text{ fs}$ to clearly show the transition between forced and free regimes. Note that the maximum of the driving pulse indeed occurs at $t = n_{bg}R/c_0 = 44.36 \text{ fs}$, with $c_0 = 299,792,458 \text{ ms}^{-1}$, Fig. 4(b). In addition, it is apparent that the maximum of the field response is delayed relatively to the driving pulse maximum, another well-known feature of harmonic oscillators driven at their resonances, see Fig. (S1-S2).

Pulse excitation, nonlinear regime

The nonlinear response of the nanorod is now studied for a pulse with the same width as in Section 2.3 but centered at $\omega_0 = \text{Re}\{\omega_{LQ}/2\} = 1.4 \text{ eV}$, i.e. at half the LQ resonance. This is done to avoid the excitation of higher order modes at the SH frequencies and thus concentrate only on the LQ and TD modes radiation which are expected to be the only contributions at the nonlinear frequencies around 2.8 eV in the small nanoparticle limit, see Fig. 2(b). The width of the pulse, $\Delta\omega = 0.071 \text{ eV}$, further ensures that the contribution of the high order modes above ω_{TD} remains negligible. In Fig. 4 we show

2.3. Dynamics of Second Harmonic Generation in a Plasmonic Silver Nanorod

the E_y component of the electric field at a distance $R = 10 \mu\text{m}$ and at a $\pm 45^\circ$ angle in the Oyz plane as well as in the Oz direction.

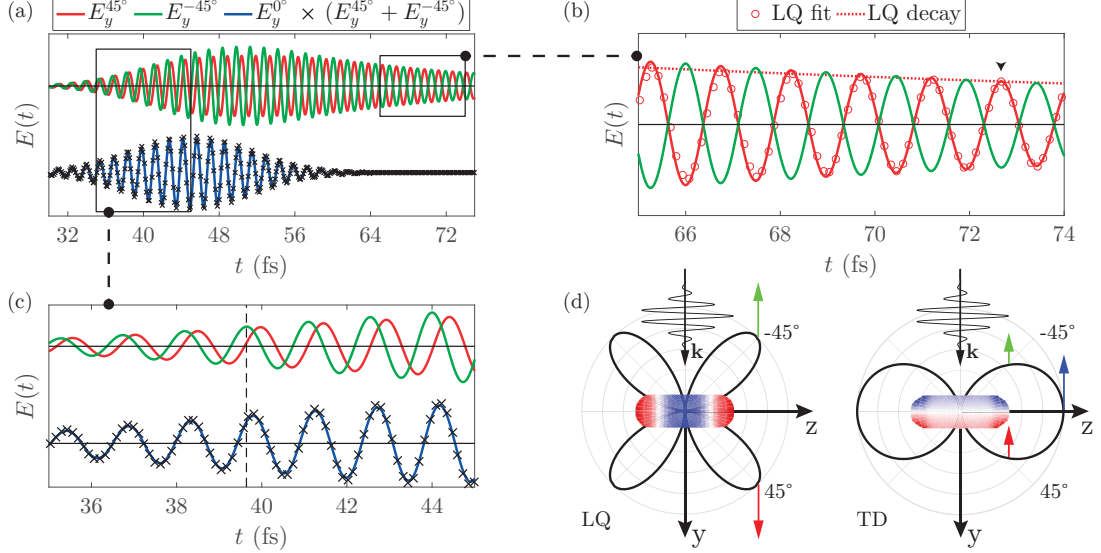


Figure 4 – Nonlinear response for a pulse of central frequency $\omega_0 = 1.4 \text{ eV}$ and width $\Delta\omega = 0.071 \text{ eV}$. (a) E_y component of the electric field at a distance of $10 \mu\text{m}$. Red, green and blue curves respectively show the field in the forward 45° ($z=y$), backward -45° ($z=-y$) and top 0° ($z=0$) directions. The black marker curve is the sum of the green and red curves. The blue and black marker curves are vertically shifted for clarity. (b,c) Details of the time evolution shown in (a). The vertical dashed line in (c) is here to highlight the phase difference between the fields. The arrowhead in (b) indicates the time where the fit with the LQ mode was made. (d) Radiation patterns of the LQ and TD modes in the Oyz plane and corresponding qualitative amplitudes of the E_y field component at the positions where the fields of panels (a-c) are evaluated.

The electric fields taken at the $\pm 45^\circ$ angles exhibit a clear resonant dynamic with a long lifetime due to the LQ mode, see Table 1. In the Oz direction (0°), the LQ mode cannot radiate and the field observed (blue curve) is thus solely due to the TD mode. Since the TD mode is driven below its resonant frequency and is relatively lossy, $\tau_{TD} = 3.93 \text{ fs}$, only its forced behavior is observed and the temporal response is symmetric with respect to its center. To understand why the TD mode shows a response as strong as the LQ mode even though its resonant frequency is relatively far from $2 \times 1.4 = 2.8 \text{ eV}$, one needs to consider a few points. First, the TD mode is spectrally broad due its large eigenfrequency imaginary part ($\text{Im}\{\omega_{TD}\} = -0.168 \text{ eV}$), and since it is a dipolar resonance it is better coupled to the far-field than the LQ. Indeed, the multipole decomposition of the SHG spectrum gives a 15% contribution of the dipole component for a harmonic planewave excitation at 2.8 eV see Fig. (S3). Second, even though the central linear frequency is fixed at 1.4 eV , the LD resonance is effectively blue-shifting the linear response maximum, making the maximum of the nonlinear excitation closer to the TD eigenfrequency. Finally, the linear pulse width is 0.071 eV , so that the effective spectral width of the nonlinear

excitation P_{NL} can be expected to be roughly twice this value, making the spectral overlap between P_{NL} and the TD even greater.

We observe in Fig. (4)(c) that the electric fields in the forward (45° , red line) and backward (-45° , green line) directions have slightly different amplitudes for $t \lesssim 60$ fs. The difference in the field amplitudes in the $\pm 45^\circ$ directions for $t \lesssim 60$ fs is caused by the interference between the LQ and TD modes, as already reported in the continuous regime in Refs. [51,52]. Indeed, the electric field orientation associated with the quadrupolar and dipolar emissions at the two observation points is different, Fig. 4(d), and interferes constructively in the backward direction and destructively in the forward direction. Let us note that the constructive/ destructive interferences can generally happen in either direction depending on the relative spectral position of the excitation, the LQ, and the TD modes [52]. To further study this phenomenon, the sum of the two responses in the $\pm 45^\circ$ directions (red+green curves) is computed and it is observed that the result, black markers in Fig. 4(a,c), fits almost perfectly with the transverse dipolar response taken in the Oz direction (blue curve). The extremely small discrepancy is fortuitous: it is due to the difference in amplitude of the dipolar and quadrupolar radiations in the $\pm 45^\circ$ and Oz direction as well as to the relative amplitude of each mode. Let us note that a similar interference effect between the TD and LQ modes also exists for the E_z component of the fields (data not shown). The temporal overlap of the sum of the two fields in the $\pm 45^\circ$ and Oz directions, respectively due to the LQ and TD modes, thus confirms that the TD resonance is indeed the source of the observed amplitude difference in the $\pm 45^\circ$ directions.

For times $t \gtrsim 65$ fs the short-lived TD mode vanishes with the exciting pulse so the interference process disappears and the two fields in the $\pm 45^\circ$ directions retrieve the same amplitude, Fig. (4)(b). As for the linear response in Section 2.3, at $t \gtrsim 65$ fs, the behavior of a free damped harmonic oscillator is observed. The parameters of the LQ mode are used to plot Eq. (2) (red circle), which fit with great accuracy the computed field evolution in the $+45^\circ$, the same agreement being expected in the backward -45° directions due to the symmetry of the geometry. We additionally notice that during the time where the interference between the two modes occurs, Fig. (4)(c), the two fields at $\pm 45^\circ$ are not perfectly out of phase as they should be if only the LQ mode was excited Fig. (4)(d). This is because the TD and LD modes do not have the same phase with respect to the nonlinear excitation and thus to each other. The interference created by the TD mode thus modifies the relative phase shift between the fields in the $\pm 45^\circ$ directions. When the dipolar mode vanishes, the two fields retrieve their relative π phase shift (4)(b), as expected for a purely quadrupolar radiation. Finally, we observe again a shift between the excitation maximum and the response of the quadrupolar mode. As was the case in the linear regime, we see that the eigenmodes are of prime importance in the study of the spectral and dynamical behavior of the SH response of plasmonic nanoparticles.

Multipolar analysis

Finally, we study the nonlinear temporal response of the nanorod for various pulse parameters. Six different pulses at two different central frequencies and with three different widths are considered, viz. $\omega_0 = 1.4$ and 1.74 eV, $\Delta\omega = 0.071, 0.14$ and 0.21 eV. The three spectral widths correspond respectively to temporal FWHM of 22, 15 and 7 fs for the field amplitude, the effective FWHM for the corresponding intensity is given by $\text{FWHM}/\sqrt{2}$. The central frequencies and widths of the pulses at the fundamental stage are shown in Fig. 2(b). The corresponding nonlinear central frequencies, obtained by multiplying by two each linear one are also shown as blue dots. Note however that the real excitation of the nonlinear process comes from the linear response, and will thus not necessarily have a maximum at $2\omega_0$ nor a Gaussian shape due to the resonant character of the linear response. For each case, we project the time-dependent linear and nonlinear far-fields onto the vector spherical harmonics to decompose the radiation into multipole moments [50]. The results are shown in Fig. 5, where the panels (a-f) show the linear and nonlinear scattered intensities and the panels (g-l) the dipolar and quadrupolar components of the nonlinear scattered intensity. Other multipolar moments are found to be negligible and the linear response is purely dipolar. To clarify the plot, the linear intensity is shown only at the peak values of the oscillations, indicated by red markers, since the dynamics does not involve any additional effect than the ones presented in Section 2.3. Additionally, the intensity is integrated over the range $25 < t < 120$ fs for both linear and nonlinear signals and normalized to the weakest case, which is $\omega_0 = 1.40$ eV and $\Delta\omega = 0.071$ eV. The corresponding data are shown in each panel, thus providing the total energy of the radiated fields. Every curve in Fig. 5 (a-f) is normalized to the maximum intensity of the corresponding curve for the case $\omega_0 = 1.4$ eV and $\Delta\omega = 0.071$ eV which gives the weaker linear and nonlinear peak signals. Finally, the exciting pulses are all normalized to have unit energy so that the comparison of the peak and integrated intensities reflect the intrinsic efficiency of the linear and nonlinear signal generations. We recall Parseval's theorem that states that the energy of a signal in the frequency domain is proportional to the energy of the temporal signal, $\int |E(\omega)|^2 d\omega \propto \int |E(t)|^2 dt$, the proportionality constant being dictated by the definition of the Fourier transform [53]. Thus the integrated intensities in time domain can be explained by analyzing the corresponding spectra. Concerning the linear dynamics, every case shows a fully dipolar response (data not shown), as expected from the excitation of the LD mode, see Fig. 2. For the pulse centered at 1.4 eV, Fig. 5 (a-c), it appears that the peak and the integrated intensity increase as the pulse shortens. Indeed, the shorter the pulse, the broader the spectrum, and since the central frequency is here below the LD peak, a broadening means a better overlap with the LD resonance at 1.74 eV and thus a stronger signal. This better overlap with the resonance also leads to a slight increase in the delay between the driving pulse and the linear response, see the black and red arrowheads respectively. On the other hand, when the pulse central frequency is tuned to the LD resonance at 1.74 eV, the shorter pulses lead to a weaker integrated signal, compare Fig. 5 (d-f), and it

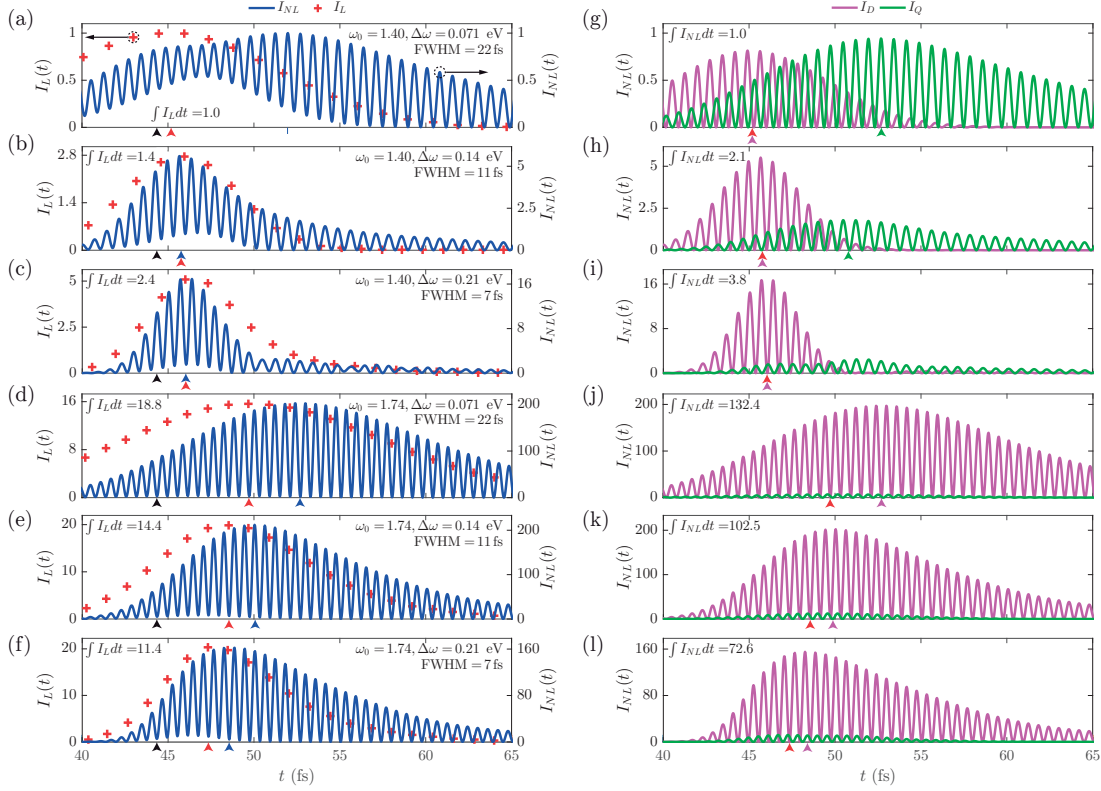


Figure 5 – Multipolar analysis of the linear and nonlinear radiations. Six different pulses are considered, at central energies ω_0 : 1.4 and 1.74 eV, and widths $\Delta\omega$: 0.071, 0.14 and 0.28 eV. (a-f) Linear (red markers, value on the left vertical axis) and nonlinear (blue curve, value on the right vertical axis) scattered intensity. The pulse parameters ($\omega_0, \Delta\omega$) are indicated in the top right corner of each plot. For clarity the linear response is taken only at the maxima of $I_L(t)$. Each linear, respectively nonlinear curve, is normalized to the corresponding curve in (a). We observe that both the linear and nonlinear peak intensities are minimal for the pulse parameters used in panel (a). The linear intensity integrated in the range $25 \text{ fs} < t < 120 \text{ fs}$ is indicated in the plots and normalized to the one in (a). The black arrowheads on the horizontal axis indicate the center of the exciting pulse at 44.36 fs whereas the red and blue ones indicate the maximum of the linear and nonlinear responses. (g-h) Corresponding multipolar decompositions of the nonlinear radiations. Multipoles other than electric dipolar and quadrupolar components are found to have negligible contributions. The intensity integrated in the range $25 \text{ fs} < t < 120 \text{ fs}$ is indicated in the top left corner of each plot and normalized to the one in (g). The colored arrowheads on the horizontal axis indicate maximum of the dipolar and quadrupolar components when possible. Note that the indicated FWHM is given for the field, not the intensity.

2.3. Dynamics of Second Harmonic Generation in a Plasmonic Silver Nanorod

additionally appears that the peak intensity slightly increases for shorter pulses. Keeping in mind that each excitation pulse is normalized to have unit energy, the broadening of the spectrum, which is linked to the reduction of the pulse duration, leads to a weaker maximum amplitude of the pulse spectrum that is centered at the LD resonance. This could explain the decrease in integrated intensity, but not the slight increase in peak intensity for shorter pulses. We first recall that the maximum of the temporal signal can be linked to the integrated signal because $E(t = 0) \propto \int E(\omega) d\omega$, which is indeed different from the energy $\int |E(\omega)|^2 d\omega$. To explain the increase in peak intensity that occurs in parallel to the decrease in integrated intensity, we multiplied three Gaussians (with the width of the pulses used in this section and having unit energy) with a damped harmonic oscillator spectral line-shape in order to simulate the linear response $E(\omega)$ of the system. We then compared the results of $\int E(\omega) d\omega$ and $\int |E(\omega)|^2 d\omega$ and found a good qualitative agreement with the previous results, namely an decrease of the energy and a slight increase of the integrated signal (data not shown). Finally, we observe that for the pulse centered at 1.74 eV, Fig. 5(d-f), the linear response delay is the largest, and it decreases for shorter pulses as expect for a pulse that shortens, see Fig. (S2). The nonlinear field dynamics is first studied for femtosecond pulses centered at 1.4 eV, Fig. 5 (a-c, g-i). In panels (a-c), the nonlinear intensity oscillations do not decrease down to zero at short times. This effect is easily understood by looking at the multipolar decomposition, panels (g-i). It appears that the dipolar and quadrupolar components, mainly due to the TD and LQ modes respectively, are out of phase, as explained in Section 2.3. When the driving pulse vanishes, only the long-lived quadrupole mode remains and the scattered intensity oscillations can indeed vanish periodically. Indeed, the TD mode has a lifetime of 3.93 fs and thus cannot outlive the exciting pulse. As the pulse shortens and its spectrum broadens, the overlap between the nonlinear excitation spectrum and the TD mode increases. Thus, it appears that the short-lived dipolar component due to the TD mode becomes predominant during the excitation and that the quadrupolar component takes the lead afterward, see panels (g-i). The strong intensity difference between the dipolar and quadrupolar components is due to the fact that dipolar modes are intrinsically more efficient to radiate in the far field, and that, as shown in Fig. (S3), there is a non-negligible dipolar contribution to the SHG around 2.8 eV. Notice the different vertical axis scales that indicate that the quadrupolar component still increases form panels (g) to (i), the maxima of the I_Q curve being respectively 1, 1.8 and 2.5. In panel (i), at around 48 fs, one can also observe a small dip in the quadrupolar component envelope, caused by the interference between the LQ mode and higher order modes having a quadrupolar far-field response. Additionally, the overall nonlinear response is also stronger both in peak and integrated intensity for shorter pulses, due to the corresponding stronger linear response. When the central pulse energy is resonant with the LD mode, $\omega_0 = 1.74$ eV, the nonlinear signal is mainly dipolar Fig. 5 (d-f, j-l). Indeed, the nonlinear excitation is now centered around $2 \times 1.74 = 3.48$ eV, close to the TD mode at 3.38 eV and far from the LQ mode. Nevertheless, a long-lived oscillation is observed for the two shortest pulses, panels (k-l). The decay observed is too slow to be attributed to the TD mode, and thus originates

from a higher order mode having a non-vanishing dipolar moment in the Oy direction. As discussed in Section 2.3, such high order modes are expected to have resonant frequencies around the nonlinear excitation P_{NL} in the present case, explaining further the strength of this dipolar component. This is also in agreement with the SHG spectrum shown in Fig. (S3), where the SHG response is mostly dipolar around the peak at 3.5 eV. The total energy of the signals follows the evolution of the linear response, i.e. a smaller integrated intensity is obtained for shorter pulses. Overall, the maximum peak and integrated intensities are indeed obtained when the pulse is centered at the longitudinal dipolar resonance mode for both the linear and nonlinear fields. The delayed-response behavior of a mode excited at resonance is also apparent in the nonlinear signals, keeping in mind that the source of the nonlinear signal is the linear response, that is itself delayed with respect to the exciting pulse. For the pulse centered at 1.4 eV, the nonlinear excitation P_{NL} is close to the LQ mode and thus the delay between the linear response and the quadrupolar component is large, and increases with the pulse duration. For the shortest pulse, panel (i), interferences with high order modes makes the measure of the delay not pertinent. On the other hand the nonlinear excitation is far from the TD mode, leading to a vanishing delay for the dipolar component. Concerning the pulse centered at 1.74 eV, the nonlinear excitation is now close to the TD mode and we observe a delay of the dipolar response that increases with the pulse duration as expected.

Conclusion

The dynamics of the linear and second order nonlinear fields scattered by a single silver nanorod under femtosecond pulse planewave illumination have been studied. The linear response was first presented to establish the method. It was shown that it is indeed possible to observe the dynamics of single eigenmodes that behaves like damped harmonic oscillators. Then the nonlinear scattered fields were studied, first in detail for the case when the longitudinal quadrupolar mode is resonant at the nonlinear frequency. It was observed that the transverse dipolar mode interfered with the quadrupolar mode during the time where the excitation pulse is still present, but that only the quadrupolar response remains afterward, due to its longer lifetime. Finally, a multipolar analysis of the scattered field was conducted for two different pulse center energies and three different widths. Different responses are observed depending upon the pulse width and center frequency, like a switch between quadrupolar and dipolar dominant emissions over time as well as changes in the peak intensity value or the total energy radiated. It appears that the modal structure of the nanorod is of high importance to correctly understand the temporal evolution of the nonlinear fields. These results provide a new insight into the linear and nonlinear dynamics of localized surface plasmons, as one could tailor the exciting pulse parameter to achieve a variety of dynamical responses. Furthermore, these results are important regarding the accurate measurement of plasmon lifetime with the help of nonlinear optics [16-18]. Indeed, to do so, one needs to carefully disentangle the

linear and nonlinear plasmon dynamics as discussed in this article.

Methods

To reconstruct a temporal signal from its frequency components, the following inverse Fourier transform is used:

$$E(t) = \mathcal{F}^{-1}\{E\}(t) = \int_{-\infty}^{\infty} E(\omega) e^{-i\omega t} d\omega. \quad (4)$$

The temporal signal $E(t)$ must be real, hence $E(-\omega) = E^*(\omega)$, where $*$ denotes the complex conjugate. Equation (4) then reduces to

$$E(t) = 2\text{Re} \left\{ \int_0^{\infty} E(\omega) e^{-i\omega t} d\omega \right\}. \quad (5)$$

A finite amount of frequencies ω_n is computed, and the above integral reduces to a sum. Consequentially $E(t)$ becomes T -periodic with $T = 2\pi/\delta\omega$, $\delta\omega$ being the constant frequency step between each considered frequency ω_n . To correctly retrieve the plasmon dynamics it is mandatory that the periodicity induced by the frequency sampling is sufficiently large compared to the largest plasmon lifetime. Plasmons are known to have lifetime of the order of fs, we choose $\delta\omega = 0.02$ eV leading to $T = 207$ fs.

To construct the linear and nonlinear temporal signals, the first step is to compute a set of N linear harmonic solutions $E_h(\omega_n)$ at equally spaced frequencies between ω_A and ω_B , that can then be used to form any signal $E(\omega)$ having a limited bandwidth $\omega_A \leq \omega \leq \omega_B$. $E_h(\omega_n)$ effectively acts as a transfer function, so that the response $E(\omega_n)$ of the nanorod to an excitation having the spectrum $S(\omega_n)$ is $E(\omega_n) = E_h(\omega_n)S(\omega_n)$, meaning that each frequency component $E_h(\omega_n)$ is weighted according to the function $S(\omega_n)$. One then has to make second order computation for each possible pair of frequencies (ω_m, ω_n) composing the femtosecond pulse, taking into account the different weights of each components

$$\begin{aligned} E(\omega_m + \omega_n) &= E(\omega_m)E(\omega_n) \\ &= E_h(\omega_m)S(\omega_m)E_h(\omega_n)S(\omega_n), \end{aligned} \quad (6)$$

and adding accordingly the pairs that give the same frequency. The total number of combination is N^2 with N SHG and $(N^2 - N)$ SFG combinations. Since the process (ω_m, ω_n) gives the same nonlinear response as (ω_n, ω_m) , only half of the SFG computations have to be performed. Thus the total number of required nonlinear computation is $N + (N^2 - N)/2 = (N^2 + N)/2$. The temporal responses, both linear and nonlinear are obtained using Eq. (5).

Acknowledgement

Funding from the Swiss National Science Foundation (project 200020_153662) and from the European Research Council (ERC-2015-AdG-695206 Nanofactory) is gratefully acknowledged.

References

- [1] Barnes, W. L.; Dereux, A.; Ebbesen, T. W. Surface plasmon subwavelength optics. *Nature* 2003, 424, 824.
- [2] Schuller, J. A.; Barnard, E. S.; Cai, W.; Jun, Y. C.; White, J. S.; Brongersma, M. L. Plasmonics for extreme light concentration and manipulation. *Nat. Mater.* 2010, 9, 193.
- [3] Kottmann, J. P.; Martin, O. J.; Smith, D. R.; Schultz, S. Dramatic localized electromagnetic enhancement in plasmon resonant nanowires. *Chem. Phys. Lett.* 2001, 341, 1-6.
- [4] Liz-Marzaán, L. M. Tailoring Surface Plasmons through the Morphology and Assembly of Metal Nanoparticles. *Langmuir* 2006, 22, 32-41.
- [5] Halas, N. J.; Lal, S.; Chang, W.-S.; Link, S.; Nordlander, P. Plasmons in Strongly Coupled Metallic Nanostructures. *Chem. Rev.* 2011, 111, 3913-3961.
- [6] Sönnichsen, C.; Franzl, T.; Wilk, T.; von Plessen, G.; Feldmann, J.; Wilson, O.; Mulvaney, P. Drastic Reduction of Plasmon Damping in Gold Nanorods. *Phys. Rev. Lett.* 2002, 88, 077402.
- [7] Stockman, M. I.; Faleev, S. V.; Bergman, D. J. Coherent Control of Femtosecond Energy Localization in Nanosystems. *Phys. Rev. Lett.* 2002, 88, 067402.
- [8] Aeschlimann, M.; Bauer, M.; Bayer, D.; Brixner, T.; García de Abajo, F. J.; Pfeiffer, W.; Rohmer, M.; Spindler, C.; Steeb, F. Adaptive subwavelength control of nano-optical fields. *Nature* 2007, 446, 301.
- [9] Lévêque, G.; Martin, O. J. F. Narrow-Band Multiresonant Plasmon Nanostructure for the Coherent Control of Light: An Optical Analog of the Xylophone. *Phys. Rev. Lett.* 2008, 100, 117402.
- [10] Accanto, N.; Nieder, J. B.; Piatkowski, L.; Castro-Lopez, M.; Pastorelli, F.; Brinks, D.; van Hulst, N. F. Phase control of femtosecond pulses on the nanoscale using second harmonic nanoparticles. *Light: Sci. Appl.* 2014, 3, e143.
- [11] Piatkowski, L.; Accanto, N.; van Hulst, N. F. Ultrafast Meets Ultrasmall: Controlling Nanoantennas and Molecules. *ACS Photonics* 2016, 3, 1401-1414.
- [12] Faggiani, R.; Losquin, A.; Yang, J.; Mårsell, E.; Mikkelsen, A.; Lalanne, P. Modal Analysis of the Ultrafast Dynamics of Optical Nanoresonators. *ACS Photonics* 2017, 4, 897-904.
- [13] Mårsell, E.; Losquin, A.; Svärd, R.; Miranda, M.; Guo, C.; Harth, A.; Lorek, E.; Mauritsson, J.; Arnold, C. L.; Xu, H.; L’Huillier, A.; Mikkelsen, A. Nanoscale Imaging of Local Few-Femtosecond Near-Field Dynamics within a Single Plasmonic Nanoantenna.

2.3. Dynamics of Second Harmonic Generation in a Plasmonic Silver Nanorod

Nano Lett. 2015, 15, 6601-6608.

[14] Razinskas, G.; Kilbane, D.; Melchior, P.; Geisler, P.; Krauss, E.; Mathias, S.; Hecht, B.; Aeschlimann, M. Normal-Incidence PEEM Imaging of Propagating Modes in a Plasmonic Nanocircuit. Nano Lett. 2016, 16, 6832-6837.

[15] Sun, Q.; Yu, H.; Ueno, K.; Kubo, A.; Matsuo, Y.; Misawa, H. Dissecting the Few-Femtosecond Dephasing Time of Dipole and Quadrupole Modes in Gold Nanoparticles Using Polarized Photoemission Electron Microscopy. ACS Nano 2016, 10, 3835-3842.

[16] Lamprecht, B.; Leitner, A.; Aussenegg, F. Femtosecond decaytime measurement of electron-plasma oscillation in nanolithographically designed silver particles. Appl. Phys. B: Lasers Opt. 1997, 64, 269-272.

[17] Lamprecht, B.; Leitner, A.; Aussenegg, F. SHG studies of plasmon dephasing in nanoparticles. Appl. Phys. B: Lasers Opt. 1999, 68, 419-423.

[18] Berweger, S.; Atkin, J. M.; Xu, X. G.; Olmon, R. L.; Raschke, M. B. Femtosecond Nanofocusing with Full Optical Waveform Control. Nano Lett. 2011, 11, 4309-4313.

[19] Davidson, R. B.; Yanchenko, A.; Ziegler, J. I.; Avanesyan, S. M.; Lawrie, B. J.; Haglund, R. F. Ultrafast Plasmonic Control of Second Harmonic Generation. ACS Photonics 2016, 3, 1477-1481.

[20] Zentgraf, T.; Christ, A.; Kuhl, J.; Giessen, H. Tailoring the Ultrafast Dephasing of Quasiparticles in Metallic Photonic Crystals. Phys. Rev. Lett. 2004, 93, 243901.

[21] Hanke, T.; Cesar, J.; Knittel, V.; Trügler, A.; Hohenester, U.; Leitenstorfer, A.; Bratschkitsch, R. Tailoring Spatiotemporal Light Confinement in Single Plasmonic Nanoantennas. Nano Lett. 2012, 12, 992-996.

[22] Kauranen, M.; Zayats, A. V. Nonlinear plasmonics. Nat. Photonics 2012, 6, 737.

[23] Butet, J.; Brevet, P.-F.; Martin, O. J. F. Optical Second Harmonic Generation in Plasmonic Nanostructures: From Fundamental Principles to Advanced Applications. ACS Nano 2015, 9, 10545-10562.

[24] Canfield, B. K.; Husu, H.; Laukkanen, J.; Bai, B.; Kuittinen, M.; Turunen, J.; Kauranen, M. Local Field Asymmetry Drives Second-Harmonic Generation in Noncentrosymmetric Nanodimers. Nano Lett. 2007, 7, 1251-1255.

[25] Butet, J.; Duboisset, J.; Bachelier, G.; Russier-Antoine, I.; Benichou, E.; Jonin, C.; Brevet, P.-F. Optical Second Harmonic Generation of Single Metallic Nanoparticles Embedded in a Homogeneous Medium. Nano Lett. 2010, 10, 1717-1721.

[26] Zhang, Y.; Grady, N. K.; Ayala-Orozco, C.; Halas, N. J. Three-Dimensional Nanostructures as Highly Efficient Generators of Second Harmonic Light. Nano Lett. 2011, 11, 5519-5523.

[27] Slablab, A.; Xuan, L. L.; Zielinski, M.; de Wilde, Y.; Jacques, V.; Chauvat, D.; Roch, J.-F. Second-harmonic generation from coupled plasmon modes in a single dimer of gold nanospheres. Opt. Express 2012, 20, 220-227.

[28] Kim, M.-K.; Sim, H.; Yoon, S. J.; Gong, S.-H.; Ahn, C. W.; Cho, Y.-H.; Lee, Y.-H. Squeezing Photons into a Point-Like Space. Nano Lett. 2015, 15, 4102-4107.

[29] Metzger, B.; Gui, L.; Fuchs, J.; Floess, D.; Hentschel, M.; Giessen, H. Strong Enhancement of Second Harmonic Emission by Plasmonic Resonances at the Second

Harmonic Wavelength. *Nano Lett.* 2015, 15, 3917-3922.

[30] Gennaro, S. D.; Rahmani, M.; Giannini, V.; Aouani, H.; Sidiropoulos, T. P. H.; Navarro-Cía, M.; Maier, S. A.; Oulton, R. F. The Interplay of Symmetry and Scattering Phase in Second Harmonic Generation from Gold Nanoantennas. *Nano Lett.* 2016, 16, 5278- 5285.

[31] Thyagarajan, K.; Rivier, S.; Lovera, A.; Martin, O. J. Enhanced second-harmonic generation from double resonant plasmonic antennae. *Opt. Express* 2012, 20, 12860-12865.

[32] Aouani, H.; Navarro-Cia, M.; Rahmani, M.; Sidiropoulos, T. P. H.; Hong, M.; Oulton, R. F.; Maier, S. A. Multiresonant Broadband Optical Antennas As Efficient Tunable Nanosources of Second Harmonic Light. *Nano Lett.* 2012, 12, 4997-5002.

[33] Celebrano, M.; Wu, X.; Baselli, M.; Grossmann, S.; Biagioni, P.; Locatelli, A.; De Angelis, C.; Cerullo, G.; Osellame, R.; Hecht, B.; Duò, L.; Ciccacci, F.; Finazzi, M. Mode matching in multiresonant plasmonic nanoantennas for enhanced second harmonic generation. *Nat. Nanotechnol.* 2015, 10, 412.

[34] Ethis de Corny, M.; Chauvet, N.; Laurent, G.; Jeannin, M.; Olgeirsson, L.; Drezet, A.; Huant, S.; Dantelle, G.; Nogues, G.; Bachelier, G. Wave-Mixing Origin and Optimization in Single and Compact Aluminum Nanoantennas. *ACS Photonics* 2016, 3, 1840- 1846.

[35] Yang, K.-Y.; Butet, J.; Yan, C.; Bernasconi, G. D.; Martin, O. J. F. Enhancement Mechanisms of the Second Harmonic Generation from Double Resonant Aluminum Nanostructures. *ACS Photonics* 2017, 4, 1522-1530.

[36] Butet, J.; Dutta-Gupta, S.; Martin, O. J. F. Surface secondharmonic generation from coupled spherical plasmonic nanoparticles: Eigenmode analysis and symmetry properties. *Phys. Rev. B: Condens. Matter Mater. Phys.* 2014, 89, 245449.

[37] Bernasconi, G. D.; Butet, J.; Martin, O. J. F. Mode analysis of second-harmonic generation in plasmonic nanostructures. *J. Opt. Soc. Am. B* 2016, 33, 768.

[38] Smirnova, D.; Smirnov, A. I.; Kivshar, Y. S. Multipolar Second- Harmonic Generation by Mie-Resonant Dielectric Nanoparticles. *Phys. Rev. A: At., Mol., Opt. Phys.* 2018, 97 DOI: 10.1103/PhysRevA. 97.013807.

[39] Kern, A. M.; Martin, O. J. F. Surface integral formulation for 3D simulations of plasmonic and high permittivity nanostructures. *J. Opt. Soc. Am. A* 2009, 26, 732-740.

[40] Boyd, R. W. *Nonlinear Optics*; Academic Press, 2003.

[41] Krause, D.; Teplin, C. W.; Rogers, C. T. Optical Surface Second Harmonic Measurements of Isotropic Thin-Film Metals: Gold, Silver, Copper, Aluminum, and Tantalum. *J. Appl. Phys.* 2004, 96, 3626- 3634.

[42] Wang, F. X.; Rodríguez, F. J.; Albers, W. M.; Ahorinta, R.; Sipe, J. E.; Kauranen, M. Surface and bulk contributions to the second-order nonlinear optical response of a gold film. *Phys. Rev. B: Condens. Matter Mater. Phys.* 2009, 80, 233402.

[43] Bachelier, G.; Butet, J.; Russier-Antoine, I.; Jonin, C.; Benichou, E.; Brevet, P.-F. Origin of optical second-harmonic generation in spherical gold nanoparticles: Local surface and nonlocal bulk contributions. *Phys. Rev. B: Condens. Matter Mater. Phys.* 2010, 82, 235403.

2.3. Dynamics of Second Harmonic Generation in a Plasmonic Silver Nanorod

- [44] Mäkitalo, J.; Suuriniemi, S.; Kauranen, M. Boundary element method for surface nonlinear optics of nanoparticles. *Opt. Express* 2011, 19, 23386-23399.
- [45] Butet, J.; Gallinet, B.; Thyagarajan, K.; Martin, O. J. F. Secondharmonic generation from periodic arrays of arbitrary shape plasmonic nanostructures: a surface integral approach. *J. Opt. Soc. Am. B* 2013, 30, 2970-2979.
- [46] Dadap, J. I.; Shan, J.; Eisenthal, K. B.; Heinz, T. F. Second- Harmonic Rayleigh Scattering from a Sphere of Centrosymmetric Material. *Phys. Rev. Lett.* 1999, 83, 4045-4048.
- [47] Dadap, J. I.; Shan, J.; Heinz, T. F. Theory of optical secondharmonic generation from a sphere of centrosymmetric material: small-particle limit. *J. Opt. Soc. Am. B* 2004, 21, 1328-1347.
- [48] Bai, Q.; Perrin, M.; Sauvan, C.; Hugonin, J.-P.; Lalanne, P. Efficient and intuitive method for the analysis of light scattering by a resonant nanostructure. *Opt. Express* 2013, 21, 27371.
- [49] Johnson, P. B.; Christy, R. W. Optical Constants of the Noble Metals. *Phys. Rev. B* 1972, 6, 4370-4379.
- [50] Mühlig, S.; Menzel, C.; Rockstuhl, C.; Lederer, F. Multipole analysis of meta-atoms. *Metamaterials* 2011, 5, 64-73.
- [51] Butet, J.; Raziman, T.; Yang, K.-Y.; Bernasconi, G. D.; Martin, O. J. Controlling the nonlinear optical properties of plasmonic nanoparticles with the phase of their linear response. *Opt. Express* 2016, 24, 17138.
- [52] Butet, J.; Bernasconi, G. D.; Petit, M.; Bouhelier, A.; Yan, C.; Martin, O. J. F.; Cluzel, B.; Demichel, O. Revealing a Mode Interplay That Controls Second-Harmonic Radiation in Gold Nanoantennas. *ACS Photonics* 2017, 4, 2923-2929.
- [53] Arfken, G. B.; Weber, H.-J.; Harris, F. E. *Mathematical Methods for Physicists: A Comprehensive Guide*; Academic Press, 2013.

Supplementary informations

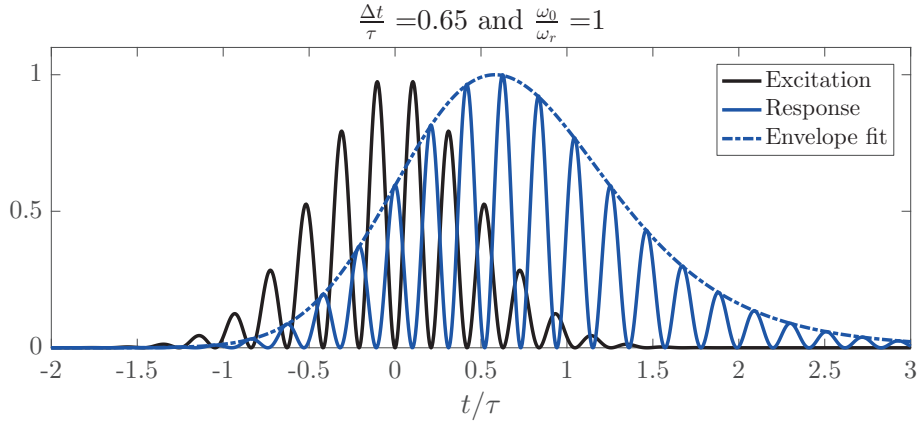


Figure S1 – Damped harmonic oscillator intensity response to a Gaussian pulse centered at $t = 0$. The envelope of the response is fitted to the maxima and allows to compute de delay between the maximum of the pulse at $t = 0$ and the maximum of the response. The horizontal axis is normalized to the lifetime τ of the oscillator.

2.3. Dynamics of Second Harmonic Generation in a Plasmonic Silver Nanorod

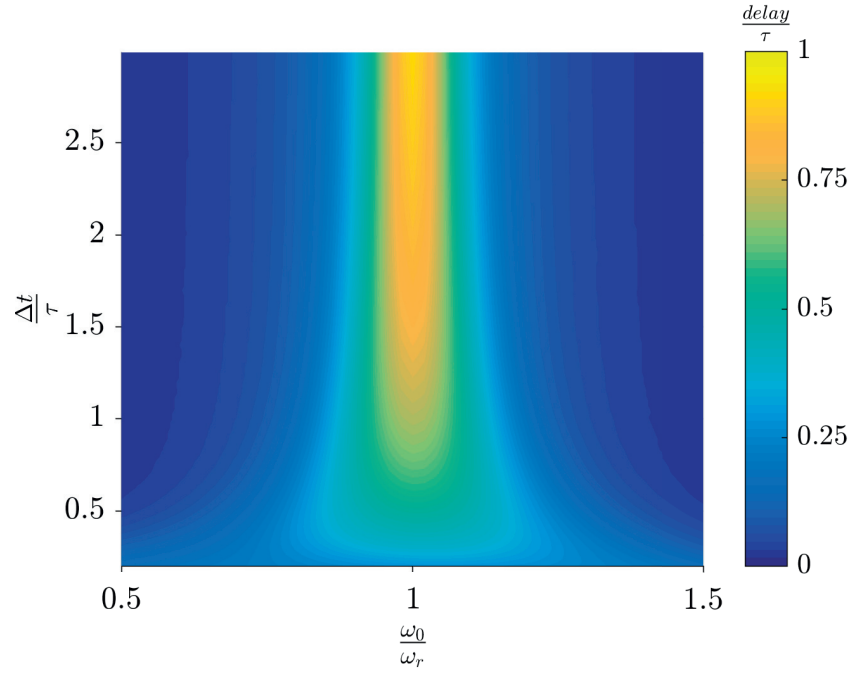


Figure S2 – Dependence of the delay with respect to the central frequency of the pulse ω_0 (normalized to the eigenfrequency of the oscillator ω_r) and the width Δt of the pulse (normalized to the lifetime τ of the oscillator).

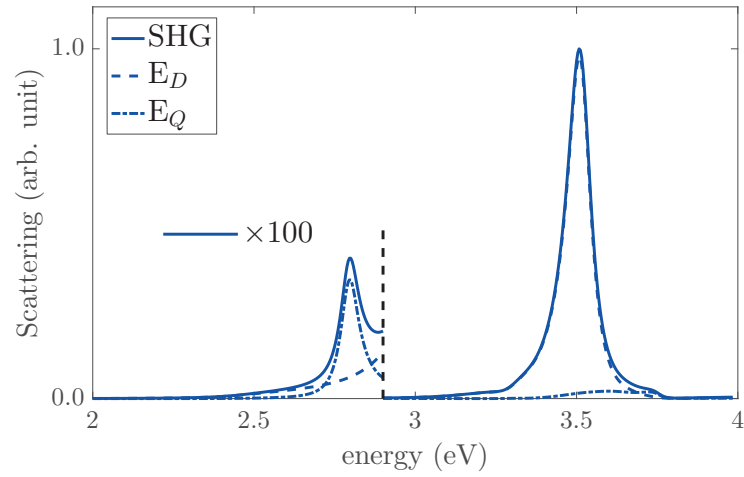


Figure S3 – Multipolar decomposition of the SHG spectrum shown in Fig. 2. E_D and E_Q respectively correspond to electric dipole and quadrupole.

3 Eigenmode Analysis and Electron Energy Loss Spectroscopy

This chapter contains four publications studying electron energy loss spectroscopy (EELS), organized as four successive sections with the corresponding references and supplementary informations following at the end of each publications. The first article describes the numerical implementation of EELS simulation as well as a novel approach for its computation: instead of computing the work done by the electron against the scattered field of the nanoparticle, we sum the energy dissipated by absorption and the energy radiated in the far field, Sec. 3.1.

The next three articles present experimental EELS results accompanied with eigenmode computations to analyse and interpret the spectra and maps. First, heterodimers made of two compositionally different metals are studied. The importance of the spatial and spectral overlap between the different modes of individual parts composing the dimer is emphasized, and the additional degree of freedom brought by the compositional difference is shown to strongly affect the hybridization pattern, Sec. 3.2. Second, dolmen-like nanostructures with 4 different geometries are analysed in detail with an emphasis on the strong coupling occurring between the nanorods comprising the dolmens. Eigenmodes of perfectly symmetric dolmens are computed to understand the modal structure of the different dolmens geometries and this knowledge is then used to understand the experimental EELS map acquired on capillary assembled dolmens (i.e. with small orientation defects and size mismatch), Sec. 3.3. Finally, the study of a Koch snowflake fractal nano-antenna is presented. The experimental EELS map are link to the different eigenmodes of the three first iterations of the fractal, revealing degenerated modes and the evolution of the modes through the iterations, Sec. 3.4. Thanks to the ability of SIE to model complex and realistic nanostructures accurately, the comparison between the experimental data and the simulations shows an overall excellent agreement in all the results presented in this chapter.

3.1 Where does the Energy go in Electron Energy Loss Spectroscopy of Nanostructures?

Manuscript state: Published

Reference: *Gabriel D. Bernasconi, *Jérémy Butet, Valentin Flauraud, Duncan T.L. Alexander, Jürgen Brugger and Olivier J.F. Martin "Where Does Energy Go in Electron Energy Loss Spectroscopy of Nanostructures?" *ACS Photonics* **4**, 156-164, (2017).

*equal contribution.

Publication date: December 5, 2016

DOI: 10.1021/acsphotonics.6b00761

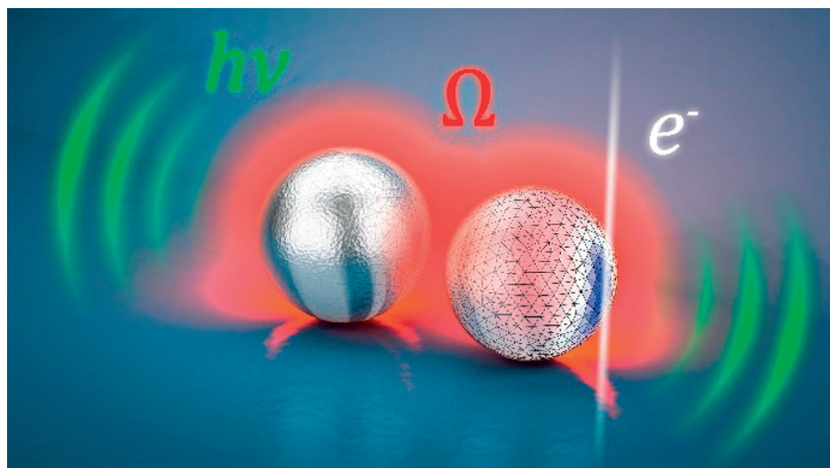
URL: <https://pubs.acs.org/doi/10.1021/acsphotonics.6b00761>

Adapted with permission from the above-mentioned reference.

Copyright (2016) American Chemical Society.

Author contributions

G. D. Bernasconi developed the code for the EELS computation and performed the numerical simulations with the standard formulation and edited the manuscript.



Where does the Energy go in Electron Energy Loss Spectroscopy of Nanostructures?

Gabriel D. Bernasconi¹, J  r  my Butet¹, Valentin Flauraud², Duncan T.L. Alexander³, J  rgen Brugger² and Olivier J.F. Martin¹

¹Nanophotonics and Metrology Laboratory, ²Microsystems Laboratory, and

³Interdisciplinary Center for Electron Microscopy, Swiss Federal Institute of Technology Lausanne (EPFL), 1015, Lausanne, Switzerland.

Corresponding author: jeremy.butet@epfl.ch

ABSTRACT: Electron energy loss spectroscopy is a method of choice for the characterization of both the spatial and spectral properties of localized surface plasmon resonances. The energy lost by the impinging electrons is commonly explained by the Lorentz force acting on their motion. Here, we adopt another point of view to compute the electron energy loss spectra. Coupling the energy conservation law with full-wave electromagnetic computations based on a surface integral equation method, we derive the electron energy loss spectra directly from two dissipative processes, namely, absorption and scattering. This antenna-based approach is applied to nanostructures with different sizes and materials, showing an excellent agreement with experimental observation and computations based on the evaluation of the Lorentz force. This formalism permits the easy separation of absorption losses in the nanostructures forming a coupled system and reveals the subtle interplay between absorption and scattering, which are controlled by the materials, the nanostructure size, and the energy range.

Introduction

Electron energy loss spectroscopy (EELS) is a well-established experimental technique based on the measurement of the energy lost by an electron owing to its interaction with a sample [1,2]. The implementation of EELS obviously requires the use of an electron beam and is in general performed in a scanning transmission electronic microscope (STEM) combined with an electron spectrometer [1,2]. EELS is an important experimental technique for both solid and surface sciences, combining very high spatial and energy resolutions [3-7]. Indeed, the spatial resolution of EELS is mainly related to the electron beam size, which can be squeezed to subangstrom dimensions, allowing for the direct observation of single atoms [3-7]. At the same time, a high energy resolution is mandatory for the identification of various chemical species and atomic bonds present in the sample under study [3-7]. In particular, the energy resolution has been increased to $\simeq 10$ meV,

allowing performing vibrational spectroscopy in STEM [8]. Examples of the successful utilization of EELS include the investigation of important biological molecules such as nucleic acid bases [9], confined fluids within individual nanobubbles [10], oxidation states in transition metal oxides [11], single-atom dopants in graphene [12], and light elements (alkali metal and halogen) [13].

The characterization of localized surface plasmon resonances (LSPRs) using swift electrons in STEM has also become an important research topic during the past decade [14,15]. This is mainly due to the combination of high spatial and spectral resolutions, which enables direct mapping of the electromagnetic hot-spots associated with LSPRs [16]. The interaction between the impinging electrons and the LSPR is observed either as energy lost by the electron beam, corresponding to EELS [16-37], or as cathodoluminescence (CL) [37-41], which corresponds to the photon emission resulting from the radiative decay of the LSPR. EELS and CL have been widely investigated in a broad variety of plasmonic systems, including nanospheres [17,18], nanorods [19,20], nanowires [21,22], nanoprisms [16,23], nanodisks [24], nanocubes [25,26], nanosquares [27], nanodecahedra [28], nanostars [29], bipyramids [30], split-ring resonators [31], nanodimers [32-34], trimers [35], chains of nanoparticles [36], and nanodolmens [37]. Recently, EELS was used to control the precise placement of gold nanorods in coupled systems obtained by capillary assembly [42]. Furthermore, EELS has been used to probe LSPR kinetics and damping in single plasmonic nanostructures [29]. Indeed, the LSPR quality factor and dephasing time depend upon the total losses, including radiative and nonradiative channels [43]. In order to support these experimental observations, numerical methods for nanophotonics have been extended to describe the interaction between plasmonic systems and propagating electrons [14]. For example, the discrete dipole approximation [44-46], the 3D Green's dyadic method [47], the finite difference time domain method [48], the discontinuous Galerkin time-domain method [49], the boundary element methods (BEM) [50-52] —in particular the MNPBEM Matlab toolbox [53]—and the finite element method [32] have been used for computing EELS and CL spectra.

In order to obtain more insights into the corresponding interaction mechanisms, the electron energy loss (EEL) spectra and maps have been related to a well-established physical quantity, the local density of states (LDOS) [54-57]. It was shown that EELS is sensitive to the component of the LDOS parallel to the electron propagation direction and that the EEL spectra are related to the total LDOS, while CL is related to the radiative part only [54-57]. Different tomography methods have been proposed for the complete reconstruction of the plasmonic eigenmodes [58,59], and a circuit model has been applied to understand the evolution of plasmon resonances observed with EELS [60,61]. However, until now, all the numerical methods developed for the computation of EEL spectra are based on the direct computation of the work done by the Lorentz force on the electron. This corresponds to a description from the point of view of the electron, thus somehow hiding the role played by the intrinsic properties of the plasmonic nanostructure in the EEL spectrum. It should be noted that the methods based on a

3.1. Where does the Energy go in Electron Energy Loss Spectroscopy of Nanostructures?

modal decomposition also use the evaluation of the Lorentz force acting on the electron as a starting point [54-57]. In parallel, the relation between EELS and absorption and scattering cross sections has been investigated. It was shown that, in specific cases, the EEL probability can be equal to only the radiative loss probability, i.e., to CL, such as the case of Al_2O_3 nanoparticles [62]. Further, it was formally proved that EELS is related to the extinction (the sum of absorption and scattering) cross sections in the case of small nanospheres [14]. Slight shifts observed between EELS and CL spectra have been explained by the differences in the scattering and absorption cross sections [37,40,57]. However, a systematic investigation of the relationship between EEL spectra and the absorption/scattering properties of the nanostructures has not yet been done, especially in the retarded case and for coupled nanostructures, although important advances have recently been made in this direction [40].

In this article, we evaluate the EEL spectrum directly from the properties of the plasmonic nanostructure. On the basis of energy conservation, the EEL spectrum is related to the fundamental electromagnetic properties of the plasmonic nanostructure—which can be viewed as an optical antenna [63]—namely, absorption and scattering. Here, the antenna theory is implemented in a surface integral equation (SIE) method [64], but this can be easily adapted for other numerical techniques. Spherical nanoparticles are considered first in order to introduce the antenna theory in a simple case. The roles of both the nanoparticle size and the constituting metal are then discussed in detail. Simple coupled plasmonic systems, i.e., nanodimers, are also investigated using the antenna theory, demonstrating that the contribution of each nanoparticle in the total EEL spectrum can be clearly identified in this framework. Finally, silver nanodiscs have been fabricated, and their EEL spectra have been interpreted using the novel theoretical approach.

Results

Theory

A swift electron propagating in a homogeneous medium generates an electromagnetic field that can probe matter with a high spatial resolution. Contrary to a planewave, which is monochromatic but spatially extended, the electromagnetic field associated with a propagating electron is strongly localized close to its trajectory but is associated with a broad spectrum. The spectral components of the electric field $\mathbf{E}(\mathbf{r}, \omega)$ and magnetic field $\mathbf{H}(\mathbf{r}, \omega)$ associated with an electron propagating along the z-axis are conveniently given by analytical expressions involving modified Bessel functions [65]:

$$\mathbf{E}(\mathbf{r}, \omega) = \frac{2q\omega e^{i\omega z/v}}{v^2\gamma_\epsilon\epsilon} \left[\frac{i}{\gamma_\epsilon} K_0 \left(\frac{\omega R}{v\gamma_\epsilon} \right) \hat{z} - K_1 \left(\frac{\omega R}{v\gamma_\epsilon} \right) \hat{R} \right] \quad (1)$$

$$\mathbf{H}(\mathbf{r}, \omega) = -\frac{2q\omega e^{i\omega z/v}}{v\gamma_\epsilon c} K_1 \left(\frac{\omega R}{v\gamma_\epsilon} \right) \hat{\phi} \quad (2)$$

Chapter 3. Eigenmode Analysis and Electron Energy Loss Spectroscopy

where $\gamma_e = 1/\sqrt{1 - \epsilon v^2/c^2}$ is the Lorentz contraction factor, v is the electron velocity, ϵ is the relative permittivity of the medium, q is the electron charge, K_0 and K_1 are the modified Bessel functions of the second kind, \hat{R} is the radial unit vector, R and z are respectively the perpendicular distance to and along the electron trajectory ($r = (R, z)$), and $\hat{\phi}$ is the azimuthal unit vector. These formulas are directly used in all the numerical methods implemented in the frequency domain for the evaluation of EEL spectra. In this work, we use a SIE method previously applied to the computation of the interaction of nanostructures with incoming planewaves and radiative dipoles [66]. This method has been proven to be very accurate for the description of the electrodynamic response of plasmonic systems, even under resonant conditions [64,66]. The nanostructure's surface is discretized with triangular mesh elements, and using surface integral equations, the electric and magnetic fields in the entire space (inside and outside the nanoparticle) are related to fictitious electric and magnetic surface currents. The incident conditions are defined using eqs 1 and 2, and the induced field, resulting from the interaction between the electromagnetic field generated by the electron and a scatterer, can be accurately determined. The spectral loss probability, the quantity measured in standard EELS experiments, is generally expressed invoking the Lorentz force exerted by the induced electric field $\mathbf{E}^{ind}(\mathbf{r}, \omega)$ on the incident electron. Considering a straight line trajectory $r_e(t)$ and a constant electron velocity \mathbf{v} (the so-called nonrecoil approximation [13]), the energy loss is expressed as [67]

$$\Delta E = e \int dt \mathbf{v} \cdot \mathbf{E}^{ind}(\mathbf{r}, t) = \int_0^\infty \hbar \omega \Gamma(\omega) d\omega \quad (3)$$

where

$$\Gamma(\omega) = \frac{e}{\pi \hbar \omega v} \int \text{Re}\{(\mathbf{v} e^{-i\omega t}) \cdot \mathbf{E}^{ind}(\mathbf{r}, \omega)\} dl \quad (4)$$

is the loss probability given per unit of frequency ω . A priori, EEL spectra can be computed with any numerical method suitable for the evaluation of the induced electric field [68]. All these numerical methods are based on the evaluation of the work done by the Lorentz force against the propagation of the electron. The current implementation of the SIE method for the evaluation of the EEL spectra has been tested and compared to the BEM (with the MNPBEM package) [52-54]; see Figure S1 in the Supporting Information. In the following, the method based on the evaluation of the Lorentz force is referred to as the standard formulation and the corresponding loss probability is denoted as $\Gamma_{stand}(\omega)$.

In this article, we introduce another point of view to describe EELS by combining antenna theory with energy conservation. Indeed, an electron does not lose energy as it propagates in a homogeneous medium with a velocity lower than the speed of light in this medium, i.e., without Cherenkov radiation [14]. As a consequence, the unique possibility for the electron to lose energy is through its interaction with the plasmonic nanostructures close to its trajectory. The energy transferred from the electron to the

3.1. Where does the Energy go in Electron Energy Loss Spectroscopy of Nanostructures?

nanostructure can then be dissipated either via heat generation in the nanostructure or by radiation into the far field. Note that a small amount of the energy absorbed in the nanostructure can be tied to the generation of hot excitons, which may leave the plasmon nanostructures without generating any phonons [69,70]. This effect is not considered in the present work. The latter dissipative process corresponds to the emission of photons and is known as CL [38-41]. Due to energy conservation, the power lost by a beam of temporally well-separated electrons, i.e., if the time separating two impinging electrons is much longer than the dissipation of the energy generated in the nanostructure by one electron, $P_{loss}(\omega)$ can be written as

$$P_{loss} = P_{sca} + P_{abs} \quad (5)$$

where P_{sca} is the power scattered by the nanostructure and P_{abs} is the absorbed power, corresponding to the ohmic losses. The absorbed power P_{abs} is easily computed as [71]

$$P_{abs}(\omega) = \frac{1}{2} \int_{\Omega} dV \text{Re}\{\sigma\} |\mathbf{E}^{ind}(\mathbf{r}, \omega)|^2 \quad (6)$$

where the integration is performed over the volume Ω of the plasmonic system. The conductivity σ is expressed as [71]

$$\sigma(\omega) = -i\omega\epsilon_0(\epsilon_m - 1) \quad (7)$$

where ϵ_m is the complex dielectric constant of the metal and ϵ_0 is the vacuum permittivity. The dielectric constants of gold and silver are extrapolated from experimental results in the present work [72]. The scattered power P_{sca} is evaluated by integrating the Poynting vector $\mathbf{S}(\mathbf{r}, \omega)$ over a surface A enclosing the nanostructure,

$$P_{sca}(\omega) = \int_A d\mathbf{A} \cdot \mathbf{S}(\mathbf{r}, \omega). \quad (8)$$

Note that scattering denotes here the electromagnetic radiation, not the electron scattering by the LSPR. In this framework, the loss probability $\Gamma_{loss}(\omega)$ per unit of frequency ω is proportional to $\frac{N}{\hbar\omega^2} P_{loss}(\omega)$, where N is the constant number of incident electrons per time unit. The loss probability $\Gamma_{loss}(\omega)$ can then be related to two dissipation processes, namely, scattering and absorption. Furthermore, in the case of coupled plasmonic systems, the absorption in each individual nanoparticle can be computed separately by an adequate definition of the integration volume as shown below.

Before discussing several examples in detail, it is worth saying that the antenna point of view proposed here is compatible with the common description of EELS based on the LDOS [54-57]. Indeed, it was recently demonstrated that the CL spectra are related to the radiative LDOS, while EEL spectra are related to the full LDOS, including the radiative and the nonradiative components [56]. However, there was a long controversy about the link between the LDOS and EELS and how they are intimately related to each

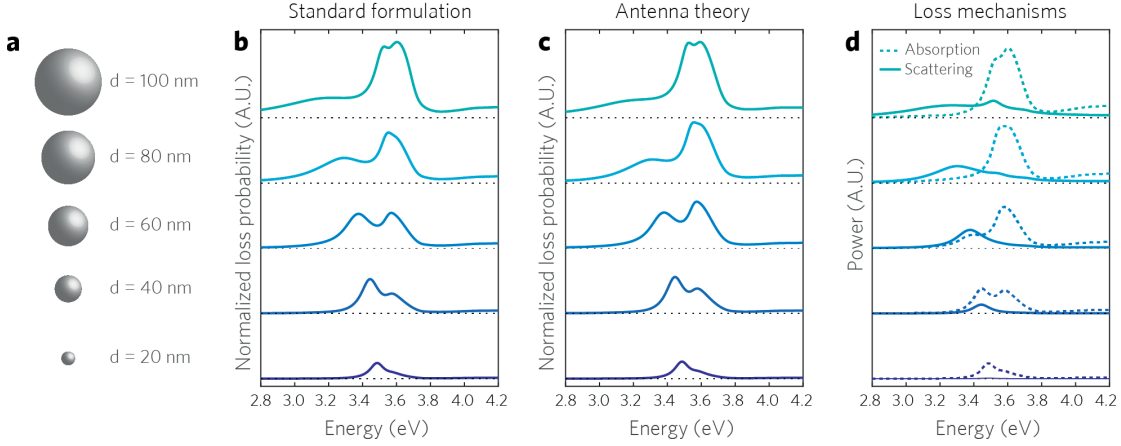


Figure 1 – (a) EEL spectra for silver nanospheres in vacuum. (b) Normalized loss probability evaluated using the standard formulation corresponding to eq 4. (c) Normalized loss probability evaluated using the antenna theory corresponding to eq 5. (d) Absorbed power (dashed lines) and scattered power (solid lines) shown as functions of the energy. The minimal distance between the nanoparticle surface and the electron trajectory is fixed to 4 nm. The incident electron energy is 300 keV.

other [54-57]. It is now well-established that EELS is able to probe only the component of the LDOS parallel to the electron trajectory [54-57]. This is generally attributed to the scalar product between the electron velocity and induced electric field in the integrand of eq 4. This scalar product is also invoked to explain that EELS is blind to some of the electromagnetic hot-spots, as the ones observed in the gap of dipolar nanoantennas, due to an inappropriate orientation of the electric field [54-57,73]. This has been intensively discussed in the frame of the modal decomposition of the EEL spectra [56]. While this point of view is correct, the approach proposed in this article emphasizes that the inability of EELS to reveal some of the hot-spots is indeed due to the specific symmetry of the incident field associated with the incoming electrons.

Silver Nanoparticles

We start with simple plasmonic systems, namely, silver nanospheres in vacuum. The sphere diameters range from $d = 20$ nm to $d = 100$ nm, Figure 1a. The incident electron energy is fixed to 300 keV. The impact parameter is $b = d + 4$ nm, meaning that the minimal distance between the sphere surface and the electron trajectory is 4 nm. The corresponding EEL spectra have been computed using the standard formulation, i.e., the evaluation of the work done on the electron by the induced field, and the antenna point of view proposed in this article. A very good agreement between the two formulations is observed, confirming the validity of the antenna point of view for EELS. For the 20 nm silver nanoparticle, the EEL spectra are composed of one maximum close to 3.49 eV with a shoulder at higher energy. The Mie theory reveals that the mode peaking at 3.49

3.1. Where does the Energy go in Electron Energy Loss Spectroscopy of Nanostructures?

eV corresponds to the electric dipole mode and the shoulder is due to the contribution of higher modes, mainly the electric quadrupole mode [74]. As the nanoparticle size increases, the dipolar mode red-shifts and its contribution to the EEL spectra evolves; see Figure 1. The contribution of the electric dipole mode to the EEL spectra is maximal for a sphere diameter d between 40 and 60 nm. As the nanoparticle size increases, the contribution of the electric quadrupole mode becomes more significant and a new (electric octupole) mode appears for the largest nanoparticles at an energy close to that of the quadrupolar mode, explaining the peak at 3.6 eV for $d = 100$ nm.

Having briefly described the evolution of the EEL spectra with the size of silver nanoparticles, we now turn our attention to the cornerstone of the approach proposed in this article: the decomposition of the EEL spectra into the different energy loss channels. The ohmic losses (dashed lines) and the scattered power (full lines) are shown in Figure 1d. First of all, it is worth noticing that the maxima are slightly shifted relatively to the ones observed in the EEL spectra. Indeed, the EEL spectra correspond to the probability that an electron undergoes an energy loss equal to $\hbar\omega$. In other words, the EEL spectra reveal the number of loss events. On the other hand, the total dissipated power is the convolution between the loss probability and the energy loss during each event, proportional to $\hbar\omega$, explaining the small shift between the two kinds of spectra. This shift is even higher for 20 nm aluminum nanoparticles, which are resonant in the UV close to 10 eV; see Figure S2 in the Supporting Information. At this energy, an energy shift as high as 0.5 eV is observed between the maximum of the EEL spectrum and the maximum of the total energy loss. For the smallest silver nanoparticles, the energy dissipation is dominated by the internal absorption, in agreement with previous discussions [17]. However, the scattering also plays a more important role as the nanoparticle increases. For example, the peak at 3.38 eV observed in the EEL spectrum of a 60 nm silver nanoparticle is mainly due to scattering, and not to absorption. This peak is associated with the electric dipole mode. In the case of 100 nm silver nanoparticle, the electric dipole mode is shifted to lower energy and the scattering associated with this mode is the main energy dissipation process for energy lower than 3.4 eV. At the same time, new modes, which are strongly absorbing, appear close to 3.6 eV, resulting in EEL spectra also dominated by absorption. Note that the small scattering peak observed at 3.5 eV corresponds to the electric quadrupole mode.

Gold Nanoparticles

As expressed by eqs 6 and 7, the ohmic losses are proportional to the imaginary part of the dielectric constant of the metal. Therefore, the metal constituting the investigated nanostructures is an important parameter in EELS, beyond its influence on the resonant frequencies of the observed modes. Furthermore, the penetration of the electromagnetic field inside the nanoparticle also depends on the dielectric constant, because this physical quantity is involved in the boundary conditions describing the electromagnetic field

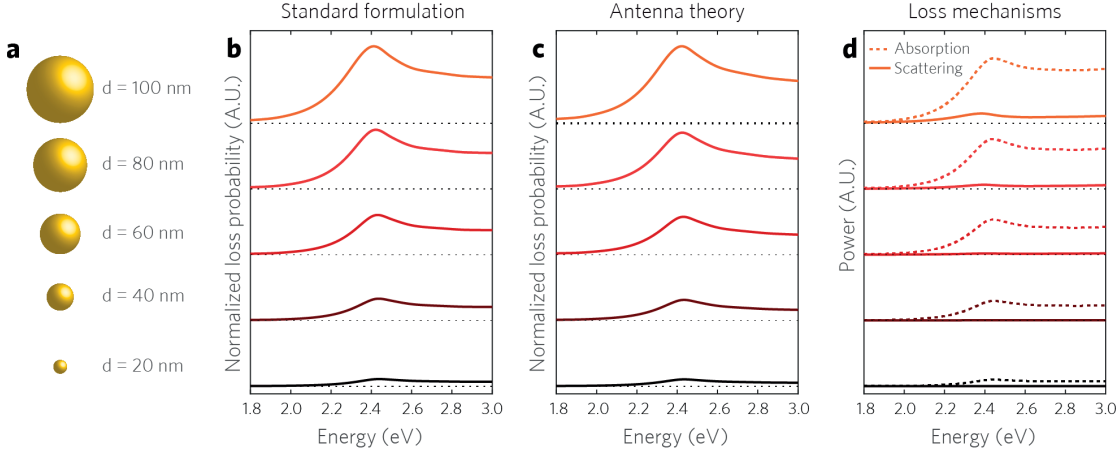


Figure 2 – (a) EEL spectra of gold nanospheres in vacuum. (b) Normalized loss probability evaluated using the standard formulation corresponding to eq 4. (c) Normalized loss probability evaluated using the antenna theory corresponding to eq 5. (d) Absorbed power (dashed lines) and scattered power (solid lines) shown as functions of the energy. The minimal distance between the nanoparticle surface and the electron trajectory is fixed to 4 nm. The incident electron energy is 300 keV.

behavior at the nanoparticle surface. To investigate the influence of the metal dielectric constant on EELS measurements, EEL spectra of gold nanoparticles with diameter d ranging from 20 to 100 nm have been evaluated in vacuum using the standard formulation and the antenna theory; see Figure 2. All the EEL spectra are characterized by two distinct features. First, a maximum at 2.41 eV, associated with the excitation of LSPRs and with an increase of the internal electric field, is observed. The second feature is a plateau for energy higher than 3 eV, corresponding to the excitation of electronic interband transitions from the d-band to the hybridized sp-band and to an increase of the imaginary part of the gold dielectric constant. The nanoparticle size modifies the relative weight of these two features in the EEL spectra. The antenna theory reveals that, for all the studied nanoparticle diameters, the energy is mainly converted into heat by ohmic losses (see Figure 2d) and that the scattering is weak, resulting in a limited CL signal. Indeed, scattering corresponds approximately to 15% of the energy lost at 2.41 eV by a 100 nm gold nanoparticle, the other part being lost by heat dissipation.

Silver Dimers

In the EELS of the isolated nanoparticles, the energy is dissipated either by scattering or by absorption. The case of coupled nanostructures is a bit more complex. Indeed, the absorption is decomposed into the ohmic losses occurring in each nanoparticle constituting the coupled plasmonic system. The absorption in each nanoparticle can be easily computed considering the appropriate volume for the integration occurring in eq 6. The simplest coupled plasmonic system is composed of two spherical nanoparticles

3.1. Where does the Energy go in Electron Energy Loss Spectroscopy of Nanostructures?

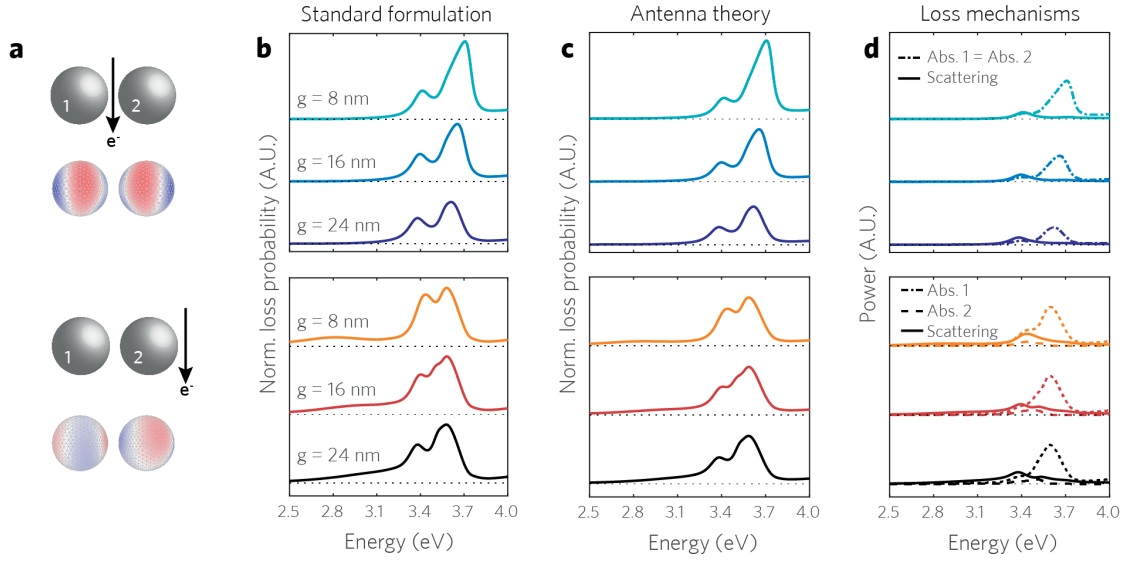


Figure 3 – (a) EELS of silver nanodimers in vacuum for an electron trajectory passing through the dimer center and perpendicular to the dimer main axis (top panels) and for an electron trajectory passing close to the dimer extremity (the minimal distance between the nanoparticle surface and the electron trajectory is fixed to 4 nm in this case) and perpendicular to the dimer main axis (bottom panels). (b) Normalized loss probability evaluated using the standard formulation corresponding to eq 4. (c) Normalized loss probability evaluated using the antenna theory corresponding to eq 5. (d) Absorbed power in nanoparticle 1 (dash-dotted lines) and in nanoparticle 2 (dashed lines) and the scattered power (solid lines) shown as functions of the energy. The incident electron energy is 300 keV.

separated by a short distance. The EEL spectra of silver dimers made of two 80 nm silver nanospheres with gaps $g = 8, 16$, and 24 nm have been evaluated using the standard formalism and the antenna theory (Figure 3). When the incident electron trajectory passes through the dimer center and is perpendicular to the dimer main axis (top panels), the EEL spectra are composed of two peaks, which red-shift as the gap between the two nanoparticles increases. This behavior is explained by the antibonding nature of the modes, where surface polarization charges with the same signs stand at each side of the gap (see the charge distributions in Figure 3a), excited in this configuration. Indeed, due to the symmetry properties of the electromagnetic field generated by the impinging electrons, the bonding modes (where surface polarization charges with opposite signs stand at each side of the gap) cannot be excited. This has been intensively discussed in the past, leading to the conclusion that the Lorentz force associated with the bonding modes vanishes since the corresponding electric field is perpendicular to the electron trajectory in this case [54,55]. A priori, in this framework one cannot determine whether a given mode is not excited or is instead excited but not probed by the electron beam. In comparison, the absorbed and scattered power are not directly related to the induced local field orientation (contrary to the Lorentz force). It follows that the vanishing

signal in the gap reveals that the bonding modes are simply not driven by the incident electrons and therefore do not provide additional channels for energy dissipation. The standard formalism and the antenna theory lead to the same physical results, but the latter description introduces a subtle conceptual difference in the interpretation of the EEL spectra. It is interesting to note that, despite the antibonding nature of the modes, a nonnegligible part of the energy is dissipated through scattering. Furthermore, the absorption in the two nanoparticles is always identical, as expected from simple symmetry considerations. This observation confirms the validity of the antenna theory for the description of the EEL spectra.

In order to go beyond the selective excitation of the antibonding modes, the electron beam is moved close to the dimer edges with a distance of 4 nm between the sphere surface and the electron trajectory. In this case, the EEL spectra reveal two main peaks as well as energy losses at lower energy (between 2.5 and 3 eV). This feature is attributed to the contribution of the dipolar bonding mode, which was not excited in the previous configuration; see the charge distributions in Figure 3a. Note that this mode is broader than the other ones due to its high radiative losses. The absorption in the two nanoparticles reveals their relative contributions to the EEL spectra. Interestingly, it is observed that the nanoparticle close to the electron beam dissipates more energy than the other one. This is expected since the internal electric field is higher inside this nanoparticle due to the fast spatial decay of the electric field generated by the incident electrons, eq 1. Note that the relative contributions of the nanoparticles cannot be easily determined using the standard formalism and the evaluation of the Lorentz force, mainly because the external electric field is associated with the complete coupled system, not to only one of the nanoparticles. These results emphasize the potential of the antenna theory for the interpretation of the EEL spectra associated with coupled plasmonic systems, especially the role played by the different nanoparticles in the global response.

Comparison with Experimental Results

Finally, the numerical method proposed in this article for simulation of EELS is compared to experimental EEL spectra obtained for silver nanodiscs with various sizes, with diameter d ranging from 25 to 100 nm and with a constant thickness of 30 nm. As discussed previously, the energy dissipation in gold nanoparticles is mainly due to ohmic losses, and silver is chosen here to emphasize the role played by the two energy loss channels (scattering and internal absorption). The silver nanodiscs were fabricated by electron beam lithography along with a standard lift-off technique on an electron-transparent silicon nitride membrane with a thickness of 30 nm. The EEL spectra were extracted from 30×30 pixel regions of high-resolution EELS maps allowing for an improved signal-to-noise ratio and low sample damages in comparison with a long single-point spectra acquisition. The comparison of the experimental spectra with the simulated EEL spectra convoluted with the experimental zero-loss peak (ZLP, with 0.12 eV fwhm)

3.1. Where does the Energy go in Electron Energy Loss Spectroscopy of Nanostructures?

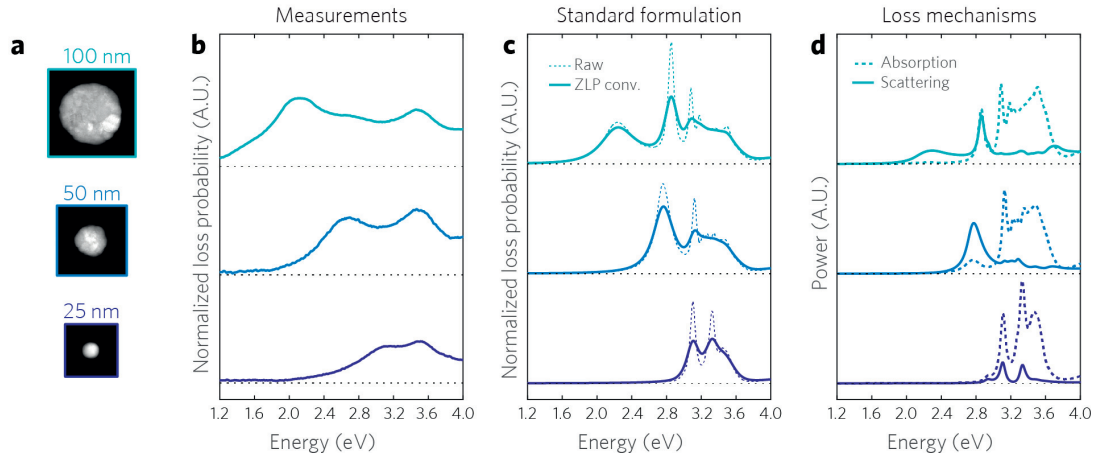


Figure 4 – (a) EEL spectra of silver nanodiscs. (b) Experimental spectra. (c) Normalized loss probability evaluated using the standard formulation corresponding to eq 4. The raw data and the convolution with the experimental zero-loss peak (ZLP) are shown in dashed lines and solid lines, respectively. (d) Absorbed power (dashed lines) and scattered power (solid lines) shown as functions of the energy. The incident electron energy is 300 keV for both experiments and computations.

shows a good agreement. The slight discrepancy is thought to come from the fact that an effective medium is used to mimic the influence of the substrate (see Methods). Especially, a gradual red-shift of the electric dipole mode as the nanodisc diameter increases and a quasi-planar mode at 3.5 eV are observed. Furthermore, both the experimental results and the theoretical predictions reveal that the number of modes distinctly observed in the EEL spectra increases as the nanodisc size grows. Now, we turn our attention to the loss mechanisms and their evolutions with the nanodisc diameter; see Figure 4d. For the smallest studied silver nanodisc ($d = 25$ nm), the energy is mainly absorbed in the nanoparticle, and the scattering remains weak over the whole spectrum. However, as the nanodisc size increases, scattering plays a more prominent role in the total energy dissipation, as observed previously in the case of the silver nanospheres. It is interesting to note that scattering mainly contributes to the EEL spectra at low energy and absorption at high energy. This observation is related to the physical properties of the modes and their coupling to far-field radiations, as emphasized by the antenna theory.

Conclusions and Perspectives

In summary, a new method for the evaluation and interpretation of the EEL spectra has been proposed. Contrary to the approaches proposed previously, the Lorentz force is not directly evaluated, but an antenna point of view is adopted instead, thus allowing distinguishing between the different loss channels provided by the nanostructure. Several examples, including gold and silver spherical nanoparticles, silver dimers with various gaps, and silver discs made by lithography, have been considered in order to confirm the

validity of this approach and to demonstrate the new insights it provides. It should also be emphasized that this approach is complementary to the LDOS description proposed in several seminal articles. Indeed, the antenna theory enables determining the relative role of each nanoparticle constituting a coupled plasmonic system, while this information is hidden in the LDOS of the global system. For this reason, the antenna point of view proposed in this article will become an important theoretical tool for the subtle interpretation of EEL spectra in complex plasmonic systems, such as those supporting Fano resonances for example [75].

Methods

Simulations

A surface integral equation method is used to compute the interaction between the electromagnetic field associated with the swift electron and the plasmonic nanostructures. The nanostructure's surface is discretized with triangular mesh elements with a typical side length between 1.5 nm for 20 nm spherical nanoparticles and 8 nm for 100 nm spherical nanoparticles, and using integral equations [61], the electric and magnetic fields in the entire space (inside and outside the nanoparticle) are related to fictitious electric and magnetic surface currents. The same numerical method is used for the implementation of both the standard formalism and the antenna theory. For the silver nanodiscs, a homogeneous medium with an effective dielectric constant ($\epsilon = 1.8$) is considered for the computation in order to mimic the influence of the silicon nitride substrate on the LSPRs ($\epsilon = 4.0$).

EELS Measurements

STEM-EELS maps were acquired using a FEI Titan Themis 80-300 equipped with a Wien-type monochromator and a Gatan GIF Quantum ERS spectrometer. A 300 keV incident electron beam was used for all experiments, monochromated to give an energy spread of ~ 110 meV fwhm in the zero-loss peak of elastically scattered electrons, and with beam currents of ~ 150 to 230 pA. A 17 mrad convergence semiangle of the probe and a 22 mrad collection semiangle on the spectrometer were used, with the probe having a mean diameter of < 1 nm for fwhm in incident intensity. Mapping was performed using the ultrafast spectrum imaging mode with typical dwell times of 0.25 to 0.5 ms per pixel and with the probe rastered in X, Y step sizes of 0.5-0.6 nm for a total of > 105 pixels per map. Each map was treated with the HQ Dark Correction plugin to reduce noise associated with dark current subtraction. Using this approach, the resultant plasmon maps have excellent spatial statistics when considering the inherently delocalized nature of this type of excitation.

3.1. Where does the Energy go in Electron Energy Loss Spectroscopy of Nanostructures?

EELS Processing

The EELS data cubes were processed using Gatan digital micrograph and custom Matlab scripts for the removal of the zero-loss radiation background and extraction of point spectra. The ZLP was first centered pixel by pixel using a Gaussian-Lorentzian approximation. The reflected tail model yielded a significantly lower signal-to-noise ratio and alignment accuracy, whereas fitting of a vacuum zero-loss offered no practical benefit while requiring a significantly longer computation time. Following zero-loss alignment, each data cube was spectrally cropped to the region of interest including ZLP (-2 to 6 eV), and artifacts from cosmic rays were removed and the ZLP subtracted. Spectra in Figure 4 were integrated over a 30×30 pixel region of interest in the periphery of the discs.

Author Contributions

G.D.B. developed and performed the numerical simulations with the standard formulation and edited the manuscript. J.Bu. developed and performed the numerical simulations with the antenna theory and wrote the manuscript. V.F. fabricated the samples, performed the STEM-EELS measurements, and edited the manuscript. D.T.L.A. performed the STEM-EELS measurements and edited the manuscript. J.Br. supervised the fabrication and edited the manuscript. O.J.F.M. supervised the project and edited the manuscript. G. D. Bernasconi and J. Butet contributed equally to this work.

Acknowledgement

The authors thank the staff of the Center of Micro/ Nanotechnology (CMI) of EPFL for the valuable discussions and support. This research was funded by the European Commission (FP7-ICT-2011-7, NANO-VISTA, under Grant Agreement No. 288263) and the Swiss National Science Foundation project 200020_153662.

References

- [1] Batson, P. E. Simultaneous STEM Imaging and Electron Energy- Loss Spectroscopy with Atomic-Column Sensitivity. *Nature* 1993, 366, 727-728.
- [2] Egerton, R. F. Electron Energy-Loss Spectroscopy in the TEM. *Rep. Prog. Phys.* 2009, 72, 016502.
- [3] Browning, N. D.; Wallis, D. J.; Nellist, P. D.; Pennycook, S. J. EELS in the STEM: Determination of Materials Properties on the Atomic Scale. *Micron* 1997, 28, 333-348.
- [4] Suenaga, K.; Tencé, M.; Mory, C.; Colliex, C.; Kato, H.; Okazaki, T.; Shinohara, H.; Hirahara, K.; Bandow, S.; Iijima, S. Element- Selective Single Atom Imaging. *Science*

2001, 290, 2280-2282.

[5] Varela, M.; Findlay, S. D.; Lupini, A. R.; Christen, H. M.; Borisevich, A. Y.; Dellby, N.; Krivanek, O. L.; Nellist, P. D.; Oxley, M. P.; Allen, L. J.; Pennycook, S. J. Spectroscopic Imaging of Single Atoms within a Bulk Solid. *Phys. Rev. Lett.* 2004, 92, 095502.

[6] Kimoto, K.; Asaka, T.; Nagai, T.; Saito, M.; Matsui, Y.; Ishizuka, K. Element-Selective Imaging of Atomic Columns in a Crystal using STEM and EELS. *Nature* 2007, 450, 702-704.

[7] Suenaga, K.; Sato, Y.; Liu, Z.; Kataura, H.; Okazaki, T.; Kimoto, K.; Sawada, H.; Sasaki, T.; Omoto, K.; Tomita, T.; Kaneyama, T.; Kondo, Y. Visualizing and Identifying Single Atoms using Electron Energy-Loss Spectroscopy with Low Accelerating Voltage. *Nat. Chem.* 2009, 1, 415-418.

[8] Krivanek, O. L.; Lovejoy, T. C.; Dellby, N.; Aoki, T.; Carpenter, R. W.; Rez, P.; Soignard, E.; Zhu, J.; Batson, P. E.; Lagos, M. J.; Egerton, R. F.; Crozier, P. A. Vibrational Spectroscopy in the Electron Microscope. *Nature* 2014, 514, 209-212.

[9] Crewe, A. V.; Isaacson, M.; Johnson, D. Electron Energy Loss Spectra of the Nucleic Acid Bases. *Nature* 1971, 231, 262-263.

[10] Taverna, D.; Kociak, M.; Stéphan, O.; Fabre, A.; Finot, E.; Décamps, B.; Colliex, C. Probing Physical Properties of Confined Fluids within Individual Nanobubbles. *Phys. Rev. Lett.* 2008, 100, 035301.

[11] Tan, H.; Turner, S.; Yücelen, E.; Verbeeck, J.; Tendeloo, G. V. 2D Atomic Mapping of Oxidation States in Transition Metal Oxides by Scanning Transmission Electron Microscopy and Electron Energy- Loss Spectroscopy. *Phys. Rev. Lett.* 2011, 107, 107602.

[12] Ramasse, Q. M.; Seabourne, C. R.; Kepaptsoglou, D.-M.; Zan, R.; Bangert, U.; Scott, A. J. Probing the Bonding and Electronic Structure of Single Atom Dopants in Graphene with Electron Energy Loss Spectroscopy. *Nano Lett.* 2013, 13, 4989-4995.

[13] Senga, R.; Suenaga, K. Single-Atom Electron Energy Loss Spectroscopy of Light Elements. *Nat. Commun.* 2015, 6, 7943.

[14] García de Abajo, F. J. Optical Excitations in Electron Microscopy. *Rev. Mod. Phys.* 2010, 82, 209-275.

[15] Kociak, M.; Stéphan, O. Mapping Plasmons at the Nanometer Scale in an Electron Microscope. *Chem. Soc. Rev.* 2014, 43, 3865- 3883.

[16] Nelayah, J.; Kociak, M.; Stéphan, O.; García de Abajo, F. J.; Tencé, M.; Henrard, L.; Taverna, D.; Pastoriza-Santos, I.; Liz-Marzán, L. M.; Colliex, C. Mapping Surface Plasmons on a Single Metallic Nanoparticle. *Nat. Phys.* 2007, 3, 348-353.

[17] Raza, S.; Kadkhodazadeh, S.; Christensen, T.; Di Vece, M.; Wubs, M.; Mortensen, N. A.; Stenger, N. Multipole Plasmons and their Disappearance in Few-Nanometer Silver Nanoparticles. *Nat. Commun.* 2015, 6, 8788.

[18] Collins, S. M.; Midgley, P. A. Surface Plasmon Ecitations in Metal Spheres: Direct Comparison of Light Scattering and Electron Energy-Loss Spectroscopy by Modal Decomposition. *Phys. Rev. B: Condens. Matter Mater. Phys.* 2013, 87, 235432.

[19] Martin, J.; Kociak, M.; Mahfoud, Z.; Proust, J.; Gérard, D.; Plain, J. High-Resolution

3.1. Where does the Energy go in Electron Energy Loss Spectroscopy of Nanostructures?

Imaging and Spectroscopy of Multipolar Plasmonic Resonances in Aluminum Nanoantennas. *Nano Lett.* 2014, 14, 5517- 5523.

[20] Guiton, B. S.; Iberi, V.; Li, S.; Leonard, D. N.; Parish, C. M.; Kotula, P. G.; Varela, M.; Schatz, G. C.; Pennycook, S. J.; Camden, J. P. Correlated Optical Measurements and Plasmon Mapping of Silver Nanorods. *Nano Lett.* 2011, 11, 3482-3488.

[21] Rossouw, D.; Botton, G. A. Plasmonic Response of Bent Silver Nanowires for Nanophotonic Subwavelength Waveguiding. *Phys. Rev. Lett.* 2013, 110, 066801.

[22] Rossouw, D.; Couillard, M.; Vickery, J.; Kumacheva, E.; Botton, G. A. Multipolar Plasmonic Resonances in Silver Nanowire Antennas Imaged with a Subnanometer Electron Probe. *Nano Lett.* 2011, 11, 1499-1504.

[23] Schmidt, F. P.; Ditlbacher, H.; Hofer, F.; Krenn, J. R.; Hohenester, U. Morphing a Plasmonic Nanodisk into a Nanotriangle. *Nano Lett.* 2014, 14, 4810-4815.

[24] Schmidt, F. P.; Ditlbacher, H.; Hohenester, U.; Hohenau, A.; Hofer, F.; Krenn, J. R. Dark Plasmonic Breathing Modes in Silver Nanodisks. *Nano Lett.* 2012, 12, 5780-5783.

[25] Nicoletti, O.; de la Peña, F.; Leary, R. K.; Holland, D. J.; Ducati, C.; Midgley, P. A. Three-Dimensional Imaging of Localized Surface Plasmon Resonances of Metal Nanoparticles. *Nature* 2013, 502, 80- 84.

[26] Li, G.; Cherqui, C.; Bigelow, N. W.; Duscher, G.; Straney, P. J.; Millstone, J. E.; Masiello, D. J.; Camden, J. P. Spatially Mapping Energy Transfer from Single Plasmonic Particles to Semiconductor Substrates via STEM/EELS. *Nano Lett.* 2015, 15, 3465-347.

[27] Bellido, E. P.; Manjavacas, A.; Zhang, Y.; Cao, Y.; Nordlander, P.; Botton, G. A. Electron Energy-Loss Spectroscopy of Multipolar Edge and Cavity Modes in Silver Nanosquares. *ACS Photonics* 2016, 3, 428-433.

[28] Myroshnychenko, V.; Nelayah, J.; Adamo, G.; Geuquet, N.; Rodriguez-Fernandez, J.; Pastoriza-Santos, I.; MacDonald, K. F.; Henrard, L.; Liz-Marzán, L. M.; Zheludev, N. I.; Kociak, M.; García de Abajo, F. J. Plasmon Spectroscopy and Imaging of Individual Gold Nanodecahedra: A Combined Optical Microscopy, Cathodoluminescence, and Electron Energy-Loss Spectroscopy Study. *Nano Lett.* 2012, 12, 4172-4180.

[29] Bosman, M.; Ye, E.; Tan, S. F.; Nijhuis, C. A.; Yang, J. K. W.; Marty, R.; Mlayah, A.; Arbouet, A.; Girard, C.; Han, M.-Y. Surface Plasmon Damping Quantified with an Electron Nanoprobe. *Sci. Rep.* 2013, 3, 1312.

[30] Collins, S. M.; Ringe, E.; Duchamp, M.; Saghi, Z.; Dunin- Borkowski, R. E.; Midgley, P. A. Eigenmode Tomography of Surface Charge Oscillations of Plasmonic Nanoparticles by Electron Energy Loss Spectroscopy. *ACS Photonics* 2015, 2, 1628-1635.

[31] von Cube, F.; Niegemann, J.; Irsen, S.; Bell, D. C.; Linden, S. Angular-Resolved Electron Energy Loss Spectroscopy on a Split-Ring Resonator. *Phys. Rev. B: Condens. Matter Mater. Phys.* 2014, 89, 115434.

[32] Koh, A. L.; Fernandez-Dominguez, A. I.; McComb, D. W.; Maier, S. A.; Yang, J. K. W. High-Resolution Mapping of Electron- Beam-Excited Plasmon Modes in Lithographically Defined Gold Nanostructures. *Nano Lett.* 2011, 11, 1323-1330.

[33] Kadkhodazadeh, S.; Rosenkrantz de Lassel, J.; Beleggia, M.; Kneipp, H.; Birkedal Wagner, J.; Kneipp, K. Scaling of the Surface Plasmon Resonance in Gold and Silver

Dimers Probed by EELS. *J. Phys. Chem. C* 2015, 118, 5478-5485.

[34] Zhang, M.; Large, N.; Koh, A. L.; Cao, Y.; Manjavacas, A.; Sinclair, R.; Nordlander, P.; Wang, S. X. High-Density 2D Homo- and Hetero- Plasmonic Dimers with Universal Sub-10-nm Gaps. *ACS Nano* 2015, 9, 9331-9339.

[35] Scholl, J. A.; Garcia-Etxarri, A.; Aguirregabiria, G.; Esteban, R.; Narayan, T. C.; Koh, A. L.; Aizpurua, J.; Dionne, J. A. Evolution of Plasmonic Metamolecule Modes in the Quantum Tunneling Regime. *ACS Nano* 2016, 10, 1346-1354.

[36] Barrow, S. J.; Rossouw, D.; Funston, A. M.; Botton, G. A.; Mulvaney, P. Mapping Bright and Dark Modes in Gold Nanoparticle Chains using Electron Energy Loss Spectroscopy. *Nano Lett.* 2014, 14, 3799-3808.

[37] Coenen, T.; Schoen, D. T.; Mann, S. A.; Rodriguez, S. R. K.; Brenny, B. J. M.; Polman, A.; Brongersma, M. L. Nanoscale Spatial Coherent Control over the Modal Excitation of a Coupled Plasmonic Resonator System. *Nano Lett.* 2015, 15, 7666-7670.

[38] Gomez-Medina, R.; Yamamoto, N.; Nakano, M.; García de Abajo, F. J. Mapping Plasmons in Nanoantennas via Catholuminescence. *New J. Phys.* 2008, 10, 105009.

[39] Barnard, E. S.; Coenen, T.; Vesseur, E. J. R.; Polman, A.; Brongersma, M. L. Imaging the Hidden Modes of Ultrathin Plasmonic Strip Antennas by Cathodoluminescence. *Nano Lett.* 2011, 11, 4265- 4269.

[40] Losquin, A.; Zagonel, L. F.; Myroshnychenko, V.; Rodriguez- Gonzalez, B.; Tencé, M.; Scarabelli, L.; Förstner, J.; Liz-Marzán, L. M.; García de Abajo, F. J.; Stéphan, O.; Kociak, M. Unveiling Nanometer Scale Extinction and Scattering Phenomena through Combined Electron Energy Loss Spectroscopy and Cathodoluminescence Measurements. *Nano Lett.* 2015, 15, 1229-1237.

[41] Atre, A. C.; Brenny, B. J. M.; Coenen, T.; Garcia-Etxarri, A.; Polman, A.; Dionne, J. A. Nanoscale Optical Tomography with Cathodoluminescence Spectroscopy. *Nat. Nanotechnol.* 2015, 10, 429-436.

[42] Flauraud, V.; Mastrangeli, M.; Bernasconi, G. D.; Butet, J.; Alexander, D. T. L.; Shahrabi, E.; Martin, O. J. F.; Brugger, J. Nanoscale Topographical Control of Capillary Assembly of Nanoparticles. *Nat. Nanotechnol.* Accepted for publication. DOI: 10.1038/nnano.2016.179.

[43] Sönnichsen, C.; Franzl, T.; Wilk, T.; von Plessen, G.; Feldmann, J.; Wilson, O.; Mulvaney, P. Drastic Reduction of Plasmon Damping in Gold Nanorods. *Phys. Rev. Lett.* 2002, 88, 077402.

[44] Geuquet, N.; Henrard, L. EELS and Optical Response of a Noble Metal Nanoparticle in the Frame of a Discrete Dipole Approximation. *Ultramicroscopy* 2010, 110, 1075.

[45] Bigelow, N. W.; Vashillo, A.; Iberi, V.; Camden, J. P.; Masiello, D. J. Characterization of the Electron- and Photon-Driven Plasmonic Excitations of Metal Nanorods. *ACS Nano* 2012, 6, 7497-7504.

[46] Bigelow, N. W.; Vashillo, A.; Camden, J. P.; Masiello, D. J. Signatures of Fano Interferences in the Electron Energy Loss Spectroscopy and Cathodoluminescence of Symmetry-Broken Nanorod Dimers. *ACS Nano* 2013, 7, 4511-4519.

[47] Arbouet, A.; Mlayah, A.; Girard, C.; Colas des Francs, G. Electron Energy Losses

3.1. Where does the Energy go in Electron Energy Loss Spectroscopy of Nanostructures?

- and Cathodoluminescence from Complex Plasmonic Nanostructures: Spectra, Maps and Radiation Patterns from a Generalized Field Propagator. *New J. Phys.* 2014, 16, 113012.
- [48] Cao, Y.; Manjavacas, A.; Large, N.; Nordlander, P. Electron Energy-Loss Spectroscopy Calculation in Finite-Difference Time- Domain Package. *ACS Photonics* 2015, 2, 369-375.
- [49] Matyssek, C.; Niegemann, J.; Hergert, W.; Busch, K. Computing Electron Energy Loss Spectra with the Discontinuous Galerkin Time- Domain Method. *Phot. Nanostruc. Fundam. Appl.* 2011, 9, 367-373.
- [50] García de Abajo, F. J.; Aizpurua, J. Numerical Simulation of Electron Energy Loss Near Inhomogeneous Dielectrics. *Phys. Rev. B: Condens. Matter Mater. Phys.* 1997, 56, 15873-15884.
- [51] García de Abajo, F. J.; Howie, A. Relativistic Electron Energy Loss and Electron-Induced Photon Emission in Inhomogeneous Dielectrics. *Phys. Rev. Lett.* 1998, 80, 5180-5183.
- [52] García de Abajo, F. J.; Howie, A. Retarded Field Calculation of Electron Energy Loss in Inhomogeneous Dielectrics. *Phys. Rev. B: Condens. Matter Mater. Phys.* 2002, 65, 115418.
- [53] Hohenester, U.; Trügler, A. MNPBEM - A Matlab Toolbox for the Simulation of Plasmonic Nanoparticles. *Comput. Phys. Commun.* 2012, 183, 370.
- [54] García de Abajo, F. J.; Kociak, M. Probing the Photonic Local Density of States with Electron Energy Loss Spectroscopy. *Phys. Rev. Lett.* 2008, 100, 106804.
- [55] Hohenester, U.; Ditzlacher, H.; Krenn, J. Electron Energy Loss Spectroscopy of Plasmonic Nanoparticles. *Phys. Rev. Lett.* 2009, 103, 106801.
- [56] Boudarham, G.; Kociak, M. Modal Decompositions of the Local Electromagnetic Density of States and Spatially Resolved Electron Energy Loss Probability in Terms of Geometric Modes. *Phys. Rev. B: Condens. Matter Mater. Phys.* 2012, 85, 245447.
- [57] Losquin, A.; Kociak, M. Link between Cathodoluminescence and Electron Energy Loss Spectroscopy and the Radiative and Full Electromagnetic Local Density of States. *ACS Photonics* 2015, 2, 1619-1627.
- [58] Hörl, A.; Trügler, A.; Hohenester, U. Tomography of Particle Plasmon Fields from Electron Energy Loss Spectroscopy. *Phys. Rev. Lett.* 2013, 111, 086801.
- [59] Hörl, A.; Trügler, A.; Hohenester, U. Full Three-Dimensional Reconstruction of the Dyadic Green Tensor from Electron Energy Loss Spectroscopy of Plasmonic Nanoparticles. *ACS Photonics* 2015, 2, 1429-1435.
- [60] Zhu, D.; Bosman, M.; Yang, J. K. W. A Circuit Model for Plasmonic resonators. *Opt. Express* 2014, 22, 9809-9819.
- [61] Duan, H.; Fernández-Domínguez, A. I.; Bosman, M.; Maier, S. A.; Yang, J. K. L. Nanoplasmonics: Classical down to the Nanometer Scale. *Nano Lett.* 2012, 12, 1683-1689.
- [62] García de Abajo, F. J.; Rivacoba, A.; Zabala, N.; Yamamoto, N. Boundary effects in Cherenkov Radiation. *Phys. Rev. B: Condens. Matter Mater. Phys.* 2004, 69, 155420.
- [63] Mühlischlegel, P.; Eisler, H.-J.; Martin, O. J. F.; Hecht, B.; Pohl, D. W. Resonant

Optical Antennas. *Science* 2005, 308, 1607-1608.

[64] Kern, A. M.; Martin, O. J. F. Surface Integral Formulation for 3D Simulation of Plasmonic and High Permittivity Nanostructures. *J. Opt. Soc. Am. A* 2009, 26, 732-740.

[65] Jackson, J. D. *Classical Electrodynamics*, 2nd ed.; Wiley: New York, 1975.

[66] Kern, A. M.; Martin, O. J. F. Excitation and Reemission of Molecules Near Realistic Plasmonic Nanostructures. *Nano Lett.* 2011, 11, 482-487.

[67] Ritchie, R. H. Plasma Losses by Fast Electrons in Thin Film. *Phys. Rev.* 1957, 106, 874-881.

[68] Gallinet, B.; Butet, J.; Martin, O. J. F. Numerical Methods for Nanophotonics: Standard Problems and Future Challenges. *Laser. Phot. Rev.* 2015, 9, 577-603.

[69] Brongersma, M. L.; Halas, N. J.; Nordlander, P. Plasmon- Induced Hot Carrier Science and Technology. *Nat. Nanotechnol.* 2015, 10, 25-34.

[70] Knight, M. W.; Sobhani, H.; Nordlander, P.; Halas, N. J. Photodetection with Active Optical Antennas. *Science* 2011, 332, 702- 704.

[71] Kern, A. M.; Martin, O. J. F. Pitfalls in the Determination of Optical Cross Sections from Surface Integral Equation Simulations. *IEEE Trans. Antennas Propag.* 2010, 58, 2158-2161.

[72] Johnson, P. B.; Christy, R. W. Optical Constants of the Noble Metals. *Phys. Rev. B* 1972, 6, 4370-4379.

[73] Batson, P. E. Surface Plasmon Coupling in Clusters of Small Spheres. *Phys. Rev. Lett.* 1982, 49, 936.

[74] Bernasconi, G. D.; Butet, J.; Martin, O. J. F. Mode Analysis of Second-Harmonic Generation in Plasmonic Nanostructures. *J. Opt. Soc. Am. B* 2016, 33, 768-779.

[75] Luk'yanchuck, B.; Zheludev, N. I.; Maier, S. A.; Halas, N. J.; Nordlander, P.; Giessen, H.; Chong, C. T. The Fano Resonance in Plasmonic Nanostructures and Metamaterials. *Nat. Mater.* 2010, 9, 707-715.

3.1. Where does the Energy go in Electron Energy Loss Spectroscopy of Nanostructures?

Supplementary informations

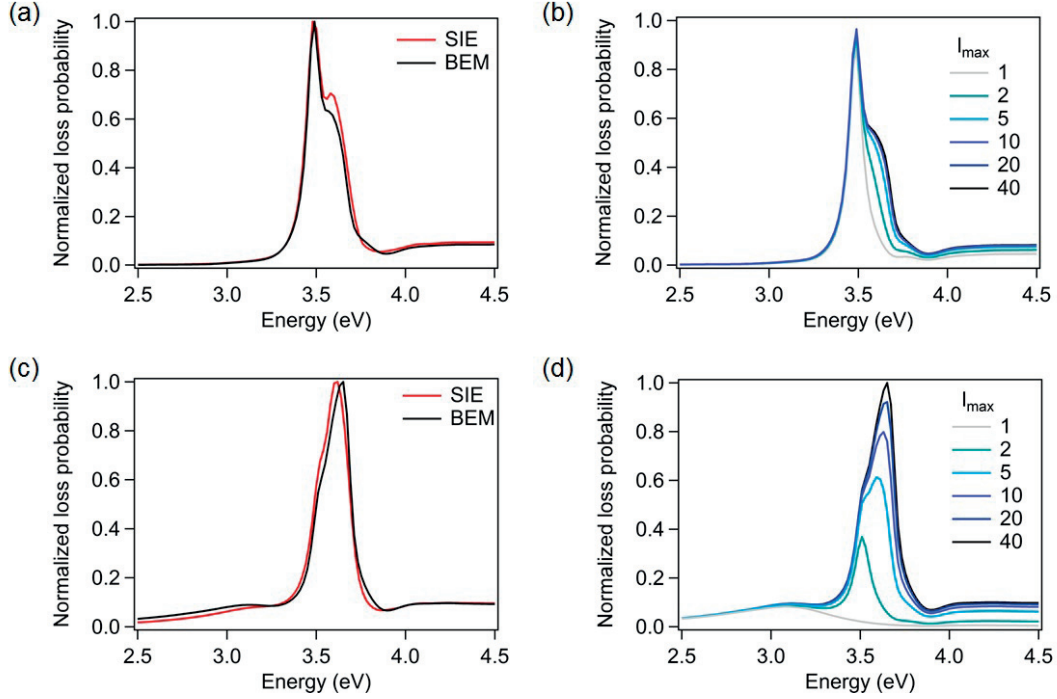


Figure S1 – (a) Comparison between the SIE and BEM (MNPBEM Matlab toolbox) for the evaluation of the EEL spectrum for a 20 nm silver nanoparticle in vacuum. (b) The same computation but performed with the Mie theory (module of the MNPBEM Matlab toolbox) considering different numbers of spherical harmonic degrees l_{max} . (c) Comparison between the SIE and BEM for the evaluation of the EEL spectrum of a 100 nm silver nanoparticle in vacuum. (d) The same computation but performed with the Mie theory considering different numbers of spherical harmonic degrees l_{max} . The minimal distance between the nanoparticle surface and the electron trajectory is fixed to 0.5 nm. The incident electron energy is 50 keV.

Influence of the surrounding medium

A convenient method for changing the ratio between the absorption and scattering from a plasmonic nanoparticle is to change the dielectric constant of the surrounding medium ϵ . Indeed, these two physical processes have different dependences on the size parameter ka , where $k = \frac{2\pi\sqrt{\epsilon}}{\lambda}$ is the wavenumber and a is the nanoparticle radius [62]. The EEL spectra for a 60 nm silver nanoparticles embedded in a homogeneous medium with a dielectric constant ranging from 1 to 1.5 have been evaluated using the standard formulation and the antenna theory, see Fig. S2. The corresponding results for a 20 nm and a 100 nm silver nanoparticles are shown in Fig. S3 and in Fig. S4. As expected, the ratio between the absorption and scattering evolves as the dielectric constant of the surrounding medium increases. Interestingly, for 60 nm silver nanosphere, the peak

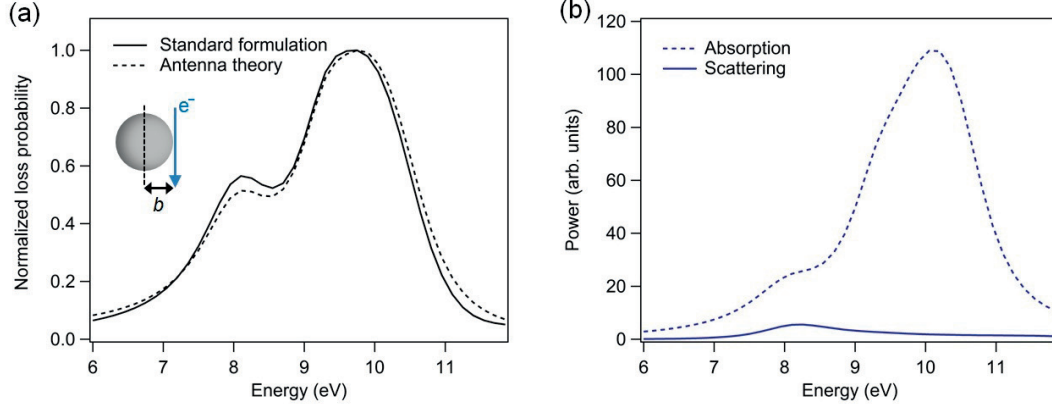


Figure S2 – EEL spectrum for a 20 nm aluminum nanosphere in vacuum. (a) Normalized loss probability evaluated using the standard formulation (solid line) and using the antenna theory (dashed line). (b) Absorbed power (dashed lines) and scattered power (solid lines) shown as functions of the energy. The minimal distance between the nanoparticle surface and the electron trajectory is fixed to 0.5 nm. The incident electron energy is 50 keV.

associated with the electric dipole mode in the EEL spectra for a dielectric constant of the surrounding medium $\epsilon > 1$ is mainly associated with scattering. For the smallest nanoparticles studied here ($d = 20$ nm), the EEL spectra is well reproduced considering only the ohmic losses. Indeed, it is well-known that the extinction spectra of small nanoparticle is dominated by absorption and, even for the highest dielectric constant of the surrounding medium ($\epsilon = 1.5$), the scattered power is approximately one order of magnitude lower than the absorbed power for a 20 nm silver nanoparticle. For the largest nanoparticles ($d = 100$ nm), the ohmic loss is also the most important loss mechanism. However, for the highest values of the dielectric constant of the surrounding medium, the quadrupolar electric mode (peak at 3.3 eV for $\epsilon = 1.5$) is explained by the two dissipation processes. These results confirm that EELS is related to both the absorption and the scattering.

3.1. Where does the Energy go in Electron Energy Loss Spectroscopy of Nanostructures?

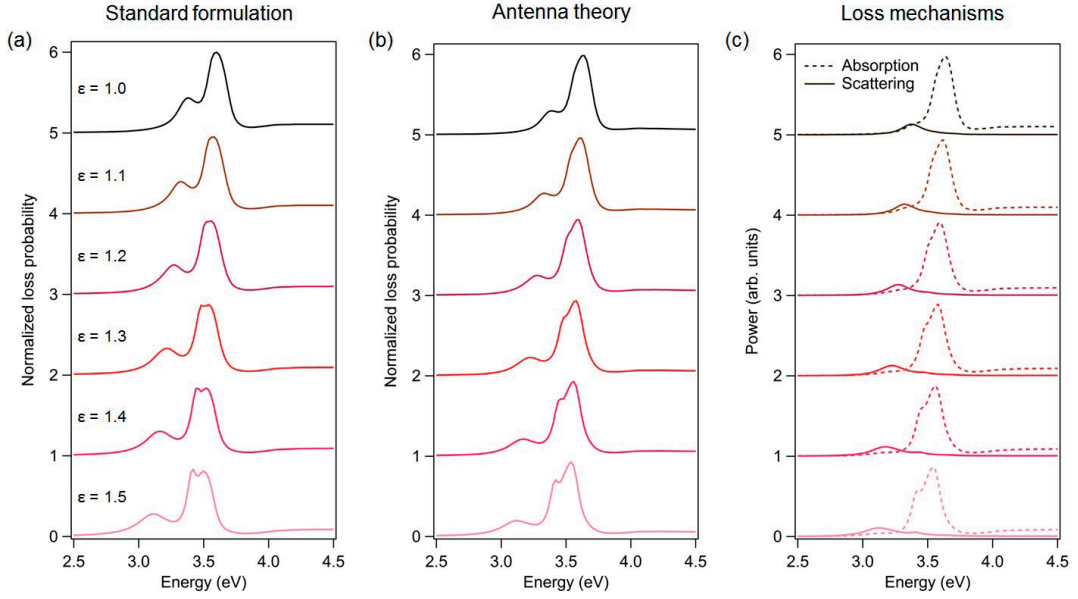


Figure S3 – EEL spectra of a 60 nm silver nanosphere embedded in a homogeneous medium with dielectric constant ranging from 1 to 1.5. (a) Normalized loss probability evaluated using the standard formulation corresponding to Eq. (4). (b) Normalized loss probability evaluated using the antenna theory corresponding to Eq. (5). (c) Absorbed power (dashed lines) and scattered power (solid lines) shown as functions of the energy. The minimal distance between the nanoparticle surface and the electron trajectory is fixed to 0.5 nm. The incident electron energy is 50 keV.

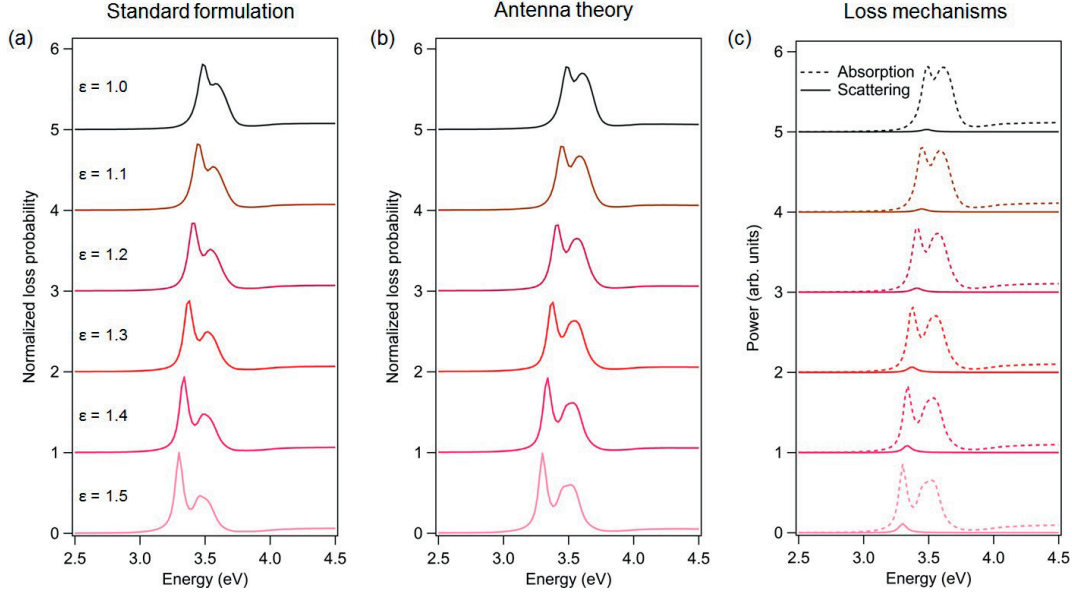


Figure S4 – EEL spectra for a 20 nm silver nanoparticle embedded in a homogeneous medium with dielectric constant ranging from 1 to 1.5. (a) Normalized loss probability evaluated using the standard formulation corresponding to Eq. (4). (b) Normalized loss probability evaluated using the antenna theory corresponding to Eq. (5). (c) Absorbed power (dashed lines) and scattered power (solid lines) shown as functions of the energy. The minimal distance between the nanoparticle surface and the electron trajectory is fixed to 0.5 nm. The incident electron energy is 50 keV.

3.1. Where does the Energy go in Electron Energy Loss Spectroscopy of Nanostructures?

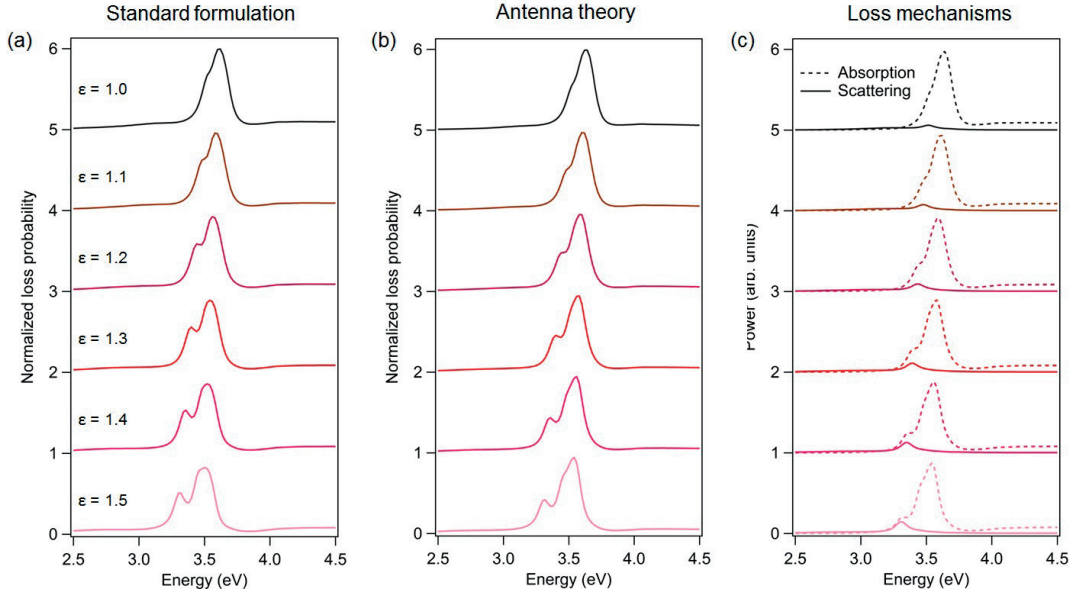


Figure S5 – EEL spectra of a 100 nm silver nanosphere embedded in a homogeneous medium with dielectric constant ranging from 1 to 1.5. (a) Normalized loss probability evaluated using the standard formulation corresponding to Eq. (4). (b) Normalized loss probability evaluated using the antenna theory corresponding to Eq. (5). (c) The absorbed power (dashed lines) and the scattered power (solid lines) shown as functions of the energy. The minimal distance between the nanoparticle surface and the electron trajectory is fixed to 0.5 nm. The incident electron energy is 50 keV.

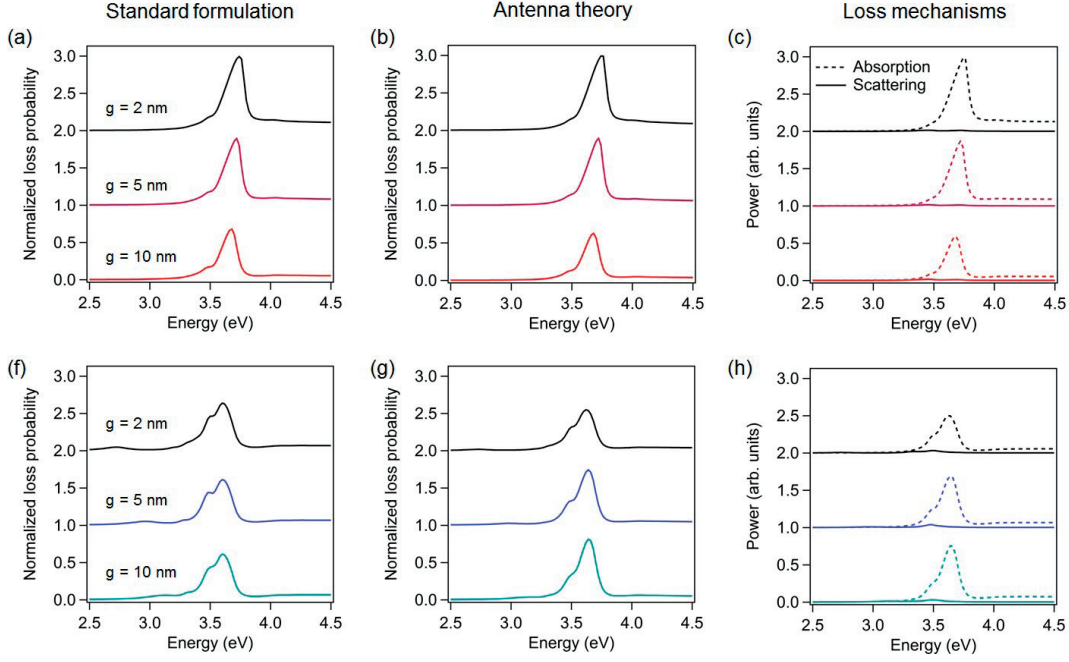


Figure S6 – EEL spectra of silver nanodimers in vacuum for (a)-(c) an electron trajectory passing through the dimer center and perpendicular to the dimer main axis and for (f)-(h) an electron trajectory passing close to the dimer extremity (the minimal distance between the nanoparticle surface and the electron trajectory is fixed to 0.5 nm) and perpendicular to the dimer main axis. (a), (f) Normalized loss probability evaluated using the standard formulation corresponding to Eq. (4). (b), (g) Normalized loss probability evaluated using the antenna theory corresponding to Eq. (5). (c), (h) Absorbed power (dashed lines) and scattered power (solid lines) shown as functions of the energy. The incident electron energy is 50 keV.

3.1. Where does the Energy go in Electron Energy Loss Spectroscopy of Nanostructures?

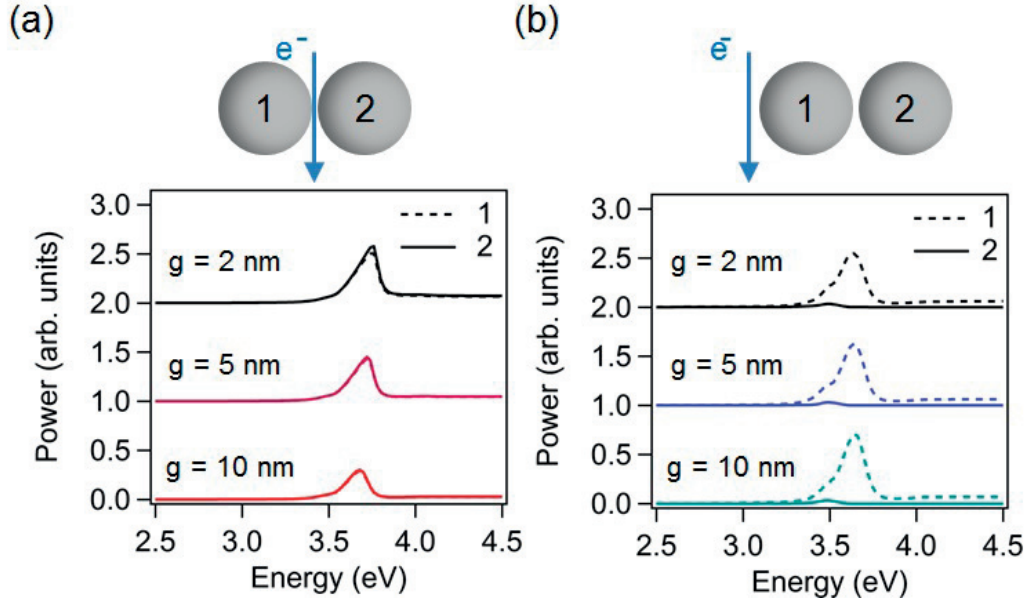


Figure S7 – EEL spectra of silver nanodimers in vacuum for (a) an electron trajectory passing through the dimer center and perpendicular to the dimer main axis and for (b) an electron trajectory passing close to the dimer extremity (the minimal distance between the nanoparticle surface and the electron trajectory is fixed to 0.5 nm) and perpendicular to the dimer main axis. The loss power is divided into the part absorbed in the nanoparticle 1 (dashed lines) and the nanoparticle 2 (solid lines). The incident electron energy is 50 keV.

3.2 Mode Coupling in Plasmonic Heterodimers Probed with Electron Energy Loss Spectroscopy

Manuscript state: Published

Reference: Flauraud, V., Bernasconi, G. D., Butet, J., Alexander, D. T. L. Martin, O. J. F., Brugger, J. "Mode Coupling in Plasmonic Heterodimers Probed with Electron Energy Loss Spectroscopy" *ACS Nano* **11**, 3485-3495, (2017).

Publication date: March 14, 2017

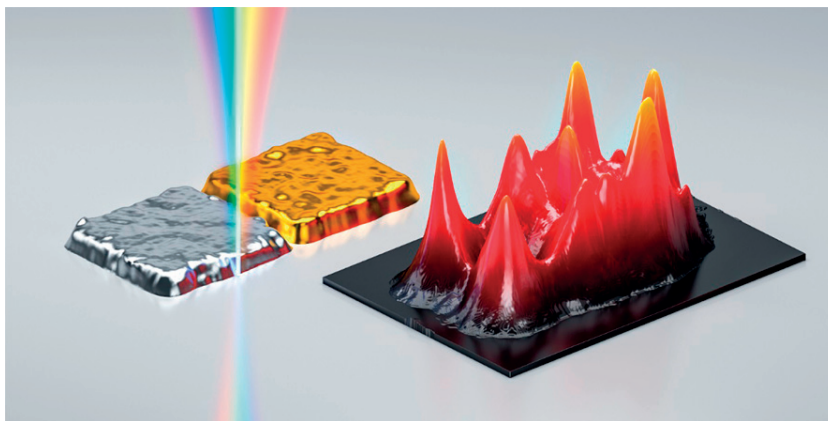
DOI: 10.1021/acsnano.6b08589

URL: <https://pubs.acs.org/doi/10.1021/acsnano.6b08589>

Adapted with permission from the above-mentioned reference.
Copyright (2017) American Chemical Society.

Author contributions

G. D. Bernasconi performed the numerical simulations and contributed to the data analysis and to the manuscript writing.



Mode Coupling in Plasmonic Heterodimers Probed with Electron Energy Loss Spectroscopy

Valentin Flauraud¹, Gabriel D. Bernasconi², J  r  my Butet², Duncan T.L. Alexander³, J  rgen Brugger¹ and Olivier J.F. Martin²

¹Microsystems Laboratory, ²Nanophotonics and Metrology Laboratory, and
³Interdisciplinary Center for Electron Microscopy, Swiss Federal Institute of
Technology Lausanne (EPFL), 1015, Lausanne, Switzerland.
Corresponding author: juergen.bugger@epfl.ch

ABSTRACT: While plasmonic antennas composed of building blocks made of the same material have been thoroughly studied, recent investigations have highlighted the unique opportunities enabled by making compositionally asymmetric plasmonic systems. So far, mainly heterostructures composed of nanospheres and nanodiscs have been investigated, revealing opportunities for the design of Fano resonant nanostructures, directional scattering, sensing and catalytic applications. In this article, an improved fabrication method is reported that enables precise tuning of the heterodimer geometry, with interparticle distances made down to a few nanometers between Au-Ag and Au-Al nanoparticles. A wide range of mode energy detuning and coupling conditions are observed by near field hyperspectral imaging performed with electron energy loss spectroscopy, supported by full wave analysis numerical simulations. These results provide direct insights into the mode hybridization of plasmonic heterodimers, pointing out the influence of each dimer constituent in the overall electromagnetic response. By relating the coupling of nondipolar modes and plasmon-interband interaction with the dimer geometry, this work facilitates the development of plasmonic heterostructures with tailored responses, beyond the possibilities offered by homodimers.

Introduction

Collective oscillations of the conduction electrons in metal nanostructures, known as localized surface plasmon resonances [1], have been intensively studied and designed by manipulating both the nanostructures size and geometry, as well as their dielectric environment [2]. These investigations, carried out over the entire visible light spectrum, including the near-UV and near-IR, have demonstrated the control of both nanoscale optical fields and far field radiation [1], leading to the concept of optical nanoantennas [2,3]. The electromagnetic properties of these structures are governed by their eigenmodes,

ranging from dipoles to high order multipoles [4,5]. When the nanoparticles are arranged in pairs or multimers, these modes couple to each other and hybridize, producing further optical properties [6-8]. In the simplest and most common geometry, involving the coupling of two self-similar spherical nanoparticles separated by a nanogap, a wellknown dipole-dipole interaction along the dimer axis is produced [6]. This coupling generates an intense and confined near field in the gap region, which can enable large nanoscale fluorescence enhancement [9] and surface enhanced Raman scattering down to the single molecule level [10,11]. Thanks to a complete description of the plasmonic coupling for spherical self-similar nanoparticle dimers, Nordlander and coauthors [7] have shown that the gap dependent hybridization in such nanostructures stems from the interaction of the uncoupled eigenmodes. Specifically, the uncoupled modes hybridize with bonding and antibonding interactions and each of these two configurations occur along the longitudinal and transverse axes of the nanodimer. As gap size decreases, and hence mode coupling increases, the bonding modes exhibit large red-shifts, whereas antibonding modes are subject to moderate blue-shifts. Additionally, the relative phase of the charge oscillation between the two nanoparticles may lead to either enhanced or vanishing net dipole moments, so forming, respectively, bright and dark modes [12].

Beyond symmetric dimers, heterogeneous pairs formed by two dissimilar nanoparticles, each having distinct spectral properties owing to a compositional or geometrical difference, have recently become a topic of wide interest. The resulting near field overlap and far field interference of eigenmodes with distinct energy or multipolar orders have been studied for a wealth of unique properties, such as directional scattering [13-15]; Fano resonances in both radiation [16-18] and absorption processes [19,20]; enhanced nonlinear processes [21]; photothermal effects [22]; sensing [15,23-25]; and catalysis [26,27]. As with symmetric dimers, the hybridized eigenmodes of these heterogeneous pairs (known as heterodimers) also originate from the uncoupled eigenmodes supported by each dimer constituent [7,16,28]. However, due to the reduced symmetry of the system, the hybridized modes of heterodimers will be less likely to possess a vanishing dipole moment, the latter effect being a direct consequence of the mirror symmetry of homodimers.

To date, most experimental studies of heterodimers have focused on their far field properties, by monitoring their dark field spectra [16,29,30] and radiation patterns [14]. Here we instead evidence the benefit of direct experimental investigations of their modal responses, especially for geometries beyond the sphere and disc dimers. Indeed, only a few experimental studies, mostly limited to large nanostructures exhibiting minimal energy mismatch [31] and limited design flexibility [32,33], have focused on measuring the near field properties of heterodimers in order to visualize and tailor their electromagnetic properties. In this article, we reveal the coupled modes of a wide range of heterodimers using electron energy loss spectroscopy (EELS) combined with a full wave analysis based on surface integral equations (SIE) methods. By fabricating heterodimers of different materials and geometries using a precise multilayer electron beam lithography fabrication process, we span a large range of energy detuning conditions and coupling strengths

3.2. Mode Coupling in Plasmonic Heterodimers Probed with Electron Energy Loss Spectroscopy

between each dimer component, thereby unveiling the rich electromagnetic properties of mismatched particle pairs.

Results and Discussion

Motivated by the unique opportunities enabled by asymmetric plasmonic systems, a vast palette of enabling nanofabrication methods has been developed. Exploiting the mode energy mismatch in heterodimers calls for techniques that can create narrow interparticle gaps in order to significantly hybridize the eigenmodes of the constituent elements [16]. To this end, colloidal assembly methods have been effective for providing simple access to few nanometer gaps, with techniques varying from capillary assembly [34,35] and electrostatic interactions [16,19,24,36] to DNA linkers [29,37] and origamis [30,38]. A different approach relies on the use of dielectric microbeads for hole-sphere lithography schemes, combined with tilted evaporation [14,15,33,39-42]. Although these various techniques are highly scalable and cost efficient, they suffer from a poor geometric degree of freedom. While mode energy detuning is the central aspect of asymmetric plasmonic systems, the mediation of coupling strength by controlling the geometry of each nanoparticle and their gap distance is essential to tailor their electromagnetic response. To this end, compositional asymmetry achieved with multistep lithography can be used advantageously to disentangle the influence of the mode energies and nanoparticle shapes on the coupled modes. To realize this capability, a double layer lift-off process based on electron beam lithography [21,25] was developed and optimized in order to reach few nanometer gap distances while exploiting the geometric freedom of lithography. The process, outlined in Figure 1a,b, is entirely carried out on freestanding Si_3N_4 membranes; an approach that enables high resolution metrology of the heterodimers by transmission electron microscopy as well as their electromagnetic characterization with EELS. Briefly, alignment marks are etched on the front side of a silicon substrate, which is subsequently coated with low-pressure chemical vapor deposition Si_3N_4 . The Si_3N_4 layer is then locally released by backside processing. Next, multiple steps of electron beam lithography, evaporation and lift-off steps are repeated on the membrane for each Au, Ag and Al layer (see Methods for details). The high quality markers and the related alignment scheme reliably enable a sub-10 nm layer-to-layer alignment accuracy and a reproducible fabrication of heterodimers arrays with few-nanometer interparticle distances. The ultimate nanogap resolution and dispersion are limited by the metal line-edge roughness and the associated thin-film polycrystallinity (Figure S1). After fabrication, structure topography was characterized by atomic force microscopy, and the overall dimensions and gaps were measured by transmission electron microscopy and high angle annular dark field scanning transmission electron microscopy (HAADF STEM), for both Au-Ag (Figure 1c-f) and Au-Al heterodimers (Figure 1g-i). In addition, scanning transmission electron microscopy energy dispersive X-ray spectroscopy (EDX) was performed to verify the quality and absence of contamination in the Ag nanostructures (Figure S2), as well

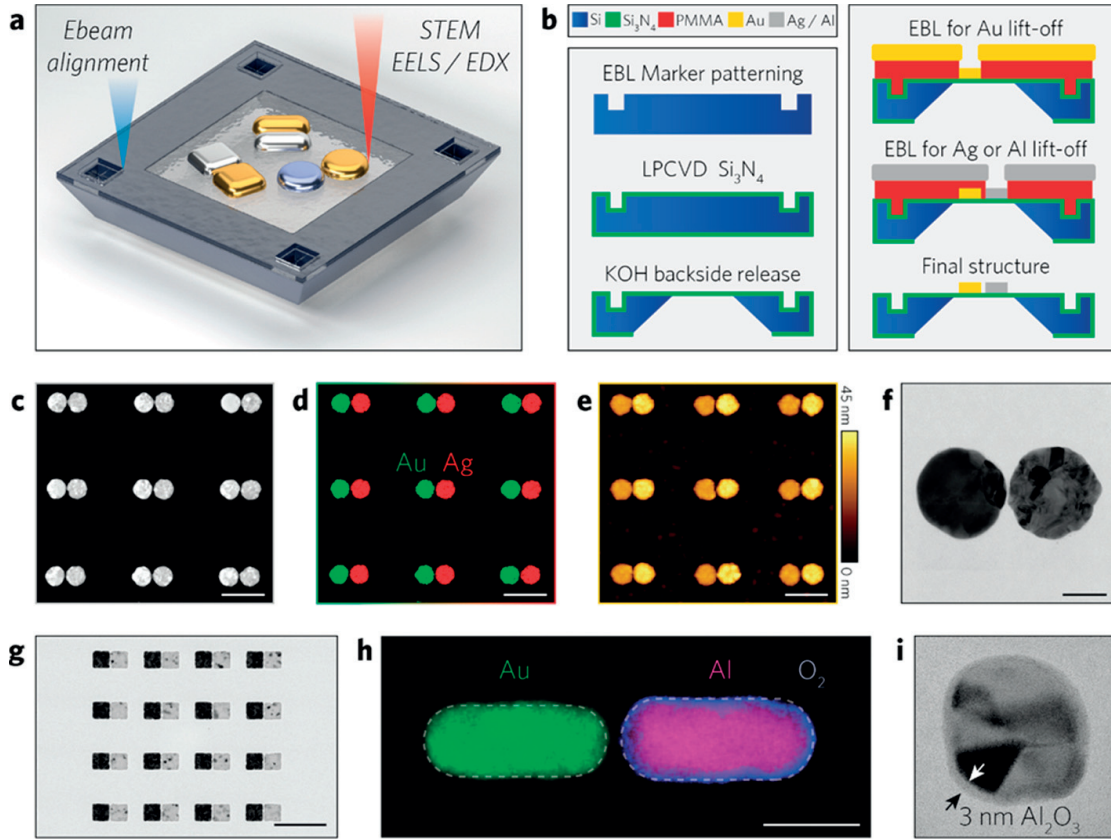


Figure 1 – Heterodimer fabrication. (a) Schematic representation of a freestanding Si_3N_4 membrane, lithographically patterned structures, and electron beam lithography alignment marks on the Si frame. (b) Fabrication process including marker patterning, membrane release, and subsequent aligned lift-off steps. (c) HAADF STEM image of Au-Ag dimers, (d) corresponding EDX Au-Ag map, and (e) AFM topography map. (f) TEM image of a single, nanometer gap dimer. (g) Au-Al square dimer array. (h) Au-Al nanorod dimer EDX map, with the Al surface oxide shown in blue. (i) TEM image of the Al_2O_3 layer, shown by a lack of diffraction contrast in comparison with the crystalline Al grain. Scale bars are 200 nm (c,d,e), 50 nm (f, h), and 500 nm (g), respectively.

3.2. Mode Coupling in Plasmonic Heterodimers Probed with Electron Energy Loss Spectroscopy

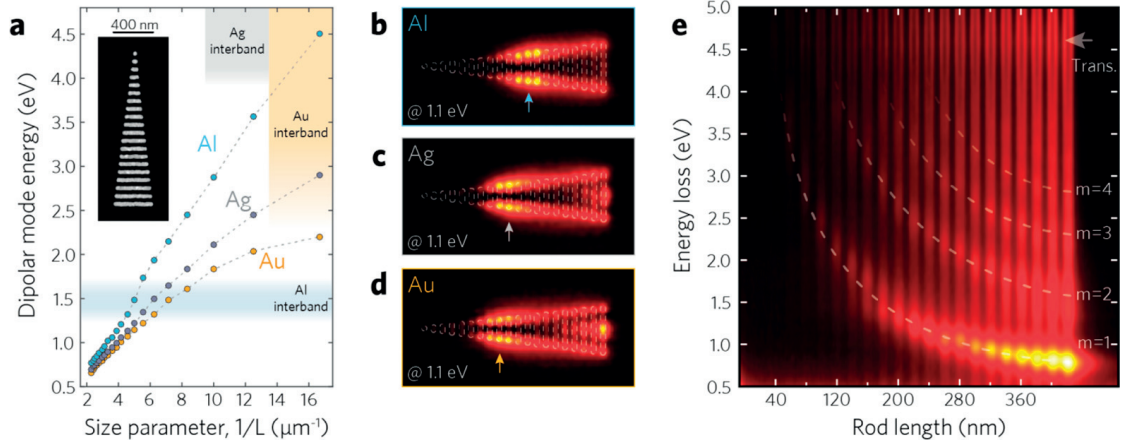


Figure 2 – Material dependent resonance energies. (a) Resonant energy of the dipole mode as a function of the inverse of the nanoparticle length L , measured from a series of nanoparticles of varying aspect ratios as shown in the HAADF STEM image in inset. Interband regions are shown schematically. (b-d) EELS intensity maps extracted at 1.1 eV from the three datacubes acquired for similar parallel nanorod sequences made with Al, Ag, and Au, respectively. (e) EELS response from the Al nanorod sequence. The datacube was binned spatially along the nanorod axis yielding an energy against rod length visualization, displayed here to highlight the size dependent evolution of higher order modes in Al nanorods.

as the composition and stability of the 3 nm-thick alumina layer on the Al nanoparticle surfaces.

Au, Ag and Al were chosen as prototypical materials of the constituent nanoparticles due to their ability to support plasmonic resonances and interband transitions at distinct energies. While layered [43] and alloyed [44] materials may also be of interest for the fabrication of heterogeneous plasmonic systems, the present study focuses on the coupling of the aforementioned pure metals [45,46]. In order to first characterize the response of each constituent metal used to make the heterodimers, EELS measurements were performed on monometallic Au, Ag and Al arrays of nanorods with varying lengths, ranging from a 40 nm diameter dot to a 400×40 nm rod. By measuring the evolution of the longitudinal dipolar mode energy as a function of the nanorod size, the spectral tunability and resonance range of the different materials is evidenced for this specific morphology evolution (Figure 2a). Resonance energy differences between each material stem from their different free electron densities and associated plasma frequencies as well as the difference in their intrinsic losses due to collisions. As particle aspect ratio decreases (and wavenumber increases), the energy difference between dipole modes of two equivalently sized nanoparticles of different materials increases. Al displays the largest energy tunability across the geometric parameter space investigated here [47], due to its higher plasma frequency [48]. Interestingly, the interband transitions of Al, occurring at 1.5 eV, are well evidenced by a discontinuity in the dispersion curve around

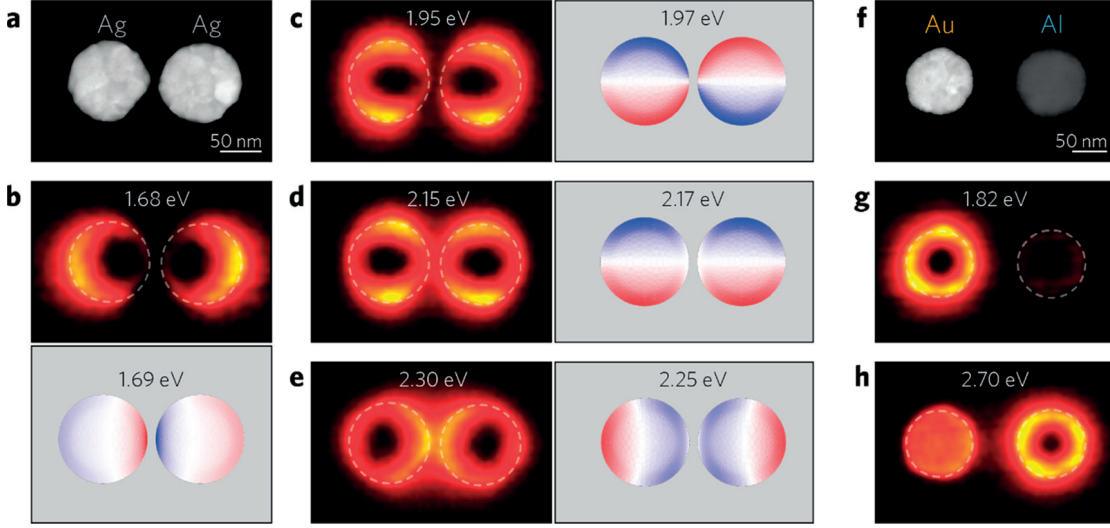


Figure 3 – EELS response of a coupled homodimer and weakly coupled heterodimer. (a) HAADF STEM image of an Ag homodimer with ~ 100 nm disc diameter and ~ 9 nm gap width. Experimental EELS maps of the homodimer and associated computed eigencharge distributions for (b) the longitudinal bonding, (c) the transverse bonding, (d) the transverse antibonding, and (e) the longitudinal antibonding modes. (f) Au-Al heterodimer with ~ 100 nm disc diameter and 60 nm gap width and the associated EELS intensity maps of the dipole modes of (g) the Au nanoparticle and (h) the Al nanoparticle.

this energy loss. Already for EELS intensity maps extracted at a relatively low energy (1.1 eV Figure 2b-d), the detuning between the different materials is clearly observed, as their dipolar modes are supported by nanorods of different lengths; a quadrupolar EELS response also appears on the longest Au and Ag nanorods. Note that the localization and symmetry of the focused electron probe used in STEM EELS allows for an efficient excitation of high order modes, regardless of their radiative nature [49] as shown in Figure 2e. Within the parameter space displayed, it is clear that bimetallic dimers formed from nanoparticles of equal dimensions may exhibit two distinct mode energy mismatch conditions. First, for large nanostructures, the dipolar and/or higher order modes of one nanoparticle may spectrally overlap with those of the other, resulting in a significant plasmonic coupling. Second, a different condition is predicted for small particle dimers, especially for Au-Al pairings, where the energy of the fundamental dipole of the Al component may be at sufficiently high energy to avoid having any significant spectral overlap with any of the modes supported by the Au component. Both of these coupling conditions are investigated in the next section, by the study of the near field response of selected heterodimers.

First we highlight the specificities of EELS signals associated with mode hybridization in symmetric pairs [50-52], by investigating the response of an Ag-Ag disc homodimer with a diameter of 100 nm and gap of 9 nm (Figure 3a). The eigenmodes of the corresponding

3.2. Mode Coupling in Plasmonic Heterodimers Probed with Electron Energy Loss Spectroscopy

structure are computed using a surface integral equation (SIE) method, solving for the eigenvectors of the associated matrix [53]. Four modes, mainly based on dipole-dipole interactions, are identified, and compared to those of an isolated Ag monomer of similar dimensions having a dipole resonance energy of ~ 2.12 eV (Figure S3). As expected, the bonding modes (longitudinal and transverse Figure 3b,c) are red-shifted in comparison to the dipolar mode supported by the solitary Ag disc. The strong coupling of the bonding longitudinal mode (Figure 3b) is evidenced by a larger red-shift, along with a strong EELS intensity inhomogeneity in each nanoparticle which vanishes in the gap region. This insensitivity of EELS to bonding modes in gap regions, as compared to strong gap sensitivity to antibonding modes, has been thoroughly discussed in relation to the field symmetry of the electron probe [54,55]. Although EELS does not directly map the electromagnetic near field and cannot reveal high intensity hot-spots formed by bonding interactions, this apparent limitation actually proves useful in distinguishing the coupling nature and symmetry of hybridized modes. The aforementioned signal silencing in the gap is also seen for the transverse bonding modes in Figure 3c, but to a lesser extent due to the weak interaction between transverse modes. In contrast, both of the higher energy transverse (Figure 3d) and longitudinal modes (Figure 3e) exhibit a strong EELS signal in the gap region, which expresses their antibonding nature. In agreement with the simulated eigenmodes, the longitudinal antibonding mode is the most blue-shifted, owing to a strong near field interaction for this dipole orientation. Besides small asymmetries in the EELS intensity maps, which arise from the grain structure of the fabricated nanodimers, the near field maps of the two dimers have a mirror symmetry, in keeping with their compositional and structural symmetry.

The EELS response of a heterodimer is now considered, but one with limited coupling. In order to minimize the electromagnetic interactions, discs made of Au and Al are chosen, yielding a large energy separation between their isolated particle plasmonic modes. They are positioned 60 nm apart from each other (Figure 3f). In consequence, each disc's unique dipolar mode is observed, at 1.82 eV (Figure 3g) and 2.70 eV (Figure 3h) for Au and Al, respectively. Due to the weak coupling between the nanoparticles, the longitudinal and transverse modes do not split and are therefore degenerated [56]. Consistent with this, the EELS maps display no nodes or specific symmetry relations to the dimer axis. At 2.70 eV the Au nanoparticle shows a strong and uniform EELS signal, corresponding to uniform interband absorption inside it (Figure 2a).

Now we move to a heterodimer displaying strong mode hybridization, by investigating an Au-Ag disc dimer (Figure 4a) with the same geometry as that of the Ag-Ag dimer discussed earlier. The EELS spectra extracted at different locations of this heterodimer (Figure 4b) show various resonances, the intensity of which varies with the position of the electron beam, as also observed in EELS simulations (Figure S4). The EELS maps suggest that the electromagnetic near field is mainly localized close to the Au nanoparticle for the two lowest energy modes (that support a dominant longitudinal (Figure 4c) and transverse (Figure 4d) dipolar contribution). This is in agreement with

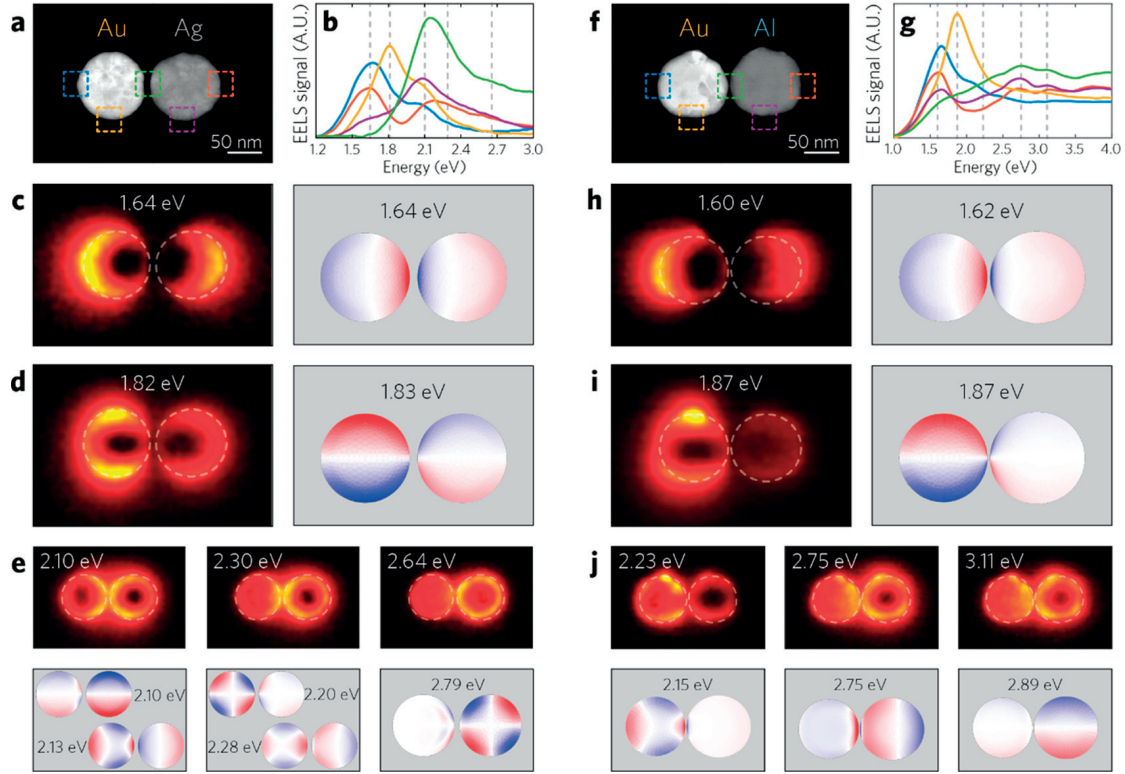


Figure 4 – Coupled Au-Ag and Au-Al disc heterodimers. (a) HAADF STEM image of an Au-Ag heterodimer with ~ 100 nm disc diameter and ~ 10 nm gap width. (b) Experimental EELS spectra corresponding to the impact positions highlighted in (a). EELS maps and associated eigencharges for modes dominated by (c) the longitudinal dipole mode in the Au nanoparticle, (d) the transverse dipole mode in the Au nanoparticle, and (e) some combinations of dipole mode in the Ag nanoparticle with high order modes of the Au nanoparticle. (f) HAADF STEM image of an Au-Al heterodimer with ~ 100 nm disc diameter and ~ 2 nm gap width. (g) Experimental EELS spectra corresponding to the impact positions highlighted in (f). EELS maps and associated eigencharges for modes dominated by (h) the longitudinal dipole mode in the Au nanoparticle, (i) the transverse dipole mode in the Au nanoparticle, and (j) some combinations of dipole mode in the Al nanoparticle with high order modes of the Au nanoparticle (j).

3.2. Mode Coupling in Plasmonic Heterodimers Probed with Electron Energy Loss Spectroscopy

previous EELS computations performed for detuned dimers [57]. As revealed by the eigenmode simulations, the charge distributions on the Ag disc surface (Figure 4c,d) also have a dipolar nature, although weaker and with opposite phase. This behavior is due to the energy mismatch of the dipolar modes of each nanoparticle and is reminiscent of the transverse antibonding mode of a symmetric structure (Figure 3c). In this Au-Ag heterostructure, the overlap between the Ag dipole (~ 2.12 eV) and Au quadrupole (~ 2.22 eV Figure S3) allows for a strong interaction between these modes (Figure 4e). This especially holds for the longitudinal hybridized modes, as also evidenced in simulations, that tend to bonding (eigenmode at 2.13 eV) and nearly antibonding (eigenmode at 2.28 eV) configurations, reminiscent of observations made in symmetric dimers (Figure 3b,e). As discussed previously, the weaker interaction between transverse modes leads to two hybridized modes with a limited coupling (and thus energy shift), one with a strong transverse dipole mode in the Ag nanoparticle (eigenmode at 2.10 eV) and another with a strong transverse quadrupole mode in the Au nanoparticle (eigenmode at 2.20 eV). Here we use the terminology transverse quadrupole for modes having an odd parity (charge-wise) relatively to the dimer axis, and longitudinal for an even parity, analogously to the dipole modes. The spectral proximity of these four modes, between 2.10 and 2.28 eV, results in a partial overlap of their contribution in the experimental EELS maps. Nevertheless, the nature of the dominant longitudinal modes is evident from the subtle differences in the EELS intensity maps such as the stronger signal confinement in the gap region at 2.30 eV from the antibonding mode compared to the bonding mode at 2.10 eV. For the quadrupole mode in the Ag nanoparticle, the EELS map (2.64 eV) shows a rotational symmetry around the center of the Ag disc, indicating that the coupling of this mode with the nearby Au disc is weak. This is in agreement with the calculated eigenmode that shows a charge distribution on the Ag disc barely affected by the neighboring Au disc. Overall, our analysis provides an important insight into the response of this system which has been previously studied for the purpose of directional color routing [14]. Namely, all the observed modes possess a net dipole moment and therefore varying degree of far-field radiation symmetry (Figure S5). When the coupled modes entail a large energy mismatch, they are predominantly supported by a single constituent (here the dipole in the Au nanodisc); whereas a collective response is favored for modes with matching energy (here the quadrupole in the Au disc and the dipole in the Ag one), even if the original modes have a distinct multipolar nature.

A similar analysis was carried out for smaller dimers with 50 nm disc diameter (Figure S6), demonstrating the influence of the dimer size, associated with energy tuning, on the mode hybridization. In the case of small Au-Ag discs, the increased energy mismatch between the Au and Ag modes (Figure 2) leads to a minimal contribution of the high order (i.e., quadrupole) modes. Indeed, only the longitudinal dipole mode of the Au nanoparticle exhibits a significant coupling with the Ag nanoparticle (Figure S6c). The intrinsic modes of the Ag nanoparticle are at energies corresponding to the Au interband transitions, and so are only weakly coupled to the Au nanoparticle. At this point, the Au

disc effectively acts as a modification of the dielectric environment of the Ag nanoparticle with nonresonant properties (Figure S6e-g).

These observations on the 50 nm disc diameter Au-Ag heterodimer, which are in excellent agreement with previous far-field optical studies of geometrically comparable systems, [29,30], prompt the investigation of phenomena occurring with the large energy detuning associated with Au-Al disc dimers (Figure 4f-j). The small gap width (2 nm) is intended to compensate for the large spectral mismatch between the modes of the isolated nanoparticles, by creating a strong near field overlap. Similarly to the Au-Ag 100 nm disc dimer studied previously, EELS spectra were recorded for various positions of the electron beam (Figure 4g) and intensity maps made for different observed resonance energies (Figure 4h-j). A near field asymmetry much larger than that for the Au-Ag 100 nm disc dimer is revealed for the low energy maps, as the dipole in the Au nanodisc couples only weakly to the dipole in the Al disc in both the longitudinal (Figure 4h) and transverse (Figure 4i) directions. Also, for this structure, the near field coupling involving the longitudinal quadrupole in the Au nanodisc is now well evidenced because of its limited overlap with other modes (Figure 4j 2.23 eV). The EELS maps for the longitudinal dipole (2.75 eV) and transverse dipole (3.11 eV) in the Al nanodisc in turn exhibit limited coupling and thus rotational symmetry. These results are similar to the observations made for the Au-Ag dimer with 50 nm disc diameter where, again, each coupled mode is mainly associated with one constituent of the dimer. Nevertheless, the EELS maps associated with the higher energy modes (Figure 4j) exhibit strong signal modulations in the Au disc. This evidences the strong absorption modulation in the off resonant system, since the near-field associated with the resonant component decays into the nonresonant nanoparticle [20,26].

In order to favor the resonant interaction between detuned modes, we exploit the opportunities of our lithographic fabrication method to design square dimers. Compared to round dimers, these structures allow for a distinct Coulomb interaction at similar gap distances. These structures also break the rotational symmetry in discs that was observed with some EELS maps, while preserving the degeneracy of the uncoupled eigenmodes along the longitudinal and transverse directions. Considering first an Au-Ag dimer with a 100 nm square side length and average 2.2 nm gap (Figure 5a), very limited asymmetry in the lowest energy mode is seen (Figure 5b) as compared to the disc case, due to the enhanced coupling. On the other hand, asymmetry in the EELS map is observed for a transverse dipole in the Au nanosquare, which is more weakly coupled (Figure 5c). Now considering higher order modes, due to the strong spatial coupling conditions induced by the gap geometry, a complex hybridization scheme is expected, involving multiple high order contributions [7]. This is seen with the coupling of the longitudinal dipole in the Ag nanoparticle to highly multipolar modes in the Au nanoparticle (Figure 5d,e), where the eigencharge distributions for the closest energy matching modes reveal numerous nodes in the gap region. Above the Au interband threshold, the 2.76 eV EELS map is characteristic of an octupole in the Ag nanoparticle (Figure 5f) with a limited coupling

3.2. Mode Coupling in Plasmonic Heterodimers Probed with Electron Energy Loss Spectroscopy

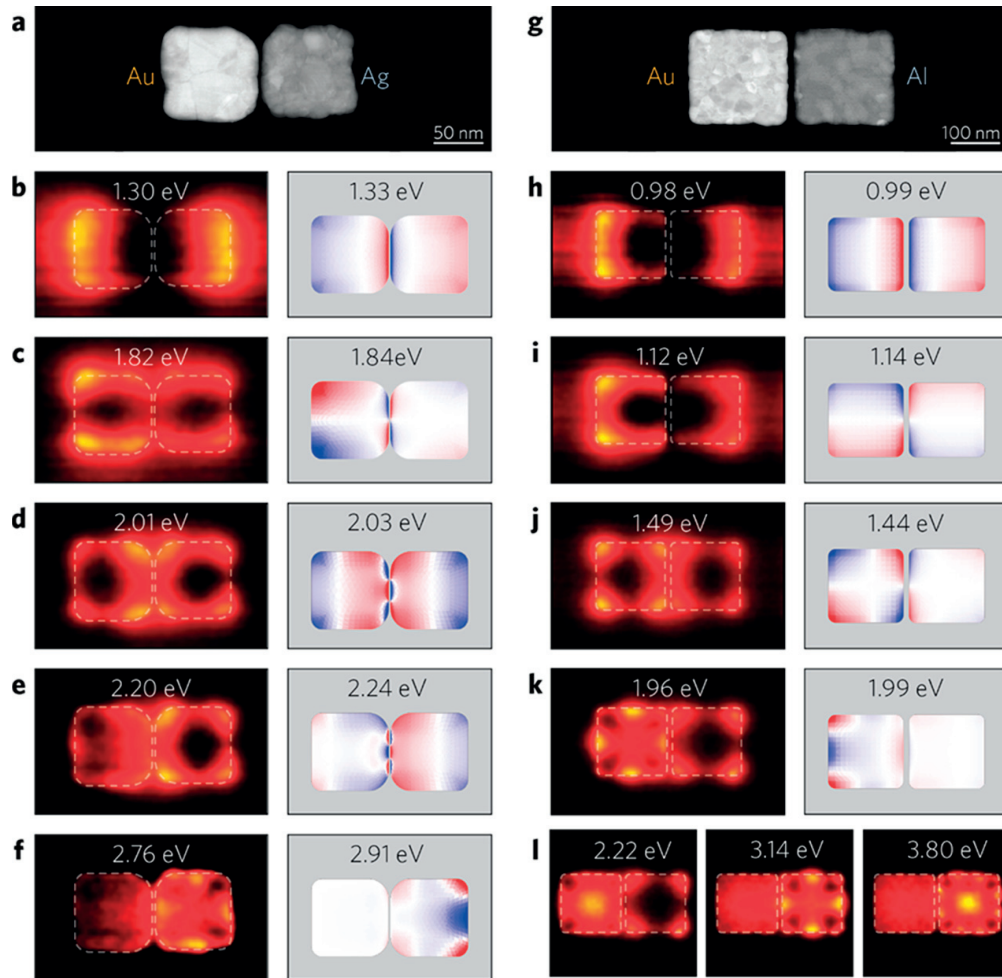


Figure 5 – Coupled Au-Ag and Au-Al square heterodimers. (a) HAADF STEM image of a Au-Ag square heterodimer with 100 nm square edge length and 1.5 nm gap. (b-f) EELS maps and the corresponding computed eigencharge distributions for the Au-Ag dimer. (g) HAADF STEM image of a Au-Al square heterodimer with 200 nm square edge length and 10 nm gap. (h-l) EELS maps and the corresponding computed eigencharge distributions for the Au-Al dimer.

to the Au nanoparticle. Similar observations are made for a larger (200 nm square side length) Au-Al dimer with 15 nm gap (Figure 5g-l). Considering the dispersion curves in Figure 2a, the large square size allows for a reduced energy mismatch between the Au and Al nanoparticles compared to the Au-Al disc dimer discussed previously. Additionally, the larger gap limits the contribution of high order modes that lead to complex nodal patterns in the gap. Low energy longitudinal (Figure 5h) and transverse (Figure 5i) modes follow the mechanisms pointed out previously; however the interplay between high order modes is better revealed in this differently coupled nanodimer. Quadrupole (Figure 5j) and octupole (three nodal lines) (Figure 5k) modes in the Au nanoparticle now couple efficiently to nondipolar modes in the Al one. Indeed, the quadrupolar mode in the Au nanoparticle is coupled to another weak quadrupolar charge distribution in the Al nanoparticle, whereas, at even higher energy, the Au octupolar mode couples weakly to the Al nanoparticle, leading to asymmetric surface charge deformations involving multiple contributions in the Al nanoparticle. At 2.22 eV, the quadrupole supported by the Al nanosquare is then imaged overlapping in energy with the breathing mode in the Au nanoparticle, with high EELS signal at the square center [56]. Uncoupled high order multipoles in the Al square are mapped at 3.14 (octupole) and 3.80 eV, with additional contribution of a breathing mode for the latter (Figure 5l). The engineering of the gap geometry therefore allows resonant coupling conditions to be achieved beyond those of the well-studied dipole-dipole interactions or dipole-quadrupole interactions observed in the disc heterodimers.

Finally, in order to tune resonant coupling conditions even further, heterodimers composed of Au and Ag nanorods are considered. Contrary to the nanodiscs and nanosquares studied previously, individual nanorods possess longitudinal and transverse modes at distinct energies. When coupled, this property is useful to favor selected interactions, depending on the spatial arrangement of the nanorods. As serial (i.e., end-to-end) nanorod homodimers are coupled by their apexes, the low energy bonding mode is bright and the high energy antibonding mode is dark [28,58]. This relation is inverted in the case of parallel (i.e., side-by-side) rod homodimers, which are coupled by their edges [28,58]. Considering these geometries in heterodimer form (Figure 6a,d), in both cases the hybridized modes observed at the lowest energy correspond to a strong excitation of the nanorod which has the lowest energy resonant dipole mode (Figure 6b,e). At the same time, the high energy mode corresponds to a strong excitation of the nanorod possessing the dipole mode resonant at the highest energy (Figure 6c,f). When the coupling is weak, i.e., when the gap is larger than ~ 10 nm, the distinct radiative signatures of both components is recognized in the global (plane wave excitation) response of the dimers, and a Fano resonance is observed due to the interference between the dipolar modes (Figure S7b) [18,59]. Upon increased coupling (e.g., by reducing gap size), the radiative nature of one or the other mode is significantly modulated, leading to a weakening of the Fano line shape as well as the appearance of a strong absorption modulation, as previously reported for spherical heterodimers. [19,20,60]. EELS does not only provide

3.2. Mode Coupling in Plasmonic Heterodimers Probed with Electron Energy Loss Spectroscopy

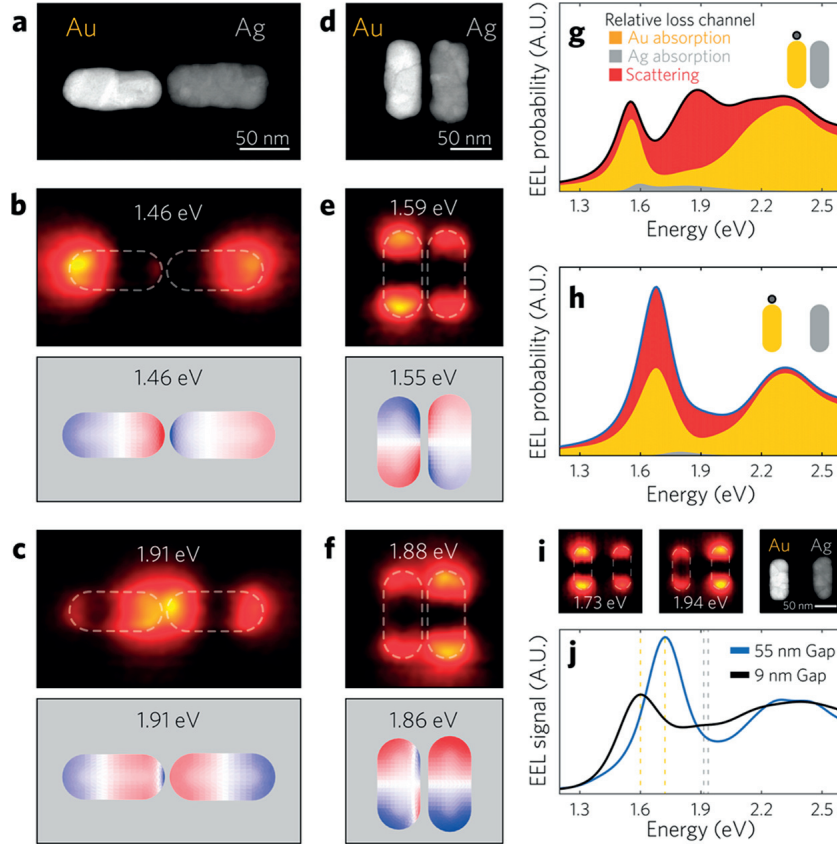


Figure 6 – Nanorod heterodimers. (a) HAADF STEM image of a Au-Ag heterodimer, where the nanorods are coupled by their apices. EELS maps and computed eigencharge distributions for (b) the bonding and (c) antibonding dipole modes. (d) HAADF STEM image of a Au-Ag heterodimer, where the nanorods are coupled by their edges. EELS maps and computed eigencharge distributions for (e) the bonding and (f) antibonding dipole modes. Computed EELS signal from the end of the Au nanorod from a parallel dimer with (g) a 9 nm gap and (h) a 55 nm gap, respectively. The decomposition into the different loss mechanisms is represented by the filled areas under the curves. (i) EELS maps and HAADF image of the 55 nm gap parallel heterodimer. (j) Measured EEL spectra integrated over the Au nanorod for the two heterodimers.

information on the near field distributions and the modal nature of the observed peaks, but also an insight into the evolution of the absorption and scattering mechanisms [61-63]. Indeed, the relative weights of these two loss channels is expected to evolve upon geometric modifications. For example, in the case of the parallel rod dimers, a strong reduction of the radiative channel is seen as the gap width reduces, as emphasized by the simulated EELS decompositions (Figure 6g,h and also evidenced by the plane wave scattering Figure S7b) [64]. This weakened scattering, responsible for the reduction of the absolute EELS signal, is well measured experimentally (Figure 6i,j and Figure S8), emphasizing that the combination of EELS with accurate modeling permits the tracking of energy loss mechanisms in heterodimers. By tuning the gap width and the parallel or serial arrangement of nanorod Au-Ag dimers, one can therefore favor or inhibit the optical access, namely the net dipole moment, of modes associated with either the Au or Ag constituent. In turn, this enables a specific engineering of the absorption within the system, as in the parallel nanorod configuration where a large enhancement of absorption in the Au nanoparticle, at the resonance energy of the Ag nanorod, may be achieved with increased coupling.

Conclusion

In conclusion, by combining the high flexibility of electron beam lithography for the fabrication of coupled plasmonic nanostructures of various geometries with near field imaging using EELS, we have reported experimental insights into the coupling occurring in heterogeneous plasmonic dimer systems. The case of heterodimers composed of discs was considered first, and then used as a benchmark for the investigation of the role of the gap lateral extent (in square nanodimers) and mode selection (in nanorod dimers). Especially, the importance of both the spatial and spectral overlap between the modes has been explored. The results provide opportunities for the design of heterodimers with tailored interactions, such as the coupling of plasmonic modes of different multipolar nature or the engineering of absorption within the dimers. They therefore provide efficient means to control of the nanoscale optical response, enabling efficient tuning of directional scattering [14], Fano interferences [65], molecular sensing [66] and multiple bright resonances for broadband fluorescence enhancement [67], as well as second harmonic generation [68].

Methods

Sample Fabrication

Silicon wafers (100 mm diameter, 380 μm thickness prime grade double side polished) were cleaned following a standard RCA procedure prior to the fabrication of front side alignment marks. Positive photoresist (AZ ECI 3000, 0.6 μm) was spun and exposed by direct laser writing (Heidelberg Instruments VPG-200) and developed. The markers were

3.2. Mode Coupling in Plasmonic Heterodimers Probed with Electron Energy Loss Spectroscopy

etched in the Si wafers by RF biased SF6 dry etching (Adixen AMS200) to a depth of 3 μm followed by another RCA cleaning step and low pressure chemical vapor deposition of 30 nm-thick silicon nitride. Backside photolithography and wet etching by potassium hydroxide were performed to release $500 \times 100 \mu\text{m}^2$ freestanding silicon nitride windows. A single layer of poly(methyl methacrylate), (PMMA 495 A2, Micro- Chem) was then spun at 2500 rpm for 60 s yielding an approximately 90 nm-thick coating following a 3 min bake at 180 °C prior to the coating of a conductive layer (Espacer 300Z ShowaDenko, 2000 rpm, 60 s). The samples were then exposed by electron beam lithography (VISTEC EBPG5000+, 100 kV), rinsed in deionized water to remove the conductive coating and developed at room temperature for 60 s in a 1:3 mixture of methyl isobutyl ketone and isopropyl alcohol. Chromium and Gold (0.5 nm/25 nm) were evaporated first by electron beam heating at a base pressure of 8×10^{-7} mBar prior to lift-off in acetone. In a second step, lithography, evaporation and lift-off were repeated for the Ag or Al structures. Al was evaporated with 35 nm thickness after overnight pumping of the evaporation chamber to reduce residual water at the wafer surface in order to obtain low line edge roughness and high shape accuracy. Ag was evaporated with 30 nm thickness using a 0.5 nm Ni wetting layer that was shown to improve the quality of otherwise poorly wetting Ag films [69]. Alignment markers were protected by Kapton stencils during each evaporation steps. After all lift-off steps, the samples were finally cleaved in $3 \times 3 \text{ mm}^2$ dies for measurements in the TEM and stored in N₂ cabinets in order to preserve Ag from ambient contamination.

Alignment Accuracy

In order to assess the accuracy and repeatability of feature dimensions and gap widths, heterodimer arrays and Vernier patterns were imaged in both TEM and STEM mode (FEI Talos 200 kV) and the images were processed with a custom Matlab toolbox. The Vernier patterns (S1) allowed for the measurement of alignment accuracy with limited influence of metal line edge roughness. Inspection of the Vernier patterns revealed consistent ($\sim 90\%$) alignment equal or better than 10 nm offset on each axis. An example with sub-5 nm alignment is shown in Figure S1c,e. In addition to layer to layer alignment, metal wetting and line edge roughness were found to be the main contributions of gap variations with a standard deviation ~ 2.5 nm (Figure S1f,g). Overall, designs included arrays with gaps down to 10 nm overlap guaranteeing that the target designs of sub-5 nm were consistently achieved.

EELS Measurements

STEM-EELS maps were acquired using a FEI Titan Themis 60-300 equipped with a Wien-type monochromator and a Gatan GIF Quantum ERS spectrometer. A 300 keV incident electron beam was used for all experiments, monochromated to give an energy

spread of ~ 110 meV fwhm in the zero-loss peak of elastically scattered electrons, and with beam currents of ~ 240 pA. A 17 mrad convergence semiangle of the probe and a 22 mrad collection semiangle on the spectrometer were used, with the probe having a mean diameter of <1 nm for full width at tenth maximum in incident intensity. Mapping was performed using the “ultrafast” spectrum imaging mode with typical dwell times of 0.20 to 0.26 ms per pixel, and with the probe rastered in X, Y step sizes of 0.5-0.6 nm for a total of $>10^5$ pixels per map. Each map was treated with the HQ Dark Correction plugin to reduce noise associated with dark current subtraction.

EELS Data Processing

The EELS data cubes were processed using Gatan Digital Micrograph and custom Matlab scripts for the removal of the background from the tails of the zero-loss peak (ZLP), and extraction of point spectra and spatial EELS maps. The ZLP was first centered pixel by pixel using a Gaussian-Lorentzian approximation. Following zero-loss alignment, each data cube was spectrally cropped to the region of interest including the ZLP (-2 to 6 eV), and artifacts from cosmic rays were removed. To account for the absorption and other scattering mechanisms inside the metal nanoparticles, the data cubes were normalized by dividing each pixel-spectrum by the integrated zero-loss fit. Spectra in Figure 3 were integrated over a 30×30 pixel region of interest centered around the point overlaid on the STEM image, whereas EELS maps were typically integrated over a 0.06 eV window. For visualization purposes, the maps were smoothed using a penalized least-square method [70]. Overall, the resonance peak positions are identified from spectra extracted in regions with high EELS signal and with minimal spatial overlap with other resonances allowing for a high fitting accuracy, the main limitations being the effect of the precision of the ZLP alignment at higher energy losses and the ZLP convolution with the resonances at lower energy losses.

Simulations

A surface integral equation method [71] is used to compute the interaction between the electromagnetic field associated with the swift electron and the plasmonic nanostructures as well as for the computation of the eigenmodes. The nanostructure’s surface is discretized with triangular mesh elements and the electric and magnetic fields in the entire space (inside and outside the nanoparticle) are related to fictitious electric and magnetic surface currents through a matrix describing the geometry and material of the structure. EELS is computed in two steps: first by exciting the structure with the fields associated with a swift electron, and then by computing the work done on the electron by the Lorentz force against this scattered field [72,73]. The eigenmodes are found by looking for the eigenvectors of the aforementioned matrix when no excitation is imposed [53]. Concerning the eigenmode analysis, a Drude model is used for the permittivities of

3.2. Mode Coupling in Plasmonic Heterodimers Probed with Electron Energy Loss Spectroscopy

Au, Ag and Al, fitted to the experimental values found in ref [74] for Au and Ag and in ref [75] for Al. The same experimental values are used for the computation of the EELS and plane wave spectra. For all simulations, a homogeneous background medium of permittivity $\epsilon = 1.8$ (index $n = 1.34$) is used to account for the influence the SiN substrate ($\epsilon = 4$).

Acknowledgement

The research leading to these results has received funding from the European Commission's Seventh Framework Programme (FP7-ICT-2011-7) under grant agreements 288263 (Nano-Vista) and ERC-2015-AdG-695206 (Nanofactory) and from the Swiss National Science Foundation (SNSF) (200020_153662). The authors gratefully acknowledge the valuable support from the EPFL center of micro and nanofabrication (CMi).

References

- [1] Biagioni, P.; Huang, J.; Hecht, B. Nanoantennas for Visible and Infrared Radiation. Rep. Prog. Phys. 2012, 75, 024402.
- [2] Mühlischlegel, P.; Eisler, H.-J.; Martin, O. J. F.; Hecht, B.; Pohl, D. W. Resonant Optical Antennas. Science 2005, 308, 1607-1609.
- [3] Novotny, L.; van Hulst, N. Antennas for Light. Nat. Photonics 2011, 5, 83-90.
- [4] Kelly, K. L.; Coronado, E.; Zhao, L. L.; Schatz, G. C. The Optical Properties of Metal Nanoparticles: The Influence of Size, Shape, and Dielectric Environment. J. Phys. Chem. B 2003, 107, 668-677.
- [5] Oldenburg, S. J.; Hale, G. D.; Jackson, J. B.; Halas, N. J. Light Scattering from Dipole and Quadrupole Nanoshell Antennas. Appl. Phys. Lett. 1999, 75, 1063-1065.
- [6] Jain, P. K.; El-Sayed, M. A. Plasmonic Coupling in Noble Metal Nanostructures. Chem. Phys. Lett. 2010, 487, 153-164.
- [7] Nordlander, P.; Oubre, C.; Prodan, E.; Li, K.; Stockman, M. I. Plasmon Hybridization in Nanoparticle Dimers. Nano Lett. 2004, 4, 899-903.
- [8] Prodan, E.; Radloff, C.; Halas, N. J.; Nordlander, P. A Hybridization Model for the Plasmon Response of Complex Nanostructures. Science 2003, 302, 419-422.
- [9] Kinkhabwala, A.; Yu, Z.; Fan, S.; Avlasevich, Y.; Mullen, K.; Moerner, W. E. Large Single-Molecule Fluorescence Enhancements Produced by a Bowtie Nanoantenna. Nat. Photonics 2009, 3, 654-657.
- [10] Arroyo, J. O.; Kukura, P. Non-Fluorescent Schemes for Single- Molecule Detection, Imaging and Spectroscopy. Nat. Photonics 2016, 10, 11-17.
- [11] Zhang, W.; Fischer, H.; Schmid, T.; Zenobi, R.; Martin, O. J. F. Mode-Selective Surface-Enhanced Raman Spectroscopy Using Nanofabricated Plasmonic Dipole Antennas. J. Phys. Chem. C 2009, 113, 14672-14675.
- [12] Chu, M.-W.; Myroshnychenko, V.; Chen, C. H.; Deng, J.-P.; Mou, C.-Y.; García de

Abajo, F. J. Probing Bright and Dark Surface- Plasmon Modes in Individual and Coupled Noble Metal Nanoparticles Using an Electron Beam. *Nano Lett.* 2009, 9, 399-404.

[13] Pakizeh, T.; Käll, M. Unidirectional Ultracompact Optical Nanoantennas. *Nano Lett.* 2009, 9, 2343-2349.

[14] Shegai, T.; Chen, S.; Miljkovic, V. D.; Zengin, G.; Johansson, P.; Kall, M. A Bimetallic Nanoantenna for Directional Colour Routing. *Nat. Commun.* 2011, 2, 481.

[15] Shegai, T.; Johansson, P.; Langhammer, C.; Käll, M. Directional Scattering and Hydrogen Sensing by Bimetallic Pd-Au Nanoantennas. *Nano Lett.* 2012, 12, 2464-2469.

[16] Brown, L. V.; Sobhani, H.; Lassiter, J. B.; Nordlander, P.; Halas, N. J. Heterodimers: Plasmonic Properties of Mismatched Nanoparticle Pairs. *ACS Nano* 2010, 4, 819-832.

[17] Peña-Rodríguez, O.; Pal, U.; Campoy-Quiles, M.; Rodríguez- Fernández, L.; Garriga, M.; Alonso, M. I. Enhanced Fano Resonance in Asymmetrical Au:Ag Heterodimers. *J. Phys. Chem. C* 2011, 115, 6410- 6414.

[18] Yang, Z.-J.; Zhang, Z.-S.; Zhang, W.; Hao, Z.-H.; Wang, Q.-Q. Twinned Fano Interferences Induced by Hybridized Plasmons in Au- Ag Nanorod Heterodimers. *Appl. Phys. Lett.* 2010, 96, 131113.

[19] Lombardi, A.; Grzelczak, M. P.; Pertreux, E.; Crut, A.; Maioli, P.; Pastoriza-Santos, I.; Liz-Marzán, L. M.; Vallée, F.; Del Fatti, N. Fano Interference in the Optical Absorption of an Individual Gold-Silver Nanodimer. *Nano Lett.* 2016, 16, 6311-6316.

[20] Bachelier, G.; Russier-Antoine, I.; Benichou, E.; Jonin, C.; Del Fatti, N.; Vallée, F.; Brevet, P. F. Fano Profiles Induced by Near-Field Coupling in Heterogeneous Dimers of Gold and Silver Nanoparticles. *Phys. Rev. Lett.* 2008, 101, 197401.

[21] Horneber, A.; Baudrion, A.-L.; Adam, P.-M.; Meixner, A. J.; Zhang, D. Compositional-Asymmetry Influenced Non-Linear Optical Processes of Plasmonic Nanoparticle Dimers. *Phys. Chem. Chem. Phys.* 2013, 15, 8031-8034.

[22] Toroghi, S.; Kik, P. G. Photothermal Response Enhancement in Heterogeneous Plasmon-Resonant Nanoparticle Trimers. *Phys. Rev. B: Condens. Matter Mater. Phys.* 2014, 90, 205414.

[23] Evlyukhin, A. B.; Bozhevolnyi, S. I.; Pors, A.; Nielsen, M. G.; Radko, I. P.; Willatzen, M.; Albrechtsen, O. Detuned Electrical Dipoles for Plasmonic Sensing. *Nano Lett.* 2010, 10, 4571-4577.

[24] Gschneidner, T. A.; Fernandez, Y. A. D.; Syrenova, S.; Westerlund, F.; Langhammer, C.; Moth-Poulsen, K. A Versatile Self- Assembly Strategy for the Synthesis of Shape-Selected Colloidal Noble Metal Nanoparticle Heterodimers. *Langmuir* 2014, 30, 3041-3050.

[25] Liu, N.; Tang, M. L.; Hentschel, M.; Giessen, H.; Alivisatos, A. P. Nanoantenna-Enhanced Gas Sensing in a Single Tailored Nanofocus. *Nat. Mater.* 2011, 10, 631-636.

[26] Swearer, D. F.; Zhao, H.; Zhou, L.; Zhang, C.; Robatjazi, H.; Martinez, J. M. P.; Krauter, C. M.; Yazdi, S.; McClain, M. J.; Ringe, E.; Carter, E. A.; Nordlander, P.; Halas, N. J. Heterometallic Antenna- Reactor Complexes for Photocatalysis. *Proc. Natl. Acad. Sci. U. S. A.* 2016, 113, 8916-8920.

[27] Zhang, C.; Zhao, H.; Zhou, L.; Schlather, A. E.; Dong, L.; McClain, M. J.; Swearer,

3.2. Mode Coupling in Plasmonic Heterodimers Probed with Electron Energy Loss Spectroscopy

- D. F.; Nordlander, P.; Halas, N. J. Al-Pd Nanodisk Heterodimers as Antenna-Reactor Photocatalysts. *Nano Lett.* 2016, 16, 6677-6682.
- [28] Slaughter, L. S.; Wu, Y.; Willingham, B. A.; Nordlander, P.; Link, S. Effects of Symmetry Breaking and Conductive Contact on the Plasmon Coupling in Gold Nanorod Dimers. *ACS Nano* 2010, 4, 4657-4666.
- [29] Sheikholeslami, S.; Jun, Y.-w.; Jain, P. K.; Alivisatos, A. P. Coupling of Optical Resonances in a Compositionally Asymmetric Plasmonic Nanoparticle Dimer. *Nano Lett.* 2010, 10, 2655-2660.
- [30] Weller, L.; Thacker, V. V.; Herrmann, L. O.; Hemmig, E. A.; Lombardi, A.; Keyser, U. F.; Baumberg, J. J. Gap-Dependent Coupling of Ag-Au Nanoparticle Heterodimers Using DNA Origami-Based Self-Assembly. *ACS Photonics* 2016, 3, 1589-1595.
- [31] Schubert, I.; Sigle, W.; van Aken, P. A.; Trautmann, C.; Toimil-Molares, M. E. STEM-EELS Analysis of Multipole Surface Plasmon Modes in Symmetry-Broken AuAg Nanowire Dimers. *Nanoscale* 2015, 7, 4935-4941.
- [32] Zhaogang, D.; Michel, B.; Di, Z.; Xiao Ming, G.; Joel, K. W. Y. Fabrication of Suspended Metal-Dielectric-Metal Plasmonic Nanostructures. *Nanotechnology* 2014, 25, 135303.
- [33] Zhang, M.; Large, N.; Koh, A. L.; Cao, Y.; Manjavacas, A.; Sinclair, R.; Nordlander, P.; Wang, S. X. High-Density 2D Homo- and Hetero- Plasmonic Dimers with Universal Sub-10-nm Gaps. *ACS Nano* 2015, 9, 9331-9339.
- [34] Greybush, N. J.; Saboktakin, M.; Ye, X.; Della Giovampaola, C.; Oh, S. J.; Berry, N. E.; Engheta, N.; Murray, C. B.; Kagan, C. R. Plasmon-Enhanced Upconversion Luminescence in Single Nanophosphor- Nanorod Heterodimers Formed through Template-Assisted Self-Assembly. *ACS Nano* 2014, 8, 9482-9491.
- [35] Flauraud, V.; Mastrangeli, M.; Bernasconi, G. D.; Butet, J.; Alexander, D. T.; Shahrabi, E.; Martin, O. J.; Brugger, J. Nanoscale Topographical Control of Capillary Assembly of Nanoparticles. *Nat. Nanotechnol.* 2017, 12, 73-80.
- [36] Diaz Fernandez, Y. A.; Gschneidtnr, T. A.; Wadell, C.; Fornander, L. H.; Lara Avila, S.; Langhammer, C.; Westerlund, F.; Moth-Poulsen, K. The Conquest of Middle-Earth: Combining Top- Down and Bottom-Up Nanofabrication for Constructing Nanoparticle Based Devices. *Nanoscale* 2014, 6, 14605-14616.
- [37] Goeken, K. L.; Subramaniam, V.; Gill, R. Enhancing Spectral Shifts of Plasmon-Coupled Noble Metal Nanoparticles for Sensing Applications. *Phys. Chem. Chem. Phys.* 2015, 17, 422-427.
- [38] Romo-Herrera, J. M.; Alvarez-Puebla, R. A.; Liz-Marzan, L. M. Controlled Assembly of Plasmonic Colloidal Nanoparticle Clusters. *Nanoscale* 2011, 3, 1304-1315.
- [39] Wersäll, M.; Verre, R.; Svedendahl, M.; Johansson, P.; Käll, M.; Shegai, T. Directional Nanoplasmonic Antennas for Self-Referenced Refractometric Molecular Analysis. *J. Phys. Chem. C* 2014, 118, 21075-21080.
- [40] Wadell, C.; Langhammer, C. Drift-Corrected Nanoplasmonic Hydrogen Sensing by Polarization. *Nanoscale* 2015, 7, 10963-10969.
- [41] Yang, A.; Huntington, M. D.; Cardinal, M. F.; Masango, S. S.; Van Duyne, R. P.;

Odom, T. W. Hetero-Oligomer Nanoparticle Arrays for Plasmon-Enhanced Hydrogen Sensing. *ACS Nano* 2014, 8, 7639- 7647.

[42] Syrenova, S.; Wadell, C.; Langhammer, C. Shrinking-Hole Colloidal Lithography: Self-Aligned Nanofabrication of Complex Plasmonic Nanoantennas. *Nano Lett.* 2014, 14, 2655-2663.

[43] Nugroho, F. A. A.; Iandolo, B.; Wagner, J. B.; Langhammer, C. Bottom-Up Nanofabrication of Supported Noble Metal Alloy Nanoparticle Arrays for Plasmonics. *ACS Nano* 2016, 10, 2871-2879.

[44] Guisbiers, G.; Mendoza-Cruz, R.; Bazán-Díaz, L.; Velázquez- Salazar, J. J.; Mendoza-Perez, R.; Robledo-Torres, J. A.; Rodríguez- Lopez, J.-L.; Montejano-Carrizales, J. M.; Whetten, R. L.; José- Yacamán, M. Electrum, the Gold-Silver Alloy, from the Bulk Scale to the Nanoscale: Synthesis, Properties, and Segregation Rules. *ACS Nano* 2016, 10, 188-198.

[45] Zorić, I.; Zäch, M.; Kasemo, B.; Langhammer, C. Gold, Platinum, and Aluminum Nanodisk Plasmons: Material Independence, Subradiance, and Damping Mechanisms. *ACS Nano* 2011, 5, 2535- 2546.

[46] McPeak, K. M.; Jayanti, S. V.; Kress, S. J. P.; Meyer, S.; Iotti, S.; Rossinelli, A.; Norris, D. J. Plasmonic Films Can Easily Be Better: Rules and Recipes. *ACS Photonics* 2015, 2, 326-333.

[47] Knight, M. W.; King, N. S.; Liu, L.; Everitt, H. O.; Nordlander, P.; Halas, N. J. Aluminum for Plasmonics. *ACS Nano* 2014, 8, 834- 840.

[48] Ordal, M. A.; Long, L. L.; Bell, R. J.; Bell, S. E.; Bell, R. R.; Alexander, R. W.; Ward, C. A. Optical Properties of the Metals Al, Co, Cu, Au, Fe, Pb, Ni, Pd, Pt, Ag, Ti, and W in the Infrared and Far Infrared. *Appl. Opt.* 1983, 22, 1099-1119.

[49] Rossouw, D.; Couillard, M.; Vickery, J.; Kumacheva, E.; Botton, G. A. Multipolar Plasmonic Resonances in Silver Nanowire Antennas Imaged with a Subnanometer Electron Probe. *Nano Lett.* 2011, 11, 1499-1504.

[50] Duan, H.; Fernández-Domínguez, A. I.; Bosman, M.; Maier, S. A.; Yang, J. K. W. Nanoplasmonics: Classical down to the Nanometer Scale. *Nano Lett.* 2012, 12, 1683-1689.

[51] Haberfehlner, G.; Trügler, A.; Schmidt, F. P.; Hörl, A.; Hofer, F.; Hohenester, U.; Kothleitner, G. Correlated 3D Nanoscale Mapping and Simulation of Coupled Plasmonic Nanoparticles. *Nano Lett.* 2015, 15, 7726-7730.

[52] Flauraud, V.; Regmi, R.; Winkler, P. M.; Alexander, D. T. L.; Rigneault, H.; van Hulst, N. F.; García-Parajo, M. F.; Wenger, J.; Brugger, J. In-Plane Plasmonic Antenna Arrays with Surface Nanogaps for Giant Fluorescence Enhancement. *Nano Lett.* 2017, 17, 1703- 1710.

[53] Bernasconi, G. D.; Butet, J.; Martin, O. J. F. Mode Analysis of Second-Harmonic Generation in Plasmonic Nanostructures. *J. Opt. Soc. Am. B* 2016, 33, 768-779.

[54] Hörl, A.; Trügler, A.; Hohenester, U. Tomography of Particle Plasmon Fields from Electron Energy Loss Spectroscopy. *Phys. Rev. Lett.* 2013, 111, 076801.

[55] Hörl, A.; Trügler, A.; Hohenester, U. Full Three-Dimensional Reconstruction of the

3.2. Mode Coupling in Plasmonic Heterodimers Probed with Electron Energy Loss Spectroscopy

Dyadic Green Tensor from Electron Energy Loss Spectroscopy of Plasmonic Nanoparticles. *ACS Photonics* 2015, 2, 1429-1435.

[56] Schmidt, F.-P.; Ditlbacher, H.; Hohenester, U.; Hohenau, A.; Hofer, F.; Krenn, J. R. Dark Plasmonic Breathing Modes in Silver Nanodisks. *Nano Lett.* 2012, 12, 5780-5783.

[57] Quillin, S. C.; Cherqui, C.; Montoni, N. P.; Li, G.; Camden, J. P.; Masiello, D. J. Imaging Plasmon Hybridization in Metal Nanoparticle Aggregates with Electron Energy-Loss Spectroscopy. *J. Phys. Chem. C* 2016, 120, 20852-20859.

[58] Kern, J.; Großmann, S.; Tarakina, N. V.; Häckel, T.; Emmerling, M.; Kamp, M.; Huang, J.-S.; Biagioni, P.; Prangsma, J. C.; Hecht, B. Atomic-Scale Confinement of Resonant Optical Fields. *Nano Lett.* 2012, 12, 5504-5509.

[59] Lovera, A.; Gallinet, B.; Nordlander, P.; Martin, O. J. F. Mechanisms of Fano Resonances in Coupled Plasmonic Systems. *ACS Nano* 2013, 7, 4527-4536.

[60] Lombardi, A.; Grzelczak, M. P.; Crut, A.; Maioli, P.; Pastoriza-Santos, I.; Liz-Marzán, L. M.; Del Fatti, N.; Vallée, F. Optical Response of Individual Au-Ag@SiO₂ Heterodimers. *ACS Nano* 2013, 7, 2522- 2531.

[61] Myroshnychenko, V.; Nelayah, J.; Adamo, G.; Geuquet, N.; Rodríguez-Fernández, J.; Pastoriza-Santos, I.; MacDonald, K. F.; Henrard, L.; Liz-Marzán, L. M.; Zheludev, N. I.; et al. Plasmon Spectroscopy and Imaging of Individual Gold Nanodecahedra: A Combined Optical Microscopy, Cathodoluminescence, and Electron Energy-Loss Spectroscopy Study. *Nano Lett.* 2012, 12, 4172-4180.

[62] Losquin, A.; Kociak, M. Link between Cathodoluminescence and Electron Energy Loss Spectroscopy and the Radiative and Full Electromagnetic Local Density of States. *ACS Photonics* 2015, 2, 1619-1627.

[63] Kawasaki, N.; Meuret, S.; Weil, R.; Lourenço-Martins, H.; Stéphan, O.; Kociak, M. Extinction and Scattering Properties of High- Order Surface Plasmon Modes in Silver Nanoparticles Probed by Combined Spatially Resolved Electron Energy Loss Spectroscopy and Cathodoluminescence. *ACS Photonics* 2016, 3, 1654-1661.

[64] Bernasconi, G. D.; Butet, J.; Flauraud, V.; Alexander, D.; Brugger, J.; Martin, O. J. F. Where Does Energy Go in Electron Energy Loss Spectroscopy of Nanostructures? *ACS Photonics* 2017, 4, 156- 164.

[65] Luk'yanchuk, B.; Zheludev, N. I.; Maier, S. A.; Halas, N. J.; Nordlander, P.; Giessen, H.; Chong, C. T. The Fano Resonance in Plasmonic Nanostructures and Metamaterials. *Nat. Mater.* 2010, 9, 707-715.

[66] Duan, X.; Kamin, S.; Sterl, F.; Giessen, H.; Liu, N. Hydrogen- Regulated Chiral Nanoplasmonics. *Nano Lett.* 2016, 16, 1462-1466.

[67] Mivelle, M.; van Zanten, T. S.; Garcia-Parajo, M. F. Hybrid Photonic Antennas for Subnanometer Multicolor Localization and Nanoimaging of Single Molecules. *Nano Lett.* 2014, 14, 4895-4900.

[68] Butet, J.; Brevet, P.-F.; Martin, O. J. F. Optical Second Harmonic Generation in Plasmonic Nanostructures: From Fundamental Principles to Advanced Applications. *ACS Nano* 2015, 9, 10545-10562.

[69] Liu, H.; Wang, B.; Leong, E. S. P.; Yang, P.; Zong, Y.; Si, G.; Teng, J.; Maier, S.

Chapter 3. Eigenmode Analysis and Electron Energy Loss Spectroscopy

A. Enhanced Surface Plasmon Resonance on a Smooth Silver Film with a Seed Growth Layer. *ACS Nano* 2010, 4, 3139-3146.

[70] Garcia, D. Robust Smoothing of Gridded Data in One and Higher Dimensions with Missing Values. *Comput. Stat. Data Anal.* 2010, 54, 1167-1178.

[71] Kern, A. M.; Martin, O. J. F. Surface Integral Formulation for 3D Simulations of Plasmonic and High Permittivity Nanostructures. *J. Opt. Soc. Am. A* 2009, 26, 732-740.

[72] Ritchie, R. H. Plasma Losses by Fast Electrons in Thin Films. *Phys. Rev.* 1957, 106, 874-881.

[73] García de Abajo, F. J. Optical Excitations in Electron Microscopy. *Rev. Mod. Phys.* 2010, 82, 209-275.

[74] Johnson, P. B.; Christy, R. W. Optical Constants of the Noble Metals. *Phys. Rev. B* 1972, 6, 4370-4379.

[75] Palik, E. D. G. *Handbook of Optical Constants of Solids*; Academic Press, 1985.

Supplementary informations

Supplementary Figures

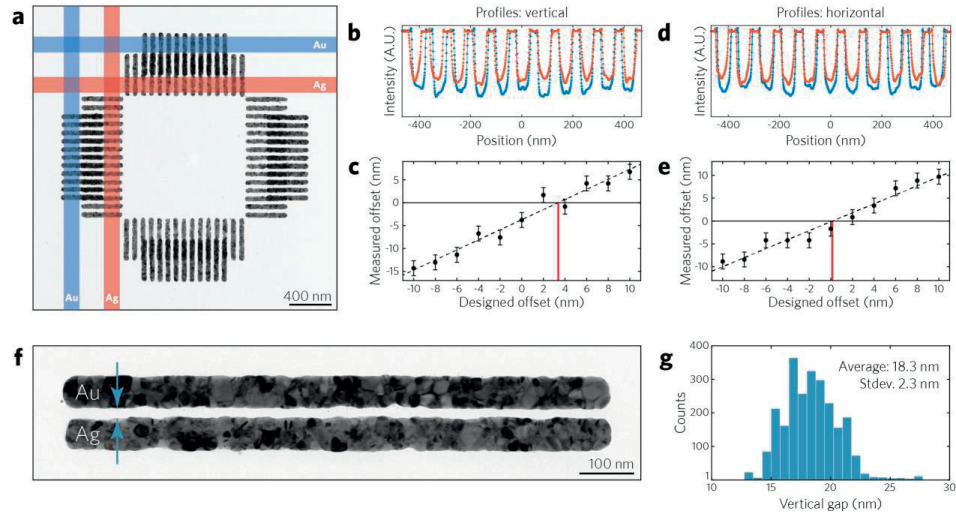


Figure S1 – **Layer to layer alignment accuracy.** (a) TEM image of a two-layer Au–Ag Vernier pattern. (b) Averaged horizontal line profiles from the Au and Ag layers and (c) measured rod offset versus designed offset. The zero crossing of the linear fit to the measured offsets defines the alignment accuracy along this axis. (d) and (e) similar measurements for the horizontal axis. TEM image of an Au–Ag parallel wire pair (f) and corresponding vertical gap histogram (g).

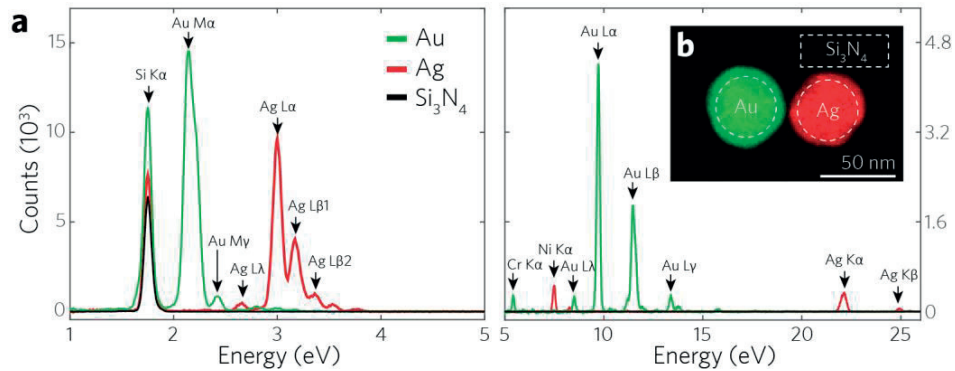


Figure S2 – **EDX spectra of an Au–Ag dimer.** (a) EDX spectra for an Au–Ag 50 nm diameter disc dimer. Au and Cr adhesion layer, Ag and the Ni wetting layer are respectively well identified in the Au and Ag spectra with a common Si peak seen for all regions of interest.

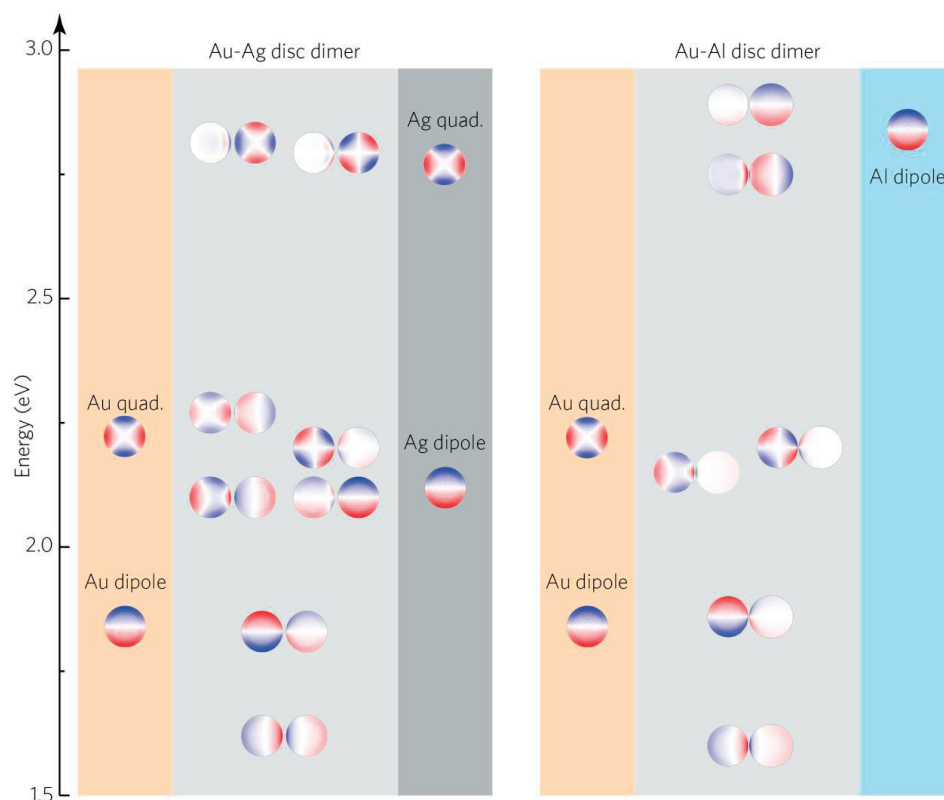


Figure S3 – **Computed eigenmodes for single and coupled Au, Ag, and Al discs.** Each eigencharge distribution is placed according to its energy.

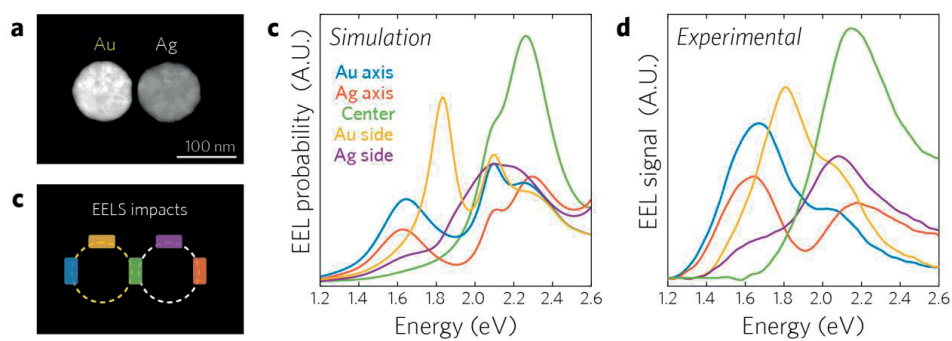


Figure S4 – **Au-Ag 100nm disc EELS simulations.** (a) HAADF STEM image of an Au-Ag dimer with 100 nm disc diameter and (b) EELS impact regions. (c) Simulated spectra and (d) corresponding experimental spectra. The experimental spectra are convoluted with the zero-loss peak of ~ 100 meV FWHM thereby explaining their wider resonances.

3.2. Mode Coupling in Plasmonic Heterodimers Probed with Electron Energy Loss Spectroscopy

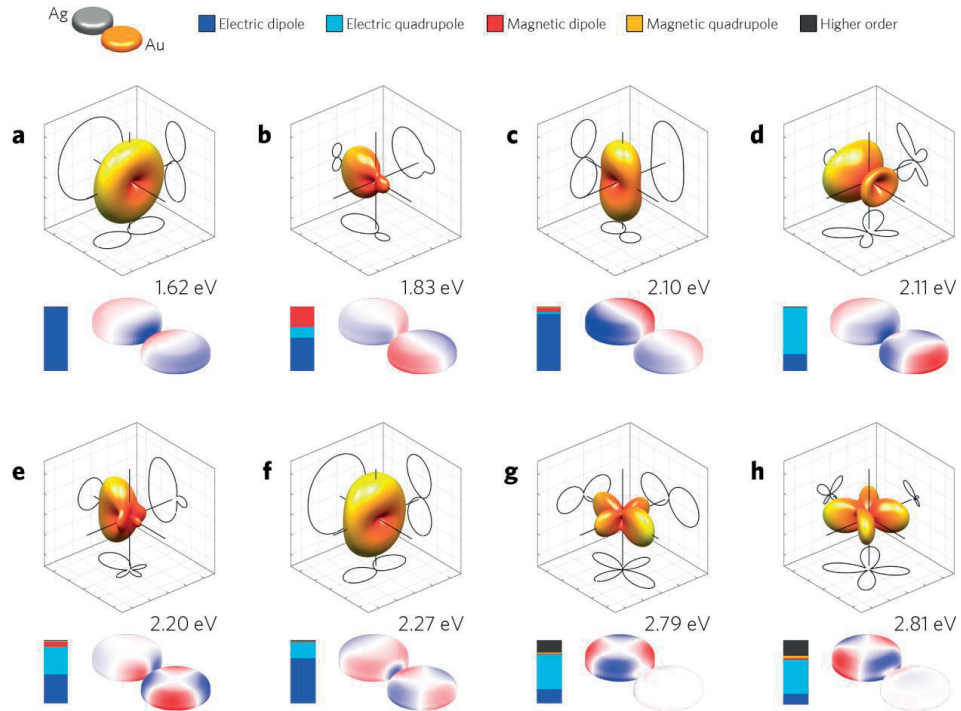


Figure S5 – **Multipolar decomposition of the Au–Ag 100nm disc eigenmode.** (a–h) Radiation pattern and multipolar decomposition associated with each eigenmode. The multipolar decomposition is made as described in Ref. [1]. The contribution of all degrees for a given multipole order (1 standing for dipoles, 2 standing for quadrupoles, etc...) are added together. The compositional and structural asymmetries allow a net dipolar moment for all the modes shown here.

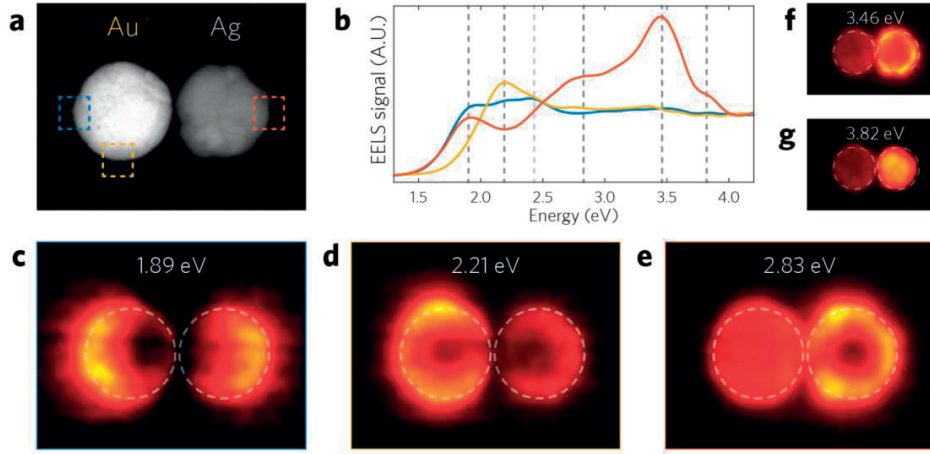


Figure S6 – **Au-Ag 50 nm disc heterodimer.** (a) HAADF STEM image of an Au-Ag dimer with 50 nm disc diameter and 2 nm gap width. (b) EELS spectra extracted for the impact positions highlighted in (a). EELS maps of the modes dominated by (c) a longitudinal dipole mode in the Au nanoparticle, (d) a transverse dipole mode in the Au nanoparticle, and (e) a dipole mode in the Ag nanoparticle. (f) EELS map of the convergence of high order modes in the Ag nanoparticle, referred to as a quasiplanar mode [2]. (g) EELS map of the Ag bulk plasmon contribution at 3.82 eV.

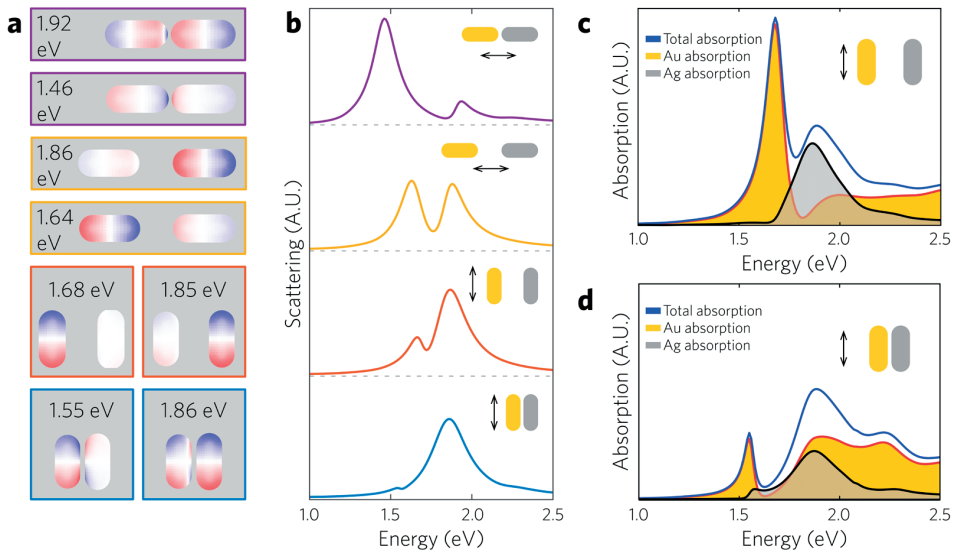


Figure S7 – **Optical response of Au-Ag rod heterodimers.** Nanorod dimensions are and gaps are 45×105 nm; the gaps are 5 nm for the serial coupled case, 9 nm for the parallel coupled case. and 55 nm for both weakly coupled cases. (a) Imaginary part of the charge distributions at the resonance energy of the modes (i.e. 90° out of phase with the excitation). (b) Scattering computed for an incident plane wave polarized along the long nanorod axis. Total and relative absorbed power for parallel heterodimer with (c) a 55 nm and (d) a 9 nm (d) gap width.

3.2. Mode Coupling in Plasmonic Heterodimers Probed with Electron Energy Loss Spectroscopy

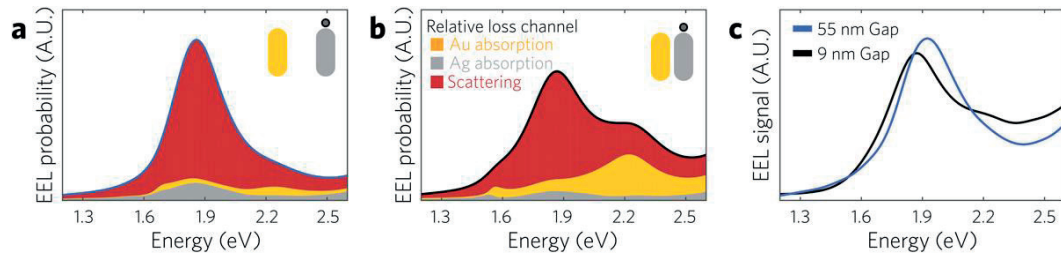


Figure S8 – **EELS spectra and loss channel decompositions with impact parameter close to the Ag nanorod apex.** Computed EELS signal for a parallel dimer with (a) a 55 nm gap and (b) a 9 nm gap. The decomposition into the different loss mechanisms is represented by the filled area under the curves. (c) Measured EELS spectra integrated over the Ag nanorod for the two heterodimers.

References

- [1]. Mühlig, S.; Menzel, C.; Rockstuhl, C.; Lederer, F. Multipole Analysis of Meta-Atoms. *Metamaterials* 2011, 5, 64-73.
- [2]. Aizpurua, J.; Rivacoba, A.; Apell, S. P. Electron-Energy Losses in Hemispherical Targets. *Phys. Rev. B* 1996, 54, 2901-2909.

3.3 Mode Evolution in Strongly Coupled Plasmonic Dolmens Fabricated by Templated Assembly

Manuscript state: Published

Reference: Valentin Flauraud, **Gabriel D. Bernasconi**, Jérémy Butet, Massimo Mastrangeli, Duncan T. L. Alexander, Olivier J. F. Martin, Jürgen Brugger, "Mode evolution in strongly coupled plasmonic dolmens fabricated by templated assembly" *ACS Photonics* **4**, 1661-1668, (2017).

Publication date: May 22, 2017

DOI: 10.1021/acsphotonics.6b01026

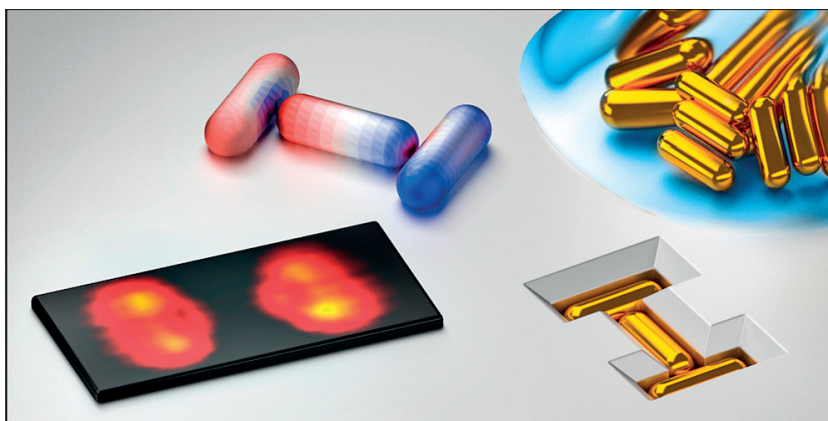
URL: <https://pubs.acs.org/doi/abs/10.1021/acsphotonics.6b01026>

Adapted with permission from the above-mentioned reference.

Copyright (2017) American Chemical Society.

Author contributions

G. D. Bernasconi performed the numerical simulations and contributed to the data analysis and to the manuscript writing.



Mode Evolution in Strongly Coupled Plasmonic Dolmens Fabricated by Templated Assembly

Valentin Flauraud¹, Gabriel D. Bernasconi², Jérémy Butet², Massimo Mastrangeli³, Duncan T.L. Alexander⁴, Jürgen Brugger¹ and Olivier J.F. Martin²

¹Microsystems Laboratory, ²Nanophotonics and Metrology Laboratory, and

⁴Interdisciplinary Center for Electron Microscopy, Swiss Federal Institute of Technology Lausanne (EPFL), 1015, Lausanne, Switzerland.

³Physical Intelligence Department, Max Planck Institute for Intelligent Systems, 70569 Stuttgart, Germany.

Corresponding author: juergen.brugger@epfl.ch

ABSTRACT: Plasmonic antennas have enabled a wealth of applications that exploit tailored near-fields and radiative properties, further endowed by the bespoke interactions of multiple resonant building blocks. Specifically, when the interparticle distances are reduced to a few nanometers, coupling may be greatly enhanced leading to ultimate near-field intensities and confinement along with a large energy splitting of resonant modes. While this concept is well-known, the fabrication and characterization of suitable multimers with controlled geometries and few-nanometer gaps remains highly challenging. In this article, we present the topographically templated assembly of single-crystal colloidal gold nanorods into trimers, with a dolmen geometry. This fabrication method enables the precise positioning of high-quality nanorods, with gaps as small as 1.5 nm, which permits a gradual and controlled symmetry breaking by tuning the arrangement of these strongly coupled nanostructures. To characterize the fabricated structures, we perform electron energy loss spectroscopy (EELS) near-field hyperspectral imaging and geometrically accurate EELS, plane wave, and eigenmode full-wave computations to reveal the principles governing the electromagnetic response of such nanostructures that have been extensively studied under plane wave excitation for their Fano resonant properties. These experiments track the evolution of the multipolar interactions with high accuracy as the antenna geometry varies. Our results provide new insights in strongly coupled single-crystal building blocks and open new opportunities for the design and fabrication of plasmonic systems.

Introduction

Plasmonic nanoantennas are well established tools for the manipulation of light at the nanoscale and for the control of light-matter interaction via the excitation of localized plasmon resonances in metallic nanostructures [1]. With continuous efforts carried out for the development of novel nanofabrication methods, along with the emergence of powerful numerical simulation techniques and models [2], optical antennas have been tailored to exploit their strong scattering and absorption cross sections as well as their deep subwavelength focusing ability [3]. Besides the intrinsic plasmonic properties of individual metal nanoparticles, many applications take advantage of the coupling between multiple plasmonic constituents. Indeed, the spectral tuning of different antenna building blocks and their controlled spatial arrangement enable, a wealth of unique properties such as nanometric mode confinement [4], directional color routing [5], and Fano line shapes [6].

These effects, all based on the interaction between multiple plasmonic modes, are highly dependent on the coupling strength. Several coupling regimes have been identified [7]. Weak coupling induces only slight shifts of the modes energies, in comparison with that of the uncoupled systems. The tailored spectral overlap and phase of the different eigenmodes may nonetheless give rise to pronounced far-field interferences [8]. Moderate coupling has been thoroughly explored, due to the relative ease of fabricating nanostructures with nanogaps larger than ~ 10 nm. By reducing gap size further to a few nanometers, extreme coupling, and hybridization of the eigenmodes are induced, leading to large spectral splitting and ultimate near-field intensities [9,10].

In this article, we investigate the influence of the coupling strength on the mode evolution of tunable nanorod dolmens. These trimer structures are composed of a pair of parallel nanorods hosting a third central one, perpendicular to them (Figure 1a). Dolmens have been widely investigated often considering optical excitations, in both 2D and 3D designs with mostly large interparticle gaps, since they support Fano resonances [11], which are advantageous for the fabrication of plasmonic sensors [12-14] and plasmonic nanorulers [15], as well as for the observation of plasmon induced transparency [16] and absorption [17]. The richness of this system arises from the interplay between bright and dark modes and from a spectral response deeply related to the intricate geometric details. Beyond the implementations proposed above, such features may be enriched through the enhanced coupling and hybridization between high order modes. The latter suggests new opportunities for the design of plasmonic nanostructures, which are however practically challenged by the demanding requirements of nanometer interparticle gap fabrication.

Indeed, the fabrication of highly coupled systems with a fully controlled geometry is still elusive to date. Several lithographic attempts for the fabrication of nanometer scale gaps have been demonstrated for simple geometries such as dimers [18] and bowties [19], but line edge roughness, repeatability, and scalability remain challenging to control. An

3.3. Mode Evolution in Strongly Coupled Plasmonic Dolmens Fabricated by Templated Assembly

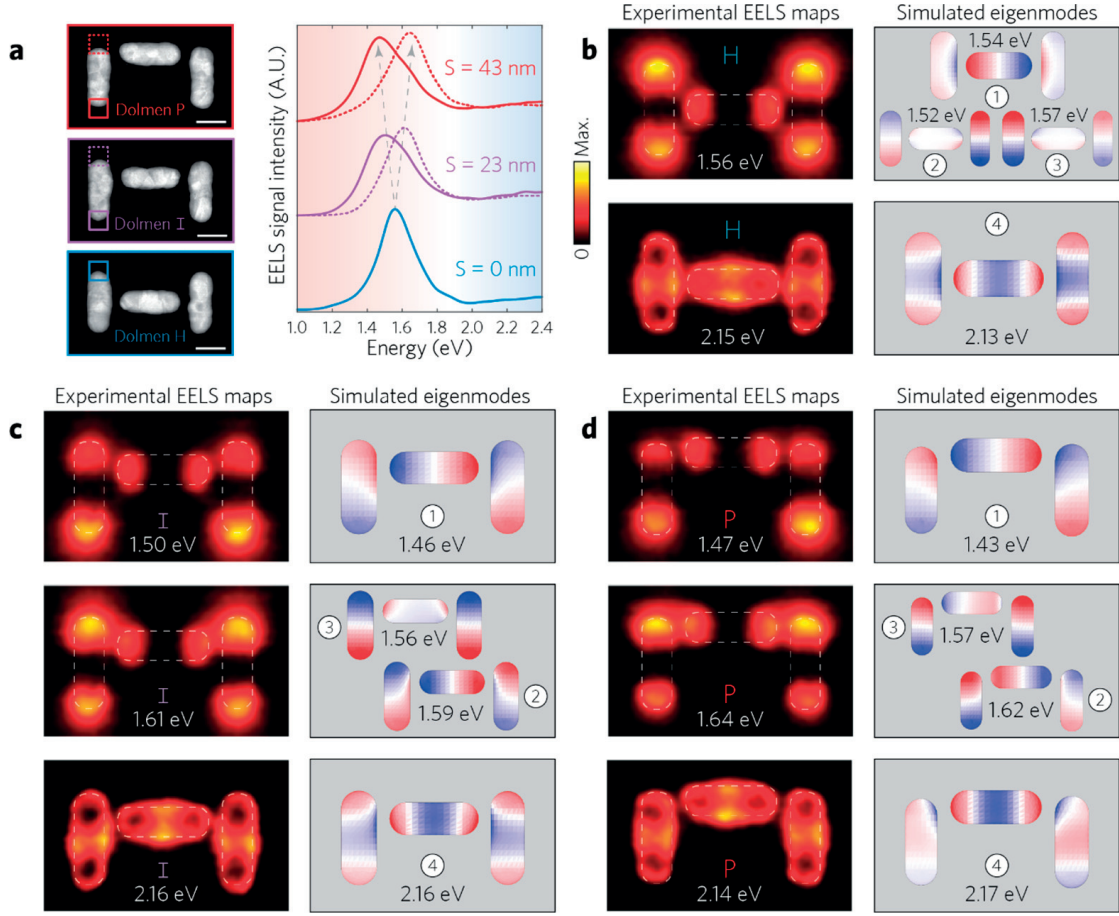


Figure 1 – EELS analysis of weakly coupled Au dolmens fabricated by electron beam lithography and thin-film patterning. (a) High angle annular dark field scanning transmission electron microscope (HAADF-STEM) images of three different dolmens with varying offset parameter S for the central horizontal nanorods and corresponding experimental EEL spectra extracted from the regions highlighted in the HAADF images. (b) Experimental EELS maps and corresponding simulated eigenmodes for the symmetric nanodolmen H ($S = 0$). (c, d) Similar analysis for the nanodolmen I ($S = 23$ nm), and the nanodolmen P, ($S = 43$ nm). All scale bars are 50 nm. Each EELS map is displayed with a colorscale normalized to its maximal energy loss probability.

efficient approach relies on the manipulation of colloids to couple them in pairs and multimers [20] or by placing them above a metallic film [21]. Prompted by the vast library of anisotropic building blocks readily available [22], surface chemistry and DNA origami [23] have successfully been employed to provide further levels of colloidal organization and functionality in static [24] and dynamic configurations [25,26]. Such techniques provide a simple access to single or few nanometer interparticle distances often defined by molecular spacers [27,28].

In the present work, we utilize a templated colloidal assembly method to fabricate highly plasmonic coupled systems. This method combines at once the intrinsic crystalline and geometric qualities of chemically synthesized nanoparticles, the simple definition of gaps by molecular elements, and the patterning versatility of nanolithography. Using this approach, and in opposition to colloid surface functionalization alone, whereby energy minima define a limited set of assembly configuration [29,30], we have recently demonstrated highly accurate nanorod positioning in predetermined patterns with arbitrary geometries by capillary assembly [31]. These are essential prerequisites for the fabrication of complex plasmonic nanostructures relying on colloidal building blocks. Here we extend this concept by performing a finely tunable assembly of multiple anisotropic building blocks within a single trap. This represents, to the best of our knowledge, the first fully deterministic assembly of such complex structures, controlling both relative and absolute position of three nanorods with gap distances of only a few nanometers.

To probe the electromagnetic response of coupled dolmens with various geometric configurations, and to assess the quality of the fabricated structures, electron energy loss spectroscopy (EELS) characterization was performed in a scanning transmission electron microscope. While both scanning near-field optical microscopy [32] and photoemission electron microscopy [33] have been used to image the near-field properties of multimetric structures, EELS in modern monochromated instruments is an ideal method for the mapping of plasmonic resonances with ultimate spatial and high spectral resolution [34]. Due to the nanometric localization of the electron probe and its intrinsic field symmetry, in addition to its sensitivity to both the radiative and nonradiative decay channels, bright modes and dark ones (with a vanishing dipole moment) are efficiently imaged [35-38]. The cylindrical symmetry of the probe also implies that asymmetric charge distributions in nanogap regions are inefficiently excited [39]. Typically, bonding modes associated with intense hotspots are not revealed in gap regions, although these modes can be probed efficiently at other locations in the structures. This distinction can be exploited to interpret the nature of the different modes in addition to measuring their inherent spectral and spatial specificities. As EELS allows direct insight into the modal nature of the system, which defines a base for its response independent of excitation conditions, here the identification of the underlying coupling mechanisms of dolmen nanostructures is complemented by a rigorous and geometry accurate full wave numerical eigenmode analysis [40] besides the simulation of the EELS spectra. By performing these experimental and computational investigations under different gap and geometric

3.3. Mode Evolution in Strongly Coupled Plasmonic Dolmens Fabricated by Templated Assembly

conditions at once, the nature and the highly geometry sensitive response of strongly coupled systems is evidenced. The article is organized as follows. The case of dolmens made by lithography with relatively large gaps is considered first, in order to address the plasmon coupling in the moderate regime. In a second part, the plasmon coupling in ideal dolmens made of gold nanorods with the same dimensions separated by 2 nm gaps is numerically investigated, allowing to discuss the mode evolutions in the strong coupling regime. Finally, gold dolmens with small gaps fabricated with capillary assembly are considered. In this last section, the experimental data are supported by simulations done considering the experimentally measured rod geometries, including the symmetry breaking induced by the size dispersion.

Results and Discussion

Dolmens Made by Lithography: The Moderate Coupling Regime

Prior to the investigation of strongly coupled structures, a baseline of interactions in the moderate coupling regime is presented. Although moderately coupled structures may also be produced by assembly, Au dolmens are first fabricated by electron beam lithography (EBL) and lift-off. This is meant to provide a direct comparison of the novel fabrication method with a benchmarked standard. PMMA is coated and exposed on freestanding 30 nm thick Si_3N_4 membranes guaranteeing a lithographic resolution mostly limited by forward scattering. A collection of dolmens with varying central nanorod offset is fabricated with target nanorod dimensions of 40 nm \times 105 nm and a gap width varying from 5 to 30 nm in 5 nm steps. After performing TEM metrology, the geometries with 15 nm gap size present the smallest distances between the nanorods while having noncontacted and uniform gap distributions, and are thus chosen as prototypical standards for the lithographic approach. Three dolmens with a vertical offset of the central nanorod, parameter S , chosen equal to 0, 20, and 40 nm are mapped and investigated by EELS (Figure 1). In the context of these structures, gold nanodolmens with π - shape and 20 nm gap distances have already been investigated using EELS [35,36].

When the EELS signal is compared at each end of one of the vertical nanorods in the three dolmen structures (Figure 1a), a gradual evolution of the initial resonance peak into multiple resonances of different energy is observed as the offset of the central nanorod increases. The EELS maps and the corresponding calculated eigenmode give insights into the nature of this evolution and underlying mode coupling mechanisms. For the symmetric dolmen, labeled H, simulations reveal that the EELS map at the resonant energy (1.56 eV) consists of an overlap of three eigenmodes, which are closely overlapped in energy and hence not spectrally resolvable in EELS. Mode ① is the longitudinal bonding dipole, which can be efficiently driven by a plane wave polarized along the central nanorod main axis whereas mode ③ corresponds to the mode that can be optically driven with a polarization along the axis of the two vertical nanorods (see Figure S1

in the Supporting Information for plane wave spectra). Mode ② is characterized by out of phase longitudinal dipoles in the vertical nanorods. For the dolmen H, no energy splitting between the modes is observed due to the limited near field overlap of the dipole modes supported by each nanorod. When the central nanorod is displaced by 23 nm (dolmen I, Figure 1c) and 43 nm (dolmen P, Figure 1d), a gradual energy splitting occurs between the longitudinal bonding mode ① moving to lower energies and the modes ②. Now that mode ① is spectrally separated, its spatial distribution can be isolated, with its bonding nature evidenced by the minimal EELS intensity in the gap [39]. The excitation of mode ②, which tends toward an antibonding dipole arrangement between the nanorods as S increases, is consequently responsible for the enhanced EELS intensity in the gap regions. This selective excitation of antibonding modes when the electron beam passes through the nanogaps effectively enables the distinction between modes ① and ②, even though the energy splitting is as small as 0.11 eV in the case of the dolmen I. While these lower order modes are sensitive to the central nanorod offset in this moderate coupling regime, that is not the case for the energy of higher order modes based on the interaction of quadrupolar modes in each nanorod, such as mode ④. This is inherent to the fast spatial decay of the electric field associated with high order modes, which results in weaker coupling strength than for dipole modes. Interestingly, as shown in Figure S1, the spectral proximity of modes ① and ② leads to the gradual appearance of a Fano profile under optical illumination due to the interference between these two modes [41].

Ideal Dolmens with 2 nm Gaps

To consider how behavior may differ in a stronger coupling regime, we investigate numerically ideal dolmens constituted of three similar hemispherical nanorods of 105 nm length and 40 nm diameter with 2 nm interparticle gaps. Five structures are considered, from the symmetric case ($S = 0$) up to a maximum vertical shift of the central nanorod $S = 40$ nm. The EELS response of these dolmens is computed for two positions of the electron beam; one at the top end of one vertical nanorod (Figure 2a) and one close to the side of the central nanorod (Figure S3) in order to probe all the modes of interest. Each eigenmode is computed and shown, as a surface charge distribution, in Figure 2b. In this ideal symmetric geometry, modes ① and ② have an odd charge parity with respect to the vertical symmetry plane, whereas modes ③ and ④ exhibit an even parity. Modes ① and ④ are respectively characterized by a longitudinal dipolar and quadrupolar charge distribution on the central nanorod, in all geometric configurations. These two modes are significantly red-shifted in comparison with the weakly coupled dolmens discussed previously; a behavior that is explained by a strong bonding interaction to the adjacent rods. In the case of mode ①, increasing the offset S results in a gradual evolution of the charge distributions in the vertical nanorods, from a transverse dipolar distribution to a longitudinal dipole. This progressively allows the coupling of three longitudinal dipoles at the same energy leading to the redshift of the mode resonance. For mode ④, the

3.3. Mode Evolution in Strongly Coupled Plasmonic Dolmens Fabricated by Templated Assembly

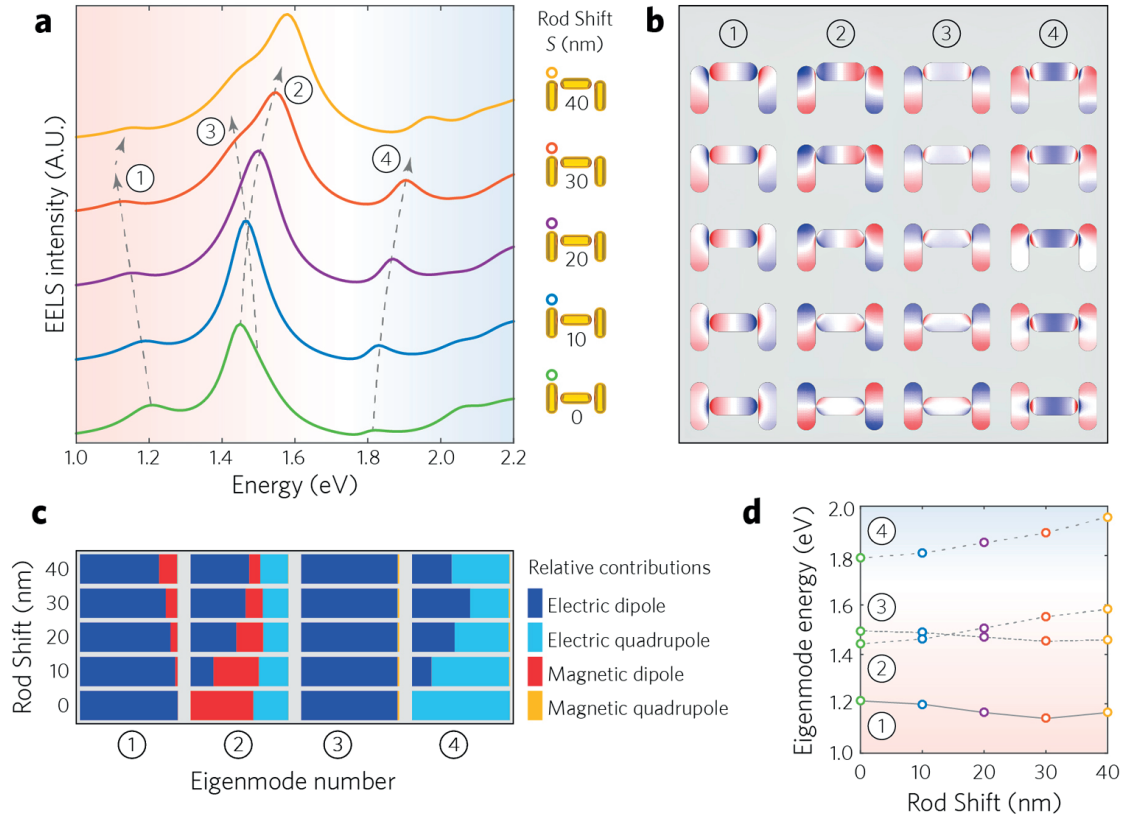


Figure 2 – EELS simulations of symmetric dolmens with 2 nm gaps. (a) EEL spectra simulated for ideal dolmen geometries with five different central nanorod offset parameters S from 0 to 40 nm. All nanorods are 40 nm \times 105 nm and are separated horizontally by a 2 nm gap. The impact parameters for the EEL spectra are indicated on the schematics of the dolmen structures. Four main resonances numbered from 1 to 4 are highlighted. (b) 20 eigencharges computed from the eigenmodes corresponding to the labeled resonances in the EEL spectra. Eigencharges colormaps were saturated to allow a clear representation of the modes when the charges were highly confined in the nanogap regions. (c) Multipolar decomposition of the four identified modes for each of the five geometries. Each bar represents the total scattering decomposed in the different contributions. (d) Eigenmode spectral positions as functions of the central nanorod offset parameter S .

inverse tendency is observed. The coupling with the adjacent nanorods is weakened by the position offset resulting in a blue shift of mode ④. Indeed, for $S = 0$, the central rod quadrupolar charge distribution is stretched toward the adjacent rods and tends to the charge distribution of the longitudinal quadrupole of an isolated nanorod (Figure S2) with increasing S . For modes ② and ③, a crossing between the resonant energies is observed as the central nanorod offset increases. This crossing indicates that modes ② and ③ do not interact due to their symmetry properties [42]. In the case of mode ②, characterized by the two out-of-phase vertical dipoles, the charge distribution supported by the central nanorod evolves from a transverse quadrupole to a longitudinal dipole with an antibonding interaction with other dipoles yielding to an effective blue shift of mode ②. For mode ③, characterized by two in-phase dipoles on the vertical nanorods, the central nanorod gradually moves into the near field of the vertical dipoles, here with a bonding interaction, yielding to a red-shift of the mode energy.

Together, these observations clearly indicate that the electromagnetic response of highly coupled nanodolmens, with a 2 nm gap, has a multipolar nature. Namely, short gaps enable an important modulation of the multipolar response of the dolmen via a collective coupling mediated by the central nanorod position. To investigate this in detail, a multipole expansion has been performed for each eigenmode (Figure 2c), that is, the contribution of the electric and magnetic multipoles to the radiation pattern has been determined [43]. The nature of mode ① corresponds to a pure electric dipole for $S = 0$, with a magnetic dipole contribution appearing as the central nanorod offset increases. Indeed, for $S = 40$ nm, a current loop is observed, similar to that of a split ring resonator [44]. For mode ②, the strong magnetic dipole contribution originating from the out-of-phase dipoles supported by the two vertical nanorods is gradually complemented by the appearance of an electric dipole contribution established on the central nanorod. Interestingly, when the central nanorod reaches the $S = 40$ offset, the gap between nanorods jumps from 2 to 2.66 nm, due to the rounded apex of the nanorods. This translates into a decrease of the near-field coupling and a resultant blue shift (Figure 2d) of mode ①. Overall, therefore, gaps in the few nanometers range in the context of dolmen structures present a 2-fold interest. First, both the spectral tunability and geometry-based mode energy shift sensitivity are enhanced. Second, important contributions of quadrupoles and transverse dipoles are enabled. This results in important redistributions of the charges as the geometry evolves, that is, as the central nanorod offset changes.

Strongly Coupled Dolmens Made with Capillary Assembly

To investigate these possibilities experimentally, dolmens with nanometer scale gaps have been fabricated by capillary assembly. In the process, a drop of colloidal solution containing Au nanorods is heated and swept across a topographically patterned template (see schematic in Figure 3a). As previously reported [31], upon heating, the nanorods tightly accumulate at the contact line of the drop, enter the topographic traps when

3.3. Mode Evolution in Strongly Coupled Plasmonic Dolmens Fabricated by Templated Assembly

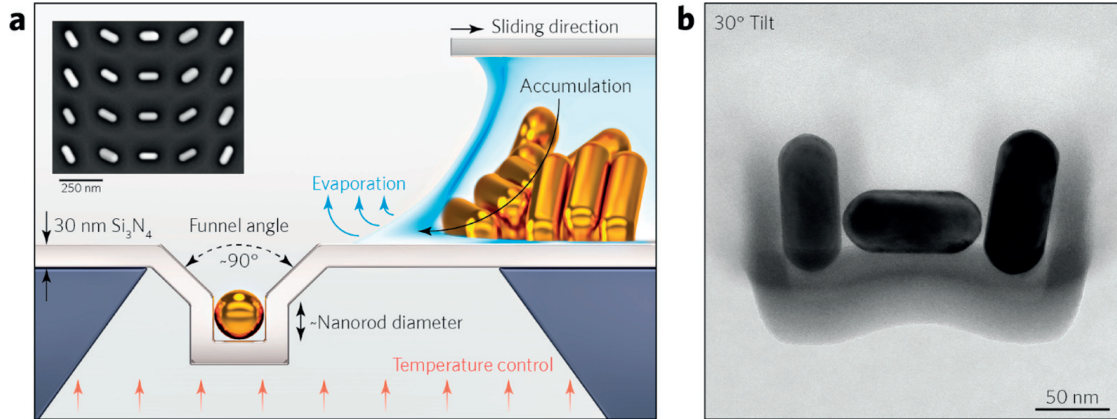


Figure 3 – Capillary assembly process for the fabrication of strongly coupled Au dolmens based on single crystal nanorods. (a) Schematic representation of the capillary assembly process. Funneled traps patterned in a 30 nm thick silicon nitride membrane selectively and tightly capture the nanorods from the solution into predetermined locations on the substrate. The designed funnel allows for a deterministic nanorod placement and orientation as highlighted in the SEM micrograph of the inset, here on a solid silicon substrate. (b) Tilted view transmission electron image of an assembled dolmen structure.

crossing them, and finally dry into a final location with deterministic position and orientation (inset Figure 3a). In order to obtain the desired trap funneled profile, a critical parameter for an efficient nanorod assembly, templates are fabricated as follows. Holes are first etched into silicon substrates by the transfer of resist tapering into the silicon to produce a straight trap decorated by an upper funnel that increases the nanorod capture cross-section (see Supporting Information for details). The silicon substrates are then coated by 30 nm of low-stress Si rich Si_xN_y by low pressure chemical vapor deposition that is subsequently released from the backside by potassium hydroxide Si wet etching. After functionalization with a hydrophobic silane, the substrates are cleaved into $17 \times 17 \text{ mm}^2$ dies for capillary assembly and subsequently cleaved into $3 \times 3 \text{ mm}^2$ samples with single Si_xN_y windows for TEM measurements. A typical dolmen structure is shown in Figure 3b, underlining that interparticle distances as short as 1.5 nm can indeed be achieved. In addition to nanometric interparticle distances, capillary assembly harnesses the plasmonic qualities of single crystalline gold [45], giving a similar design versatility as previously demonstrated by the FIB milling of single crystal gold flakes [46,47].

Among all the fabricated nanostructures, symmetric dolmens (denoted H1, H2, and H3) with gap sizes between 1.5 and 6 nm are studied first (Figure 4a). As shown from the previous simulations and measurements, the lowest energy bonding mode ① is the most sensitive to gap variations within the structure. This is experimentally demonstrated by integrating the EELS signal along the side of the dolmens H1, H2, and H3 (Figure 4b). The energy of mode ① gradually shifts from 1.4 to 1.15 eV as the gaps

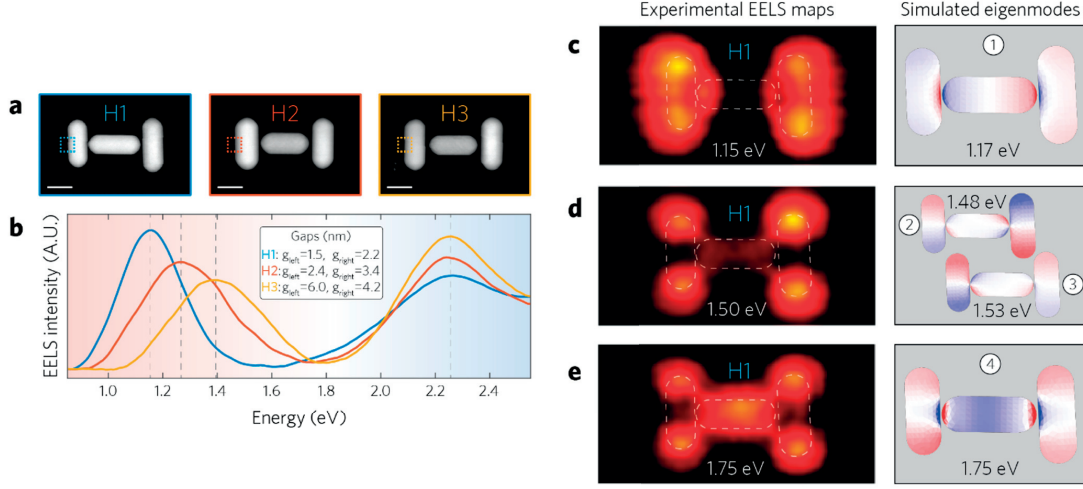


Figure 4 – Gradual coupling and EELS analysis for symmetric dolmens fabricated by capillary assembly. (a) HAADF image of three quasisymmetric assembled dolmens with gaps ranging from 1.5 to 6 nm. (b) Experimental EELS spectra extracted at the highlighted impact positions. (c-e) EELS maps and eigenmodes of dolmen H1. (c) EELS map and eigenmode associated with the low energy bonding mode. (d) EELS map at 1.50 eV with modes 2 and 3 that are spectrally overlapped. (e) EELS map of the higher order mode 4 dominated by quadrupoles and corresponding eigencharges. Each EELS map is displayed with a colorscale normalized to its maximal energy loss probability.

are reduced, in good agreement with the expected shift calculated for the simulated dolmens. As mentioned previously, modes ② and ③ spectrally overlap for symmetric dolmens. Although these two modes cannot be resolved directly in EELS because of their overlap, a slight asymmetry of the structure H1 (with the smallest gap sizes) appears to yield a stronger charge localization on the rightmost nanorod. This is well shown in its EELS map, in accordance with the computed eigenmode (Figure 4d). Mode ④ also exhibits a strong red-shift in comparison with the ~ 15 nm gap lithographic nanodolmens, as predicted by simulations. Further comparing to mode ④ in the lithographic structures (Figure 1), in H1 we also observe the disappearance of the two dark regions close to the central nanorod extremities, which correspond to nodes in the charge distributions. Additionally, strong EELS signal is measured in the central nanorod (Figure 4e). These observations are direct consequences of the stretching of the central quadrupole via the coupling to the adjacent nanorods.

Upon a shift of the central nanorod, a splitting of modes ① and ④ is expected along with the crossing of modes ② and ③ (Figure 2). To study this, we finally consider two assembled dolmens with central nanorod offset of 19 and 46 nm and average gap sizes of 2.5 nm (Figure 5a,b). Following the methodology described above, the EELS signal is extracted from the bottom end of one of the vertical nanorods along with the EELS signal from a gap region for both nanostructures. The comparison between experimental

3.3. Mode Evolution in Strongly Coupled Plasmonic Dolmens Fabricated by Templated Assembly

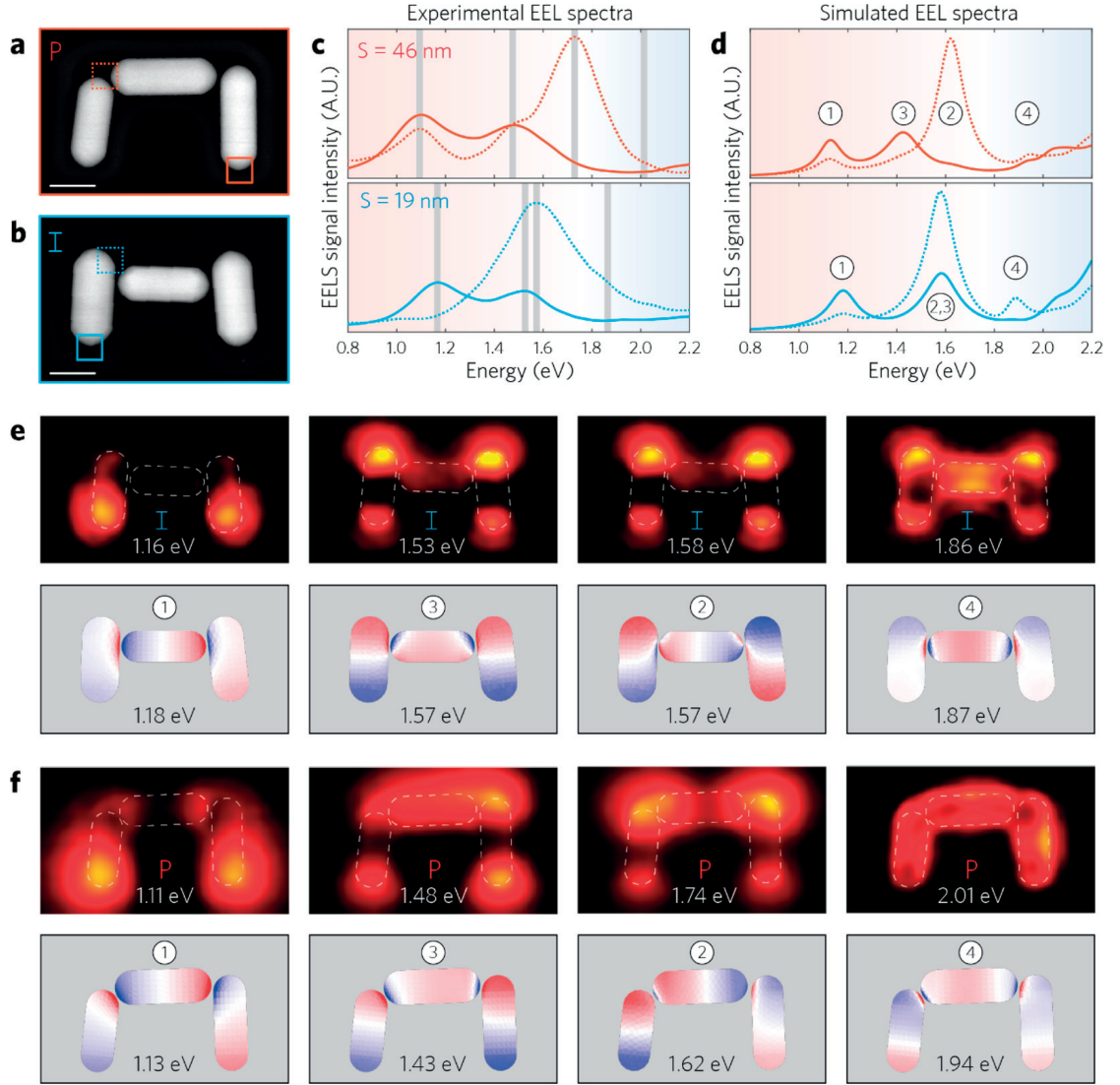


Figure 5 – EELS analysis for intermediate and fully offset dolmens fabricated by capillary assembly. (a) HAADF image of an assembled dolmens with 19 nm central rod offset and (b) 43 nm offset. (c) Experimental EELS spectra extracted from the locations highlighted in the HAADF images and corresponding simulations (d). (e) EELS maps and associated eigencharges of dolmen I with 19 nm central rod offset. (f) EELS maps and associated eigencharges of dolmen P with 43 nm central rod offset. Each EELS map is displayed with a colorscale normalized to its maximal energy loss probability.

(Figure 5c) and simulated (Figure 5d) spectra reveals an excellent spectral agreement and broader resonances for experimental data are primarily due to the convolution with the EELS zero-loss peak of 0.11 eV fwhm. For both dolmens, the low energy bonding mode ① is gradually red-shifted to 1.16 and 1.11 eV for $S = 19$ nm and $S = 46$ nm, respectively. The same mode was measured at 1.26 eV for the symmetric dolmen H2 with similar gap dimensions. For the intermediate dolmen I made by capillary assembly (Figure 5e), modes ② and ③ are not distinguished experimentally owing to a spectral overlap revealed by the simulations. In comparison, these modes are well distinguished for a large offset of the central nanorod (Figure 5f), as evidenced in both the EELS spectra and the EELS maps. The energy difference between the modes ① and ④, which increases from 0.7 to 0.9 eV, is another useful metric demonstrating the control of the assembly and sensitivity of the displacement of the central nanorod in this highly coupled system.

Remarkably, the capillary-assembled nanorod structures are stable even under prolonged electron beam irradiation, also when they are separated by the smallest possible interparticle distance as determined by the collapsed cetyltrimethylammonium bromide (CTAB) surfactant bilayer (1.5 nm). By instead fusing neighboring nanorods using an oxygen plasma treatment and annealing, the lower energy modes are red-shifted to energies below 1 eV, indicating the formation of charge transfer plasmons [31,48] (Figure S4). This hints to a unique alternative to Au flake milling for the fabrication of monomeric antennas with single crystal building blocks [46,47]. Additionally, we have also investigated the influence of asymmetries for a dolmen in which a vertical nanorod is significantly longer than the other ones while having zero offset for the shorter vertical nanorod respectively to the horizontal one (Figure S5). These measurements allow us to highlight the significant impact of asymmetry on near field localization and energy splitting of modes ② and ③, which respectively support out-of-phase and in-phase longitudinal dipoles on the vertical nanorods. In the case of this asymmetric dolmen, modes ② and ③ become strongly localized on the longer and shorter nanorods, respectively, and markedly split in energy. Owing to the different net dipole moments in each vertical nanorod, modified modes ② and ③ are expected to present a radiative nature, providing a good metric for the far-field analysis of the dolmen symmetry disentangled from offset parameter and gap width.

Conclusion

In conclusion, we have experimentally and theoretically investigated the near field coupling mechanisms in gold nanodolmens with different arrangements and interparticle distances. By using capillary assembly, interparticle gaps as short as 1.5 nm were produced leading to enhanced coupling and large energy splitting between bonding and antibonding modes. Additionally, the short gap distances produce a strong contribution from high energy quadrupole and transverse dipole modes. Their influence on the electromagnetic response

3.3. Mode Evolution in Strongly Coupled Plasmonic Dolmens Fabricated by Templated Assembly

were tracked by a gradual symmetry breaking of the nanodolmen via controlled vertical offsetting of the central nanorod. By relating the experimental findings to eigenmode simulations and multipolar decompositions, an excellent agreement was found between the response of idealized and fabricated structures. This work therefore paves the way for the fabrication of complex plasmonic nanoparticle assemblies that may enable new opportunities for the design of plasmonic rulers, refractive index sensors, and nonlinear antennas based on single crystal, low loss building blocks. Furthermore, and although our experiments have been fully interpreted and simulated relying on classical theory, combining the capillary assembly method with specific molecular spacers is a promising way to control plasmon resonances with molecular tunnel junction [49].

Acknowledgement

The research leading to these results has received funding from the European Commission's Seventh Framework Programme (FP7-ICT-2011-7) under Grant Agreements 288263 (Nano- Vista) and ERC-2015-AdG-695206 (Nanofactory) and the Swiss National Science Foundation (SNSF; 200020_153662). The authors gratefully acknowledge the valuable support from the EPFL center of micro- and nanofabrication (CMi).

References

- [1] Maier, S. A. *Plasmonics: Fundamentals and Applications*; Springer Science + Business Media LLC: New York, 2007.
- [2] Gallinet, B.; Butet, J.; Martin, O. J. F. Numerical methods for nanophotonics: standard problems and future challenges. *Laser Photonics Rev.* 2015, 9, 577-603.
- [3] Paolo, B.; Jer-Shing, H.; Bert, H. Nanoantennas for visible and infrared radiation. *Rep. Prog. Phys.* 2012, 75, 024402.
- [4] Chikkaraddy, R.; de Nijs, B.; Benz, F.; Barrow, S. J.; Scherman, O. A.; Rosta, E.; Demetriadou, A.; Fox, P.; Hess, O.; Baumberg, J. J. Single-molecule strong coupling at room temperature in plasmonic nanocavities. *Nature* 2016, 535, 127-130.
- [5] Shegai, T.; Chen, S.; Miljković, V. D.; Zengin, G.; Johansson, P.; Käll, M. A bimetallic nanoantenna for directional colour routing. *Nat. Commun.* 2011, 2, 481.
- [6] Verellen, N.; Sonnefraud, Y.; Sobhani, H.; Hao, F.; Moshchalkov, V. V.; Van Dorpe, P.; Nordlander, P.; Maier, S. A. Fano Resonances in Individual Coherent Plasmonic Nanocavities. *Nano Lett.* 2009, 9, 1663-1667.
- [7] Prodan, E.; Radloff, C.; Halas, N. J.; Nordlander, P. A hybridization model for the plasmon response of complex nanostructures. *Science* 2003, 302, 419-422.
- [8] Luk'yanchuk, B.; Zheludev, N. I.; Maier, S. A.; Halas, N. J.; Nordlander, P.; Giessen, H.; Chong, C. T. The Fano resonance in plasmonic nanostructures and metamaterials. *Nat. Mater.* 2010, 9, 707-715.
- [9] Halas, N. J.; Lal, S.; Chang, W. S.; Link, S.; Nordlander, P. Plasmons in strongly

coupled metallic nanostructures. *Chem. Rev.* 2011, 111, 3913-61.

[10] Kauranen, M.; Zayats, A. V. Nonlinear plasmonics. *Nat. Photonics* 2012, 6, 737-748.

[11] Yan, C.; Martin, O. J. F. Periodicity-Induced Symmetry Breaking in a Fano Lattice: Hybridization and Tight-Binding Regimes. *ACS Nano* 2014, 8, 11860-11868.

[12] Gallinet, B.; Martin, O. J. Refractive index sensing with subradiant modes: a framework to reduce losses in plasmonic nanostructures. *ACS Nano* 2013, 7, 6978-87.

[13] Gallinet, B.; Siegfried, T.; Sigg, H.; Nordlander, P.; Martin, O. J. Plasmonic radiance: probing structure at the Angstrom scale with visible light. *Nano Lett.* 2013, 13, 497-503.

[14] Butet, J.; Martin, O. J. Refractive index sensing with Fano resonant plasmonic nanostructures: a symmetry based nonlinear approach. *Nanoscale* 2014, 6, 15262-70.

[15] Liu, N.; Hentschel, M.; Weiss, T.; Alivisatos, A. P.; Giessen, H. Three-Dimensional Plasmon Rulers. *Science* 2011, 332, 1407-1410.

[16] Liu, N.; Langguth, L.; Weiss, T.; Kastel, J.; Fleischhauer, M.; Pfau, T.; Giessen, H. Plasmonic analogue of electromagnetically induced transparency at the Drude damping limit. *Nat. Mater.* 2009, 8, 758-762.

[17] Taubert, R.; Hentschel, M.; Kästel, J.; Giessen, H. Classical Analog of Electromagnetically Induced Absorption in Plasmonics. *Nano Lett.* 2012, 12, 1367-1371.

[18] Zhu, W.; Crozier, K. B. Quantum mechanical limit to plasmonic enhancement as observed by surface-enhanced Raman scattering. *Nat. Commun.* 2014, 5, 5228.

[19] Duan, H.; Fernández-Domínguez, A. I.; Bosman, M.; Maier, S. A.; Yang, J. K. W. Nanoplasmonics: Classical down to the Nanometer Scale. *Nano Lett.* 2012, 12, 1683-1689.

[20] Punj, D.; Regmi, R.; Devilez, A.; Plauchu, R.; Moparthi, S. B.; Stout, B.; Bonod, N.; Rigneault, H.; Wenger, J. Self-Assembled Nanoparticle Dimer Antennas for Plasmonic-Enhanced Single-Molecule Fluorescence Detection at Micromolar Concentrations. *ACS Photonics* 2015, 2, 1099-1107.

[21] Hu, M.; Ghoshal, A.; Marquez, M.; Kik, P. G. Single Particle Spectroscopy Study of Metal-Film-Induced Tuning of Silver Nanoparticle Plasmon Resonances. *J. Phys. Chem. C* 2010, 114, 7509-7514.

[22] Sau, T. K.; Rogach, A. L. Nonspherical noble metal nanoparticles: colloid-chemical synthesis and morphology control. *Adv. Mater.* 2010, 22, 1781-804.

[23] Tan, S. J.; Campolongo, M. J.; Luo, D.; Cheng, W. Building plasmonic nanostructures with DNA. *Nat. Nanotechnol.* 2011, 6, 268-276.

[24] Acuna, G. P.; Möller, F. M.; Holzmeister, P.; Beater, S.; Lalkens, B.; Tinnefeld, P. Fluorescence Enhancement at Docking Sites of DNADirected Self-Assembled Nanoantennas. *Science* 2012, 338, 506-510.

[25] Kuzyk, A.; Schreiber, R.; Zhang, H.; Govorov, A. O.; Liedl, T.; Liu, N. Reconfigurable 3D plasmonic metamolecules. *Nat. Mater.* 2014, 13, 862-866.

[26] Yang, S.; Ni, X. J.; Yin, X. B.; Kante, B.; Zhang, P.; Zhu, J.; Wang, Y.; Zhang, X. Feedback-driven self-assembly of symmetrybreaking optical metamaterials in solution. *Nat. Nanotechnol.* 2014, 9, 1002-1006.

[27] Ciraci, C.; Hill, R. T.; Mock, J. J.; Urzhumov, Y.; Fernández-Domínguez, A. I.;

3.3. Mode Evolution in Strongly Coupled Plasmonic Dolmens Fabricated by Templated Assembly

- Maier, S. A.; Pendry, J. B.; Chilkoti, A.; Smith, D. R. Probing the Ultimate Limits of Plasmonic Enhancement. *Science* 2012, 337, 1072-1074.
- [28] Bidault, S.; Devilez, A.; Maillard, V.; Lermusiaux, L.; Guigner, J.- M.; Bonod, N.; Wenger, J. Picosecond Lifetimes with High Quantum Yields from Single-Photon-Emitting Colloidal Nanostructures at Room Temperature. *ACS Nano* 2016, 10, 4806-4815.
- [29] Gao, B.; Arya, G.; Tao, A. R. Self-orienting nanocubes for the assembly of plasmonic nanojunctions. *Nat. Nanotechnol.* 2012, 7, 433- 437.
- [30] Jones, S. T.; Taylor, R. W.; Esteban, R.; Abo-Hamed, E. K.; Bomans, P. H.; Sommerdijk, N. A.; Aizpurua, J.; Baumberg, J. J.; Scherman, O. A. Gold nanorods with sub-nanometer separation using cucurbit[n]uril for SERS applications. *Small* 2014, 10, 4298-303.
- [31] Flauraud, V.; Mastrangeli, M.; Bernasconi, G. D.; Butet, J.; Alexander, D. T. L.; Shahrabi, E.; Martin, O. J. F.; Brugger, J. Nanoscale topographical control of capillary assembly of nanoparticles. *Nat. Nanotechnol.* 2016, 12, 73-80.
- [32] Khunsin, W.; Dorfmueller, J.; Esslinger, M.; Vogelgesang, R.; Rockstuhl, C.; Et- rich, C.; Kern, K. Quantitative and Direct Near-Field Analysis of Plasmonic-Induced Transparency and the Observation of a Plasmonic Breathing Mode. *ACS Nano* 2016, 10, 2214-24.
- [33] Yu, H.; Sun, Q.; Ueno, K.; Oshikiri, T.; Kubo, A.; Matsuo, Y.; Misawa, H. Explor- ing Coupled Plasmonic Nanostructures in the Near Field by Photoemission Electron Microscopy. *ACS Nano* 2016, 10, 10373-10381.
- [34] Bellido, E. P.; Bicket, I. C.; McNeil, J.; Botton, G. A. Very High Resolution Energy Loss Spectroscopy: Applications in Plasmonics. *Microsc. Microanal.* 2016, 22, 974-975.
- [35] Coenen, T.; Schoen, D. T.; Mann, S. A.; Rodriguez, S. R.; Brenny, B. J.; Polman, A.; Brongersma, M. L. Nanoscale Spatial Coherent Control over the Modal Excitation of a Coupled Plasmonic Resonator System. *Nano Lett.* 2015, 15, 7666-70.
- [36] Coenen, T.; Schoen, D. T.; Brenny, B. J. M.; Polman, A.; Brongersma, M. L. Combined electron energy-loss and cathodoluminescence spectroscopy on individual and composite plasmonic nanostructures. *Phys. Rev. B: Condens. Matter Mater. Phys.* 2016, 93, 195429.
- [37] Losquin, A.; Zagonel, L. F.; Myroshnychenko, V.; Rodríguez- González, B.; Tencé, M.; Scarabelli, L.; Förstner, J.; Liz-Marzán, L. M.; García de Abajo, F. J.; Stéphan, O.; Kociak, M. Unveiling Nanometer Scale Extinction and Scattering Phenomena through Combined Electron Energy Loss Spectroscopy and Cathodoluminescence Measurements. *Nano Lett.* 2015, 15, 1229-1237.
- [38] Bernasconi, G. D.; Butet, J.; Flauraud, V.; Alexander, D.; Brugger, J.; Martin, O. J. F. Where Does Energy Go in Electron Energy Loss Spectroscopy of Nanostructures? *ACS Photonics* 2017, 4, 156- 164.
- [39] Hohenester, U.; Ditlbacher, H.; Krenn, J. R. Electron-Energy- Loss Spectra of Plasmonic Nanoparticles. *Phys. Rev. Lett.* 2009, 103, 106801.
- [40] Bernasconi, G. D.; Butet, J.; Martin, O. J. F. Mode analysis of second-harmonic generation in plasmonic nanostructures. *J. Opt. Soc. Am. B* 2016, 33, 768-779.

- [41] Gallinet, B.; Martin, O. J. F. Relation between near-field and far-field properties of plasmonic Fano resonances. *Opt. Express* 2011, 19, 22167-22175.
- [42] Nordlander, P.; Oubre, C.; Prodan, E.; Li, K.; Stockman, M. I. Plasmon Hybridization in Nanoparticle Dimers. *Nano Lett.* 2004, 4, 899-903.
- [43] Mühlig, S.; Menzel, C.; Rockstuhl, C.; Lederer, F. Multipole analysis of meta-atoms. *Metamaterials* 2011, 5, 64-73.
- [44] Sarychev, A. K.; Shvets, G.; Shalaev, V. M. Magnetic plasmon resonance. *Phys. Rev. E* 2006, 73, 036609.
- [45] Shao, L.; Tao, Y. T.; Ruan, Q. F.; Wang, J. F.; Lin, H. Q. Comparison of the plasmonic performances between lithographically fabricated and chemically grown gold nanorods. *Phys. Chem. Chem. Phys.* 2015, 17, 10861-10870.
- [46] Huang, J. S.; Callegari, V.; Geisler, P.; Bruning, C.; Kern, J.; Prangsma, J. C.; Wu, X.; Feichtner, T.; Ziegler, J.; Weinmann, P.; Kamp, M.; Forchel, A.; Biagioni, P.; Sennhauser, U.; Hecht, B. Atomically flat single-crystalline gold nanostructures for plasmonic nanocircuitry. *Nat. Commun.* 2010, 1, 150.
- [47] Celebrano, M.; Wu, X.; Baselli, M.; Grossmann, S.; Biagioni, P.; Locatelli, A.; De Angelis, C.; Cerullo, G.; Osellame, R.; Hecht, B.; Duò, L.; Ciccacci, F.; Finazzi, M. Mode matching in multiresonant plasmonic nanoantennas for enhanced second harmonic generation. *Nat. Nanotechnol.* 2015, 10, 412-417.
- [48] Pérez-González, O.; Zabala, N.; Borisov, A. G.; Halas, N. J.; Nordlander, P.; Aizpurua, J. Optical Spectroscopy of Conductive Junctions in Plasmonic Cavities. *Nano Lett.* 2010, 10, 3090-3095.
- [49] Tan, S. F.; Wu, L.; Yang, J. K. W.; Bai, P.; Bosman, M.; Nijhuis, C. A. Quantum Plasmon Resonances Controlled by Molecular Tunnel Junctions. *Science* 2014, 343, 1496-1499.

Supplementary informations

Methods

Sample fabrication: Lithographic samples

Silicon wafers (100 mm diameter, prime grade double side polished) were cleaned following a standard RCA procedure prior to low pressure chemical vapor deposition of 30 nm-thick silicon nitride. Backside photolithography and wet etching by potassium hydroxide were performed to release $500 \times 100 \mu\text{m}^2$ freestanding silicon nitride windows. A single layer of polymethylmethacrylate, (PMMA 495 A2, MicroChem) was then spun at 2500rpm for 60 s yielding an approximately 90 nm-thick coating following a 3 min bake at 180°C prior to the coating of a conductive layer (Espacer 300Z ShowaDenko). The samples were then exposed by electron beam lithography (VISTEC EBPG5000+, 100 kV) and developed at room temperature for 60 s in a 1:3 mixture of methyl isobutyl ketone / isopropyl alcohol. Chromium and Gold (1nm / 25 nm) were then evaporated by electron beam heating at a pressure of $8 \cdot 10^{-7}$ mBar prior to lift-off in acetone. The samples were finally cleaved in $3 \times 3 \text{ mm}^2$ dies for measurements in the TEM.

Sample fabrication: Assembly templates

Silicon wafers (100 mm diameter, prime grade double side polished) were cleaned following a standard RCA procedure. Topographical traps defining the 2D dolmen geometries were defined using ZEP-520A (Zeon Chemicals) resist spun at 2500 rpm (~ 150 nm-thickness), exposed by electron beam lithography, developed at room temperature for 60 s in n-amyl-acetate and rinsed in a mixture of methyl isobutyl ketone / isopropyl alcohol (9:1) for 60 s before being blow dried with a nitrogen gun. The funnel profile of the traps was obtained by exploiting resist faceting during Cl₂-based inductively-coupled plasma reactive ion etching of silicon (STS Multiplex ICP) that was transferred to the underlying silicon substrate. Low pressure chemical vapor deposition of 30 nm-thick silicon nitride was then performed followed by the release of freestanding membranes as described above. The substrates were then cleaved, surface-activated by exposure to oxygen plasma (Tepla Gigabatch, 1000 W, 5 min, 500 SCCM O₂) and finally rendered hydrophobic by vapor-phase absorption of 1H,1H,2H,2H- perfluorodecyltrichlorosilane (Aldrich) under vacuum for 1 h. The wettability of the substrates was characterized through static contact angle measurements by the sessile drop method before experiments, obtaining values in excess of 110° for water and 63° C for CTAB solution at its CMC at room temperature.

Nanoparticle assembly

Nanoparticle assembly was performed relying on the same equipment and methodology as previously reported [1]. Briefly, CTAB stabilized nanorods purchased from Nanopartz (USA) were concentrated at $\sim 2.64 \cdot 10^{11}$ particles \cdot ml $^{-1}$ and washed in CTAB 0.9 mM. 50–70 μ L of the prepared solution was injected between the templates and a static coverslip. Upon heating (45–50°C) the template was set in relative motion to the coverslip at $\sim 2 \mu\text{m} \cdot \text{s}^{-1}$ in order to generate nanoparticle accumulation at the meniscus and cross the topographic traps.

EELS measurements

STEM-EELS maps were acquired using a FEI Titan Themis 60–300 equipped with a Wien-type monochromator and a Gatan GIF Quantum ERS spectrometer. A 300 keV incident electron beam was used for all experiments, monochromated to give an energy spread of 110 meV full width half maximum in the zero-loss peak of elastically-scattered electrons, and with beam currents of ~ 240 pA. A 17 mrad convergence semi-angle of the probe and a 22 mrad collection semi-angle on the spectrometer were used, with the probe having a mean diameter inferior to 1 nm for full width tenth maximum in incident intensity. Mapping was performed using the “ultrafast” spectrum imaging mode with typical dwell times of 0.20–0.26 ms per pixel, and with the probe rastered in X, Y step sizes of 0.5–0.6 nm for a total of $>10^5$ pixels per map. Each map was treated with the HQ Dark Correction plugin to reduce noise associated with dark current subtraction.

EELS data processing

The EELS data cubes were processed using Gatan Digital Micrograph and custom Matlab® scripts for the removal of the background from the tails of the zero-loss peak (ZLP) and extraction of point spectra and spatial EELS maps. The ZLP was first aligned at 0 eV pixel by pixel by fitting the ZLP of each pixel spectrum with a Gaussian-Lorentzian approximation to identify its center. Following zero-loss alignment, each data cube was spectrally cropped to the region of interest including ZLP (–2 eV to 4 eV), and intensity spikes from cosmic rays were removed. To account for the absorption and scattering inside the Au film or nanoparticles, the data cubes were normalized by dividing each pixel-spectrum by the integrated intensity of its corresponding fitted ZLP. In this way the “true” projected plasmon intensity distribution is retrieved [2]. Experimental spectra shown in the figures were integrated over 50×50 pixel regions of interest at the positions indicated on the corresponding HAADF-STEM images, whereas EELS intensity maps were typically integrated over an energy window of 0.06 eV width centered on the relevant plasmon peak resonance energy. For visualization purposes, the maps were smoothed using a penalized least square method [3].

3.3. Mode Evolution in Strongly Coupled Plasmonic Dolmens Fabricated by Templated Assembly

Simulations

A surface integral equation method [4] is used to compute the interaction between the electromagnetic field associated to the swift electron and the plasmonic nanostructures as well as for the computation of the eigenmodes. The nanostructure's surface is discretized with triangular mesh elements and the electric and magnetic fields in the entire space (inside and outside the nanoparticle) are related to fictitious electric and magnetic surface currents through a matrix describing the geometry and material of the structure. EELS is computed in two steps: first by exciting the structure with the fields associated to a swift electron, and then by computing the work done on the electron by the Lorentz force against this scattered field [5-6]. The eigenmodes are found by looking for the eigenvectors of the aforementioned matrix when no excitation is imposed [7]. Only the real part of the surface charge of the eigenmodes is shown, as the imaginary part is either vanishing or negligible compared to the real part and does not bring any useful information to associate the modes to the EELS map.

Supplementary figures

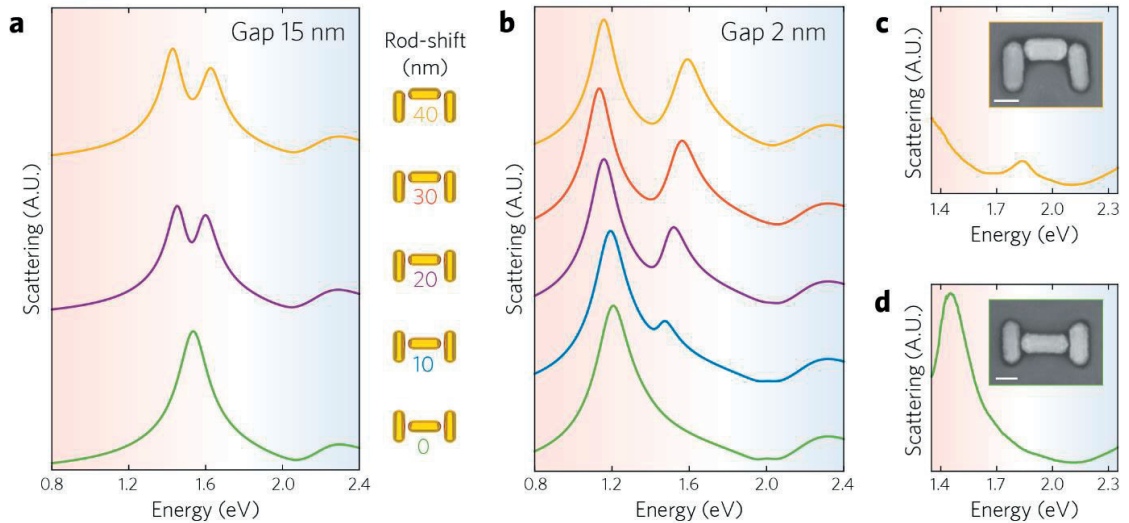


Figure S1 – **Plane wave excitation.** (a) Scattering spectra computed for a normal incidence plane wave excitation polarized along the central rod long axis for the lithographically defined dolmen geometries of Figure 1. (b) Similar simulation for the 2 nm gap ideal dolmens of Figure 2. (c) and (d) experimental dark field scattering spectra for two extreme cases of the central rod offset for two dolmens assembled on SiO_2 templates. The slight blue-shift between experiments and simulations is due to the different surrounding index. Simulations were computed for comparison with EELS experiments where assembly was performed on Si_xN_y membranes (refractive index $n \approx 2$) whereas the samples for optical excitations are on SiO_2 ($n \approx 1.5$).

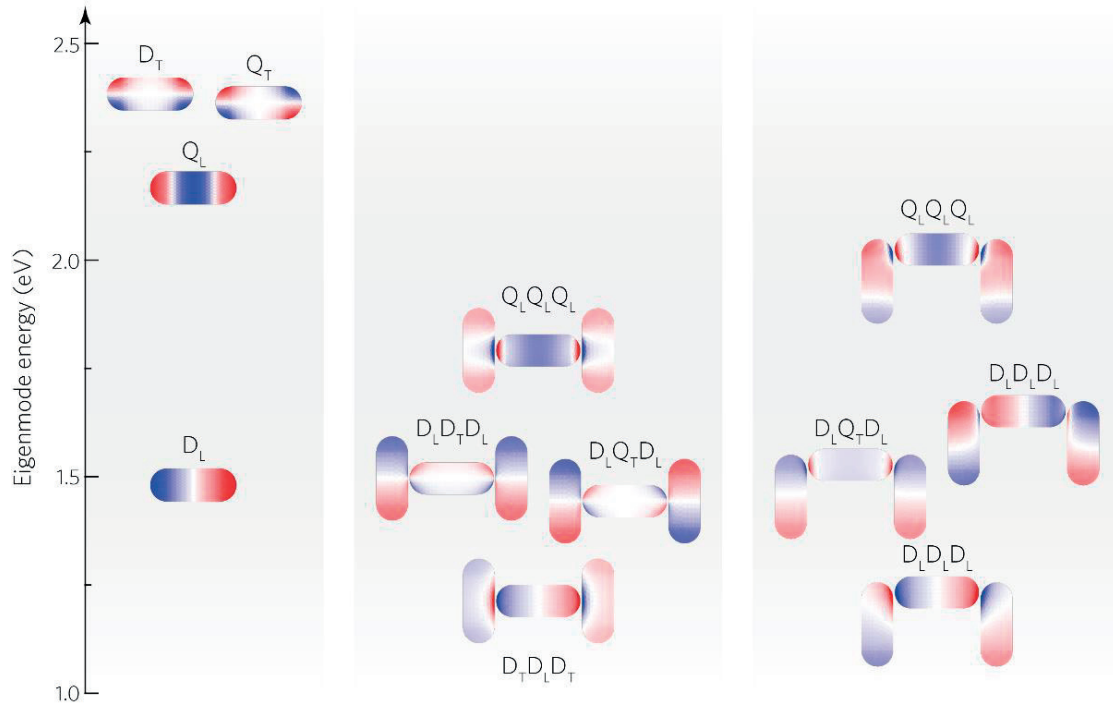


Figure S2 – **Hybridization pattern.** Eigencharges for the modes of an isolated nanorod ($40 \text{ nm} \times 105 \text{ nm}$) with, in increasing energy, the longitudinal dipole D_L , longitudinal quadrupole Q_L , transverse quadrupole Q_T and transverse dipole D_T . Eigenmodes of dolmens with two extreme offset parameters for the central rod ($S = 0 \text{ nm}$ and $S = 40 \text{ nm}$) show the evolution and decomposition of the coupled system from the eigenmodes of the isolated nanorod.

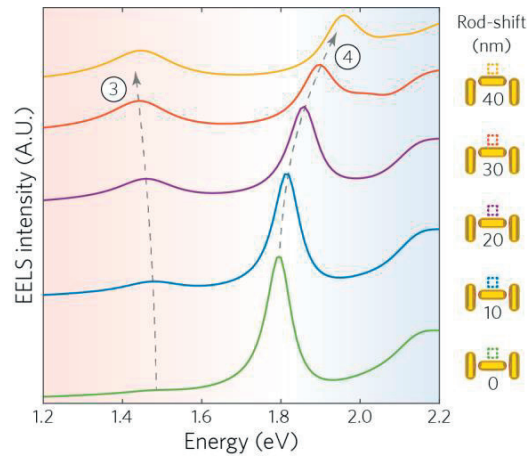


Figure S3 – **Second impact parameter.** EELS spectra computed for an impact parameter 8 nm away from the central top side of the central rod. Due to symmetry reasons only mode 3 is driven confirming its progressive red-shift independently from mode 2.

3.3. Mode Evolution in Strongly Coupled Plasmonic Dolmens Fabricated by Templated Assembly

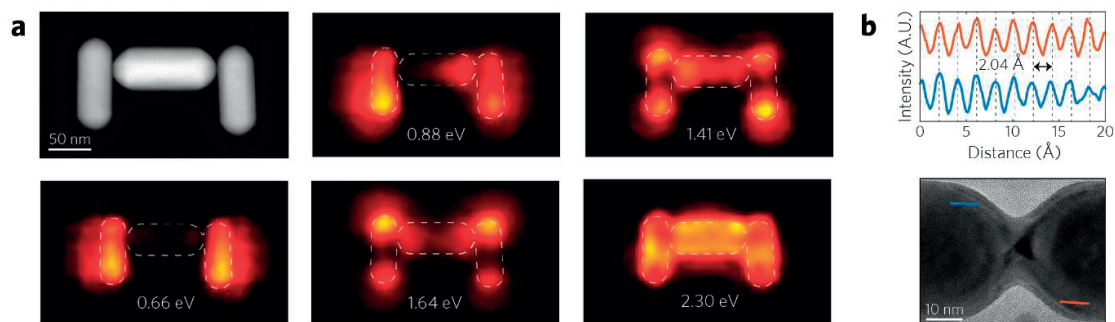


Figure S4 – **Fused nanorods**. (a) HAADF image and associated plasmon resonance EELS intensity maps of fused dolmen structure induced by oxygen plasma treatment. Charge transfer plasmon modes are created, leading to a strong red-shift of the lower energy modes down to 0.66 eV. (b) Line profiles of Au lattice fringes observed by high resolution TEM from the locations indicated with corresponding colors on the image below, showing that the crystallinity of the Au nanorods has been preserved after oxygen plasma and annealing. Diffraction contrast suggests the presence of only a thin ~ 5 nm amorphous layer on the surface.

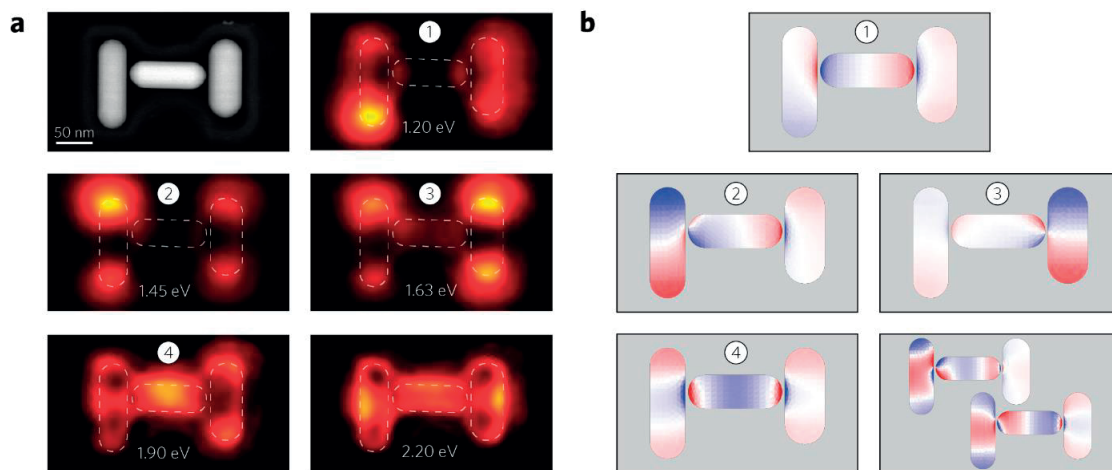


Figure S5 – **Asymmetric dolmen assembly**. (a) HAADF image and associated plasmon resonance EELS intensity maps of an asymmetric dolmen. (b) Corresponding eigencharge distributions.

References

- [1]. Flauraud, V.; Mastrangeli, M.; Bernasconi, G. D.; Butet, J.; Alexander, D. T. L.; Shahrabi, E.; Martin, O. J. F.; Brugger, J., Nanoscale topographical control of capillary assembly of nanoparticles. *Nat. Nanotechnol.* 2017, 12, 73-80.
- [2]. Le Thomas N.; Alexander, D.T.L.; Cantoni, M.; Sigle, W.; Houdré, R.; Hébert, C., Imaging of high-Q cavity optical modes by electron energy-loss spectroscopy. *Phys. Rev. B* 2013, 87, 155314.
- [3]. Garcia, D., Robust smoothing of gridded data in one and higher dimensions with missing values. *Comput Stat Data Anal* 2010, 54, 1167-1178.
- [4]. Kern, A. M.; Martin, O. J. F., Surface integral formulation for 3D simulations of plasmonic and high permittivity nanostructures. *J. Opt. Soc. Am. A* 2009, 26 , 732-740.
- [5]. Ritchie, R. H., Plasma Losses by Fast Electrons in Thin Films. *Phy. Rev.* 1957, 106, 874-881.
- [6]. García de Abajo, F. J., Optical excitations in electron microscopy. *Reviews of Modern Physics* 2010, 82, 209-275.
- [7]. Bernasconi, G. D.; Butet, J.; Martin, O. J. F., Mode analysis of second-harmonic generation in plasmonic nanostructures. *Rev. Mod. Phys.* 2016, 33, 768-779.

3.4 Self-Similarity of Plasmon Edge Modes on Koch Fractal Antennas

Manuscript state: Published

Reference: Edson P. Bellido, **Gabriel D. Bernasconi**, David Rossouw, Jérémy Butet, Olivier J. F. Martin, and Gianluigi A. Botton "Self-Similarity of Plasmon Edge Modes on Koch Fractal Antennas", *ACS Nano* (11), 11240-11249, (2017).

Publication date: October 30, 2017

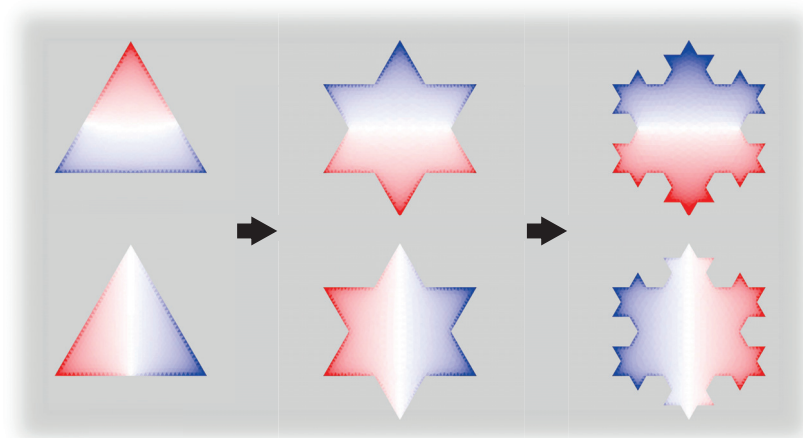
DOI: 10.1021/acs.nano.7b05554

URL: <https://pubs.acs.org/doi/10.1021/acs.nano.7b05554>

Adapted with permission from the above-mentioned reference.
Copyright (2017) American Chemical Society.

Author contributions

G. D. Bernasconi performed the numerical simulations with the surface integral method and contributed to the data analysis and to the manuscript writing.



Self-Similarity of Plasmon Edge Modes on Koch Fractal Antennas

Edson P. Bellido¹, Gabriel D. Bernasconi², David Rossouw¹, Jérémy Butet², Olivier J. F. Martin², and Gianluigi A. Botton¹

¹Department of Materials Science and Engineering, McMaster University, 1280 Main Street W., Hamilton, Ontario L8S 4L7, Canada.

²Nanophotonics and Metrology Laboratory, Swiss Federal Institute of Technology Lausanne (EPFL), 1015, Lausanne, Switzerland.

Corresponding author: jgbotton@mcmaster.ca

ABSTRACT: We investigate the plasmonic behavior of Koch snowflake fractal geometries and their possible application as broadband optical antennas. Lithographically defined planar silver Koch fractal antennas were fabricated and characterized with high spatial and spectral resolution using electron energy loss spectroscopy. The experimental data are supported by numerical calculations carried out with a surface integral equation method. Multiple surface plasmon edge modes supported by the fractal structures have been imaged and analyzed. Furthermore, by isolating and reproducing self-similar features in long silver strip antennas, the edge modes present in the Koch snowflake fractals are identified. We demonstrate that the fractal response can be obtained by the sum of basic self-similar segments called characteristic edge units. Interestingly, the plasmon edge modes follow a fractal-scaling rule that depends on these self-similar segments formed in the structure after a fractal iteration. As the size of a fractal structure is reduced, coupling of the modes in the characteristic edge units becomes relevant, and the symmetry of the fractal affects the formation of hybrid modes. This analysis can be utilized not only to understand the edge modes in other planar structures but also in the design and fabrication of fractal structures for nanophotonic applications.

Introduction

The use of fractal geometries has significantly impacted many areas of science and engineering. One such area is antenna design, where fractal geometries are often utilized in portable communication devices for their compact, broadband characteristics [1,2]. The term fractal is used to describe curves (most commonly in two dimensions) that present repeating patterns (exact, quasi, or statistical self-similarity), at all scale, often obtained by iteratively applying some transformation on a system [3]. This particular property, as well as their ability to compactly fill space, makes fractals ideal candidates

3.4. Self-Similarity of Plasmon Edge Modes on Koch Fractal Antennas

for broadband antennas, and they have indeed inspired the design of several macroscopic antennas that exhibit broadband behavior and improved performance in the GHz regime [4-9].

In recent years, interest in a new type of antenna based on surface plasmon resonances, designed to operate at visible light frequencies, has been motivated by potential applications in sensing [10], imaging [11], energy harvesting [12,13], and disease prevention and cure [14]. These so-called “optical antennas” or “nano-antennas” have characteristic dimensions at nanometer-length scales, requiring nanometer precision for their fabrication and characterization [15]. With improved nanofabrication tools, including focused ion beam and electron beam lithography (EBL) [16], their fabrication is becoming increasingly feasible. Early prototype structures studied include dipole [17] gap [18,19] bowtie [20], and Yagi-Uda [21] antennas. The nanoscale dimensions of optical antennas call for demanding characterization requirements and experimental techniques that can image beyond the optical diffraction limit are necessary for the detailed study of subwavelength field confinements in optical antennas. Electron energy loss spectroscopy (EELS), performed in a scanning transmission microscope (STEM), is one of the few techniques which meets all these requirements, combining subnanometer spatial resolution and spectral resolution exceeding 100 meV [22]. Although the EELS energy resolution is lower compared with its optical counterparts, deconvolution techniques and new designs of monochromators can achieve resolutions close to 10 meV [23,24]. The STEM-EELS technique has been used successfully to map optical excitations in a variety of nanostructure geometries, including triangular prisms [25], rods [26,27], wires [28], cubes [27], among others [29-42]. Early studies of optical fractal antenna designs, including the Cayley tree [43], Sierpinski fractals [44-47], and other self-similar geometries [48-51], suggest that broadband absorption can be achieved in fractal plasmonic nanoantennas. Plasmonic fractal structures have also been tested to improve the efficiency in application such as photovoltaics [52,53], extraordinary transmission [47], fluorescence enhancement [54], third harmonic generation [55], and molecular detection [56]. In this work, we focus on the Koch snowflake fractal geometry. A Koch fractal is constructed by starting with an equilateral triangle (iteration 0) and repeating the following procedure iteratively: Divide each edge of the structure into three segments of equal length and then place an equilateral triangle pointing outward in the central segment in each line, that is, the central segment is the base of the new triangle. The fractals are defined by the number of times the described procedure was applied (i.e., an iteration). Figure S1 in the Supporting Information shows the iterations of the Koch fractal geometry. Furthermore, the insets in Figures 1a, 2a, and 5a show annular dark-field (ADF) images of the Koch fractal iterations 0, 1, and 2, respectively. We use EBL to fabricate a set of nanoscale fractal antennas, and STEM-EELS is used to image the optical excitations supported by the structures (see Methods section). The high spatial resolution achieved with STEM-EELS allows us to visualize the multiple plasmonic modes supported by the fractal structures, to analyze the structural origin of the modes present, and to study the

effect of self-similarity by comparing the response of different fractal geometry iterations. The experimental results are complemented with numerical calculations of both EELS spectra and eigenmodes, as described in the Methods section. In this work, we show that the localized plasmon resonances in a complex geometry such as the Koch snowflake fractal follow simple scaling rules based on the number of self-similar segments found in the structure. These scaling rules may be used in the design of fractal antennas for applications in sensing and compact nanophotonic architectures.

Results and Discussion

To analyze the effect of self-similarity on the spectral response of metallic nanoantennas, silver Koch snowflake fractal antennas of iterations 0, 1, and 2 have been fabricated, as shown in the insets in Figures 1a, 2a, and 5a. The iteration 0 structure has a side length of $2\ \mu\text{m}$ and a thickness of 30 nm. The first and second iteration structures maintain a thickness of 30 nm. Figures 1a, 2a, and 5a show the experimental (top) and simulated (bottom) EELS spectra of the fractal structures obtained at several positions indicated by the color-coded boxes in the insets. Overall, we observe a fair agreement between the simulation and the experiment with plasmon peaks and energies well reproduced. The increasing difference of the peaks energy between experiment and simulation is assumed to be due to the absence of the substrate in the simulations, whose influence can change with increasing mode energy [57], as well as possible deviations of the actual Ag permittivity from the Drude model used for computations. The spectral response of each structure exhibits several surface plasmon resonances with a first resonant peak at approximately the same energy ($0.22 \pm 0.04\ \text{eV}$) for all the iterations of the Koch fractal behavior. The simulations confirm this effect.

Edge Modes and Koch Fractal Iteration Zero

As previously described in the literature, the resonances in a planar structure can be described as quasi one-dimensional resonances (edge modes) along the edge of a structure [33,58-60]. Even the fundamental dipolar and quadrupolar modes can be described in terms of edge modes [61]. An edge mode of order m is noted E_m , m being the number of nodes along the edge. Also, edge modes can be designated as odd or even depending on the number of nodes m (or, equivalently, with opposite or identical charges at the edge extremities). The maps in Figure 1b show the resonances of the fractal iteration 0 that display along each one of the edges the characteristic node distribution of edge modes. Thus, the first resonant peak at $0.22 \pm 0.03\ \text{eV}$ corresponds to a dipolar mode or edge mode order one (E_1), and the following peaks can be identified as formed by edge modes order two (E_2), three (E_3), four (E_4), five (E_5), and six (E_6) at 0.44, 0.62, 0.78, 0.90, and 1.06 eV respectively (with an effective energy resolution of 30 meV). These results are supported by simulations of the eigenmodes, in Figure 1c, that

3.4. Self-Similarity of Plasmon Edge Modes on Koch Fractal Antennas

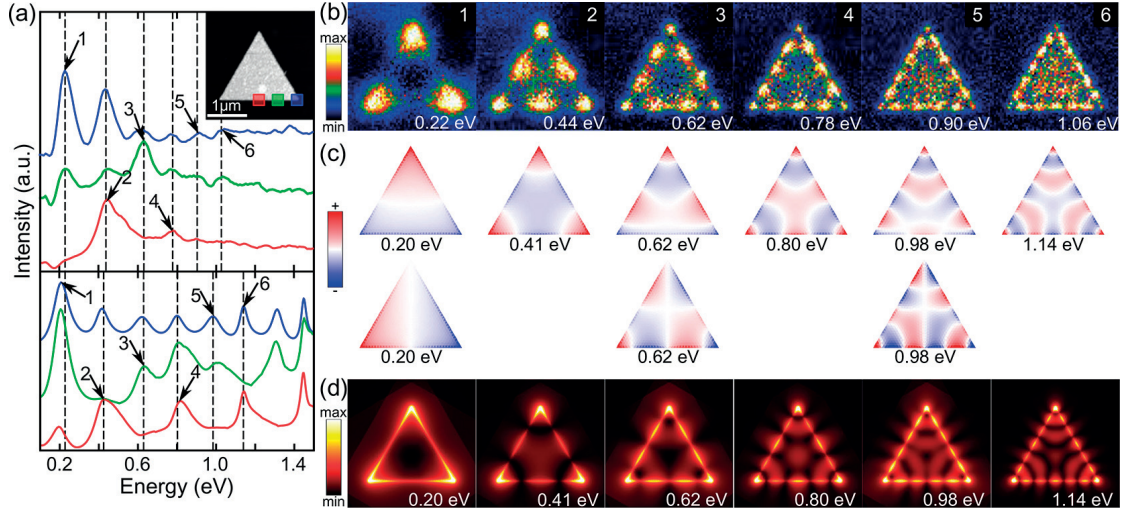


Figure 1 – (a) Experimental (top) and computed (bottom) EEL spectra of Koch fractal antenna iteration 0, acquired at the color-coded positions indicated in the ADF image in the inset. The numbers indicate the resonant peaks. (b) Experimental EELS maps of the resonant peaks, indicated in (a), formed by edge modes. (c) Computed charge distributions of the equilateral triangle eigenmodes. The even edge modes only form one eigenmode, while the odd edge modes form two degenerate modes one symmetric and one antisymmetric. (d) Symmetrized near-field intensity distributions of the eigenmodes found in the Koch fractal antennas of iteration 0. Degenerate eigenmodes display identical symmetrized near-field intensities. The EELS maps are obtained at the energies corresponding to the peaks in the EEL spectra ± 30 meV. The energies indicated in the near-field intensity maps are those of the eigenmodes, not the energy of the peaks in the EEL spectra.

show the charge distribution of edge modes at the edges of the equilateral triangle according to the symmetry of the nanostructure. Based on the symmetry of the Koch fractal structures, we will designate as symmetric or antisymmetric the eigenmodes with symmetric or antisymmetric charge distributions with respect to the vertical axis. Due to the structure symmetry, each eigenmode having only the mirror symmetry (symmetric or antisymmetric) will implicitly exist 3 times for the iteration 0 and 6 times for higher iterations. Since this does not bring any additional information, this “degeneracy” will not be mentioned further, and the term degeneracy will only refer to eigenmodes having the same energy but different charge distributions that cannot be matched by mirror or rotation operation. The choice of the vertical axis as the reference axis is arbitrary, and considering one of the other two symmetry axes would give the same results. EELS maps also follow the structure symmetry because the signal is obtained by exciting and probing at the same location, the simplest example being the resonances of a nanodisk that appear like concentric rings [62]. For the same reason, Koch snowflake fractals EELS maps always have a C_3 or C_6 symmetry, for iteration 0 and higher, respectively. Otherwise, this is not the case for all the computed eigenmodes, and to be able to identify them easily in the EELS maps, the electric near-field intensity of each eigenmode (Figures 1d, 2d, and 5d) is “symmetrized” by adding itself 3 times following 0° , 120° , and 240° rotations. These symmetrized maps provide a qualitative link between the measurements and the simulations. Interestingly, we observe that degenerate eigenmodes give the same symmetrized near-field map, despite different charge distributions. The electric near-field intensities of the eigenmodes before being symmetrized are shown in in Figures S2-S4.

Following this description, the eigenmodes present in the equilateral triangle (Koch fractal of iteration 0) can be analyzed. Figure 1c,d shows the surface charge distributions and the simulated, symmetrized, electric near-field intensity distributions of the eigenmodes for the fractal iteration 0. From the surface charge distributions, it is clear that all three edges of the triangle in the eigenmodes of the resonant peaks 2, 4, and 6 display a charge distribution corresponding to a one-dimensional mode of the same order E_2 , E_4 , and E_6 (with even edge modes), respectively. For the case of the eigenmodes formed by E_1 , E_3 , and E_5 (with odd edge modes), two degenerate eigenmodes are present: one in which two edges have the same charge distribution corresponding to an edge mode (symmetric eigenmode), and another eigenmode in which only one edge exhibits the charge distribution corresponding to an edge mode and the two other edges have opposite charge distribution sign relatively to each other (antisymmetric eigenmode). The eigenmodes E_2 , E_4 , and E_6 follow the same C_3 symmetry as the triangle, whereas other eigenmodes only have the mirror symmetry with degeneracy two (antisymmetric and symmetric respectively to the vertical axis). Based on the symmetry of the triangle, the formation of two degenerate eigenmodes for odd edge modes is understandable. This is due to the fact that in all odd edge modes the charge at the extremities of the edge (the triangle corner) must be opposite, and in a triangle only two edges at maximum can fulfill this constraint at the same time. The odd edge modes therefore split into

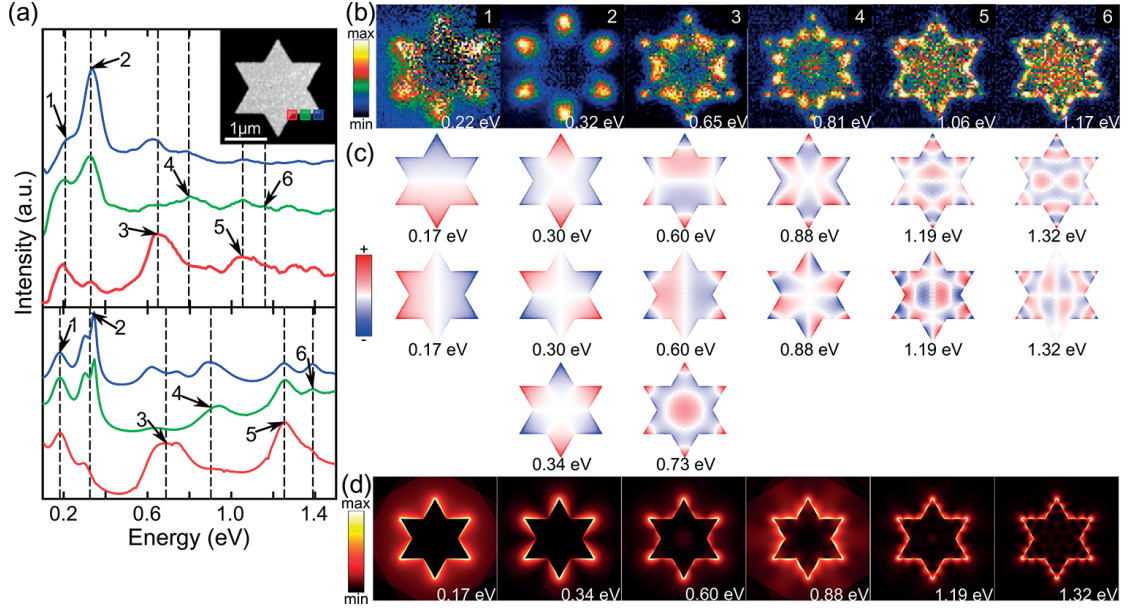


Figure 2 – (a) Experimental (top) and computed (bottom) EEL spectra of Koch fractal antenna iteration 1, acquired at the color-coded positions indicated in the ADF image in the inset. The numbers indicate the resonant peaks. (b) Experimental EELS maps of the resonant peaks, indicated in (a), displaying the modes formed by edge modes that can be analyzed by isolating its characteristic “V” edge unit as shown in Figure 3a,b. The analysis shows that the first peak is a dipolar mode, and the next modes are formed by E_m ($m = 1-5$) modes in the characteristic edge units. (c) Computed charge distributions of the fractal iteration 1 eigenmodes. All the eigenmodes formed by edge modes are degenerate, and they can be understood considering the interaction of the edge modes within the fractal structure and its symmetry as shown in Figures 4b,c and S9. (d) Symmetrized near-field intensity distributions of the eigenmodes found in the Koch fractal antennas of iteration 1. Degenerate eigenmodes display identical symmetrized near-field intensities.

symmetric and antisymmetric degenerate edge modes. The surface charge distributions of the eigenmodes of iteration 0 confirm that it is possible to describe them as formed by edge modes.

Characteristic Edge Units and Koch Fractal Iteration one

As is the case of the Koch fractal iteration 0, the lowest energy mode in the fractals of iteration 1 is also identified as a dipolar mode. Although the geometry modification from iteration 0 to 1 is large, the energy of the dipolar mode shifts only by 30 meV in the simulations. Figure 2c shows the surface charge distributions for the modes of the fractal iteration 1. For the dipolar mode, two degenerate eigenmodes are supported, one with a vertical dipole moment and the other with a horizontal dipole moment, as observed for the dipolar modes of the fractal iteration 0. However, the higher order modes of the

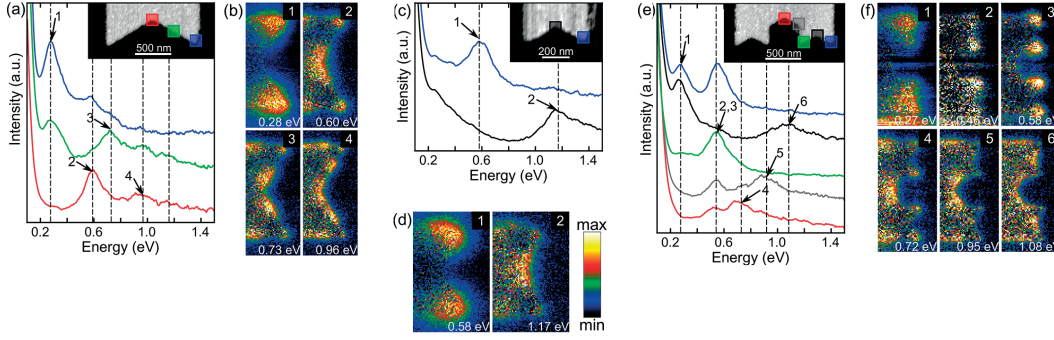


Figure 3 – Experimental EEL spectra of the characteristic edge units of Koch fractal antennas of iterations 1 (a) and 2 (c,e) reproduced at the very end of a 50 μm long silver strip, acquired at the color-coded positions indicated in the ADF image in the insets. The arrows indicate the peaks corresponding to resonant edge modes. EELS maps of the plasmon modes found in the characteristic edge units of Koch fractal antennas of iteration 1 (b) and 2 (d,f). The second peak in (e) is labeled as “2,3” because it represents two different resonant modes that are energetically close. The modes have been separated with a Gaussian fit yielding EELS maps 2 and 3, in (f), at 0.46 ± 0.07 eV and 0.58 ± 0.09 eV, respectively.

Koch snowflakes of iteration 1 display complex EELS maps and charge distributions as observed in Figure 2b,c. To understand these complex modes, the edges of the fractal structure are divided into characteristic edge units, composed of two segments with a 120° angle between them (“V” shape), as shown in Figure S1 and in the inset of Figure 3a. To isolate the characteristic edge unit of the Koch fractal iteration 1, we reproduced this “V” shape at the end of a 50 μm -long silver strip (extending vertically beyond the insets in Figure 3). Figure 3a,b shows the EELS spectra and energy-filtered maps of the silver strip representing the characteristic edge units of the Koch snowflake fractal iteration 1. Here we are able to identify four resonant peaks that correspond to edge modes, in a similar manner to the modes found in straight edges on silver strips [58,60], despite the fact that the characteristic edge unit of the Koch fractal is formed by two edges at an angle. Hence, the EELS intensity distribution of these resonant peaks corresponds to edge modes of order one (E_1), two (E_2), three (E_3), and four (E_4). A similar behavior was found in bent silver nanowires in which the plasmon modes were unaffected by the presence of kinks [28].

To further support the hypothesis that bent edges will maintain the same quasi one-dimensional modes than those found in straight edges, let us draw a parallel with the one-dimensional modes of silver nanowires. We performed simulations of a straight wire and two bent wires at 120° and 60° as shown in Figure S5. For a 120° bending, which is the angle of the characteristic unit in the Koch fractals, the bending produces only an energy shift of the odd edge modes, compared to the straight wire, while maintaining their nodal distributions. For a 60° bending, modes E_3 and E_4 begin to merge. The

3.4. Self-Similarity of Plasmon Edge Modes on Koch Fractal Antennas

angle at which this process occurs is characteristic of each pair of modes and depends on the order of the modes and the dimensions of the wires. A detailed study of this interaction is beyond the scope of this work and will be discussed elsewhere.

Based on the observation that bent edges can support edge modes equivalent to those in straight edges, we can now compare the EELS maps of the isolated edges that form a characteristic edge unit with those of the Koch snowflake iteration 1. From the EELS energy filtered maps shown in Figures 2b and 3b, we can recognize that the second peak in the snowflake, at 0.32 eV, is formed by edge modes of order one (E_1) or edge dipolar modes in each one of its characteristic edge units. In a similar manner, the third, fourth, fifth, and sixth peaks in Figure 2a are formed by edge modes of order two (E_2), three (E_3), four (E_4), and five (E_5), respectively, by comparison with the isolated characteristic “V” edge unit. The excellent agreement between the nodal distributions observed in the EELS maps of the isolated edge units (strip extremities) and the snowflake iteration 1 is revealed by a side-by-side comparison, shown in Figure S6. If we compare the spectra from the Koch snowflake and the isolated characteristic “V” edge unit in Figures 2a and 3a, respectively, we observe that the peak corresponding to the E_1 edge mode in the isolated edges is red-shifted by 70 meV with respect to the second mode in the snowflake. If we align these peaks by red shifting the spectra in the Koch snowflake iteration 1, as shown in the side-by-side comparison in Figure S6a, then we observe an excellent match between the peaks present in the Koch snowflake fractal and the modes of the isolated edge unit in the 50 μm silver strips. This supports the analysis of the charge and nodal distribution of the modes in the fractal and confirms that the modes in the Koch fractal are equivalent to the modes in the isolated edge units. The small energy difference between the modes present in both structures can be attributed, to a greater extent, to the interaction between the edge modes within the Koch snowflake [61] and to imperfections in the fabricated structures.

Eigenmodes and Coupling of Edge Modes

In the simulated EELS spectra of the Koch snowflake iteration 1 (Figure 2a), we notice that the second peak at 0.32 eV, which is formed by E_1 modes, is actually composed of two close resonant peaks separated by only 46 meV. Due to the intrinsic and experimental broadening, the experimental EEL spectra cannot resolve those two peaks, and thus only one peak appears. To further analyze the formation of these two peaks, we simulated the EELS spectra of Koch snowflake fractals iteration 1 of several sizes while maintaining the thickness of the structure constant as shown in Figure 4a. The changes in these two peaks, as we change the size of the fractal, will indicate if these two peaks are produced by the coupling of edge modes. As the size of the fractal reduces, all of the peaks will blue-shift. However, we want to examine the energy splitting between the modes formed by E_1 edge modes, and not the shift in energy due to the different fractal sizes; therefore, we align the second peak of each fractal to the second peak in the fractal with the initial

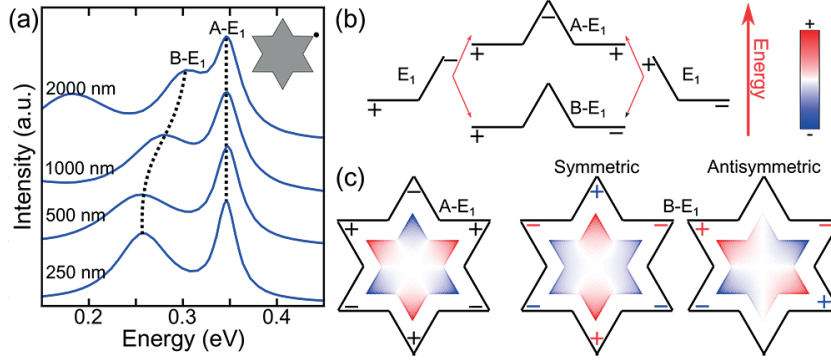


Figure 4 – (a) Simulated spectra of Koch fractal iteration 1 for several initial side lengths of the fractal. The spectra are shifted to align the second resonant peak. The two peaks show the evolution of the interaction of the bonding (B) and antibonding (A) E_1 edge modes; as the structure shrinks, a stronger interaction between E_1 modes results in larger splitting energy of these peaks. The inset shows the position where the spectra were calculated. (b) Energy diagram (not to scale) showing the formation of bonding and antibonding modes due to the coupling of two E_1 edge modes. (c) Charge distribution diagrams of the bonding and antibonding E_1 modes in Koch fractal iteration 1. Due to the symmetry of the structure, the bonding mode supports two degenerate eigenmodes; the calculated eigenmodes are displayed inside the diagrams.

length of $2 \mu\text{m}$. To this end, the spectra of the fractals of initial length of $1 \mu\text{m}$, 500 nm , and 250 nm were red-shifted by 0.27 , 0.69 , and 1.2 eV , respectively. The energy splitting is a measure of coupling strength, and we observe that, as we increase the size of the fractal, the energy splitting reduces. This behavior corresponds to a mode splitting caused by coupling of edge modes within a structure, as shown in the work of Schmidt et al. in rectangular structures [61]. Thus, this might suggest that interaction of the E_1 edge modes is responsible for the formation of these two peaks. As the size of the fractal increases, the distance between edges increases, and the interaction between edge modes is weaker, thus the energy splitting is reduced.

The simulations also show that the second and third resonant peaks, observed experimentally, are formed by three eigenmodes each, two eigenmodes being degenerate as shown in Figure 2c. Although the experimental results could be explained by neglecting the formation of these three eigenmodes, their charge distributions indicate the interaction of edge modes within the fractal structure. To understand the charge distributions of the eigenmodes in the Koch fractal iteration 1, we use the hybridization model [63]. When edge modes interact, the hybridization model dictates the formation of a bonding and an antibonding mode. In the case of the Koch fractal formed by connected characteristic edge units, the hybridized modes become bonding (B) and antibonding (A) charge-transfer hybridized modes [64,65], as shown in Figures 4b and S9 for modes E_1 and E_2 , respectively. These modes can be understood intuitively as the coupling of two edges through a conductive junction (using the terminology from ref [65]) in which

3.4. Self-Similarity of Plasmon Edge Modes on Koch Fractal Antennas

charges can indeed be “transferred”. From Figure 4b, we observe that the E_1 antibonding edge mode is formed by two E_1 modes with equal charges at the junction which, due to the charge-transfer, merge and become one antinode. The E_1 bonding mode is formed by opposite charges at the junction that cancel each other by charge transfer, leaving the bonding modes with two opposite charges at the extremities. The C_3 symmetry of the Koch fractal would allow a configuration in which all the edges can display the antibonding modes as shown in Figures 4c and S9 for edge modes E_1 and E_2 , respectively. However, for the bonding modes, in which the charges at the extremities are opposite, the symmetry only allows two sides of the structure to fulfill this constrain. As it was the case for the edge modes in Koch fractal iteration 0, this constraint promotes the formation of a symmetric and an antisymmetric degenerate eigenmodes. The symmetric eigenmodes can be classified into two distinct groups, each group formed by bonding edge modes at the left and right sides of the fractal (blue and red \pm signs in Figures 4c and S9): one group with a junction between bonding edge modes at the top apex and the other with the junction at the bottom apex. For the antisymmetric eigenmodes, two bonding edge modes at opposite upper and lower part of the fractal are observed (blue and red \pm signs in Figures 4c and S9), displaying indeed an antisymmetric charge distribution. This description of the formation of eigenmodes in the Koch fractal order 1 based on the hybridization of edge modes suggests that the eigenmodes are formed by the interaction of edge modes within the fractal structures. However, an in-depth analysis of edge modes coupling that goes beyond the purpose of this work is required to confirm this hypothesis. In this analysis, we show how the edge modes formed in the characteristic “V” edge units and the symmetry of the structure determine the three different charge distributions of eigenmodes. Equivalently, the energy loss peaks four, five, and six in Figure 2a that are formed by edge modes of order three, four, and five, respectively, exhibit eigenmodes. However, for these peaks, we were only able to find two degenerate eigenmodes as shown in Figure 2c. Indeed, the symmetry and spectral proximity between the expected additional nondegenerated mode and the degenerated ones make their numerical extraction very difficult.

Koch Fractal Iteration 2

The edge isolation approach is now applied to understand the structure modes present in the Koch fractal of iteration 2. We therefore divided the edges of the snowflake structure to find the characteristic edge unit, which is the same “V” shape as for the iteration 1 but one-third smaller, as shown in Figures 3d and S1. In the EELS spectra and energy filtered maps of the isolated characteristic shape, shown in Figure 3c,d, two resonant peaks that correspond to edge modes E_1 and E_2 , similar to those found in the iteration 1 fractal, but at higher energies due to the shorter length of the edge, are identified. A comparison of these two modes, excited in the characteristic isolated edge unit, with the modes present in the Koch snowflake fractal of Figure 5a,b enables us to identify peak four of the fractal as formed by edge mode order one (E_1) of the isolated edge

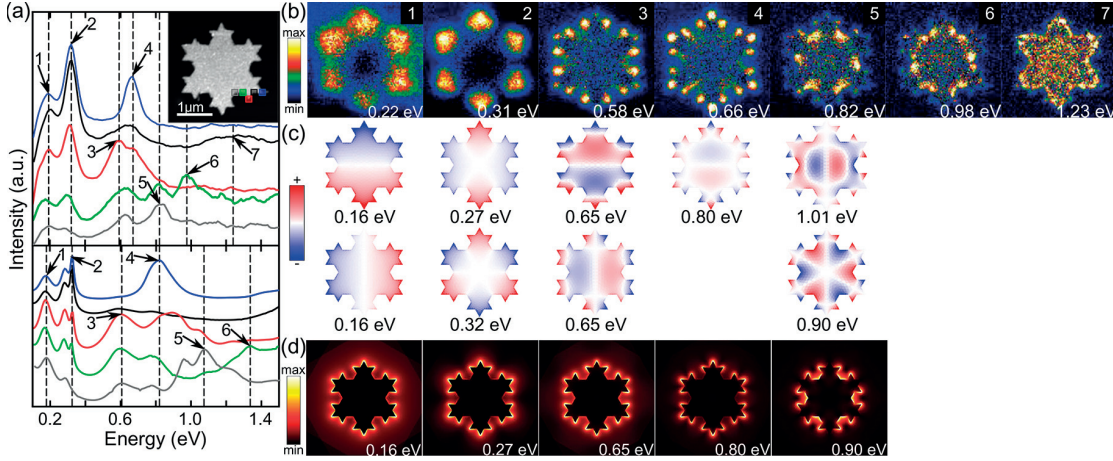


Figure 5 – (a) EEL spectra of Koch fractal antennas of iteration 2 (experimental (top) and computed (bottom)) acquired at the color-coded positions indicated in the ADF image in the inset. The arrows indicate the peaks corresponding to resonant modes. (b) Experimental EELS maps of the resonant peaks, (c) computed charge distributions, and (d) near-field intensity distributions of the eigenmodes found in the Koch fractal antennas of iteration 2. The EELS maps are obtained at the energy corresponding to the peak in the EEL spectra ± 30 meV. The energy indicated in the near-field intensity map is the one of the eigenmode, not the energy of the peak in the EEL spectra.

(because of the same strong EELS signal on each small vertex) and peak seven of the fractal as formed by an edge mode order two (E_2) of the isolated edge on the strip. To corroborate this argument, a side-by-side comparison of the maps and spectra of the isolated characteristic “V” edge unit and the snowflake fractal iteration 2 is shown in Figure S7. This comparison emphasizes the excellent nodal distribution agreement of the modes between the Koch fractal and the isolated edge. As we did in the comparison between the fractal iteration 1 and its characteristic isolated edge unit, for iteration 2 we also red shift the spectra in the Koch snowflake iteration 2 by 70 meV, as shown in Figure S7a. We observe that, after this shift, the energy peaks corresponding to the E_1 and E_2 modes in the isolated characteristic units in the 50 μm silver strips match the peaks present in the Koch snowflake fractal.

For the fractal structure iteration 2, we also isolate and analyze a larger portion of the structure, as shown in Figure 3e,f, that is, the characteristic edge unit of the Koch fractal iteration 1 to which an additional fractal iteration is applied. In this larger portion of the fractal, five peaks are observed, as shown in Figure 3e. The first peak at 0.27 ± 0.04 eV corresponds to a E_1 mode or dipolar mode, which is the same mode displayed in the silver strip of the Koch fractal iteration 1 at 0.28 ± 0.04 eV. This result suggests that the dipolar mode of iteration 1 can still be excited in the next iteration of the fractal as the dipolar mode is the most fundamental one (as seen in Figure 5c) and is thus expected to be marginally affected by the small modification of the second iteration. This effect is also observed in the Koch snowflake fractal iteration 1 (Figure 2a), where the second

3.4. Self-Similarity of Plasmon Edge Modes on Koch Fractal Antennas

peak, which is a dipolar edge mode (E_1), at 0.32 ± 0.04 eV is also present in the Koch snowflake iteration 2 (Figure 5a) at 0.31 ± 0.04 eV.

The second peak in Figure 3e is labeled as “2,3” because in the spectrum image, two dissimilar intensity localizations, one with the antinodes located in the inner vertices and the other located in all vertices, are observed in the maps two and three in Figure 3f, respectively. To extract the EELS maps corresponding to each surface plasmon resonance, we isolate the contribution from each edge mode to the spectrum image using the nonlinear least-squares fitting tool of the “Digital Micrograph” software [66], which fits Gaussian peaks to a spectrum image. The separation fits two Gaussians to the peak at 0.55 eV yielding the two EELS maps at 0.46 ± 0.07 eV and 0.58 ± 0.09 eV for the second and third modes, respectively. The third and sixth peaks of the isolated characteristic edge units of fractal iteration 2 on the strip shown in Figure 3e,f are the same two modes found in the isolated characteristic edge unit of Koch fractal iteration 2 shown in Figure 3c,d. Thus, the modes of the isolated characteristic edge units can be described as edge modes order one (E_1) and two (E_2) and represent peaks four and seven found in the Koch snowflake fractal iteration 2 in Figure 5. These results confirm that the modes present in the strips are a good representation of modes present in the Koch snowflakes.

When two of the characteristic “V” edge units of Koch fractal iteration 2 are joined by a 120° angle, an inverted “U”-like shape is generated as shown in the central area of the inset in Figure 3e and in Figure S1. This characteristic “U” shape, despite the multiple kinks, also sustains edge modes. Modes E_1 (dipolar edge mode), E_2 , and E_3 are identified at 0.46 ± 0.07 , 0.72 ± 0.04 eV, and 0.95 ± 0.04 eV as seen in Figure 3f. This “U” shape is also present in the full Koch snowflake fractal iteration 2 in Figure 5, and by comparison, it displays the same edge modes found in the isolated edge seen in Figure 3e,f. The third, fifth, and sixth peaks in the full Koch snowflake can be identified as being formed by E_1 or dipolar edge mode, E_2 , and E_3 edge modes, respectively. To confirm this identification, Figure S8 shows the good match of the nodal distributions between the modes present in the Koch snowflake fractal iteration 2 and the modes isolated in the $50\text{ }\mu\text{m}$ silver strips. The spectra in Figure S8 also shows a good energy overlap between the modes in the isolated characteristic edge units on the strip and the modes of the snowflakes after the latter is red-shifted by 70 meV. This nodal and energy match supports the evidence that the isolated modes on the silver strip are equivalent to the modes present in the Koch snowflake fractals. The energy shift can be mainly attributed to interaction of edge modes in the snowflake [61] and to a lower extent to the fabrication procedure that did not produce equal edges and sizes in both structures and locally modifies the plasmon response [67]. To support the proposed concept that a “U” characteristic unit structure can sustain plasmonic edge modes similar to the ones found in a straight edge, we draw a parallel and analyze the modes in a simulated “U” shape bent silver nanowire. Figure S10 shows the spectra and the energy-filtered maps of the bent nanowire, demonstrating that, despite the bending, the nanowire still supports edge

modes. This was also demonstrated by Rodríguez-Fortuño et al [68].

Self-Similarity of Edge Modes

Now that the modes present in the Koch snowflake fractals have been identified, we can analyze their self-similarity (i.e., fractal character) as the number of iterations increases. Due to the C_3 symmetry of the Koch snowflake fractal, each mode exists 3 times. As stated above, we ignore this “degeneracy” in our analysis. For each edge mode in the Koch snowflake fractal structure, multiple eigenmodes can be found. However, in our analysis of self-similarity of edge modes, we will not consider these eigenmodes, and we only focus on the modes found experimentally. Figure 6 shows a diagram depicting the evolution of edge modes as the Koch fractal iteration increases. For the iteration 0, only one mode of a particular order is observed for each edge. In the Koch snowflake fractal of iteration 1, two modes that originate from a dipolar/ E_1 mode and only one mode formed by each higher order edge mode are observed. The first mode is the same dipolar mode found in iteration 0, and the second mode is formed by the E_1 modes in the characteristic “V” edge unit in this iteration as shown in Figures 3c and S1. In the case of the Koch fractal iteration 2, four modes formed by dipolar/ E_1 edge modes are present, one coming from fractal iteration 0, one from the E_1 mode of fractal iteration 1, and two new modes originated by E_1 modes. As discussed previously, this structure presents two types of characteristic edge units, one is the characteristic “V” shape and the other is the “U” shape as shown in Figures 3e and S1, and each one of these two units can support edge modes, thus two new E_1 formed modes are created during this iteration. Also two new modes, one per type of characteristic edge unit, of a particular higher order are supported. Fractals of iterations 0 and 1 have only one type of characteristic edge unit, therefore, only one mode is supported for each higher order edge mode. From this analysis, the fractal character of the Koch snowflake is reflected in the number of dipolar/ E_1 modes supported by the fractal structure. In addition, the total number of edge modes in a Koch snowflake is equal to the number of dipolar/ E_1 modes in the previous fractal iteration plus the modes formed on all the characteristic edge units present in the fractal. In Figure 6, we also observe Koch iteration 3 that we have not analyzed in the previous sections. The small features introduced in iteration 3 make the fabrication as well as the simulation challenging. However, as seen in the ADF in Figure S11, we were able to fabricate and reproduce some of the features of iteration 3. The EELS maps of iteration 3 show that the fractal character of the Koch snowflake fractal is also identified in this iteration, with the dipolar/ E_1 modes of the previous iterations also supported in this iteration. Due to the fabrication constraints, the characteristic edge units of iteration 3 are not well reproduced, but despite this fact, we can observe the antinodes corresponding to E_1 modes in a few of the smaller corners of the fractal. Because the experimental results show that the modes in the fractal are governed by the modes in the characteristic edge units, this analysis can be applied to other planar fractal structures.

3.4. Self-Similarity of Plasmon Edge Modes on Koch Fractal Antennas

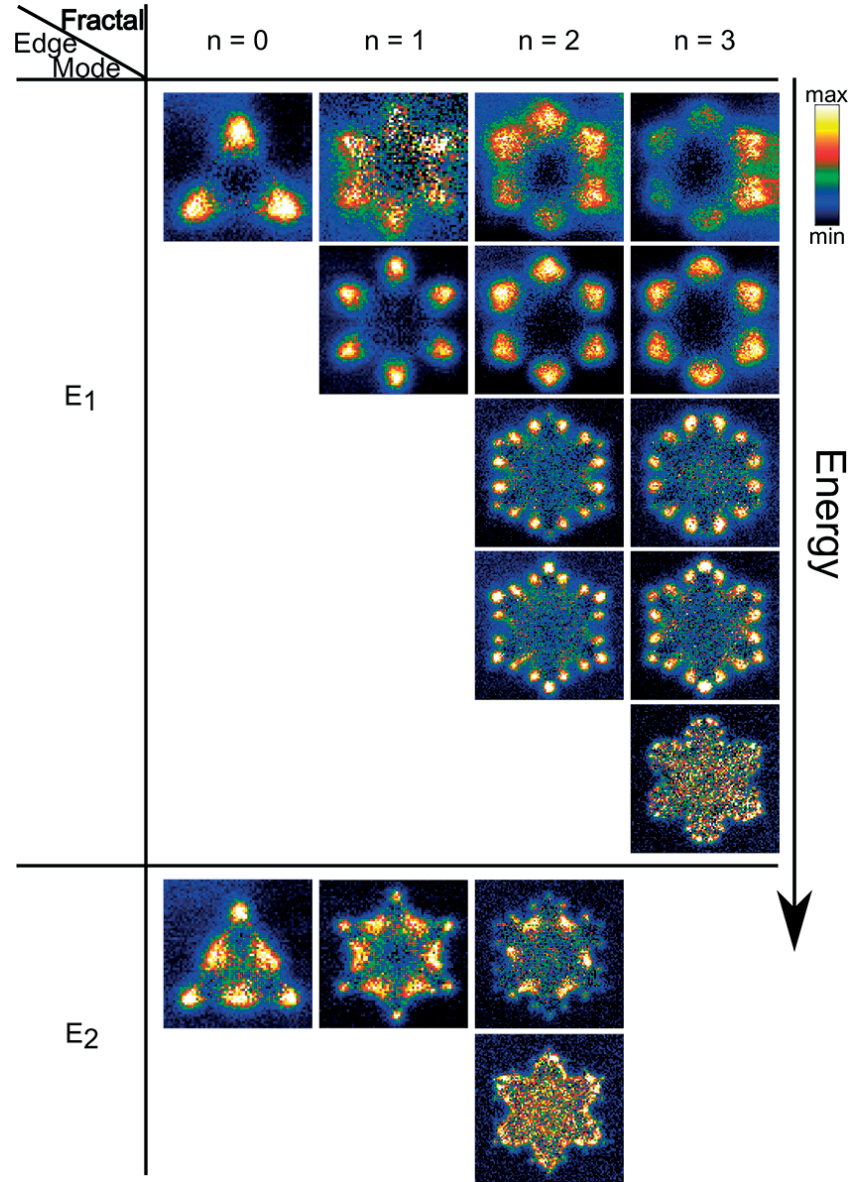


Figure 6 – Diagram of the formation of the plasmon modes in Koch snowflake fractal antennas. The diagram shows the fractal character of the Koch snowflake structures, in which the dipolar/ E_1 modes of each iteration are carried to higher iterations. Due to the small size of the features in iteration 3, the characteristic edge units were not well reproduced, and only a few edges supported E_1 modes as seen in the EELS map.

Now that we understand how the modes evolve as the fractal iteration increases, we can extend and quantify the number of dipolar/ E_1 modes (N_n^{modes}) generated by the self-similarity in the Koch snowflake fractal iteration “ n ”. From this analysis, one can infer how many types of characteristic edge units in the Koch fractal are produced after “ n ” iterations of the fractal. For $n = 0$ and 1, only one type of characteristic edge unit is produced, however for $n > 1$, after each iteration two types of characteristic edge units are produced, the “V” and the “U” shapes. Therefore, $N_0^{modes} = 1$, and for $n > 0$, $N_n^{modes} = 2n$. Additionally, the Koch fractal structure will have one mode for each higher order mode for $n = 0, 1$ and two modes for each higher order mode for $n > 1$. The results show that the plasmons excited on Koch snowflake fractal structures show a self-similar fractal response with the number of modes increasing after each iteration. This confirms that plasmonic fractal optical antennas can exhibit a multiresonant or broadband behavior while maintaining a compact structure similar to those found in macro-scale antennas. The simple scaling rule described here can be used for nanoantenna design. However, this scaling has limits due to mode coupling within the fractal, as pointed out in the coupling of edge modes section. The smaller the structure, the stronger is the effect of the coupling. In measurements where coupling within the fractal is relevant, the symmetry of the fractal structure plays a critical role, as shown above. In that case, one can also think of the fractal structure as the sum of characteristic edge units, each one contributing the basic components for the formation of the fractal eigenmodes. Taking into consideration the coupling of edge modes[60] and analyzing how the symmetry affects the nodal distribution and therefore the hybridization of the modes, the final distribution of the hybrid modes could be predicted. This analysis can be applied to other 2D fractal structures to understand how the fractal character affects the plasmon modes and guide the design and fabrication of fractal structures for nanophotonic applications.

Conclusion

The plasmon modes present in planar silver Koch snowflake fractal antennas have been investigated using EELS and numerical computations. The lowest energy modes present in all of the fractal structures were identified as dipolar modes. For the higher energy modes, insight into their origin was gained by measuring simplified geometries describing the basic building block segments of the fractal structures. Two types of basic segments were found and studied: a “V” characteristic edge unit, formed by two lines at 120° angle, and a “U” characteristic edge unit, formed joining two characteristic “V” edge units also at 120° angle. In spite of the fact that these two geometries presented were not straight-line segments, the modes sustained were edge modes (E_i). All the edge modes supported in the Koch snowflake fractal have been identified from an analysis of the isolated characteristic edge units. Interestingly, the fractal response can be obtained by the sum of the modes supported by its characteristic edge units that are the basic components of the fractal. We also showed that, as the size of the fractal structure is

3.4. Self-Similarity of Plasmon Edge Modes on Koch Fractal Antennas

reduced, the coupling within the structure can become relevant and how the influence of the symmetry of the fractal on edge mode coupling of the basic components must be considered. When the coupling is weak and it can be neglected, the total number of edge modes in a Koch snowflake of a given number of iterations depends on the number of characteristic edge units created in the fractal. Introducing this simple rule, we observed that the number of plasmon dipolar/ E_1 edge modes increases by two after a fractal iteration, confirming that the plasmonic Koch snowflake fractal antennas can exhibit a multiresonant or broadband behavior while maintaining a compact structure reflecting the characteristics of their macro-scale counterparts.

Method

Simulations

The computation of the EELS spectra and the eigenmodes of the Koch snowflake fractals were done using a full wave surface integral equation (SIE) method [69,70]. The fractal structures are considered in a homogeneous medium with a permittivity of $\epsilon = 1.8$ to account for the substrate influence. A Drude model was used for the permittivity of Ag with a plasma frequency $\omega_p = 9.3$ eV, losses $\gamma = 0.03$ eV, and $\epsilon_\infty = 4.3$. The simulations of the bent nanowires were performed using the MNPBEM toolbox [71,72] that uses the boundary element method to solve Maxwell's equations. The wires were calculated using a tabulated dielectric function [73], and a permittivity of 2 for the medium surrounding the structure to account for the substrate influence. A comparison between SIE and BEM can be found in the Supporting Information of ref [69].

Sample Fabrication

The structures were fabricated by EBL directly onto silicon nitride TEM grids [23]. We deposited poly(methyl methacrylate), 950,000 molecular weight at 3% anisole, on a 50 nmthick silicon nitride TEM grid (Norcada) by spin coating at 6000 rpm. The sample was then baked at 175 °C for 2 min. The patterning was performed on a JSM-7000F SEM (JEOL) equipped with Nano Pattern Generation System (NPGS). Development was done in a 3:1 isopropyl alcohol:methyl isobutyl ketone solution for 70 s and rinsed in isopropyl alcohol and dried with N_2 . Ag was deposited in an electron beam evaporator system, with a 6 keV and 250 μ A electron source. Finally, the lift-off was done by soaking the sample in acetone, followed by isopropyl alcohol rinsing.

EELS Measurements

The EELS spectral response of the structures was characterized using an ultrastable STEM-TEM (FEI Titan 80-300) equipped with an electron monochromator. We focused

an 80 keV electron beam on the sample and rastered it over a region of interest, and we simultaneously acquired signals from an annular darkfield detector and an EELS spectrometer (Gatan Imaging Filter, Tridiem model 865) from each position in the raster scan. The spectra were recorded with an exposure time of 1 ms/spectrum and a dispersion of 10 meV per channel for the Koch snowflake fractals and 5 meV per channel for the isolated characteristic edge units. To further improve the energy resolution, we performed the Richardson-Lucy algorithm procedure [23], achieving an effective energy resolution up to 30 meV in our spectrum images. Each spectrum image was deconvoluted using seven deconvolution iterations and normalized by the total electron count at each pixel position. To have a better comparison between experiments and simulations, that do not have the “zero-loss-peak” (ZLP), we subtract it from the spectra. After deconvolution, we remove the ZLP contribution to the spectra by fitting the ZLP tails using a power function.

Acknowledgement

E.P.B., D.R., and G.A.B. acknowledge support from NSERC under the Discovery Grant Program. The experimental work was carried out at the Canadian Centre for Electron Microscopy, a National Facility supported by The Canada Foundation for Innovation under the MSI program, NSERC, and McMaster University. O.J.F.M. and G.D.B. acknowledge funding from the Swiss National Science Foundation (project 200020_153662) and from the European Research Council (ERC-2015-AdG-695206 Nanofactory).

References

- [1] Werner, D. H.; Haupt, R. L.; Werner, P. L. Fractal Antenna Engineering: The Theory and Design of Fractal Antenna Arrays. *IEEE Antennas Propag. Mag.* 1999, 41, 37-58.
- [2] Werner, D. H.; Ganguly, S. An Overview of Fractal Antenna Engineering Research. *IEEE Antennas Propag. Mag.* 2003, 45, 38-57.
- [3] Mandelbrot, B. B. *The Fractal Geometry of Nature*; W. H. Freeman and Company: New York, 1977.
- [4] Puente-Baliarda, C.; Romeu, J.; Pous, R.; Cardama, A. On the Behavior of the Sierpinski Multiband Fractal Antenna. *IEEE Trans. Antennas Propag.* 1998, 46, 517-524.
- [5] Baliarda, C.; Romeu, J.; Cardama, A. The Koch Monopole: a Small Fractal Antenna. *IEEE Trans. Antennas Propag.* 2000, 48, 1773- 1781.
- [6] Behera, S.; Vinoy, K. J.; Member, S. Multi-Port Network Approach for the Analysis of Dual Band Fractal Microstrip Antennas. *IEEE Trans. Antennas Propag.* 2012, 60, 5100-5106.
- [7] Omar, A. A. Design of Ultrawideband Coplanar Waveguide-Fed Koch-Fractal Triangular Antenna. *Int. J. RF Microwave Comput.-Aided Eng.* 2013, 23, 200-207.
- [8] Ismahayati, A.; Soh, P. J.; Hadibah, R.; Vandenbosch, G. A. E. Design and Analysis of

3.4. Self-Similarity of Plasmon Edge Modes on Koch Fractal Antennas

- a Multiband Koch Fractal Monopole Antenna. Proceedings from the IEEE International RF and Microwave Conference, Malaysia, December 12-14, 2011; IEEE: New York, 2011; pp 58-62.
- [9] Karim, M. A.; Rahim, M.; Majid, H.; et al. Log Periodic Fractal Koch Antenna for UHF Band Applications. *Prog. Electromagn. Res.* 2010, 100, 201-218.
- [10] Anker, J. N.; Hall, W. P.; Lyandres, O.; Shah, N. C.; Zhao, J.; Van Duyne, R. P. Biosensing with Plasmonic Nanosensors. *Nat. Mater.* 2008, 7, 442-53.
- [11] Kawata, S.; Inouye, Y.; Verma, P. Plasmonics for Near-Field Nano-Imaging and Superlensing. *Nat. Photonics* 2009, 3, 388-394.
- [12] Atwater, H. A.; Polman, A. Plasmonics for Improved Photovoltaic Devices. *Nat. Mater.* 2010, 9, 205-13.
- [13] Neumann, O.; Urban, A. S.; Day, J.; Lal, S.; Nordlander, P.; Halas, N. J. Solar Vapor Generation Enabled by Nanoparticles. *ACS Nano* 2013, 7, 42-9.
- [14] Lal, S.; Clare, S. E.; Halas, N. J. Nanoshell-Enabled Photothermal Cancer Therapy: Impending Clinical Impact. *Acc. Chem. Res.* 2008, 41, 1842-51.
- [15] Mühlischlegel, P.; Eisler, H.-J.; Martin, O. J. F.; Hecht, B.; Pohl, D. W. Resonant Optical Antennas. *Science* 2005, 308, 1607-1609.
- [16] Duan, H.; Hu, H.; Kumar, K.; Shen, Z.; Yang, J. K. W. Direct and Reliable Patterning of Plasmonic Nanostructures with Sub-10-nm Gaps. *ACS Nano* 2011, 5, 7593-600.
- [17] Schnell, M.; García-Etxarri, A.; Huber, a. J.; Crozier, K.; Aizpurua, J.; Hillenbrand, R. Controlling the Near-Field Oscillations of Loaded Plasmonic Nanoantennas. *Nat. Photonics* 2009, 3, 287-291.
- [18] Knebl, D.; Hörl, A.; Trügler, A.; Kern, J.; Krenn, J. R.; Puschnig, P.; Hohenester, U. Gap Plasmonics of Silver Nanocube Dimers. *Phys. Rev. B: Condens. Matter Mater. Phys.* 2016, 93, 081405.
- [19] Ghenuche, P.; Cherukulappurath, S.; Taminiau, T. H.; Van Hulst, N. F.; Quidant, R. Spectroscopic Mode Mapping of Resonant Plasmon Nanoantennas. *Phys. Rev. Lett.* 2008, 101, 116805.
- [20] Fromm, D. P.; Sundaramurthy, A.; James Schuck, P.; Kino, G.; Moerner, W. E. Gap-Dependent Optical Coupling of Single "Bowtie" Nanoantennas Resonant in the Visible. *Nano Lett.* 2004, 4, 957-961.
- [21] Kosako, T.; Kadoya, Y.; Hofmann, H. F. Directional Control of Light by a Nano-Optical Yagi - Uda Antenna. *Nat. Photonics* 2010, 4, 312-315.
- [22] Egerton, R. F. Electron Energy-Loss Spectroscopy in the TEM. *Rep. Prog. Phys.* 2009, 72, 016502.
- [23] Bellido, E. P.; Rossouw, D.; Botton, G. A. Toward 10 meV Electron Energy-Loss Spectroscopy Resolution for Plasmonics. *Microsc. Microanal.* 2014, 20, 767-78.
- [24] Krivanek, O. L.; Lovejoy, T. C.; Dellby, N.; Carpenter, R. W. Monochromated STEM with a 30 meV-wide, Atom-Sized Electron Probe. *Microscopy* 2013, 62, 3-21.
- [25] Nelayah, J.; Kociak, M.; Stéphan, O.; García de Abajo, F. J.; Tencé, M.; Henrard, L.; Taverna, D.; Pastoriza-Santos, I.; Liz-Marzán, L. M.; Colliex, C. Mapping Surface Plasmons on a Single Metallic Nanoparticle. *Nat. Phys.* 2007, 3, 348-353.

- [26] Rossouw, D.; Couillard, M.; Vickery, J.; Kumacheva, E.; Botton, G. A. Multipolar Plasmonic Resonances in Silver Nanowire Antennas Imaged with a Subnanometer Electron Probe. *Nano Lett.* 2011, 11, 1499-1504.
- [27] Nicoletti, O.; de la Peña, F.; Leary, R. K.; Holland, D. J.; Ducati, C.; Midgley, P. A. Three-Dimensional Imaging of Localized Surface Plasmon Resonances of Metal Nanoparticles. *Nature* 2013, 502, 80-4.
- [28] Rossouw, D.; Botton, G. A. Plasmonic Response of Bent Silver Nanowires for Nanophotonic Subwavelength Waveguiding. *Phys. Rev. Lett.* 2013, 110, 066801.
- [29] Liang, H.; Zhao, H.; Rossouw, D.; Wang, W.; Xu, H.; Botton, G. A.; Ma, D. Silver Nanorice Structures: Oriented Attachment- Dominated Growth, High Environmental Sensitivity, and Real-Space Visualization of Multipolar Resonances. *Chem. Mater.* 2012, 24, 2339- 2346.
- [30] Rossouw, D.; Botton, G. A. Resonant Optical Excitations in Complementary Plasmonic Nanostructures. *Opt. Express* 2012, 20, 6968-73.
- [31] Barrow, S. J.; Rossouw, D.; Funston, A. M.; Botton, G. A.; Mulvaney, P. Mapping Bright and Dark Modes in Gold Nanoparticle Chains Using Electron Energy Loss Spectroscopy. *Nano Lett.* 2014, 14, 3799-808.
- [32] Boudarham, G.; Feth, N.; Myroshnychenko, V.; Linden, S.; García de Abajo, J.; Wegener, M.; Kociak, M. Spectral Imaging of Individual Split-Ring Resonators. *Phys. Rev. Lett.* 2010, 105, 255501.
- [33] Bellido, E. P.; Manjavacas, A.; Zhang, Y.; Cao, Y.; Nordlander, P.; Botton, G. A. Electron Energy-Loss Spectroscopy of Multipolar Edge and Cavity Modes in Silver Nanosquares. *ACS Photonics* 2016, 3, 428-433.
- [34] Bosman, M.; Keast, V. J.; Watanabe, M.; Maarroof, A. I.; Cortie, M. B. Mapping Surface Plasmons at the Nanometre Scale with an Electron Beam. *Nanotechnology* 2007, 18, 165505.
- [35] Schmidt, F. P.; Ditlbacher, H.; Hofer, F.; Krenn, J. R.; Hohenester, U. Morphing a Plasmonic Nanodisk Into a Nanotriangle. *Nano Lett.* 2014, 14, 4810-5.
- [36] Flauraud, V.; Regmi, R.; Winkler, P. M.; Alexander, D. T. L.; Rigneault, H.; van Hulst, N. F.; Garcia-Parajo, M. F.; Wenger, J.; Brugger, J. In-Plane Plasmonic Antenna Arrays with Surface Nanogaps for Giant Fluorescence Enhancement. *Nano Lett.* 2017, 17, 1703- 1710.
- [37] Flauraud, V.; Mastrangeli, M.; Bernasconi, G. D.; Butet, J.; Alexander, D. T. L.; Shahrabi, E.; Martin, O. J. F.; Brugger, J. Nanoscale Topographical Control of Capillary Assembly of Nanoparticles. *Nat. Nanotechnol.* 2017, 12, 73-80.
- [38] Flauraud, V.; Bernasconi, G. D.; Butet, J.; Alexander, D. T. L.; Martin, O. J. F.; Brugger, J. Mode Coupling in Plasmonic Heterodimers Probed with Electron Energy Loss Spectroscopy. *ACS Nano* 2017, 11, 3485-3495.
- [39] Flauraud, V.; Bernasconi, G. D.; Butet, J.; Mastrangeli, M.; Alexander, D. T. L.; Martin, O. J. F.; Brugger, J. Mode Evolution in Strongly Coupled Plasmonic Dolmens Fabricated by Templated Assembly. *ACS Photonics* 2017, 4, 1661-1668.
- [40] Alber, I.; Sigle, W.; Müller, S.; Neumann, R.; Picht, O.; Rauber, M.; van Aken, P. a.;

3.4. Self-Similarity of Plasmon Edge Modes on Koch Fractal Antennas

- Toimil-Molares, M. E. Visualization of Multipolar Longitudinal and Transversal Surface Plasmon Modes in Nanowire Dimers. *ACS Nano* 2011, 5, 9845-53.
- [41] Bosman, M.; Anstis, G. R.; Keast, V. J.; Clarke, J. D.; Cortie, M. B. Light Splitting in Nanoporous Gold and Silver. *ACS Nano* 2012, 6, 319-26.
- [42] Koh, A. L.; Bao, K.; Khan, I.; Smith, W. E.; Kothleitner, G.; Nordlander, P.; Maier, S. A.; McComb, D. W. Electron Energy-Loss Spectroscopy [EELS] of Surface Plasmons in Single Silver Nanoparticles and Dimers: Influence of Beam Damage and Mapping of Dark Modes. *ACS Nano* 2009, 3, 3015-3022.
- [43] Gottheim, S.; Zhang, H.; Govorov, A. O.; Halas, N. J. Fractal Nanoparticle Plasmonics: The Cayley Tree. *ACS Nano* 2015, 9, 3284- 3292.
- [44] Rosa, L.; Sun, K.; Juodkasis, S. Sierpinski Fractal Plasmonic Nanoantennas. *Phys. Status Solidi RRL* 2011, 5, 175-177.
- [45] Sederberg, S.; Elezzabi, A. Sierpiński Fractal Plasmonic Antenna: a Fractal Abstraction of the Plasmonic Bowtie Antenna. *Opt. Express* 2011, 19, 10456-10461.
- [46] Volpe, G.; Volpe, G.; Quidant, R. Fractal Plasmonics: Subdiffraction Focusing and Broadband Spectral Response by a Sierpinski Nanocarpet. *Opt. Express* 2011, 19, 3612-3618.
- [47] Bao, Y.-J.; Li, H.-M.; Chen, X.-C.; Peng, R.-W.; Wang, M.; Lu, X.; Shao, J.; Ming, N.-B. Tailoring the Resonances of Surface Plasmas on Fractal-Featured Metal Film by Adjusting Aperture Configuration. *Appl. Phys. Lett.* 2008, 92, 151902.
- [48] Aouani, H.; Rahmani, M.; Šířová, H.; Torres, V.; Hegnerová, K.; Beruete, M.; Homola, J.; Hong, M.; Navarro-Cía, M.; Maier, S. A. Plasmonic Nanoantennas for Multispectral Surface-Enhanced Spectroscopies. *J. Phys. Chem. C* 2013, 117, 18620-18626.
- [49] Li, K.; Stockman, M.; Bergman, D. Self-Similar Chain of Metal Nanospheres as an Efficient Nanolens. *Phys. Rev. Lett.* 2003, 91, 227402.
- [50] Aslan, E.; Aslan, E.; Wang, R.; Hong, M. K.; Erramilli, S.; Turkmen, M.; Saracoglu, O. G.; Dal Negro, L. Multispectral Cesaro- Type Fractal Plasmonic Nanoantennas. *ACS Photonics* 2016, 3, 2102- 2111.
- [51] Kenney, M.; Grant, J.; Shah, Y. D.; Escorcia-Carranza, I.; Humphreys, M.; Cumming, D. R. S. Octave-Spanning Broadband Absorption of Terahertz Light Using Metasurface Fractal-Cross Absorbers. *ACS Photonics* 2017, 4, 2604-2612.
- [52] Zhu, L.-H.; Shao, M.-R.; Peng, R.-W.; Fan, R.-H.; Huang, X.-R.; Wang, M. Broadband Absorption and Efficiency Enhancement of an Ultra-Thin Silicon Solar Cell With a Plasmonic Fractal. *Opt. Express* 2013, 21, A313-A323.
- [53] Fang, J.; Wang, D.; DeVault, C. T.; Chung, T.-F.; Chen, Y. P.; Boltasseva, A.; Shalae, V. M.; Kildishev, A. V. Enhanced Graphene Photodetector with Fractal Metasurface. *Nano Lett.* 2017, 17, 57-62.
- [54] Höppener, C.; Lapin, Z. J.; Bharadwaj, P.; Novotny, L. Self- Similar Gold-Nanoparticle Antennas for a Cascaded Enhancement of the Optical Field. *Phys. Rev. Lett.* 2012, 109, 017402.
- [55] Navarro-Cia, M.; Maier, S. A. Broad-Band Near-Infrared Plasmonic Nanoantennas for Higher Harmonic Generation. *ACS Nano* 2012, 6, 3537-3544.

- [56] Coluccio, M. L.; Gentile, F.; Das, G.; Nicastri, A.; Perri, A. M.; Candeloro, P.; Perozziello, G.; Proietti Zaccaria, R.; Gongora, J. S. T.; Alrasheed, S.; Fratalocchi, A.; Limongi, T.; Cuda, G.; Di Fabrizio, E. Detection of Single Amino Acid Mutation in Human Breast Cancer by Disordered Plasmonic Self-Similar Chain. *Sci. Adv.* 2015, 1, e1500487.
- [57] Fischer, H.; Martin, O. J. F. Engineering the Optical Response of Plasmonic Nanoantennas. *Opt. Express* 2008, 16, 9144-9154.
- [58] Schmidt, F.-P.; Ditlbacher, H.; Hohenester, U.; Hohenau, A.; Hofer, F.; Krenn, J. R. Universal Dispersion of Surface Plasmons in Flat Nanostructures. *Nat. Commun.* 2014, 5, 3604.
- [59] Campos, A.; Arbouet, A.; Martin, J.; Gerard, D.; Proust, J.; Plain, J.; Kociak, M. Plasmonic Breathing and Edge Modes in Aluminum Nanotriangles. *ACS Photonics* 2017, 4, 1257-1263.
- [60] Bellido, E. P.; Zhang, Y.; Manjavacas, A.; Nordlander, P.; Botton, G. A. Plasmonic Coupling of Multipolar Edge Modes and the Formation of Gap Modes. *ACS Photonics* 2017, 4, 1558-1565.
- [61] Schmidt, F.-P.; Ditlbacher, H.; Hohenau, A.; Hohenester, U.; Hofer, F.; Krenn, J. R. Edge Mode Coupling within a Plasmonic Nanoparticle. *Nano Lett.* 2016, 16, 5152-5155.
- [62] Schmidt, F. P.; Ditlbacher, H.; Hohenester, U.; Hohenau, A.; Hofer, F.; Krenn, J. R. Dark Plasmonic Breathing Modes in Silver Nanodisks. *Nano Lett.* 2012, 12, 5780-5783.
- [63] Prodan, E.; Radloff, C.; Halas, N. J.; Nordlander, P. A Hybridization Model for the Plasmon Response of Complex Nanostructures. *Science* 2003, 302, 419-22.
- [64] Duan, H.; Fernández-Domínguez, A. I.; Bosman, M.; Maier, S. A.; Yang, J. K. W. Nanoplasmonics: Classical Down to the Nanometer Scale. *Nano Lett.* 2012, 12, 1683-9.
- [65] Wen, F.; Zhang, Y.; Gottheim, S.; King, N. S.; Zhang, Y.; Nordlander, P.; Halas, N. J. Charge Transfer Plasmons: Optical Frequency Conductances and Tunable Infrared Resonance. *ACS Nano* 2015, 9, 6428-6435.
- [66] Leapman, R.; Swyt, C. Separation of Overlapping Core Edges in Electron Energy Loss Spectra by Multiple-Least-Squares Fitting. *Ultramicroscopy* 1988, 26, 393-403.
- [67] Mazzucco, S.; Geuquet, N.; Ye, J.; Stéphan, O.; Van Roy, W.; Van Dorpe, P.; Henrard, L.; Kociak, M. Ultralocal Modification of Surface Plasmons Properties in Silver Nanocubes. *Nano Lett.* 2012, 12, 1288-94.
- [68] Rodríguez-Fortuño, F. J.; García-Meca, C.; Ortuño, R.; Martí, J.; Martínez, A. Modeling High-Order Plasmon Resonances of a UShaped Nanowire Used to Build a Negative-Index Metamaterial. *Phys. Rev. B: Condens. Matter Mater. Phys.* 2009, 79, 075103.
- [69] Bernasconi, G. D.; Butet, J.; Flauraud, V.; Alexander, D.; Brugger, J.; Martin, O. J. F. Where Does Energy Go in Electron Energy Loss Spectroscopy of Nanostructures? *ACS Photonics* 2017, 4, 156- 164.
- [70] Bernasconi, G. D.; Butet, J.; Martin, O. J. F. Mode Analysis of Second-Harmonic Generation in Plasmonic Nanostructures. *J. Opt. Soc. Am. B* 2016, 33, 768-779.
- [71] Hohenester, U.; Trügler, A. MNPBEM - A Matlab Toolbox for the Simulation of

3.4. Self-Similarity of Plasmon Edge Modes on Koch Fractal Antennas

Plasmonic Nanoparticles. *Comput. Phys. Commun.* 2012, 183, 370-381.

[72] Hohenester, U. Simulating Electron Energy Loss Spectroscopy with the MNPBEM Toolbox. *Comput. Phys. Commun.* 2014, 185, 1177-1187.

[73] Babar, S.; Weaver, J. H. Optical Constants of Cu, Ag, and Au Revisited. *Appl. Opt.* 2015, 54, 477.

Supplementary informations

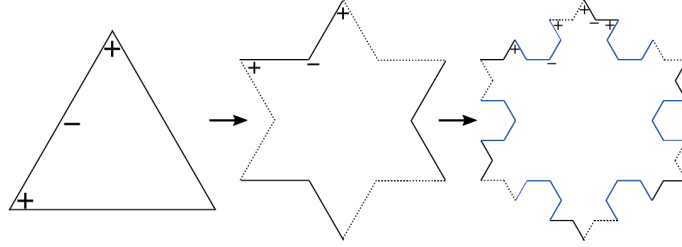


Figure S1 – (Left) Equilateral triangle which is the iteration 0 of the Koch snowflake fractal. (Center) Koch snowflake fractal iteration 1 showing the characteristic "V" edge unit of the structure formed by two line segments at an 120 degrees angle. (Right) Koch snowflake fractal iteration 2 showing its two types of chracteristic edge units: One type is the characteristic "V" shape (in black). The other type is the "U" shape (in blue) formed by two characteristic "V" shapes at 120 degrees angle. The figure shows the charge distribution of an edge mode that is supported in each one of the edges.

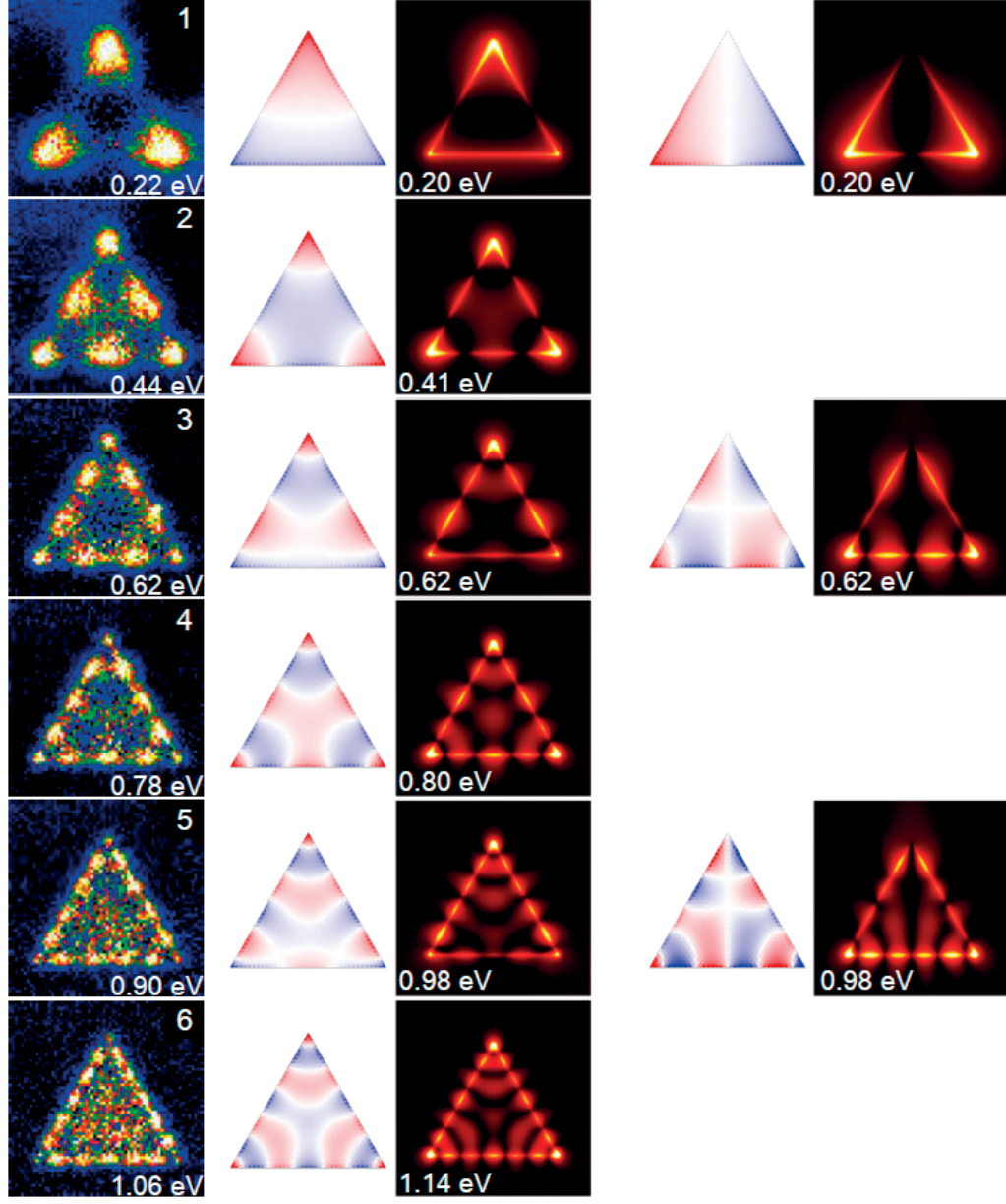


Figure S2 – Measured energy filtered maps of the Koch snowflake fractal iteration 0 and their corresponding calculated eigenmodes and their near-field distribution. The numbers on the EELS maps correspond to resonance peaks in Figure 1a in the main text, and the numbers on the near-field distributions correspond to the eigen-energies.

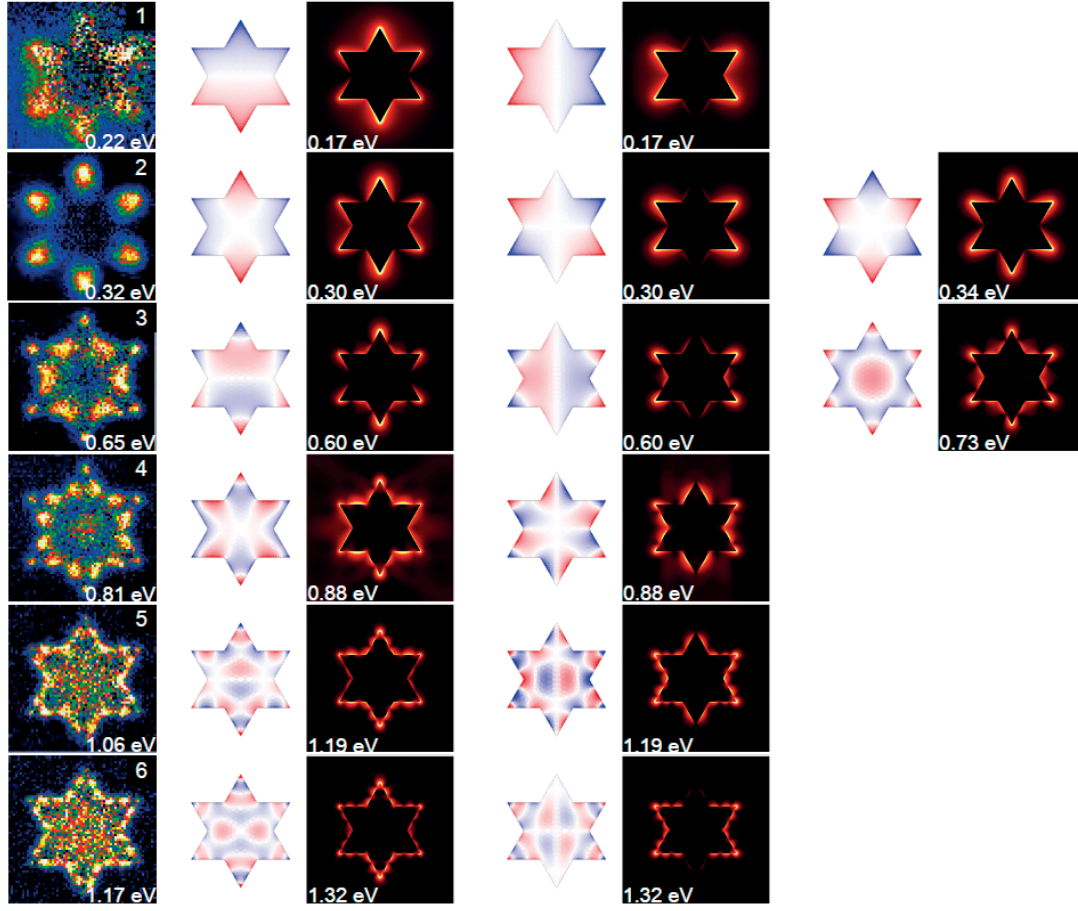


Figure S3 – Measured energy filtered maps of the Koch snowflake fractal iteration 1 and their corresponding calculated eigenmodes and their near-field distribution. The numbers on the EELS maps correspond to resonance peaks in Figure 2a in the main text, and the numbers on the near-field distributions correspond to the eigen-energies.

3.4. Self-Similarity of Plasmon Edge Modes on Koch Fractal Antennas

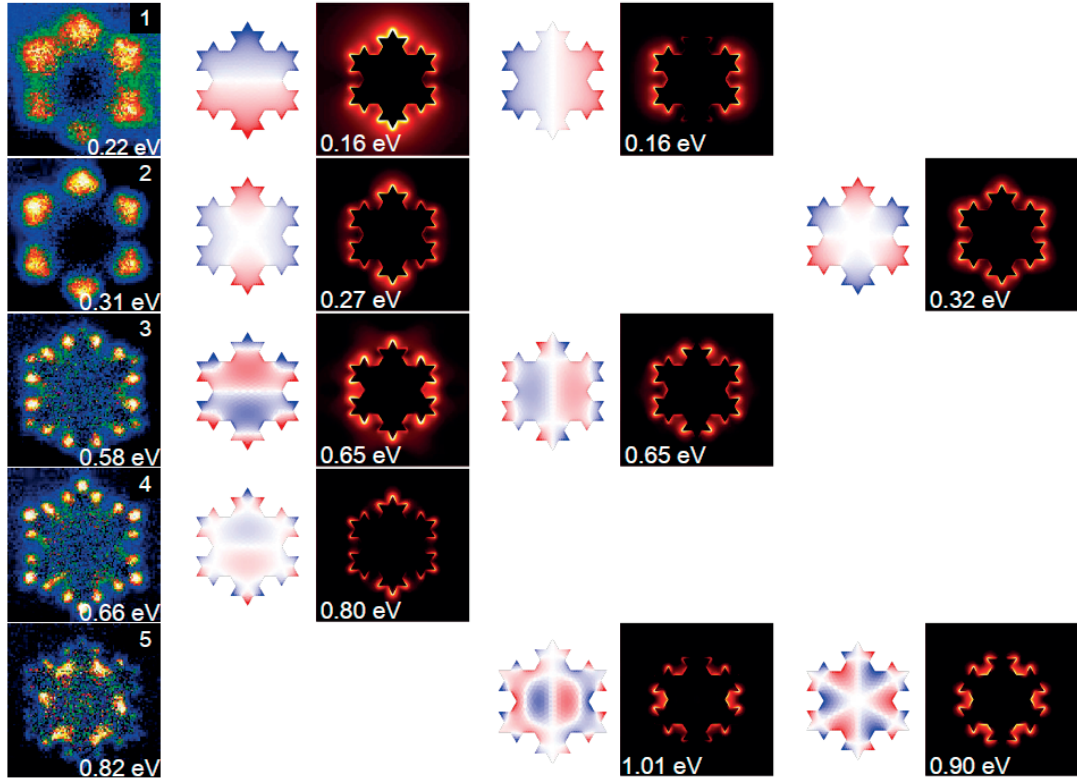


Figure S4 – Measured energy filtered maps of the Koch snowflake fractal iteration 2 and their corresponding calculated eigenmodes and their near-field distribution. The numbers on the EELS maps correspond to resonance peaks in Figure 5a in the main text, and the numbers on the near-field distributions correspond to the eigen-energies.

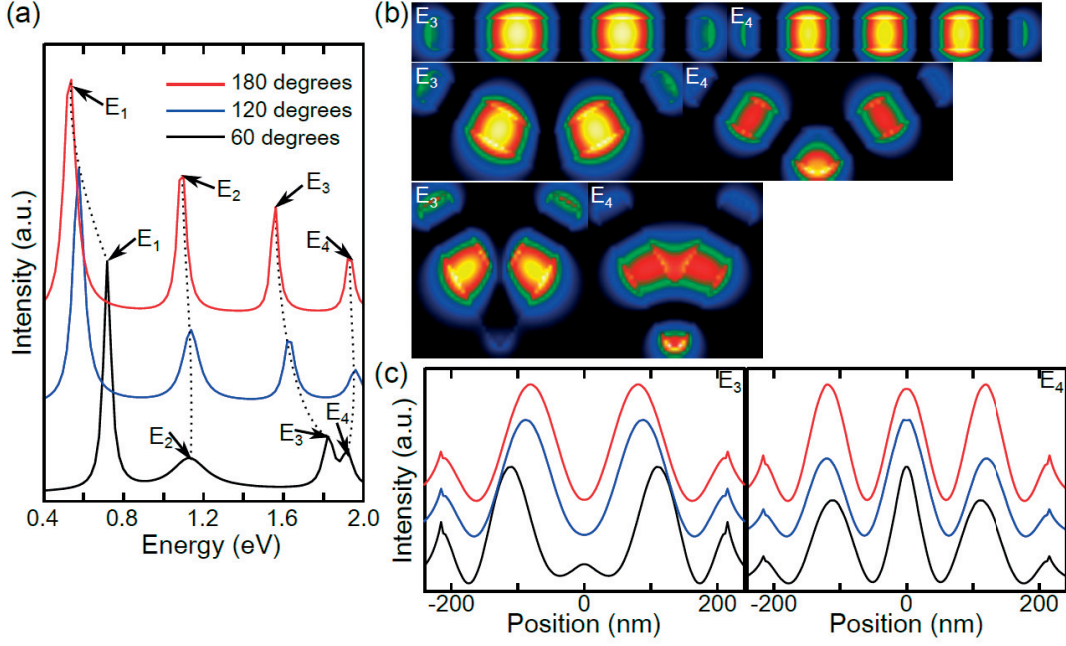


Figure S5 – Simulated EELS spectra (a) and energy filtered maps (b) of bent silver nanowires $222 \times 44 \times 30 \text{ nm}^3$. We observe that as the angle decreases from 180 to 60 degrees the odd edge modes shift to higher energies. The maps (b) show that the nodal distribution of the modes is preserve in the 120 degrees bent nanowire. However in the case of the 60 degrees bent nanowire the nodal distribution is distorted due to the interaction of the fields in each side of the nanowire. Intensity crosscuts of the E_3 and E_4 modes taken from the side of the bent nanowires.

3.4. Self-Similarity of Plasmon Edge Modes on Koch Fractal Antennas

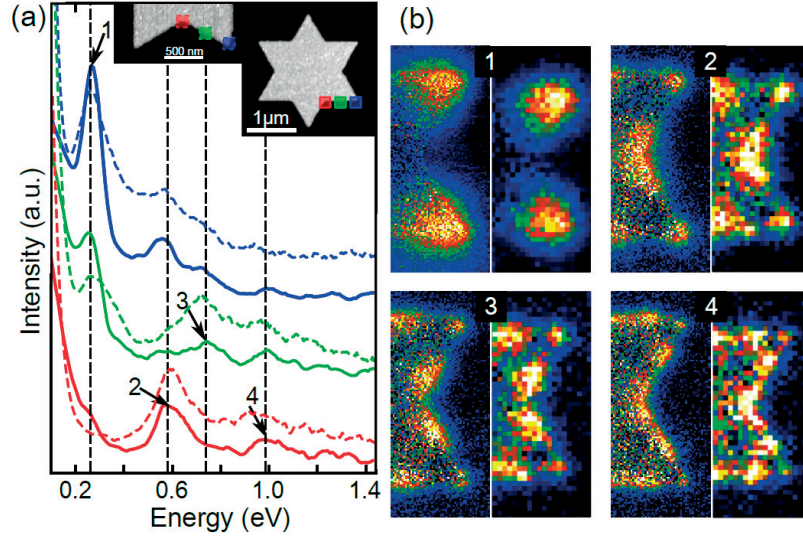


Figure S6 – Side-to-side comparison of the modes in the isolated characteristic edge units in the 50 μm silver strips (dashed lines) and in the full Koch snowflake fractals (solid lines) of iteration 1. (a) EELS spectra acquired at the positions marked on the insets. The spectra of the full Koch snowflake fractal is red shifted 70 meV to align the E_1 modes of both structures. (b) Comparison of the EELS energy filtered maps of the isolated characteristic edge units (left) and of the full snowflake (right) showing that the modes on both structures are equivalent.

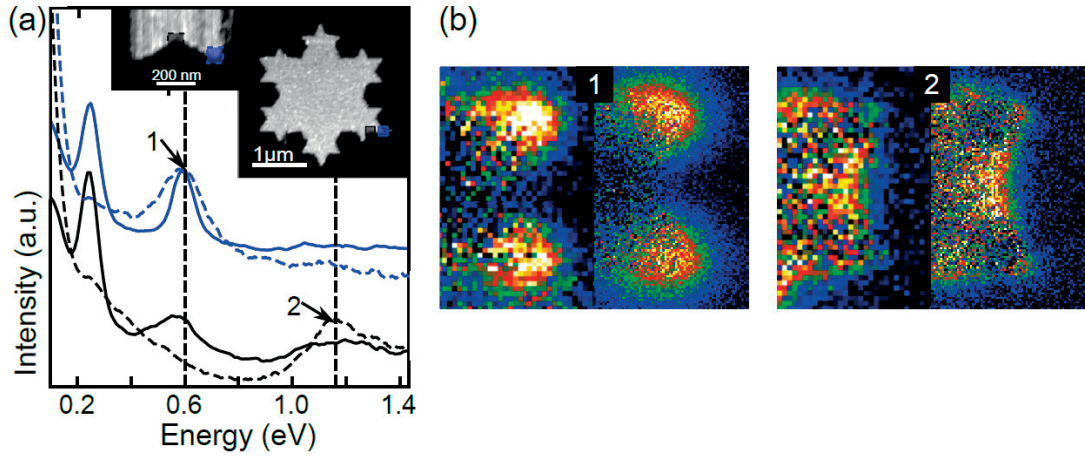


Figure S7 – Side-to-side comparison of the modes in the isolated characteristic edge unit in the 50 μm silver strips (dashed lines) and in the full Koch snowflake fractals (solid lines) of iteration 2. (a) EELS spectra acquired at the positions marked on the insets. The spectra of the full Koch snowflake fractal is red shifted 70 meV to align the E_1 modes of both structures. (b) Comparison of the EELS energy filtered maps of the isolated characteristic edge units (right) and of the full snowflake (left) showing that the modes on both structures are equivalent.

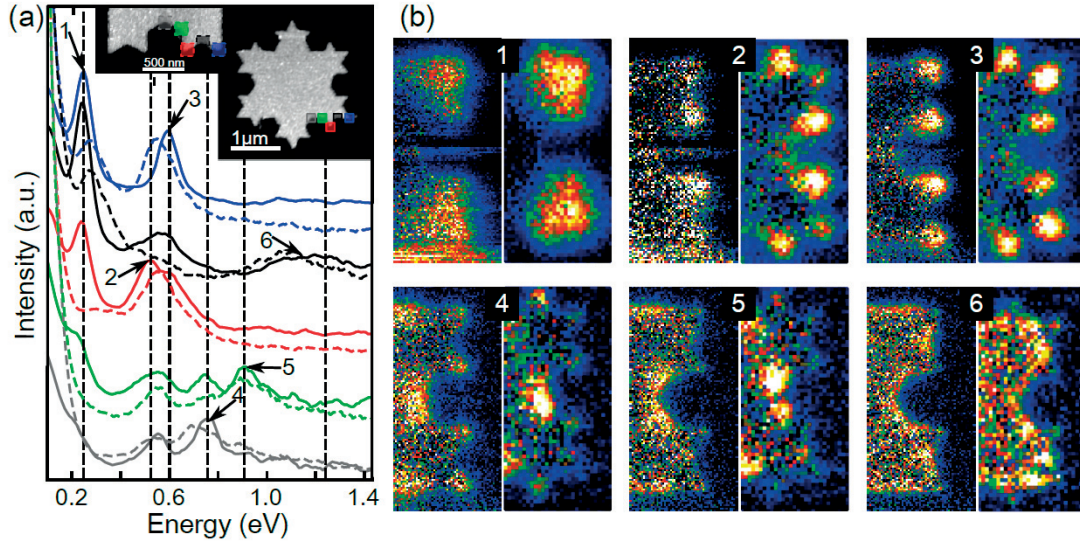


Figure S8 – Side-to-side comparison of the modes in the isolated characteristic edge units in the 50 μm silver strips (dashed lines) and in the full Koch snowflake fractals (solid lines) of iteration 2. (a) EELS spectra acquired at the positions marked on the insets. The spectra of the full Koch snowflake fractal is red shifted 70 meV to align the E_1 modes of both structures. (b) Comparison of the EELS energy filtered maps of the isolated characteristic edge units (left) and of the full snowflake (right) showing that the modes on both structures are equivalent.

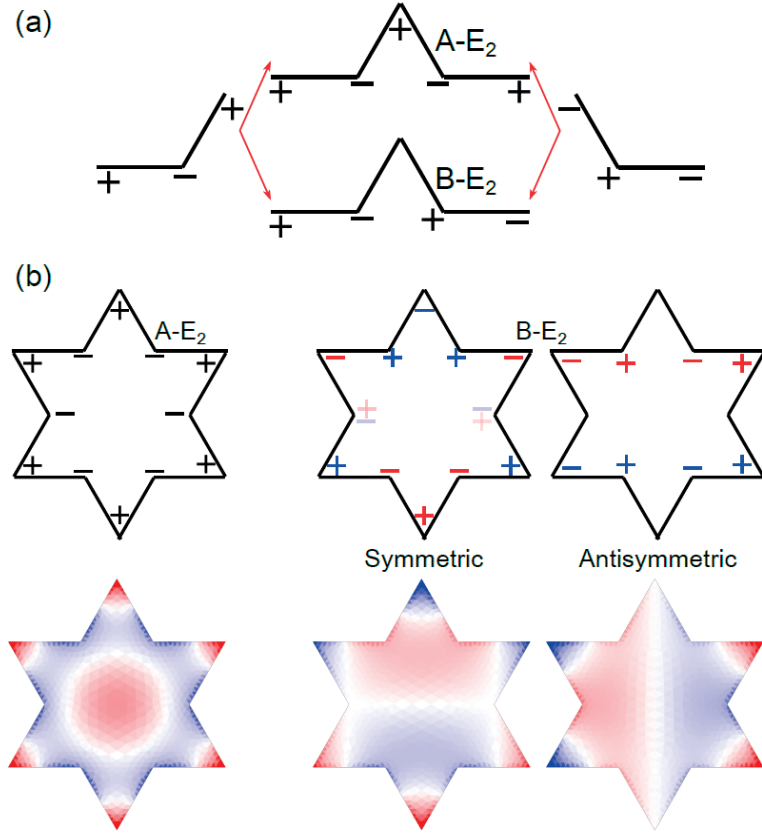


Figure S9 – (a) Energy diagram (not to scale) showing the formation of bonding and antibonding modes due to coupling of E_2 edge modes. (b) Charge distribution diagrams and calculated eigenmodes of the bonding (B) and antibonding (A) E_2 modes in Koch fractal iteration 1. Due to the symmetry of the structure the bonding mode supports two degenerate eigenmodes, and the antibonding mode one non-degenerate eigenmode.

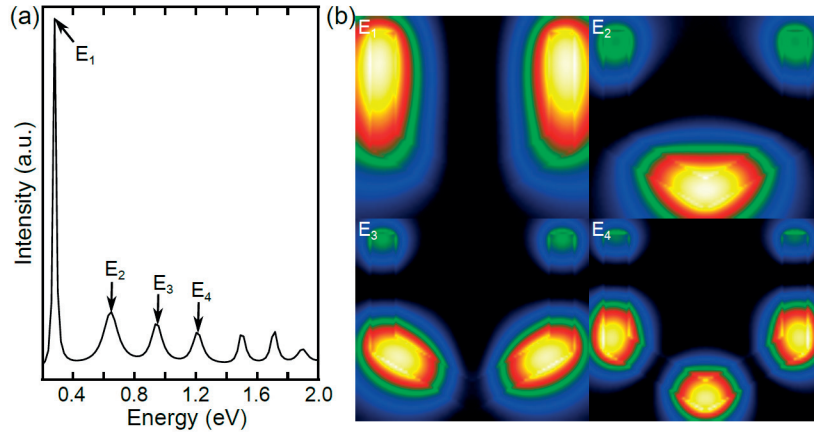


Figure S10 – Simulated EELS spectra (a) and energy filtered maps (b) of a $444 \times 44 \times 30 \text{ nm}^3$ silver nanowire bent in a "U" shape formed by joining two 120 degrees bent nanowires. The maps (b) show that the nodal distribution of a straight nanowires is maintained in the "U" shaped nanowire.

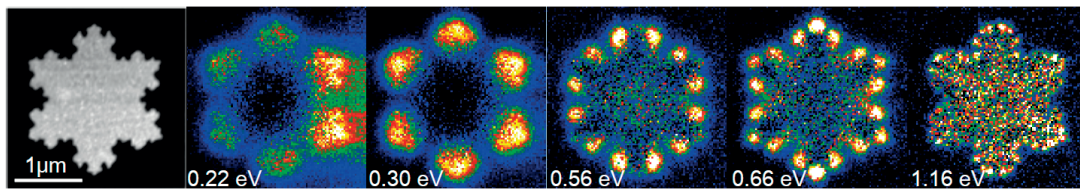


Figure S11 – ADF image on Koch snowflake fractal iteration 3 on the left, and EELS energy filtered maps of the E_1 modes in this fractal structure. The EELS maps have an energy window of 60 meV, with exception of the last map at 1.16 eV that has an energy window of 100 meV.

4 Conclusion and Outlook

Conclusion

In this thesis, eigenmodes of plasmonic nanostructures were used to analyse and interpret several experimental results from SHG and EELS experiments. First, the different approaches for the numerical computation of eigenmodes were presented in details. Three main methods arise from the mathematical formulation of the problem: 1) looking for vanishing determinants/eigenvalues of the matrix describing the system, 2) searching for a diverging response of the system driven by a complex-valued frequency excitation, and 3) a contour integral-based approach that allows finding all resonances included in a given domain of the complex plane. It was found that for the SIE method used in this thesis, the last method was the most efficient, both in terms of computation time, and in terms of ease of use, as it requires little prior knowledge of the structure's response. However, a general approach combining the contour integral method and the complex excitation method seems to be the most advantageous to rapidly obtain accurate results. The integral method is used to effortlessly obtain a good first estimate of the poles positions, and the complex-valued excitation is then used to converge to a more accurate value of each pole, ideally in a few steps.

With respect to SHG, it was first shown how one can use eigenmodes as fundamental sources to compute the corresponding SHG, as opposed to the complete linear response to an excitation. This allows to study separately the different channels of SHG and it was shown that for a nanosphere, a nanorod, and a nanospheres dimer, the fundamental dipolar mode always leads to a quadrupolar resonance. It was also emphasized that the value of the material permittivity at the second harmonic wavelength is of great importance for an efficient SHG. A rigorous multipolar analysis was then used to explain the change of maximum SHG emission direction for gold nanorods of increasing sizes. The interference between the dipolar and quadrupolar second harmonic emissions varies as the relative phase between the different modes changes with the nanorod size. This analytical and numerical analysis gives results in good agreement with the experimental

measurement for the length at which this flip occurs. Finally, the dynamical second harmonic response of a silver nanorod to femtosecond Gaussian pulses was investigated numerically. It was shown that for both linear and nonlinear regimes, the free response of the eigenmodes can be fitted with damped harmonic oscillator models, the parameters of which were deduced from the eigenfrequency of the corresponding eigenmode. The interference effect mentioned previously is observed dynamically, and lasts only while the short-lived transverse dipolar mode is driven by the exciting pulse. Additionally, it was shown that the width and central frequency of the pulse can greatly influence the multipolar dynamics, peak intensity and total radiated energy of the response, both in the linear and nonlinear regimes.

Regarding EELS, eigenmodes and numerical simulations allowed comprehending and analysing experimental EELS spectra of complex metallic nanostructure. First, a new approach to numerically evaluate EELS was proposed. Instead of the usual approach which consists in integrating the work done by the impinging electron against the field scattered by the nanostructure, we add the energy radiated by the nanostructure to the energy dissipated inside it. Both methods show a good agreement, and the new approach allows decomposing the extinction spectra given by EELS into the contributions from scattering (cathodoluminescence) and absorption. Compositionally asymmetric heterodimers of different shapes and metals were then studied. The additional degree of freedom given by the difference between the materials of the two components of the dimer leads to a rich variety of asymmetric modes, increasing the possibilities for the design of specific resonance properties. The experimental EELS maps and spectra showed excellent agreement with the eigenmodes computations, highlighting the importance of both spatial and spectral overlap of the modes of the different constituents to obtain a strong hybridization. Then, dolmen shaped nanostructures with varying central nanorod positions were studied. EELS simulations and eigenmodes computations were conducted on ideal (perfectly symmetric mesh) and realistic (SEM image based mesh) dolmens with very short inter-particle gaps in order to first understand the modal structure of the different geometries, and then investigate the deviation from the ideal cases due to imperfections. The contribution of high order modes such as longitudinal quadrupole as well as transverse dipoles and quadrupoles from the constitutive nanorods was observed numerically and correlated with the experimental EELS data. The eigenmodes evolution with the varying position of the central nanorod was analysed in detail and showed very good agreement with the experimental EELS maps and central energy of the modes. Finally, the first 3 iterations of a Koch fractal antenna were studied. The eigenmodes computation helped disentangle the different contributions of degenerated modes that give the same EELS map, as well as to interpret the modal structure in terms of edge modes. It was also observed that degenerated modes occur by pairs, each having only two odd and/or even reflection symmetries, whereas non-degenerated modes have the C_3 or C_6 rotation symmetry of the structure. Finally, eigenmodes were also computed for the analysis of double resonant antennas for efficient SHG [1], capillary assembled gold

nanorods dimers [2] and graphene discs and disc dimers [3].

Future Developments

The most recent numerical method I have implemented to compute eigenmodes, based on the contour integral method, is extremely faster and more efficient than the first version implemented, namely the vanishing eigenvalue method. However, there are still a few improvements that can be made to facilitate its use. First and foremost, the application of the Cauchy integral method to dielectric nano-structures is still problematic due to the occurrence of spurious poles. As hinted in Ref. [4], this can be due to the RWG basis functions, in which case it will be hard to solve this problem without an in-depth modification of the SIE code. On the other hand, since the apparition of the spurious poles seems to be due to the specific value of the matrix entries, it could be that a different formulation of the SIE matrix than the PMCHWT one could help solve this problem [5]. For now, the contour integral is evaluated with a crude rectangle rule approximation that already gives good results, but the implementation of at least a trapezoidal integration scheme will certainly give more accurate results. One could also envision an algorithm that can separate the spurious poles from the real ones, as it seems that the former are relatively sensitive to the integration path and the number of elements discretizing it. Finally, the natural extension of the actual codes used to compute the eigenmodes would be for the user to use it as a black box, i.e. to be able to give only the mesh of the structure and the permittivities of the different domains, the output being the complex resonant frequencies and the eigenvectors corresponding to the eigenmodes, without the need for the user to guide the program in any way. The application of the code to find the eigenmodes of periodic structures should be relatively straightforward as the matrix corresponding to the periodic case still describes the same phenomenon as in the non-periodic cases [6].

Another point worth addressing is the normalization of the eigenmodes and their use as a basis. Indeed, this is one of the main attractive point of the eigenmode formalism. QNMs lead to some difficulties concerning normalization procedures, although those issues have been investigated in details and partly solved for specific cases [7, 8]. In the framework of SIE, it should be possible to straightforwardly adapt the theory exposed in [4], although it seems that even slight modifications in the numerical formulation of Maxwell's equation can change the rigorous validity of such normalization and expansion procedures [9]. A correct normalization should open the door to several applications, the most natural one being to be able to project the response of a nanostructure onto the eigenmode basis, and thus gain quantitative information about the different eigenmodes participating into the nanostructure response. The other natural use of the eigenmode basis is the possibility to compute the response of the nanostructure to any excitation without having to make a complete SIE computation. Such a projection of the excitation on the eigenmode basis should be much faster than a complete SIE computation, as it

Chapter 4. Conclusion and Outlook

would only need handling several eigenvectors without having to invert the SIE matrix.

Regarding SHG, the eigenmode-based approach proposed in the second chapter (Sec. 2.1) can be extended to the use of different modes (i.e. other than the longitudinal dipole) as well as the combination of two different modes. Using two modes stems from the fact that SHG is a second order nonlinear process, hence it comes from the combination of two fundamental fields. However, instead of using a single mode for each fundamental field, one could also combine different modes in order to study more complex nonlinear responses. This would however require a normalization of the modes to be able to assess the relative influence of one mode in a two-mode channel. Additionally, a normalized eigenmode basis could allow projecting the nonlinear response and thus quantitatively analyse the SHG modal contribution. Finally, the double resonant connected dimer proposed in Ref. [10] is worth investigating in greater details. Indeed, this preliminary study showed that the double resonant condition seemed to be too sensitive to the exact geometry of the junction, making its practical use difficult. However, the mechanism at play is still promising as a way to achieve efficient SHG through double resonance.

Concerning EELS simulations, the question of the possibility of implementing penetrating trajectories in an accurate way is still open. I have made some unsuccessful attempts but the definition of the problem itself is non-trivial [11]; it is also not clear how valid and justifiable certain approximations may be. It is worth noting that penetrating trajectories were successfully implemented in a boundary element scheme [12], which shares a lot of similarities with the SIE method, hinting that it should be possible to do the same in the SIE framework.

As nanofabrication methods allow building more and more complex nanostructures, there is no doubt that an efficient, versatile, and easy-to-use eigenmode methods can benefit the nano-optics community.

Bibliography

- [1] K.-Y. Yang, J. Butet, C. Yan, G. D. Bernasconi, and O. J. F. Martin, “Enhancement Mechanisms of the Second Harmonic Generation from Double Resonant Aluminum Nanostructures,” *ACS Photonics* **4**, 1522–1530, (2017).
- [2] V. Flauraud, M. Mastrangeli, G. D. Bernasconi, J. Butet, D. T. L. Alexander, E. Shahrabi, O. J. F. Martin, and J. Brugger, “Nanoscale topographical control of capillary assembly of nanoparticles,” *Nat. Nanotechnol.* **12**, 73–80, (2016).
- [3] B. Majérus, J. Butet, G. D. Bernasconi, R. T. Valapu, M. Lobet, L. Henrard, and O. J. F. Martin, “Optical second harmonic generation from nanostructured graphene: A full wave approach,” *Opt. Express* **25**, 27015, (2017).
- [4] D. A. Powell, “Interference between the Modes of an All-Dielectric Meta-atom,” *Phys. Rev. Appl.* **7**, (2017).
- [5] C. Forestiere, G. Iadarola, G. Rubinacci, A. Tamburrino, L. Dal Negro, and G. Miano, “Surface integral formulations for the design of plasmonic nanostructures,” *J. Opt. Soc. Am. A* **29**, 2314, (2012).
- [6] B. Gallinet, A. M. Kern, and O. J. F. Martin, “Accurate and versatile modeling of electromagnetic scattering on periodic nanostructures with a surface integral approach,” *J. Opt. Soc. Am. A* **27**, 2261, (2010).
- [7] C. Sauvan, J. P. Hugonin, I. S. Maksymov, and P. Lalanne, “Theory of the Spontaneous Optical Emission of Nanosize Photonic and Plasmon Resonators,” *Physical Review Letters* **110**, (2013).
- [8] P. Lalanne, W. Yan, K. Vynck, C. Sauvan, and J.-P. Hugonin, “Light Interaction with Photonic and Plasmonic Resonances,” *Laser Photonics Rev.* **12**, 1700113, (2018).
- [9] J. Mäkitalo, M. Kauranen, and S. Suuriniemi, “Modes and resonances of plasmonic scatterers,” *Physical Review B* **89**, 165429, (2014).
- [10] G. D. Bernasconi, J. Butet, V. Flauraud, D. T. L. Alexander, J. Brugger, and O. J. F. Martin, “Second harmonic generation in plasmonic nanostructures: A double dipolar

Bibliography

- resonant antenna design,” in *2017 Conference on Lasers and Electro-Optics Europe European Quantum Electronics Conference (CLEO/Europe-EQEC)*, 1–1, (2017).
- [11] I. Tamm, “Radiation emitted by uniformly moving electrons,” *Journal of Physics-USSR* **1**, 439–454, (1939).
- [12] U. Hohenester, “Simulating electron energy loss spectroscopy with the MNPBEM toolbox,” *Computer Physics Communications* **185**, 1177–1187, (2014).

Publications and Conferences

Publications

Published

1. **Gabriel D. Bernasconi**, J       Butet, and Olivier J. F. Martin, "Mode analysis of second-harmonic generation in plasmonic nanostructures", *J. Opt. Soc. Am. B* **33**, 768-779 (2016).
2. J       Butet, T. V. Raziman, Kuang-Yu Yang, **Gabriel D. Bernasconi**, and Olivier J. F. Martin, "Controlling the nonlinear optical properties of plasmonic nanoparticles with the phase of their linear response", *Opt. Express* **24**, 17138-17148 (2016).
3. Valentin Flauraud, Massimo Mastrangeli, **Gabriel D. Bernasconi**, Jeremy Butet, Duncan T. L. Alexander, Elmira Shahrabi, Olivier J. F. Martin and Juergen Brugger, "Nanoscale topographical control of capillary assembly of nanoparticles", *Nat. Nanotech.* **12**, 73-80 (2017).
4. **Gabriel D. Bernasconi**, J       Butet, Valentin Flauraud, Duncan T.L. Alexander, J       Brugger and Olivier J.F. Martin "Where Does Energy Go in Electron Energy-Loss Spectroscopy of Nanostructures?", *ACS Photonics* **4**, 156-164, (2017).
5. Valentin Flauraud, **Gabriel D. Bernasconi**, Jeremy Butet, Massimo Mastrangeli, Duncan T.L. Alexander, Olivier J.F. Martin, and J       Brugger "Mode Evolution in Strongly Coupled Plasmonic Dolmens Fabricated by Templated Assembly", *ACS Photonics* **4**, 1661-1668, (2017).
6. Valentin Flauraud, **Gabriel D. Bernasconi**, J       Butet, Duncan T.L. Alexander, Olivier J.F. Martin, and J       Brugger "Mode Coupling in Plasmonic Heterodimers Probed with Electron Energy Loss Spectroscopy", *ACS Nano* **11**, 3485-3495, (2017).
7. Edson P. Bellido, **Gabriel D. Bernasconi**, David Rossouw, J       Butet, Olivier J. F. Martin, and Gianluigi A. Botton "Self-similarity of plasmon edge modes on Koch fractal antennas", *ACS Nano* **11**, 11240-11249, (2017).

Bibliography

8. Jérémy Butet, **Gabriel D. Bernasconi**, Marlène Petit, Alexandre Bouhelier, Chen Yan, Olivier J.F. Martin, Benoît Cluzel, and Olivier Demichel "Revealing a Mode Interplay That Controls Second-Harmonic Radiation in Gold Nanoantennas", *ACS Photonics* **4**, 2923-2929, (2017).
9. Kuang-Yu Yang, Jérémy Butet, Chen Yan, **Gabriel D. Bernasconi**, and Olivier J.F. Martin "Enhancement Mechanisms of the Second Harmonic Generation from Double Resonant Aluminum Nanostructures", *ACS Photonics* **4**, 1522-1530, (2017).
10. Bruno Majérus, Jérémy Butet, **Gabriel D. Bernasconi**, Raziman Thottungal Valapu, Michaël Lober, Luc Henrard and Olivier J.F. Martin "Optical second harmonic generation from nanostructured graphene: A full wave approach", *Opt. Express* **25**, 27015-27027, (2017).
11. **Gabriel D. Bernasconi**, Jérémy Butet and Olivier J. F. Martin, "Dynamics of Second Harmonic Generation in a Plasmonic Silver Nanorod", *ACS Photonics* **5**, 3246-3254, (2018).
12. Karim Achouri, **Gabriel D. Bernasconi**, Jérémy Butet and Olivier J. F. Martin, "Homogenization and Scattering Analysis of Second-Harmonic Generation in Nonlinear Metasurfaces", *IEEE Trans. Ant. Prop.*, **66**, 6061-6075 (2018).
13. Jérémy Butet, **Gabriel D. Bernasconi** and Olivier J.F. Martin "Silencing the Optical Second Harmonic Generation from Plasmonic Nanodimers: A Comprehensive Discussion", *Beilstein J. Nanotechnol.* **9**, 2674-2683, (2018).

In preparation

1. Enrico Rossi, Duncan T.L. Alexander, Jérémy Butet, **Gabriel D. Bernasconi**, Olivier Martin and Vincenzo Amendola "Surface plasmon resonance in single Au-Fe nanoalloys", in preparation.
2. Jiyong Wang, Jérémy Butet, **Gabriel D. Bernasconi**, Anne-Laure Baudrion, Andreas Horrer, Anke Horneber, Olivier J. F. Martin, Alfred J. Meixner, Monika Fleischer, Pierre-Michel Adam and Dai Zhang "Resonant Oscillating Second-harmonic Generation from Plasmonic Nanoantennas", in preparation.
3. Debdatta Ray, T.V. Raziman, Christian Santschi, **Gabriel D. Bernasconi**, Dordaneh Etezadi, Hatice Altug, and Olivier J.F. Martin "Hybrid metal-dielectric metasurfaces for refractive index sensing", in preparation.
4. **Gabriel D. Bernasconi**, Jérémy Butet and Olivier J. F. Martin, "Eigenmodes and Optical Resonances in Nanoparticles", in preparation.

Conference Contributions

1. **Gabriel D. Bernasconi**, Jérémy Butet, and Olivier J. F. Martin, "*Second harmonic generation reveals dark modes in plasmonic nanostructures*", Poster presentation, The 7th International Conference on Surface Plasmon Photonics (SPP7), Jerusalem, May-June 2015.
2. **Gabriel D. Bernasconi**, Jérémy Butet, and Olivier J. F. Martin, "*Optimization of second harmonic generation in plasmonic nanostructures by mode matching*", Oral presentation, The 36th Progress In Electromagnetics Research Symposium (PIERS), Prague, Czech Republic, July 2015.
3. **Gabriel D. Bernasconi**, Jérémy Butet, Valentin Flauraud, Duncan T.L. Alexander, Chen Yan, Jürgen Brugger and Olivier J.F. Martin "*New insights into plasmonic responses with an eigenmodes analysis*", Poster presentation, Gordon Research Conference (GRC) on plasmonics and nanophotonics, Newry, Maine, USA, July 2016.
4. **Gabriel D. Bernasconi**, Jérémy Butet, Valentin Flauraud, Duncan T.L. Alexander, Chen Yan, Jürgen Brugger and Olivier J.F. Martin "*Second harmonic generation from connected dimers: a double resonant design based on charge transfer plasmon*", Poster presentation, The 14th International Conference of Near-Field Optics, Nanophotonics and Related Techniques (NFO14), Hamamatsu, Japan, September 2016.
5. **Gabriel D. Bernasconi**, Valentin Flauraud, Jérémy Butet, Duncan T.L. Alexander, Jürgen Brugger and Olivier J.F. Martin "*Eigenmode study of coupled plasmonic nanostructures: Hetero dimer and dolmen structures*", Oral presentation, The 38th Progress In Electromagnetics Research Symposium (PIERS), St-Petersburg, Russia, May 2017.
6. **Gabriel D. Bernasconi**, Jérémy Butet, Valentin Flauraud, Duncan T.L. Alexander, Jürgen Brugger and Olivier J.F. Martin "*Second Harmonic Generation in Plasmonic Nanostructures: A Double Dipolar Resonant Antenna Design*", Oral presentation, Conference on Lasers and Electro-Optics Europe & European Quantum Electronics Conference (CLEO-EQEC), Munich, Germany, June 2017.
7. **Gabriel D. Bernasconi**, Jérémy Butet, and Olivier J. F. Martin, "*Second Harmonic Generation Dynamics in Plasmonic Nanoparticles*", Oral presentation, SPIE Optics+Photonics, San Diego, California, USA, August 2018.
8. **Gabriel D. Bernasconi**, Jérémy Butet, and Olivier J. F. Martin, "*Modes Interplay in the Second Harmonic Generation Dynamics of Plasmonic Nanoparticles*" Poster presentation, The 15th International Conference of Near-Field Optics, Nanophotonics and Related Techniques (NFO15), Troyes, France, August 2018.

Acknowledgements

During the four years I spent at EPFL as a PhD student, I had the chance to enjoy a perfect balance between freedom and guided supervision, I could not have wished for a better environment. Additionally, I was given the chance and encouraged to travel the world to participate to some of the best conferences in the field, a most enriching experience. My time at the NAM was one of discovery, of curiosity fulfilment, and of learning. For all of that, I would like to sincerely thank my thesis supervisor Prof. Olivier Martin.

I would like to thank Prof. Cécile Hébert, Prof. Ulrich Hohenester and Prof. Martti Kauranen for accepting to be examiners of my thesis, as well as Prof. Jacques-Edouard Moser for taking the role of jury president. Thanks to all my NAM colleagues throughout those 4 years, Kuang-Yu, Chen, Volodymyr, Banafsheh, Robert, Xiaolong, Shourya, Madasamy, Hsiang-Chu, Jenna, Marco, Mintae, Debdatta, Michail, Christian, Andrei, Aleksa, Karim, Toralf and David. A very special thanks to Raziman whose insights into plasmonics and physics were always helpful, and without whom I would not have gotten very far with my limited coding skills. Jérémy Butet, thanks for everything you taught me. I realize that I was very lucky to have you as a co-supervisor, colleague and friend. Béatrice, thank you for taking care of the coffee supply, the Christmas parties, and every (little) things that I am not aware of but I am sure make the life in the lab run smoothly. Cathy, thank you for taking care of the EDPO-related administration.

Thanks to the "dream team", Dr. V. Flauraud, Dr. M. Didier, Dr. M. Sison and Vincent, for all the good times. Collaborations are aimed to use each other's competences, but if you are lucky you can also find someone with whom you get along with; Valentin, if I had to list everything I should thank you for, well, it would be too long. From a "Fameux Wafer" to a $+10i$, passing by conferences and holidays as well as many great paper ideas that will never see the light of day, our many stimulating discussions, serious and less serious, lead to a most fruitful collaboration that shaped a large part of this thesis. Bresh, merci pour ces moments nectarifères pendant ta présence au début de ma thèse.

A very big thanks to Duncan Alexander for investing so much time into the EELS measurements. Thanks to the dedication and efficiency of the staff of the CM2420,

Bibliography

especially Jean-Luc, Albano and Bastien. A special thanks to Prof. Vincenzo Savona who suggested iterative methods to compute the smallest eigenvalue of a matrix during my candidacy exam, and to Prof. Ulrich Hohenester and Dr. Andreas Trügler who talked to me about the contour integral method to find the poles of a matrix. I would also like to thank Hervé Eusèbe who was my supervisor during my bachelor projects at hepia and who is partly responsible for my interest in electromagnetism and my choice of pursuing a PhD; tu avais raison, c'est souvent un problème de mode. Finally, I'd like to thank my parents who always supported me during my studies and let me choose my own path.

Lausanne, December 2018

Gabriel Bernasconi

Chemin Vermont 18
1006 Lausanne
+41 79 793 63 09

Born on May the 20th 1990
Nationality: Swiss
bernasconi.gabriel.david@gmail.com

Gabriel Bernasconi

Education

- 11.2014 – 12.2018 **EPFL**: PhD student, Photonics Doctoral School.
Study of second harmonic generation in plasmonic nanostructures and eigenmode analysis. Nanophotonics and Metrology Laboratory (NAM).
Supervisors: Olivier J. F. Martin & Jérémy Butet.
- Development of numerical methods for electrodynamic full-wave simulations and eigenmodes computation.
 - Analysis of resonant properties of metallic nanostructures and their link with the generation of second-harmonic light as well as their electron energy loss spectroscopy response.
 - Teaching assistant in Bachelor and Master classes.
- 03.2014 – 07.2014 **Swiss Army**: Mandatory service in nuclear, biological and chemical defense.
- 09.2012 – 03.2014 **EPFL**: Master of science in microengineering, applied optics.
- Diploma project: *Design and analysis of a near the eye display*. Recording of RGB holograms on photopolymers, conception of a device to measure the diffraction efficiency of holograms at the Laboratory of Applied Photonic Devices (LAPD).
 - Semester projects :
 - *Development of augmented reality glasses*: Recording of RGB holograms on photopolymers at the LAPD.
 - *Accelerated simulations for thin film photovoltaics*: Theoretical work and Matlab simulation of periodic structures at the Optics & Photonics Technology Laboratory (OPT).
- 09.2011 – 06.2012 **EPFL**: HES pathway year to join the microengineering master.
- 09.2008 – 06.2011 **hepia (HES)**, Geneva: Bachelor of science in microengineering, applied physics.
- Diploma project: *Hyperfrequency filter for single photon detection*. Conception (design, simulation, fabrication and measure) of a microwave interferometric filter and study of an avalanche photodiode for single photon detection, in collaboration with the GAP optique of the Geneva university. Obtained with honours.
09. 2005 – 06.2008 **Ecole d'enseignement technique**, Geneva : Technical maturity.

Work experience

- 07.2013 – 10.2013 **Rofin Lasag**, Thun: Internship. Measurement of the nonlinear efficiency conversion from 1064nm to 532nm of a NdYAG laser and study of a way to compensate for the thermal lensing effect.
- 09.2012 – 12.2012 **EPFL**, Lausanne: Assistant in the analyse III exercice sessions.
- 08.2011 – 09.2011 **Creative Heating Service SA**, Geneva: Engineer. Comsol Simulation of a microwave oven for the obtention of a patent (153 hours of work).
- 07.2008 **Selba SA**, Versoix: Employee.
- 04.2008 – 06.2008 **MFG.com**, Chavannes des bois: Intern in informatics.

Publications ([google scholar](#))

- **Gabriel D. Bernasconi**, Jérémy Butet, and Olivier J. F. Martin, "Mode analysis of second-harmonic generation in plasmonic nanostructures", *J. Opt. Soc. Am. B* **33**, 768-779 (2016).
- Jérémy Butet, T. V. Raziman, Kuang-Yu Yang, **Gabriel D. Bernasconi**, and Olivier J. F. Martin, "Controlling the nonlinear optical properties of plasmonic nanoparticles with the phase of their linear response", *Opt. Express* **24**, 7138-17148 (2016).
- Valentin Flauraud, Massimo Mastrangeli, **Gabriel D. Bernasconi**, Jeremy Butet, Duncan T. L. Alexander, Elmira Shahrabi, Olivier J. F. Martin and Juergen Brugger, "Nanoscale topographical control of capillary assembly of nanoparticles", *Nat. Nanotech.* **12**, 73-80 (2017).
- **Gabriel D. Bernasconi**, Jérémy Butet, Valentin Flauraud, Duncan T.L. Alexander, Jürgen Brugger and Olivier J.F. Martin "Where Does Energy Go in Electron Energy-Loss Spectroscopy of Nanostructures?", *ACS Photonics* **4**, 156-164, (2017).
- Valentin Flauraud, **Gabriel D. Bernasconi**, Jeremy Butet, Massimo Mastrangeli, Duncan T.L. Alexander, Olivier J.F. Martin, and Jürgen Brugger "Mode Evolution in Strongly Coupled Plasmonic Dolmens Fabricated by Templated Assembly", *ACS Photonics* **4**, 1661-1668, (2017).
- Valentin Flauraud, **Gabriel D. Bernasconi**, Jérémy Butet, Duncan T.L. Alexander, Olivier J.F. Martin, and Jürgen Brugger "Mode Coupling in Plasmonic Heterodimers Probed with Electron Energy Loss Spectroscopy", *ACS Nano* **11**, 3485- 3495, (2017).
- Edson P. Bellido, **Gabriel D. Bernasconi**, David Rossouw, Jérémy Butet, Olivier J. F. Martin, and Gianluigi A. Botton "Self-similarity of plasmon edge modes on Koch fractal antennas", *ACS Nano* **11**, 11240-11249, (2017).
- Jérémy Butet, **Gabriel D. Bernasconi**, Marlène Petit, Alexandre Bouhelier, Chen Yan, Olivier J.F. Martin, Benoît Cluzel, and Olivier Demichel "Revealing a Mode Interplay That Controls Second-Harmonic Radiation in Gold Nanoantennas", *ACS Photonics* **4**, 2923-2929, (2017).
- Kuang-Yu Yang, Jérémy Butet, Chen Yan, **Gabriel D. Bernasconi**, and Olivier J.F. Martin "Enhancement Mechanisms of the Second Harmonic Generation from Double Resonant Aluminum Nanostructures", *ACS Photonics* **4**, 1522-1530, (2017).
- Bruno Majérus, Jérémy Butet, **Gabriel D. Bernasconi**, Raziman Thottungal Valapu, Michaël Lober, Luc Henrard and Olivier J.F. Martin "Optical second harmonic generation from nanostructured graphene: A full wave approach", *Opt. Express* **25**, 27015-27027, (2017).
- **Gabriel D. Bernasconi**, Jérémy Butet and Olivier J. F. Martin, "Dynamics of Second Harmonic Generation in a Plasmonic Silver Nanorod", *ACS Photonics* **5**, 3246-3254, (2018).
- Karim Achouri, **Gabriel D. Bernasconi**, Jérémy Butet and Olivier J. F. Martin, "Homogenization and Scattering Analysis of Second-Harmonic Generation in Nonlinear Metasurfaces", *IEEE Trans. Ant. Prop.*, **66**, 6061-6075 (2018).
- Jérémy Butet, **Gabriel D. Bernasconi** and Olivier J.F. Martin "Silencing the Optical Second Harmonic Generation from Plasmonic Nanodimers: A Comprehensive Discussion", *Beilstein J. Nanotechnol.* **9**, 2674-2683, (2018).

Technical skills

IT

- Finite element method simulation for electrodynamics.
- Matlab: good general knowledge and basics in signal and image processing.
- Comsol multiphysics: radiofrequency, microwave heating modules and meshing.
- Latex: basic knowledge.
- C/C++: basic knowledge.

Specific practical and theoretical skills

- Good knowledge in theoretical electrodynamics and optics.
- Optical devices:
 - Hologram recording.
 - Optical alignment.
 - NdYAG laser and second harmonic generation.
- Basic knowledge in acoustics.
- Basic knowledge in nuclear physics and notion of radioprotection.

Soft Skills

Persistence, proactive, creative, critical thinking, teamwork.

Interests

Sciences in general, especially electrodynamics and its history, music.

Languages

French:	Mother tongue
English:	Fluent
German:	Basic

